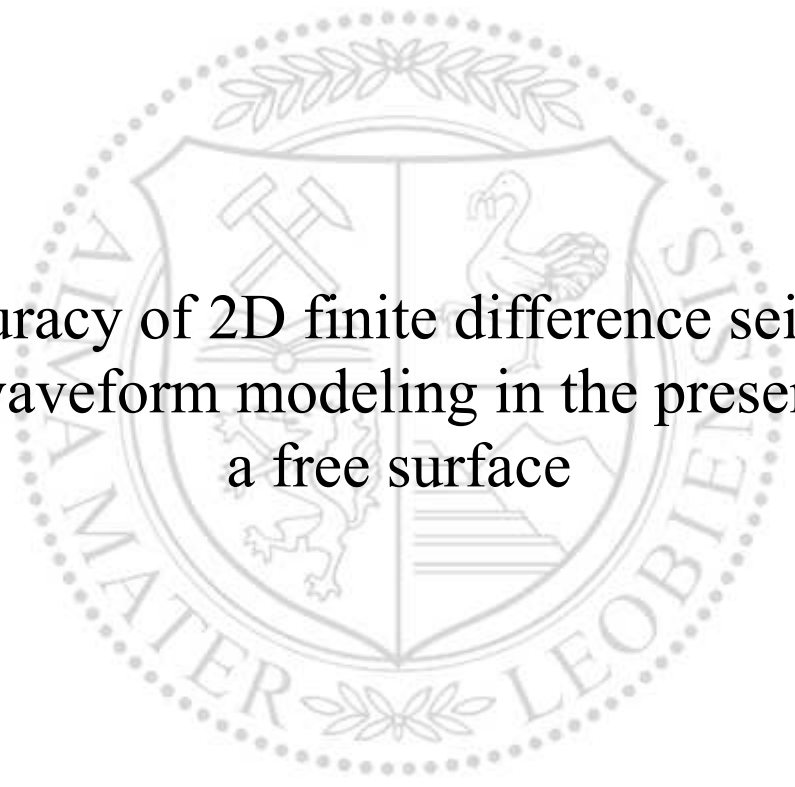




Chair of Applied Geophysics

Master's Thesis



Accuracy of 2D finite difference seismic
full-waveform modeling in the presence of
a free surface

Timo Sebastian Krause, BSc

May 2023



MONTANUNIVERSITÄT LEOBEN

www.unileoben.ac.at

EIDESSTÄTLICHE ERKLÄRUNG

Ich erkläre an Eides statt, dass ich diese Arbeit selbständig verfasst, andere als die angegebenen Quellen und Hilfsmittel nicht benutzt, und mich auch sonst keiner unerlaubten Hilfsmittel bedient habe.

Ich erkläre, dass ich die Richtlinien des Senats der Montanuniversität Leoben zu "Gute wissenschaftliche Praxis" gelesen, verstanden und befolgt habe.

Weiters erkläre ich, dass die elektronische und gedruckte Version der eingereichten wissenschaftlichen Abschlussarbeit formal und inhaltlich identisch sind.

Datum 23.05.2023

Unterschrift Verfasser/in
Timo Sebastian Krause

Acknowledgements

I would like to thank Prof. Florian Bleibinhaus for the interesting topic and his guidance during my work. Special thanks to Daniel Köhn from the Christian-Albrechts-Universität zu Kiel for the support regarding his DENISE code. Next, I want to thank Natalia Banasiak for proofreading this thesis and all the discussions about the topic of this thesis.

Furthermore, I would like to thank all other members of the Chair of Applied Geophysics at the Montanuniversität Leoben for the pleasant work environment, especially Natalia Banasiak and Bernd Trabi, with whom I shared an office during most of the time. Also, I would like to thank Elham Hashem for the IT-support especially during the home office times. Many thanks to Christiane Pretzenbacher for the help with all sorts of administrative issues.

Many thanks to Franziska Yaldez for all the love and support, not only but especially during writing this thesis. Special thanks to my cat Sushi (alias Chonky) for the countless hours of company and sitting on my lap purring while working on this thesis. I wish you would still be with us.

Last but not least, I want to thank my family and friends for all the support during my studies at Montanuniversität Leoben.

Abstract

Full-waveform inversion is a widely used method in seismic imaging, which involves the numerical modeling of the seismic wavefield. The question of how accurate this modeling is, is seldom discussed. This is a particular problem in land seismics and in the presence of topographic variations. For various reasons, the standard approach to waveform modeling in exploration seismology is the finite difference (FD) method. The implementation of a free surface boundary for a topographic surface in FD waveform modeling may be done as an internal boundary of the model in the heterogeneous approach or as an explicit condition at the free surface in the homogeneous approach. The widely used implementation of the image method (homogeneous), and the improved vacuum formulation (heterogeneous), are tested for their accuracy using two 2D FD modeling algorithms, `ve2d_ref` and `DEINSE Black Edition`, which implement these conditions to define an irregular free surface. These algorithms are first tested for their accuracy using analytical solutions in an elastic homogeneous full space, then for elastic homogeneous half-spaces with a planar and tilted free surface between 0 and 20°. Furthermore, the application to a viscoelastic inhomogeneous model with a topographic free surface is investigated. For all models, errors are introduced in the near-field for various reasons. At higher offsets, errors associated with the absorbing boundary frames or free surface become more prevalent. For a planar free surface, the accuracy tests show that the image method requires fewer points per minimum wavelength to accurately model the full waveforms than the improved vacuum formulation. In the case of a free surface not aligned with the axis of the FD grid, the free surface conditions show different behaviour, with the improved vacuum formulation producing higher errors than the image method at very small tilt angles ($<5^\circ$). The accuracy of the improved vacuum formulation is highly dependent on the tilt angle. The convergence behaviour of the image method moves smoothly towards smaller errors, while the improved vacuum formulation remains constant and, after reaching a critical point in the discretisation, rapidly converges to small errors comparable, or better, than those achieved by the image method. This smooth convergence behaviour of the image method is easier to interpret than the fluctuation of relative differences in convergence tests, especially when dealing with inhomogeneous models with a topographic free surface, where there is no analytical solution available.

Zusammenfassung

Die Vollwellenform-Inversion ist eine weit verbreitete Methode in der seismischen Bildgebung, die eine numerische Modellierung des seismischen Wellenfelds beinhaltet. Die Frage, wie gut diese Modellierung ist, wird selten thematisiert. Das ist ein Problem insbesondere in der Landseismik und bei Vorhandensein topografischer Variationen. Aus verschiedenen Gründen ist der Standardansatz der Wellenformmodellierung in der Explorationsseismik die Finite-Differenzen (FD) Methode. Die Implementierung einer freien Oberfläche mit Topografie in die FD-Wellenform-Modellierung kann als interne Grenze des Modells beim heterogenen Ansatz oder als explizite Bedingung an der freien Oberfläche beim homogenen Ansatz erfolgen. Die weit verbreitete Implementierung der Image-Methode (homogen) und die verbesserte Vakuum-Formulierung (heterogen) werden anhand von zwei 2D-FD-Modellierungsalgorithmen, `ve2d_ref` und `DEINSE Black Edition`, die diese Bedingungen zur Definition einer unregelmäßigen freien Oberfläche umsetzen, auf ihre Genauigkeit geprüft. Diese Algorithmen werden zunächst auf ihre Genauigkeit in einem elastischen homogenen Vollraum und anschließend für elastische homogene Halbräume mit einer ebenen und geneigten freien Oberfläche zwischen 0 und 20° geprüft für die es einen analytischen Vergleich gibt. Weiters wird die Anwendung auf ein viskoelastisches inhomogenes Modell mit einer topographischen freien Oberfläche untersucht. Während der gesamten Modellierung treten im Nahfeld Fehler auf, für die es verschiedene Gründe gibt, die schwer zu pauschalisieren sind. Diese Fehler nehmen mit zunehmendem Offset schnell ab, und bei größeren Offsets treten Fehler im Zusammenhang mit den absorbierenden Modellgrenzen oder der freien Oberfläche stärker in Erscheinung. Für eine ebene freie Oberfläche zeigen die Genauigkeitstests, dass die Image-Methode für eine genaue Modellierung der vollen Wellenformen weniger Punkte pro minimaler Wellenlänge benötigt als die verbesserte Vakuum-Formulierung. Im Falle einer freien Oberfläche, die nicht mit der Achse des FD-Gitters ausgerichtet ist, zeigen die Bedingungen der freien Oberfläche Unterschiede auf, wobei die verbesserte Vakuum-Formulierung bei sehr kleinen Neigungswinkeln ($<5^\circ$) höhere Fehler als die Image-Methode produziert, was dazu führt, dass die Genauigkeit der verbesserten Vakuum-Formulierung stark vom Neigungswinkel abhängt. Das Konvergenzverhalten der Image-Methode verläuft stetig zu niedrigeren Fehlern hin, während die verbesserte Vakuum-Formulierung konstant bleibt und nach Erreichen eines kritischen Punktes in der Diskretisierung schnell zu niedrigen Fehlern konvergiert, die vergleichbar oder besser sind als Fehler der Image-Methode. Dieses gleichmäßige Konvergenzverhalten der Image-Methode ist leichter zu interpretieren als das teilweise erratische Verhalten der verbesserten Vakuum-Formulierung. Das ist besonders relevant für die Anwendung auf inhomogene Modelle mit einer topographischen freien Oberfläche, für die es keine analytische Lösung gibt.

Contents

1. Introduction	1
2. Theory	3
2.1. Attenuation model	5
2.2. Analytical Solutions and 2D Grid approximation	7
2.3. Discretization of the wave equation	10
2.4. Finite difference approach	11
2.5. Numerical Stability	14
2.5.1. Grid dispersion	15
2.5.2. Courant instability	16
2.6. Absorbing boundary conditions	17
2.7. Free Surface	18
2.8. Source implementation	22
3. Programs and implementations	25
3.1. Analytical solution	26
3.2. Numerical waveform modeling programs	26
3.2.1. DENISE Black Edition	26
3.2.2. Viscoelastic wavepropagation in 2 dimensions (ve2d_ref)	27
3.3. Model parametrisation	28
3.3.1. Source function	28
3.3.2. Test model dimensions, boundaries, and modeling parameters	29
4. Processing of synthetic data	33
4.1. Synthetic amplitude normalisations	33
4.2. Error calculation	35
4.3. Wavefield investigation	36
5. Elastic homogeneous full space	38
5.1. Model specifics	38
5.2. Modelled wavefields	39
5.2.1. Spatial divergence	39
5.2.2. Spatial curl	40
5.3. Receiver components	41
5.3.1. Horizontal particle velocity	41
5.3.2. Vertical particle velocity	44

5.3.3.	Mean relative error	47
5.4.	Summary of modeling errors	48
6.	Elastic homogeneous half-space with a horizontal free surface	49
6.1.	Model specifics	49
6.2.	Modelled wavefields	50
6.2.1.	Spatial divergence	50
6.2.2.	Spatial curl	51
6.3.	Receiver components	52
6.3.1.	Horizontal component	52
6.3.2.	Mean relative error	59
6.4.	Convergence tests	62
6.5.	Summary of modeling errors	64
7.	Elastic homogeneous half-space with a tilted free surface	66
7.1.	Model specific parameters	66
7.2.	Numerically modelled wavefields	67
7.2.1.	Spatial divergence	67
7.2.2.	Spatial curl	68
7.3.	Receiver components	71
7.3.1.	Horizontal component	71
7.4.	Convergence tests	80
7.5.	Summary of modeling errors	82
8.	Inhomogeneous model with a topographic free surface	84
8.1.	SAFOD Seismic refraction survey	84
8.2.	Model parametrisation	85
8.3.	Numerically modelled wavefields	88
8.3.1.	Spatial divergence	88
8.3.2.	Spatial curl	89
8.4.	Receiver components	90
8.4.1.	Horizontal particle velocity	90
8.5.	Convergence tests	91
8.6.	Summary of the modeling	96
9.	Discussion	97
10.	Conclusion	99
11.	References	100

List of figures	104
List of tables	109
Appendix A Relative errors of the vertical component for a flat free surface	110
Appendix B Relative errors over offset for tilted free surfaces with 1, 5 and 20°	112
Appendix C SAFOD model convergence over offsets horizontal component	118

1. Introduction

Creating models of the subsurface from seismic data may be achieved by a multitude of methods such as reflection seismic imaging or seismic tomography. Accurate models that describe the data acquired by seismic surveys may be inverted for seismic velocities using travel time tomography or waveform inversion.

The full waveform inversion (FWI) has the capability to find high resolution subsurface models by utilizing full seismograms as opposed to extracted features such as travel time. As the name suggests, FWI models the full wavefield as the forward problem. The first theoretical concepts of FWI were already developed by Tarantola (1984) but at this time the computation was too expensive to be fully realised. Advancements in computational power over the past 40 years have made the resource heavy computation of wavefields a viable option for large models. However, the FWI processes are highly nonlinear and require a good starting model to generate proper results for complex models. The waveform modeling required for the FWI approach is influenced by a lot of factors such as boundaries source implementation, spatial and temporal discretisation (Virieux et al., 2012).

A problem of specific interest is the surface boundary, since any type of seismic survey, be it land- or marine based, has to deal in some way with a surface boundary. While marine surveys deal with the flat water level, land surveys are affected by the topography of the survey area, which may incorporate significant topographic height differences. One such survey affected by topography is the 2D seismic refraction survey near the San Andreas Fault Observatory at Depth (SAFOD) which has a topography varying a total span of 800 m across a 48 km profile. Investigations by Bleibinhaus et al. (2007) also use an acoustic waveform inversion to better describe the subsurface. Models such as this are highly affected by the shape of the surface and a topographic free surface condition must be applied.

The free surface of a model is a crucial determining factor in modeling seismic wavefields since here surface waves are generated as well as conversions of other wave phases are happening. The implementation of the free surface in the model space may be done as an explicit free surface condition or the free surface may be handled as an internal boundary. These approaches were called the homogeneous and heterogeneous approach by Bohlen and Saenger (2006). Some modeling techniques such as the finite element method enable the adaptation of the mesh to follow the free surface, making an implementation of an explicit boundary relatively easy (Komatitsch & Tromp, 1999). A ridged definition of the modeling grid as used in the popular finite difference (FD) modeling approach has problems dealing with irregular surfaces and generate a stepped staircase function (Robertsson, 1996; Zeng et al., 2012).

Most surface boundaries assume a vacuum above the free surface where no waves are traveling and directly at the boundary no stresses may be present. This method of defining the surface is called at traction free surface (Levander, 1988) and is the most popular definition of a surface boundary. An explicit boundary condition is the image method by Levander (1988) which has been extended to incorporate the topography by Robertsson (1996). Another method to implement such a boundary is assuming an implicit vacuum layer above the surface (Graves, 1996; Zahradník et al., 1993). These methods are quite attractive due to the ease of implementing such a boundary since there would be no need to implement explicit conditions at the surface (Bohlen & Saenger, 2006) but have severe numerical problems for higher order FD operators (Gottschämmer & Olsen, 2001; Graves, 1996; Zeng et al., 2012).

Both approaches are plagued by numerical inaccuracies if a free surface is described by a stepped staircase function (Bohlen & Saenger, 2006; Zeng et al., 2012) and fine spatial discretisation are required to achieve good accuracies while modeling Rayleigh waves (Bohlen & Saenger, 2006).

To estimate the accuracy of a numerical result, it is compared with an analytical solution to the problem the numerical method is trying to solve. These analytical solutions exist for modeling seismic waves for simple cases as elastic homogeneous full and half-spaces. In these cases, an error may be estimated directly for any numerical result. If no analytical solution exists for a model estimating the accuracy of a numerical solution to that problem proves to be difficult. Here convergence tests are commonly applied, which monitor the change of the numerical solution with the increasing resolution (Igel, 2016). For FD waveform modeling with a free surface the main weak point is the spatial resolution which has to be high in order to avoid severe numerical inaccuracies (Bohlen & Saenger, 2006; Zeng et al., 2012) and convergence tests are conducted with increasing spatial resolutions.

However, convergence tests only determine the resolution required to reach a result close to the point a numerical method converges to. This does not imply that the method converges towards a true solution and further determining the accuracy is only possible by comparison to other methods but here the question again is how accurate these are (Igel, 2016).

The goal of this work is to investigate the accuracy of 2D full-waveform modeling with a free surface boundary and its convergence behaviour with the spatial discretisation of the model. This is done for varying two-dimensional models with two different modeling algorithms implementing the two most widely used free surface conditions, the image method (Robertsson, 1996) and the improved vacuum formulation (Zeng et al., 2012), to test the required spatial discretisation, computational cost and the resulting accuracy.

This work starts out in chapter 2 with a description of the underlying principles of full-waveform modeling. During this study, a number of simple test models are used to compare numerical results to analytical solutions. The initialisation of these, together with a description of the used modeling algorithms are described in chapter 3 and necessary processing steps and estimation of error are outlined in chapter 4. Since two modeling algorithms are used during this study, the first step is to ensure comparability through the comparison of both with an analytical solution in an elastic homogeneous full space in chapter 5. To determine the accuracy of the numerical result of both free surface boundary conditions accuracy and convergence tests are performed for an elastic homogeneous half-space with a free surface aligned with the grid, which is described in chapter 6. Chapter 7 deals with an elastic homogeneous half-space with a tilted free surface, where analytical solutions exist and a direct estimate of the effects of a free surface not aligned with the grid axis can be made. Here convergence tests are also applied to determine the behaviour a free surface condition has with an irregular free surface. Lastly in chapter 8, I discuss the application of both free surface conditions to an inhomogeneous model with a topographic free surface. Here convergence tests must be applied since no analytical solution exists.

2. Theory

Waveform modeling is an integral part of the of the process of full-waveform inversion since it represents the forward problem of this approach. The goal of modeling seismic waveforms in most cases is to compute synthetic seismograms for a given model. This requires calculating how waves propagate in a medium. This problem is covered extensively by Aki and Richards (2002) and Fichtner (2011), who describe the derivation of the equations that govern wave propagation in more detail.

For an elastic medium in a cartesian coordinate system (O, x, y, z) a linear relationship between the second order tensors of stress (σ_{ij}) and strain (ϵ_{kl}) is valid. This linear relation is described by the fourth order stiffness tensor C and its components C_{ijkl} in the generalised Hook's Law, which states that strain and stress are directly proportional and occur simultaneously

$$\sigma_{ij} = C_{ijkl} \epsilon_{kl}, \quad i, j, k, l \in [1,3], \quad (2.1)$$

with C_{ijkl} being a fourth order tensor it has 81 elastic components of which not all are independent.

The strain tensor ϵ_{kl} is an expression of the displacement u if the displacement is small

$$\epsilon_{kl} = \frac{1}{2} \left(\frac{\partial u_k}{\partial x_l} + \frac{\partial u_l}{\partial x_k} \right). \quad (2.2)$$

The inherent symmetry of $\epsilon_{kl} = \epsilon_{lk}$ resulting in the symmetry of the shear strains. The same symmetry is also valid for shear stresses $(\sigma_{ij} = \sigma_{ji})$ dictated by Newton's third law. This means that by extension also the symmetry $C_{ijkl} = C_{jikl} = C_{ijlk}$ caused by the symmetry of strain and stress tensors reducing the number of independent components of C to 36.

If we consider an elastic material all the energy loaded on the material is fully recoverable. Therefore, the derivative of the strain energy φ in respect to the strain is

$$\frac{\partial \varphi}{\partial \epsilon_{ij}} = \sigma_{ij} \quad (2.3)$$

Since a linear relationship between stress and strain has been assumed the expression

$$\frac{\partial \sigma_{ij}}{\partial \epsilon_{kl}} = C_{ijkl} \quad (2.4)$$

is valid. The stress can now be substituted into this relation resulting in:

$$C_{ijkl} = \frac{\partial}{\partial \epsilon_{kl}} \left(\frac{\partial \varphi}{\partial \epsilon_{ij}} \right) = \frac{\partial^2 \varphi}{\partial \epsilon_{ij} \partial \epsilon_{kl}} = \frac{\partial^2 \varphi}{\partial \epsilon_{kl} \partial \epsilon_{ij}} = C_{klij} \quad (2.5)$$

The order of differentiation here does not matter since the strain energy is a simple function and the symmetry $C_{ijkl} = C_{klij}$ is established reducing the number of independent components of the stiffness tensor C to 21. This is the maximum number of independent components of C an anisotropic body can possibly have. Isotropy of a body or special forms of anisotropy can reduce the number of independent components further. If an isotropic medium is considered, a simplified version of the stress strain relation can be used with just two parameters, λ and μ called the Lamè constants

$$\sigma_{ij} = \delta_{ij} \lambda \epsilon_{kk} + \mu (\epsilon_{ij} + \epsilon_{ji}), \quad i, j \in [1,3], \quad (2.6)$$

where δ_{ij} is the Kronecker delta and ϵ_{kk} is the dilatation ($\epsilon_{kk} = \epsilon_{11} + \epsilon_{22} + \epsilon_{33}$). Here μ relates shear strain to shear stress and is called the shear modulus, while λ more commonly expressed through the bulk modulus $\kappa = \lambda + \frac{2}{3}\mu$ relates the strain to the scalar pressure.

The Lamè constants can be considered time-invariant and can be used to express the seismic velocities of the P-waves (v_p) and S-wave (v_s)

$$v_p = \sqrt{\frac{\lambda + 2\mu}{\rho}} , \quad (2.7)$$

$$v_s = \sqrt{\frac{\mu}{\rho}} .$$

The conservation of linear momentum allows to equate the change of momentum of particles in a volume V to the forces acting upon it. Considering infinitesimal deformations results in small particle velocities, which makes it possible not to consider nonlinear terms in the momentum conservation and express it as a purely linear equation. This means that the temporal change in momentum must be equal to the body forces f_i acting on the volume and sum of normal and shear stresses acting on the surface boundary A of the volume

$$\frac{\partial}{\partial t} \iiint_V \rho \frac{\partial u_i}{\partial t} dV = \iiint_V f_i dV + \iint_A \sum_j \sigma_{ij} n_j dA . \quad (2.8)$$

Here, the left side of the equation represents the momentum change in time, expressed through the density ρ and the time derivative of the particle displacement u_i in the i -th direction. The right side of the equation are the inertial forces of V and the sum of body forces f_i on the material in the i -th direction. The stresses σ_{ij} on the unit surface multiplied with the unit vector component n_j pointing outward of the boundary represents the surface forces applied.

The expression $\sum_j \sigma_{ij} n_j$ can also be written in vector form as the traction vector T acting on the surface A . Gauss' theorem for a surface integral of a vector acting on the surface can be applied to the second term on the right-hand side resulting in

$$\iint_A T dA = \iiint_V \text{div } T dV , \quad (2.9)$$

and by extension in the component notation

$$\iint_A \sum_j \sigma_{ij} n_j dA = \iiint_V \sum_j \frac{\partial \sigma_{ij}}{\partial x_j} dV . \quad (2.10)$$

By inserting this expression into equation (2.8) and removing the arbitrary integral over the volume one gets the equation of motion

$$\rho \frac{\partial^2 u_i}{\partial t^2} = \sum_j \frac{\partial \sigma_{ij}}{\partial x_j} + f_i \quad (2.11)$$

Equations (2.2), (2.6) and (2.11) can be combined to form linear partial differential equation for the propagation of waves in an elastic medium with respect to the particle displacement. This is called the Stress-Displacement formulation and the equations can be combined to form the elastic wave equation

$$\rho \ddot{u} = \nabla \lambda (\nabla * u) + [\nabla u + \nabla u^T] + (\lambda + 2\mu) \nabla (\nabla * u) - \mu \nabla \times (\nabla \times u) + f, \quad (2.12)$$

where u is the displacement vector field and f the vector of body force exerted and ∇ the nabla-operator. For finite difference modeling this equation is in fact not useful and overly complicated.

An alternative formulation of the equations (2.2), (2.6) and (2.11) is often used taking the time derivative of the relationships in (2.2), (2.6) and (2.11) resulting in the Stress-Velocity formulation, which is possible since the Lamé parameters λ and μ do not vary with time:

$$\begin{aligned} \rho \frac{\partial v_i}{\partial t} &= \sum_j \frac{\partial \sigma_{ij}}{\partial x_j} + f_i && \text{Newton,} \\ \frac{\partial \sigma_{ij}}{\partial t} &= \delta_{ij} \lambda \frac{\partial \epsilon_{kk}}{\partial t} + \mu 2 \frac{\partial \epsilon_{ij}}{\partial t} && \text{Hooke's Law,} \\ \frac{\partial \epsilon_{ij}}{\partial t} &= \frac{1}{2} \left(\frac{\partial v_i}{\partial x_j} + \frac{\partial v_j}{\partial x_i} \right) && \text{Strain tensor,} \end{aligned} \quad (2.13)$$

where v_i is the particle velocity in the i -th direction. This formulation is particularly useful for computing numerical solutions since this yields the particle velocity as a solution.

2.1. Attenuation model

To include the effects of viscoelasticity in the modeling an absorption mechanism should be implemented. This may be achieved by using the linear viscoelasticity of a generalised standard linear solid which consists of a linear combination of L Maxwell bodies. These are a combination of spring and piston, where each body is described by their spring constant k_l and Newtonian viscosities η_l for $l = 1, \dots, L$. All of them are parallelly connected with a spring with the constant k_0 . To integrate this into the wave equation the complex bulk modulus M can be expressed in the frequency domain as (Bohlen & Milkereit, 2001)

$$M(\omega) = k_0 \left\{ 1 - L + \sum_{l=1}^L \frac{1 + i\omega\tau_{\epsilon l}}{1 + i\omega\tau_{\sigma l}} \right\}, \quad (2.14)$$

where ω is the angular frequency and the relaxation times for stress $\tau_{\sigma l}$ and strain $\tau_{\epsilon l}$ are written as

$$\tau_{\sigma l} = \frac{\eta_l}{k_l} \text{ and } \tau_{\epsilon l} = \frac{\eta_l}{k_0} + \frac{\eta_l}{k_l}. \quad (2.15)$$

The attenuation can be described with the quality factor Q as the quotient of the real and imaginary parts of M which amounts to the expression (Bohlen & Milkereit, 2001)

$$Q(w, \tau_{\sigma l}, \tau) = \frac{\text{Re}\{M\}}{\text{Im}\{M\}} = \frac{1 + \sum_{l=1}^L \frac{w^2 \tau_{\sigma l}^2}{1 + w^2 \tau_{\sigma l}^2} \tau}{\sum_{l=1}^L \frac{w \tau_{\sigma l}}{1 + w^2 \tau_{\sigma l}^2} \tau}, \quad (2.16)$$

$$\text{with } \tau = \frac{\tau_{\epsilon l}}{\tau_{\sigma l}} - 1.$$

Most materials have a constant quality factor over a limited range of frequency which may be used to create a realistic dispersion relation. For this Q has to be optimised by finding the minimum of the function for the desired frequency band $[\omega_1, \omega_2]$ by numerical means

$$J(\tau_{\sigma l}, \tau) = \int_{\omega_1}^{\omega_2} (Q^{-1}(\omega, \tau_{\sigma l}, \tau) - \tilde{Q}^{-1})^2 d\omega, \quad (2.17)$$

where \bar{Q} denotes the desired constant value of Q . This scheme works for strong ($Q > 10$) as well as lower absorptions. This process must be done for both P- and S-wave quality factors yielding values for the relaxation times for P- and S-waves (τ_p and τ_s). In the case of one relaxation mechanism ($L = 1$) the expression $\tau = 2/Q$ is a good estimate for τ (Bohlen & Milkereit, 2001).

To incorporate this attenuation, the stress can be expressed in terms of the stress relaxation modulus G and written for individual stress components

$$\sigma_{ij} = G_{ijkl} * \varepsilon_{kl} . \quad (2.18)$$

G_{ijkl} is a component of the fourth order tensor, called relaxation function, which is the inverse Fourier transformed complex bulk modulus (Robertsson et al., 1994)

$$G(t) = k_0 \left(1 - \sum_{l=1}^L \left(1 - \frac{\tau_{\varepsilon l}}{\tau_{\sigma l}} \right) e^{-\frac{t}{\tau_{\sigma l}}} \right) H(t) , \quad (2.19)$$

with $H(t)$ representing the Heaviside function $H(x) = \begin{cases} 0 & \text{for } x < 0 \\ 1 & \text{for } x \geq 0 \end{cases}$.

Analogous to the derivation of equation (2.6) and its time derivative in (2.13) the relation may be derived. For simplicity the problem is formulated as one dimensional

$$\frac{\partial \sigma}{\partial t} = \left(1 - \sum_{l=1}^L \left(\frac{\tau_{\varepsilon l}}{\tau_{\sigma l}} - 1 \right) \right) \frac{\partial v}{\partial x} + k_0 \left(1 - \sum_{l=1}^L \left(1 - \frac{\tau_{\varepsilon l}}{\tau_{\sigma l}} \right) e^{-\frac{t}{\tau_{\sigma l}}} \right) H(t) * \frac{\partial v}{\partial x} . \quad (2.20)$$

The second term in this equation involves a convolution which is inconvenient for calculation. To circumvent the convolution a memory variable r_l is introduced, defined as the second term including the convolution. The time derivative of r_l can be calculated without the need of a convolution (Robertsson et al., 1994)

$$\frac{\partial r_l}{\partial t} = -\frac{1}{\tau_{\sigma l}} r_l + k_0 \frac{1}{\tau_{\sigma l}} \left(1 - \frac{\tau_{\varepsilon l}}{\tau_{\sigma l}} \right) \frac{\partial v}{\partial x} . \quad (2.21)$$

Following the same approach the two-dimensional wave equation with one relaxation mechanism ($L = 1$) the velocity formulation of equation (2.13) expands to

$$\begin{aligned} \frac{\partial \sigma_{xx}}{\partial t} &= (\lambda + 2\mu) \frac{\tau_{\varepsilon p}}{\tau_{\sigma}} \left(\frac{\partial v_x}{\partial x} + \frac{\partial v_y}{\partial y} \right) - 2\mu \frac{\tau_{\varepsilon s}}{\tau_{\sigma}} \frac{\partial v_y}{\partial y} + r_{xx} , \\ \frac{\partial \sigma_{yy}}{\partial t} &= (\lambda + 2\mu) \frac{\tau_{\varepsilon p}}{\tau_{\sigma}} \left(\frac{\partial v_x}{\partial x} + \frac{\partial v_y}{\partial y} \right) - 2\mu \frac{\tau_{\varepsilon s}}{\tau_{\sigma}} \frac{\partial v_x}{\partial x} + r_{yy} , \\ \frac{\partial \sigma_{xy}}{\partial t} &= \mu \frac{\tau_{\varepsilon s}}{\tau_{\sigma}} \left(\frac{\partial v_x}{\partial x} + \frac{\partial v_y}{\partial y} \right) + r_{xy} , \\ \frac{\partial v_x}{\partial t} &= \frac{1}{\rho} \left(\frac{\partial \sigma_{xx}}{\partial x} + \frac{\partial \sigma_{xy}}{\partial y} \right) + f_x , \quad \frac{\partial v_y}{\partial t} = \frac{1}{\rho} \left(\frac{\partial \sigma_{yy}}{\partial y} + \frac{\partial \sigma_{xy}}{\partial x} \right) + f_y , \\ \frac{\partial r_{xx}}{\partial t} &= -\frac{1}{\tau_{\sigma}} \left(r_{xx} + (\lambda + 2\mu) \left(\frac{\tau_{\varepsilon p}}{\tau_{\sigma}} - 1 \right) \left(\frac{\partial v_x}{\partial x} + \frac{\partial v_y}{\partial y} \right) - 2\mu \left(\frac{\tau_{\varepsilon p}}{\tau_{\sigma}} - 1 \right) \frac{\partial v_y}{\partial y} \right) , \\ \frac{\partial r_{yy}}{\partial t} &= -\frac{1}{\tau_{\sigma}} \left(r_{yy} + (\lambda + 2\mu) \left(\frac{\tau_{\varepsilon p}}{\tau_{\sigma}} - 1 \right) \left(\frac{\partial v_x}{\partial x} + \frac{\partial v_y}{\partial y} \right) - 2\mu \left(\frac{\tau_{\varepsilon p}}{\tau_{\sigma}} - 1 \right) \frac{\partial v_x}{\partial x} \right) , \\ \frac{\partial r_{xy}}{\partial t} &= -\frac{1}{\tau_{\sigma}} \left(r_{xy} + (\lambda + 2\mu) \left(\frac{\tau_{\varepsilon p}}{\tau_{\sigma}} - 1 \right) \left(\frac{\partial v_x}{\partial y} + \frac{\partial v_y}{\partial x} \right) \right) , \end{aligned} \quad (2.22)$$

Here, three memory variables r_{xx} , r_{yy} and r_{xy} are needed for the computation (Robertsson et al., 1994). For more relaxation mechanisms further memory variables r_{ijl} have to be introduced, amounting to $3L$ memory variables (Bohlen & Milkereit, 2001).

2.2. Analytical Solutions and 2D Grid approximation

It is useful to evaluate the wave equations analytically for simple models by finding an exact non-trivial solution for the system of equations (2.2), (2.6) and (2.11). This can be used to check the accuracy of any numerical solutions. For introducing the concept of computing an analytical solution, the two-dimensional acoustic wave equation will be considered here for simplicity.

The 2D acoustic wave equation can be written in terms of the pressure p , the constant P-wave velocity v_p and the body forces f as the source term (Rienstra & Hirschberg, 2004)

$$\frac{\partial^2 p}{\partial t^2} - v_p^2 \left(\frac{\partial^2 p}{\partial x^2} + \frac{\partial^2 p}{\partial y^2} \right) = f . \quad (2.23)$$

Green's theorem is used to construct a response function of the wavefield to an impulse at the location x_s, y_s happening at the time t_s . The Green's function $G(x, y, t)$ is defined as the response to the impulse function of the combination of Dirac delta functions in time and space $\delta(t - t_s)\delta(x - x_s)\delta(y - y_s)$

$$\frac{\partial^2 G}{\partial t^2} - v_p^2 \left(\frac{\partial^2 G}{\partial x^2} + \frac{\partial^2 G}{\partial y^2} \right) = \delta(t - t_s)\delta(x - x_s)\delta(y - y_s) . \quad (2.24)$$

By applying Fourier transforms in the time and spatial domains to equation (2.24) and solving this for the Fourier transformed Green's function $\hat{G}(k_x, k_y, \omega)$ and applying the inverse Fourier transform in time and space domains yields the solution (Igel, 2016):

$$G(x, y, t) = \frac{1}{2\pi v_p^2} \frac{H\left((t - t_s) - \frac{|r|}{v_p}\right)}{\sqrt{(t - t_s)^2 - \frac{r^2}{v_p^2}}} , \quad (2.25)$$

with $r = \sqrt{(x - x_s)^2 + (y - y_s)^2}$ and H denoting the Heaviside function $H(x) = \begin{cases} 0 & \text{for } x < 0 \\ 1 & \text{for } x \geq 0 \end{cases}$.

Finding solutions to $G(x, y, t)$ involves solving multiple integrals that include poles as described in detail for the one dimensional in Rienstra and Hirschberg (2004) and the steps leading to the solution are omitted for brevity. The resulting pressure for a receiver at a point $x = 500, y = 0$ and a source located at $x_s = 0, y_s = 0$ is plotted in Figure 2.1. It shows the tailing of the pulse function which is called a coda. This coda is the effect of the source function being defined as an infinite line source which is the result of an approximation of a 2D space (Igel, 2016).

This effect of the coda is not present for a 3D space as is evident from the Green's function $G(x, y, z, t)$

$$G(x, y, z, t) = \frac{1}{4\pi v_p^2 r} \delta\left((t - t_s) - \frac{|r|}{v_p}\right) , \quad (2.26)$$

with $r = \sqrt{(x - x_s)^2 + (y - y_s)^2 + (z - z_s)^2}$ and the Dirac delta function $\delta(f) = f(0)$ for a differentiable function f . As is evident from equation (2.25) in the case of a 3D space no coda is

present and the function resembles a δ -function scaled by separation from the source point (Igel, 2016).

Convolving a source function with the Green's function for any dimensional space results in the pressure response for an elastic homogeneous medium for the acoustic wave equation of that specific dimensionality. For a 2D space the convolution results in a slight shift of the source function in the time and in the frequency domain which is depicted in Figure 2.2 for a Ricker wavelet (as defined in chapter 3.3.1) with a centre frequency of 4 Hz.

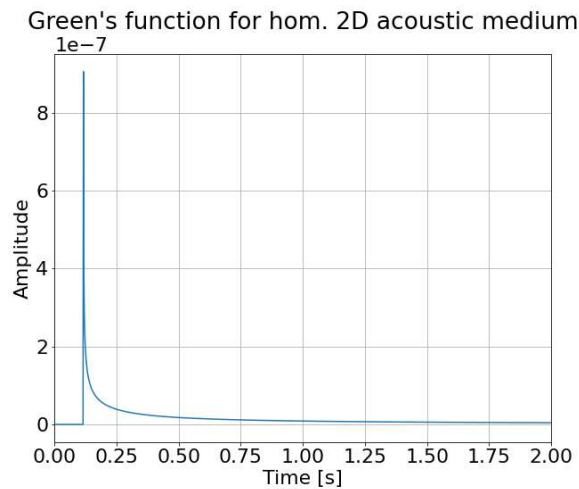


Figure 2.1: Greens function for a 2D acoustic homogeneous medium for a receiver at 500 m offset from the source.

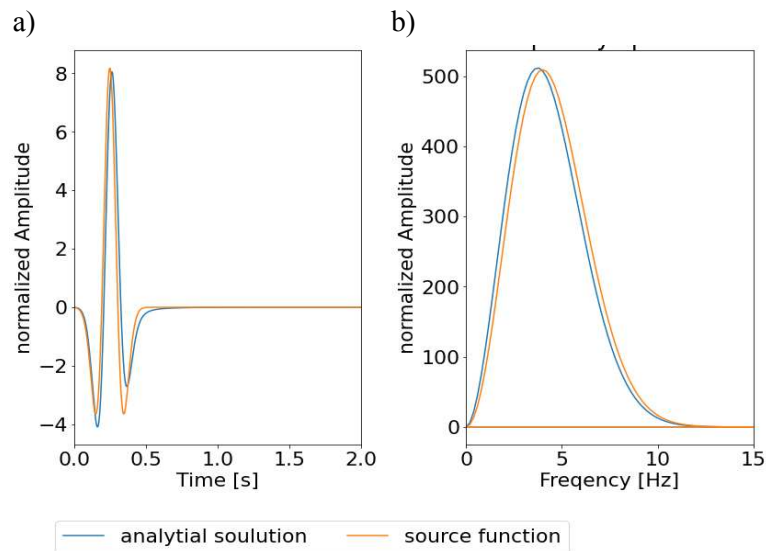


Figure 2.2: Comparison of source function (4 Hz Ricker-wavelet) and the acoustic analytical solution at 0 m offset in time- (a) and frequency domain (b)

The process of finding a Green's function is, however, not always straightforward and boundary conditions may further complicate finding a Green's function (Rienstra & Hirschberg, 2004). Such a problem is Garvin's problem which considers an elastic two-dimensional half-space with a free surface at $y = 0$ and a theoretical horizontal line blast source with Heaviside function as the pressure source function at an arbitrary depth h . This problem can be solved analytically using the Cagniard-de Hoop method after Hoop (1960) for the displacement responses at the free surface. This is done by contour integration where the integral paths are deformed so the integral may be solved analytically.

The time domain solution may be written as a double inverse Laplace transform of the formulation in frequency and wavenumber domain. This enables the formulation of a contour integral, which is deformed to a known transform (Sánchez-Sesma et al., 2013). The general solution to this problem yields the response functions for the displacement at the surface u_x and u_z is written as

$$u_x(x, 0, t, h) = \frac{1}{\pi\mu r} \text{Im} \left\{ \frac{2q_a \sqrt{1+q_a^2} \frac{\partial q_a}{\partial \tau}}{R(q_a^2)} \right\} \text{sgn}(x) H(\tau - a) ,$$

$$u_z(x, 0, t, h) = \frac{-1}{\pi\mu r} \text{Re} \left\{ \frac{1+q_a^2 \frac{\partial q_a}{\partial \tau}}{R(q_a^2)} \right\} H(\tau - a) ,$$
(2.27)

where

$$R(q_a^2) = (1 + q_a^2)^2 - 4q_a^2 \sqrt{a^2 + q_a^2} \sqrt{1 + q_a^2} ,$$

$$q_a = i\tau \frac{|x|}{r} + \frac{h}{r} \sqrt{\tau^2 - a^2} ,$$

$$\frac{\partial q_a}{\partial \tau} = i \frac{|x|}{r} + \frac{\tau \frac{h}{r}}{\sqrt{\tau^2 - a^2}} ,$$

$$a = \sqrt{\frac{1-2\nu}{2(1-\nu)}} , \quad r = \sqrt{x^2 + h^2} .$$
(2.28)

These equations have to be solved for the dimensionless time τ which has values for all arrivals that depend on the wave speeds with the general normalisation being (Sánchez-Sesma et al., 2013)

$$\tau = \frac{t v_s}{r} .$$
(2.29)

To get the response functions of a receiver, the coefficients q_a , $\frac{\partial q_a}{\partial \tau}$, and the Rayleigh functions R , must be inverted for all arrivals, which can then be combined to form a displacement response function. The resulting displacement function in horizontal direction is plotted in Figure 2.3 for a source at a depth of $h = 1$ and a receiver location of $x = z = 1$ for a Poisson's ratio of $\nu = 0.25$. The three peaks in Figure 2.3 correspond from left to right to the P, PP and PS waves (Sánchez-Sesma et al., 2013).

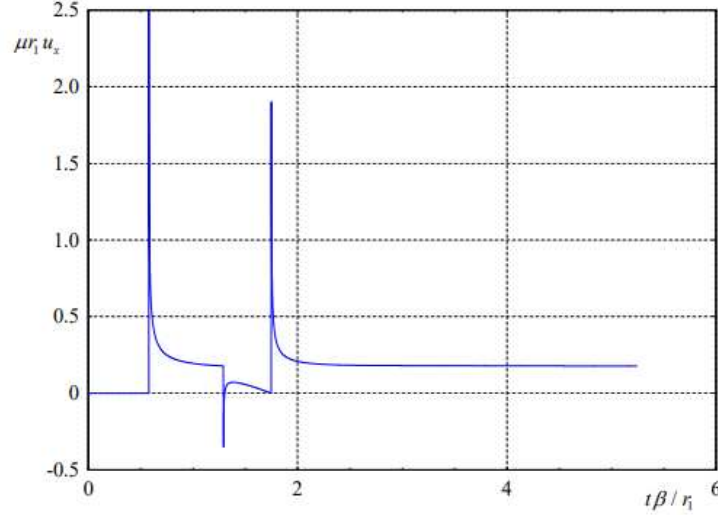


Figure 2.3: Horizontal response function in normalized time and amplitude for a source at $h = 1$ and a receiver at $x = z = 1$ for a Poisson's ratio of $\nu = 0.25$ as shown by Sánchez-Sesma et al. (2013)

2.3. Discretization of the wave equation

The wave equations, as described in the system of equations (2.2), (2.6) and (2.11) in terms of displacements and for equations (2.13) in terms of particle velocity, have analytical solution albeit only for very simple models, such as homogeneous elastic half-spaces. To compute complex models that involve subsurface inhomogeneities no such solution exists, and the system must be solved numerically.

Complex models require discretisation of a continuous wavefield $u(x, t)$ dependent on space and time. In the space domain the wavefield can be approximated by a finite number of time dependent coefficients $\bar{u}_i(t)$, ($i = 1, \dots, N$). These can represent a discrete value at a point of the wavefield $u(x, t)$ (Fichtner, 2011). Alternatively, $\bar{u}_i(t)$ may be used to store coefficients of Lagrange polynomials representing a function on the element when using the spectral element method (Komatitsch & Tromp, 1999).

The focus here lies on the approach of finite differences, therefore the discretisation in the space domain as discrete point values of the wavefield $u(x, t)$ arranged in an equidistant gridded pattern. The discretization for the time dependency of $u(x, t)$ can be approached either in the time- or frequency domain (Virieux et al., 2012). In the time domain the equations (2.2) and (2.11) are solved by advancing the wavefield by a discrete time step dt and $u(x, t + dt)$ is calculated from $u(x, t)$ using an appropriate solver (such as a finite difference scheme). In discrete terms this means that the wavefield at the discrete time step $n + 1$ is calculated from the values of the wavefield at the previous time steps (Fichtner, 2011).

The wave equation may also be written in matrix notation as a differential equation of the mass matrix M and stiffness matrix K defining a discrete force density vector \bar{f} as

$$M \cdot \frac{\partial^2 \bar{u}(t)}{\partial t^2} + K \cdot \bar{u}(t) = \bar{f} . \quad (2.30)$$

In the frequency-domain the Fourier transformed version of the matrix formulation results in

$$-\omega^2 M \cdot \bar{u}(\omega) + K \cdot \bar{u}(\omega) = \bar{f}(\omega) , \quad (2.31)$$

where M and K denote the mass and stiffness matrix respectively.

Solving this equation for the discrete wavefield \bar{u} yields a discrete wavefield for a discrete frequency ω . Here the inverted matrix $[-\omega^2 M + K]^{-1}$ may be used to compute any source in the model, reducing computational costs significantly (Fichtner, 2011). This approach however lacks scalability due to the complexities of the matrix decomposition required to solve equation (2.31) (Virieux et al., 2012).

This results for the two-dimensional case in every point of the wavefield \bar{u} can be mapped on a spatial grid for each time step. Therefore, a discrete point of the displacement wavefield at the i -th and j -th x and y coordinate and at the k -th timestep may be written as $u_{i,j}^k$ (Fichtner, 2011).

2.4. Finite difference approach

Modeling the seismic wavefield requires solving the partial differential equations described in the system of equations (2.2), (2.6) and (2.11) as displacement or in (2.13) as particle velocity. To find the solution of the temporal and spatial derivatives in the formulation of the wave equation the finite difference approach can be used to solve these derivatives. Here the derivative of an arbitrary function $\frac{\partial f(x_i)}{\partial x}$ at the discrete point x_i is approximated by the values of the function at adjacent evenly spaced points with the spacing Δx . A central second-order finite difference operator is written as (Fichtner, 2011):

$$\frac{\partial f(x_i)}{\partial x} = \frac{1}{2 \Delta x} (f(x_i + \Delta x) - f(x_i - \Delta x)) + O(\Delta x)^2 \quad (2.32)$$

Where $O(\Delta x^2)$ denotes the truncation error of the system.

This approximation stems from a linear combination of Taylor series for $f(x_i + \Delta x)$ and $f(x_i - \Delta x)$. The Taylor series expansion also yields the second order FD-operators for forward, backward, and central operators with minimal effort:

$$\begin{aligned} D_x^+ &= \frac{f[i + 1] - f[i]}{\Delta x}, & \text{forward operator} \\ D_x^- &= \frac{f[i] - f[i - 1]}{\Delta x}, & \text{backward operator} \\ D_x^c &= \frac{f[i + 1] - f[i - 1]}{2 \Delta x}, & \text{central operator} \end{aligned} \quad (2.33)$$

These FD-operator require little computation and are easy to implement, but the accuracy can be expanded by using higher order operators. Operators of higher order may be constructed identically by linearly combining Taylor series expansions. A central operator of the N -th order will always have the following form:

$$\frac{\partial f(x_i)}{\partial x} + O(\Delta x)^{2N} = \sum_{n=1}^N \beta_n (f(x_i + n\Delta x) - f(x_i - n\Delta x)) , \quad (2.34)$$

where β_n denotes coefficients for every discrete point pair $\pm n\Delta x$ away from the point x_i . All values for β_n have to be computed for each order of FD-operator separately (Fichtner, 2011).

Generally, FD-operators have a decreasing truncation error with higher FD-order and since produce more accurate representations of the derivative but come at a higher computational cost due to the amount of adjacent points used in the calculation (Lele, 1992). This leads to more accurate results but the gain in accuracy decreases with increasing order and a marginal increase in accuracy may not justify an increase in computational complexity (Fichtner, 2011).

A problem FD-schemes face is a growing inaccuracy at higher wavenumbers/frequencies (Lele, 1992). This may be improved by introducing coefficients β_n which optimise the relative error in a frequency band to be modelled (Holeberg, 1987), which are called Holberg coefficients.

Schemes for FD-operators may also be constructed with non-symmetric or unconventional and compact stencils. These might improve the resolution over a wider range of wavenumbers (Lele, 1992). To solve the differential equations of the wave equations the particle displacement u or particle velocity v , stresses σ_{ij} and Lamé parameters λ and μ are discretised on a Cartesian grid system (x, y) at discrete times t . These parameters do not lie on the same position but are rather shifted by half a spatial grid spacing creating the standard staggered grid (Levander, 1988; Virieux, 1986). A 2D staggered grid is depicted in Figure 2.4.. This shift of variable reduces the numerical dispersion and increases stability for large Poisson's ratios (Levander, 1988).

To solve the two-dimensional seismic wave equation using finite difference operators on a staggered grid the velocity formulation of the wave equation (2.13) is a very useful formulation for the problem since only first order differences are present. The discretisation described here follows the scheme proposed by Virieux (1986) and (Levander, 1988).

For the notational convention $v_x^n[i, j]$ denotes the particle velocity in x direction at the n -th timestep at the i -th grid point in x direction and the j -th grid point in y direction. To update the particle velocity components the central second order finite difference operator can be used to approximate the time derivative of the particle velocity in x- and y-direction at the timestep n and at the respective spatial points with dt denoting the discrete timestep

$$\left. \frac{\partial v_x}{\partial t} \right|_{[i + \frac{1}{2}, j]}^n \approx \frac{v_x^{n+\frac{1}{2}}[i + \frac{1}{2}, j] - v_x^{n-\frac{1}{2}}[i + \frac{1}{2}, j]}{dt} \quad (2.35)$$

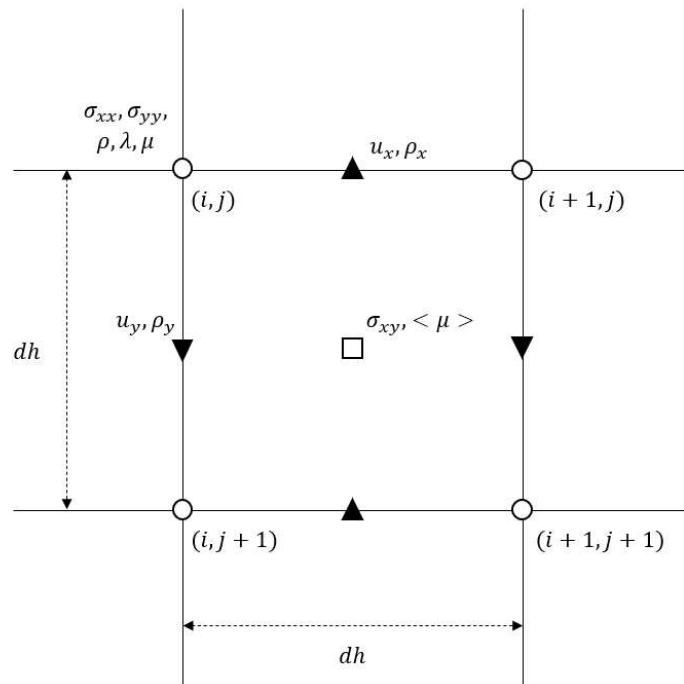


Figure 2.4: Standard staggered grid geometry in a discrete spatial 2D Cartesian coordinate system as described by Virieux (1986) and Levander (1988).

Rearranging these relations yields the particle velocity at the next timestep $n + \frac{1}{2}$

$$\begin{aligned} v_x^{n+\frac{1}{2}}\left[i + \frac{1}{2}, j\right] &= v_x^{n-\frac{1}{2}}\left[i + \frac{1}{2}, j\right] + dt \left. \frac{\partial v_x}{\partial t} \right|^n \left[i + \frac{1}{2}, j\right] \\ v_y^{n+\frac{1}{2}}\left[i, j + \frac{1}{2}\right] &= v_y^{n-\frac{1}{2}}\left[i, j + \frac{1}{2}\right] + dt \left. \frac{\partial v_y}{\partial t} \right|^n \left[i, j + \frac{1}{2}\right] \end{aligned} \quad (2.36)$$

The time derivative of the particle displacement may be calculated with the velocity formulation of the equation of motion (2.13). by substituting the spatial derivative of the corresponding stresses with finite difference operators. Here an example with a central second order operator is shown which can easily be substituted by other operators of different order. This yields the formulation of the time derivative of displacement velocity

$$\begin{aligned} \left. \frac{\partial v_x}{\partial t} \right|^n \left[i + \frac{1}{2}, j\right] &= \frac{\sigma_{xx}^n[i + 1, j] - \sigma_{xx}^n[i, j] + \sigma_{xy}^n\left[i, j + \frac{1}{2}\right] - \sigma_{xy}^n\left[i, j - \frac{1}{2}\right]}{\rho_x\left[i + \frac{1}{2}, j\right] dh} \\ \left. \frac{\partial v_y}{\partial t} \right|^n \left[i, j + \frac{1}{2}\right] &= \frac{\sigma_{xy}^n\left[i + \frac{1}{2}, j\right] - \sigma_{xy}^n\left[i - \frac{1}{2}, j\right] + \sigma_{yy}^n[i, j + 1] - \sigma_{yy}^n[i, j]}{\rho_y\left[i, j + \frac{1}{2}\right] dh} \end{aligned} \quad (2.37)$$

ρ_x and ρ_y refer to the averaged density at the positions $i + \frac{1}{2}, j$ and $i, j + \frac{1}{2}$ respectively. These are parameters independent of time since the density is assumed to be time invariant. As outlined in the relation above the density is required at the spatial location of the particle velocity and therefore density has to be averaged arithmetically in x and y direction to assure stability in the presence of strong discontinuities (Graves, 1996; Moczo, 2002)

$$\begin{aligned} \rho_x\left[i + \frac{1}{2}, j\right] &= \frac{1}{2}(\rho[i + 1, j] + \rho[i, j]) \\ \rho_y\left[i, j + \frac{1}{2}\right] &= \frac{1}{2}(\rho[i, j + 1] + \rho[i, j]) \end{aligned} \quad (2.38)$$

Now the derivative of the stresses at the time step $n + \frac{1}{2}$ can be approximated and reformulated in the same manner as shown for the particle velocity above (equations (2.35) and (2.36)) to express the stresses at the timestep $n + 1$:

$$\begin{aligned} \sigma_{kk}^{n+1}[i, j] &= \sigma_{kk}^n[i, j] + dt \left. \frac{\partial \sigma_{kk}}{\partial t} \right|^n \left[i, j\right] \\ \sigma_{xy}^{n+1}\left[i + \frac{1}{2}, j + \frac{1}{2}\right] &= \sigma_{xy}^n\left[i + \frac{1}{2}, j + \frac{1}{2}\right] + dt \left. \frac{\partial \sigma_{xy}}{\partial t} \right|^n \left[i + \frac{1}{2}, j + \frac{1}{2}\right] \end{aligned} \quad (2.39)$$

By using the stress-strain relationship of the particle velocity formulation combined with the definition of strain discussed in equation (2.13) the stresses at the time $n + 1$ can be expressed as:

$$\begin{aligned}
 \sigma_{xx}^{n+1}[i, j] &= \sigma_{xx}^n[i, j] \\
 &+ dt \left(\lambda[i, j] \left(\left. \frac{\partial v_x}{\partial x} \right|^{n+\frac{1}{2}} [i, j] + \left. \frac{\partial v_y}{\partial y} \right|^{n+\frac{1}{2}} [i, j] \right) + 2 \mu[i, j] \left. \frac{\partial v_x}{\partial x} \right|^{n+\frac{1}{2}} [i, j] \right) \\
 \sigma_{yy}^{n+1}[i, j] &= \sigma_{yy}^n[i, j] \\
 &+ dt \left(\lambda[i, j] \left(\left. \frac{\partial v_x}{\partial x} \right|^{n+\frac{1}{2}} [i, j] + \left. \frac{\partial v_y}{\partial y} \right|^{n+\frac{1}{2}} [i, j] \right) + 2 \mu[i, j] \left. \frac{\partial v_y}{\partial y} \right|^{n+\frac{1}{2}} [i, j] \right) \\
 \sigma_{xy}^{n+1} \left[i + \frac{1}{2}, j + \frac{1}{2} \right] &= \sigma_{xy}^n \left[i + \frac{1}{2}, j + \frac{1}{2} \right] \\
 &+ dt \mu_{xy} \left[i + \frac{1}{2}, j + \frac{1}{2} \right] \left(\left. \frac{\partial v_x}{\partial y} \right|^{n+\frac{1}{2}} \left[i + \frac{1}{2}, j + \frac{1}{2} \right] + \left. \frac{\partial v_y}{\partial x} \right|^{n+\frac{1}{2}} \left[i + \frac{1}{2}, j + \frac{1}{2} \right] \right)
 \end{aligned} \tag{2.40}$$

Similarly to the density, the shear modulus μ is also necessary at points of the shear stresses σ_{xy} . To ensure stability and accuracy of the FD-scheme in the presence of strong discontinuities the μ is calculated at the location $i + \frac{1}{2}, j + \frac{1}{2}$ by an harmonic average of the four adjacent μ -values (Graves, 1996; Moczo, 2002). This averaged value is as μ time invariant and is denoted as μ_{xy} :

$$\mu_{xy} \left[i + \frac{1}{2}, j + \frac{1}{2} \right] = \frac{4}{\mu[i, j]^{-1} + \mu[i + 1, j]^{-1} + \mu[i, j + 1]^{-1} + \mu[i + 1, j + 1]^{-1}} \tag{2.41}$$

The spatial derivative of the displacement velocity is also required for the stress updates in equations (2.40). This spatial derivative can be calculated using the updated displacement velocities v_x and v_y at the time $n + \frac{1}{2}$. Here the spatial derivatives are as well approximated by a central second order derivative and can be easily substituted by higher order operators:

$$\begin{aligned}
 \left. \frac{\partial v_x}{\partial x} \right|^{n+\frac{1}{2}} [i, j] &\approx \frac{v_x^{n+\frac{1}{2}} \left[i + \frac{1}{2}, j \right] - v_x^{n+\frac{1}{2}} \left[i - \frac{1}{2}, j \right]}{dh} \\
 \left. \frac{\partial v_y}{\partial y} \right|^{n+\frac{1}{2}} [i, j] &\approx \frac{v_y^{n+\frac{1}{2}} \left[i, j + \frac{1}{2} \right] - v_y^{n+\frac{1}{2}} \left[i, j - \frac{1}{2} \right]}{dh} \\
 \left. \frac{\partial v_x}{\partial y} \right|^{n+\frac{1}{2}} \left[i + \frac{1}{2}, j + \frac{1}{2} \right] &\approx \frac{v_x^{n+\frac{1}{2}} \left[i + \frac{1}{2}, j + 1 \right] - v_x^{n+\frac{1}{2}} \left[i + \frac{1}{2}, j \right]}{dh} \\
 \left. \frac{\partial v_y}{\partial x} \right|^{n+\frac{1}{2}} \left[i + \frac{1}{2}, j + \frac{1}{2} \right] &\approx \frac{v_y^{n+\frac{1}{2}} \left[i + 1, j + \frac{1}{2} \right] - v_y^{n+\frac{1}{2}} \left[i, j + \frac{1}{2} \right]}{dh}
 \end{aligned} \tag{2.42}$$

2.5. Numerical Stability

The utilization of discrete time and space sampling requires a sufficient sampling rate in those dimensions. Since the finite difference approach to solving the seismic wave equation is a numerical method, it is prone to produce numerical artifacts and instabilities. Two common sources of these are the spatial and temporal sampling rate in relation to the propagated frequencies (Köhn, 2011).

2.5.1. Grid dispersion

The first source of numerical inaccuracies is numerical dispersion which is an inherent property of numerical methods, though the degree to which they are affected by it varies. Therefore, a comparison with an analytical solution is a preferred method to evaluate the dispersiveness of a numerical approximation (Fichtner, 2011). To represent the wavefield, a sufficient sampling should be achievable by using the Nyquist-Shannon sampling theorem with a spatial sampling rate of $dh = \frac{\lambda}{2}$. This however, does not hold up well for numerical solutions, introducing significant inaccuracies (Köhn, 2011).

These inaccuracies stem from the discretisation of the equation and can be quantified using a Von Neumann analysis. For simplicity the one-dimensional wave equation for the displacement u is considered which may be written as:

$$\frac{\partial^2 u}{\partial t^2} = c^2 \frac{\partial^2 u}{\partial x^2} \quad (2.43)$$

The wavefield $u(x, t)$ is approximated by the discrete approximation its Fourier series with the Fourier coefficients $\psi_k(t)$ in a homogeneous medium in the interval $[\pi, -\pi]$

$$\bar{u}^n(t) = \sum_{k=-N/2}^{N/2} \bar{\psi}_k(t) e^{-ikn\Delta x} , \quad (2.44)$$

where $\Delta x = 2\pi/N$.

By inserting this into the spatially discretised form of the one-dimensional seismic wave equation and solving it for the Fourier coefficients $\bar{\psi}_k(t)$ the relation for the wave equation in matrix notation is obtained (Fichtner, 2011):

$$\begin{pmatrix} \bar{\psi}_k(t + \Delta t) - \bar{\psi}_k(t) \\ \bar{\psi}_k(t + \Delta t) \end{pmatrix} = \begin{pmatrix} 1 & -\frac{v^2 \Delta t^2}{\Delta x^2} \sin^2(k\Delta x) \\ 1 & 1 - \frac{v^2 \Delta t^2}{\Delta x^2} \sin^2(k\Delta x) \end{pmatrix} \begin{pmatrix} \bar{\psi}_k(t) - \bar{\psi}_k(t - \Delta t) \\ \bar{\psi}_k(t) \end{pmatrix} \quad (2.45)$$

The initial conditions of these coefficients ($\bar{\psi}_k(0)$) are an eigenvector $\lambda_k = |\lambda_k| e^{-ikj\Delta t \bar{v}_k}$ of the Matrix in the above relation. With the eigenvector formulation of the discrete displacement field is rewritten as:

$$\bar{u}^n(j\Delta t) = \sum_{k=-N/2}^{N/2} \bar{\psi}_k(0) |\lambda_k| e^{-ik(j\Delta t \bar{v}_k + n\Delta x)} \quad (2.46)$$

From this relation it may be determined that \bar{v}_k has the equivalent function of the wave speed but is dependent on the wavenumber k causing the numerical solution to be dispersive. Waves with shorter wavelengths travel at a reduced wave speed in the numerical solution while components with wavenumbers close to zero travel with the correct wave speed (Fichtner, 2011).

To avoid this dispersion the spatial sampling must be chosen according to criterion incorporating the minimal wavelength λ_{min} propagated in the model. The spatial sampling dh shall satisfy the condition

$$dh \leq \frac{\lambda_{min}}{n} = \frac{V_{min}}{n f_{max}} , \quad (2.47)$$

where V_{min} denotes the minimal seismic velocity occurring and f_{max} the maximum frequency propagated in the model. The factor n is dependent on the FD operator used, but as a general rule the

higher the order of the FD operator is, the higher n values are required resulting in a finer grid (Köhn, 2011).

2.5.2. Courant instability

To understand the limit of the temporal sampling one can again analyse the 1D elastic wave equation (2.43) for the displacement u . This equation can be discretised in time and space as u_i^n for the discrete times n and positions i with the discrete step lengths dt and dx using a second order finite difference approximation.

$$\frac{u_i^{n+1} - 2u_i^n + u_i^{n-1}}{dt^2} = c^2 \frac{u_{i+1}^n - 2u_i^n + u_{i-1}^n}{dx^2} \quad (2.48)$$

From the above equation the displacement at the time $n + 1$ can be calculated from displacements at previous times n and $n - 1$ as well as locations $n + 1$ as follows

$$u_i^{n+1} \approx 2 \left[1 - \left(\frac{c dt}{dx} \right)^2 \right] u_i^n + \left(\frac{c dt}{dx} \right)^2 (u_{i+1}^n + u_{i-1}^n) - u_i^{n-1} \quad (2.49)$$

The quantity

$$S = \frac{c dt}{dx} \quad (2.50)$$

is called the Courant number and was first introduced by Courant et al. (1928) and has an important effect on the numerical stability. From equation (2.49) it is evident that the Courant number must have a value lower than 1 in order not to introduce instabilities. This means for any point in the medium $S \leq 1$ must be valid and for a fixed value for dx and c , dt should be chosen to fulfil this criterion (Virieux et al., 2012). If indeed $S > 1$, the series will become divergent resulting in the growth of amplitudes to infinity.

Modeling of seismic waves is mostly done in a three- or two-dimensional space, so the temporal stability criterion should also be extended to a two-dimensional space since this is the focus here. Generalizing this stability criterion to a 2D grid with a spatial step length dh and for multiple orders of finite difference operators yields the Courant-Friedrichs-Lewy criterion for a two dimensional space (Courant et al., 1928)

$$dt \leq \frac{dh}{h \sqrt{2} v_{max}} , \quad (2.51)$$

where v_{max} is the maximum velocity in the model. The influence of the FD operator is represented by the factor h which is the sum of the weighting coefficients β_i

$$h = \sum_{i=1}^N \beta_{i,N} . \quad (2.52)$$

Here the weighting coefficients are as well dependent on the type of FD operators used. A list of values for h for Taylor and Holberg operators and 2nd to 16th FD orders is provided in Table 2.1 (Köhn, 2011).

From relation in equation (2.51) it is evident that a time step must be smaller than the travel time between two adjacent grid points separated by the grid spacing dh . To validate the stability for the entire model space the maximum velocity present is used (Köhn, 2011). If the Courant-Friedrichs-

Lewy criterion is not fulfilled then the calculation becomes divergent and the amplitudes grow to infinity after a few time steps, meaning the simulation has become unstable.

Table 2.1: Results for the factor h for FD orders of 2nd to 12th order for Taylor and Holberg FD operators calculated according to equation (2.52) after Köhn (2011)

FD order	h (Taylor)	h (Holberg)
2 nd	1.0	1.0
4 th	7/6	1.184614
6 th	149/120	1.283482
8 th	2161/1680	1.345927
10 th	53089/40320	1.387660
12 th	1187803/887040	1.417065

2.6. Absorbing boundary conditions

Modeling a wave traveling in an unbound medium would require an infinite model space, which is not possible. The simplest approach would be extending a finite model further than the wave would travel in the simulated time which comes at a huge computational cost. To reduce the memory and computational requirements the model is reduced in size and artificial boundaries are implemented to absorb energy of reflected waves and approximate an unbound model. These boundaries may be defined by either an absorbing boundary condition or an absorbing boundary layer (Gao et al., 2017).

An absorbing boundary condition separates the wave equation into incoming and outgoing parts and only the outwards propagated part is used in a layer on the edge of the model to avoid reflections going back into the model space. This approach gives good results at small incident angles close to normal to the boundary and considerably worse results at high incidence angles (Gao et al., 2017).

Absorbing boundary layers are layers around the model attenuating the wavefield gradually and are most commonly used in finite difference modeling (Gao et al., 2017). The sponge layer is a type of absorbing boundary layer proposed by Cerjan et al. (1985) which dampens the seismic wave field by adding an exponential decay function in the boundary layer. This gradual absorption can be expressed by damping functions such as exponential or Gaussian functions (Cerjan et al., 1985). An example of a Gauss damping term $G(i)$ at the index i denoting the point along the width of a boundary layer is given by

$$G(i) = \exp(-\theta^2(w_b - i)^2) , \quad (2.53)$$

where w_b is the index of the boundary width and θ denotes the damping coefficient (Gao et al., 2017). The attenuation coefficients should be optimised for the boundary width. This damping function is applied onto the numerical solution in the boundary region (Cerjan et al., 1985). Sochacki et al. (1987) suggested using a damping term $A(x, y)$ incorporated in the wave equation by expanding it to

$$\frac{\partial^2 u}{\partial t^2} + A(x, y) \frac{\partial u}{\partial t} = c^2 \left(\frac{\partial^2 u}{\partial x^2} + \frac{\partial^2 u}{\partial y^2} \right) , \quad (2.54)$$

where $A(x, y) = 0$ is valid in the model space and $A(x, y)$ is a damping function in the boundary region (Sochacki et al., 1987).

When conducting viscoelastic modeling no further additions to the wave equation are needed to create a sponge boundary. Rather the attenuation may be gradually increased in the boundary layer through a low quality-factor Q to dampen the seismic wave to a point where it has no significant contribution to the wavefield. The value 2 for the quality factor has proven to be effective at sufficiently damping the wavefield (Robertsson et al., 1994).

A more effective boundary than a sponge layer is a perfectly matched layer (PML) boundary proposed by Berenger (1994). Here propagating waves are split into parallel and normal derivatives and a function $d_x(x)$ acting as the damping factor in the boundary is added. $d_x(x)$ is defined such that in the boundary $d_x(x) > 0$ while in the model space $d_x(x) = 0$ so no damping is introduced. For this purpose the complex variable $\tilde{x}(x)$ is introduced and a substitution of the derivative is the core of a PML boundary (Collino & Tsogka, 2001):

$$\frac{\partial}{\partial x} \rightarrow \frac{\partial}{\partial \tilde{x}} = \frac{1}{1 + \frac{d_x(x)}{i\omega}} \frac{\partial}{\partial x} = \frac{1}{s_x} \frac{\partial}{\partial x} \quad (2.55)$$

This relation can be applied to the Fourier transformed wave equation and transformed back into the time domain (Komatitsch & Martin, 2007). This results in the transformation of the propagating waves into exponentially decaying waves by continuing these into complex coordinates (Gao et al., 2017). The PML boundary is very efficient but for a discretised wave equation at grazing incident angles the efficiency is very poor (Komatitsch & Martin, 2007).

To increase efficiency a convolutionally perfectly matched layer (C-PML) was introduced by Komatitsch and Martin (2007). The C-PML boundary uses the same approach as a PML but with a more general definition of the variable s_x which adds $\kappa_x \geq 1$ and $\alpha_x \geq 0$:

$$s_x = \kappa_x + \frac{d_x(x)}{\alpha_x + i\omega} \quad (2.56)$$

The substitution of the spatial derivative works in the same manner as with the PML boundary. In the time domain the spatial derivative is expressed as a convolution of the inverse Fourier transformed expression of $1/s_x$ about ω denoted as \bar{s}_x (Komatitsch & Martin, 2007)

$$\frac{\partial}{\partial x} \rightarrow \frac{\partial}{\partial \tilde{x}} = \bar{s}_x(t) * \frac{\partial}{\partial x} = \frac{1}{\kappa_x} \frac{\partial}{\partial x} + \zeta_x(t) * \frac{\partial}{\partial x}, \quad (2.57)$$

with

$$\zeta_x(t) = -\frac{d_x}{\kappa_x^2} H(t) e^{-\left(\frac{d_x}{\kappa_x} + \alpha_x\right)t}, \quad (2.58)$$

where $H(t)$ denotes the Heaviside function (Komatitsch & Martin, 2007).

2.7. Free Surface

The surface of a model poses a particular problem since the discontinuity at the free surface raises concerns about the numerical stability of the finite difference modeling (Graves, 1996).

In FD modeling the free surface can be defined by a strong formulation which requires the stress to be zero at the free surface (Virieux et al., 2012). This means for a planar surface the stresses σ_{yy} and σ_{xy} at the free surface must satisfy the boundary condition:

$$\sigma_{yy} = \sigma_{xy} = 0 \quad (2.59)$$

This condition can be fulfilled using the image method proposed by Levander (1988) by considering equations (2.2), (2.6) and (2.11) resulting in:

$$\begin{aligned}\sigma_{yy} = 0 &= \lambda \frac{\partial u_x}{\partial x} + (\lambda + 2\mu) \frac{\partial u_y}{\partial y} \\ \sigma_{xy} = 0 &= \mu \left(\frac{\partial u_x}{\partial y} + \frac{\partial u_y}{\partial x} \right)\end{aligned}\tag{2.60}$$

Here horizontal derivatives and vertical derivatives are present and the horizontal derivatives pose no problem for a planar free surface along the horizontal axis (Levander, 1988).

For the vertical derivatives the grid has to be extended two grid points above the free surface located at the vertical node with the index k and an antisymmetry for the stress components must be imposed as follows assuming a second order FD-operator (Levander, 1988):

$$\begin{aligned}\sigma_{yy}^{k-1} &= -\sigma_{yy}^{k+1} \\ \sigma_{xy}^{k-1/2} &= \sigma_{xy}^{k+1/2}, \sigma_{xy}^{k-3/2} = \sigma_{xy}^{k+3/2}\end{aligned}\tag{2.61}$$

With these conditions applied the stresses σ_{yy}^k and σ_{xy}^k at the planar free surface become zero and the condition in equation (2.59) is fulfilled. This method is called the image method proposed by Levander (1988).

The equations at the free surface should be discretised with a second order FD-operator in the vertical direction since higher order FD-operators lead to worse results due to the required velocity values 3/2 grid points above the free surface (Gottschämmer & Olsen, 2001).

For a nonplanar surface however, the problem gets more complicated and horizontal and vertical derivatives must be considered. Robertsson (1996) generalized the image method for a topographic surface. To approximate an irregular surface each grid node along the free surface must be classified according to which point of the grid point it passes through and location of its neighbour free surface grid point. This creates seven subclasses of boundary grid points for a 2D model which regulate how the stress and velocity components are updated by either setting a component to zero or imaging a component above the surface. These seven classes are listed in Table 2.2 (Robertsson, 1996). This approach creates a fine-grid stepped staircase topography (Zeng et al., 2012) as depicted in Figure 2.5. A limitation of this approach is, that internal discontinuities cannot easily be handled such as a tunnel, which is frequently investigated in near-surface seismics (Zeng et al., 2012). The image method also requires a finer sampling near the free surface to avoid scattering and diffraction at the free surface (Robertsson, 1996). This reduces the accuracy of the Rayleigh-waves along the surface, hence a finer spatial sampling is required (Zeng et al., 2012).

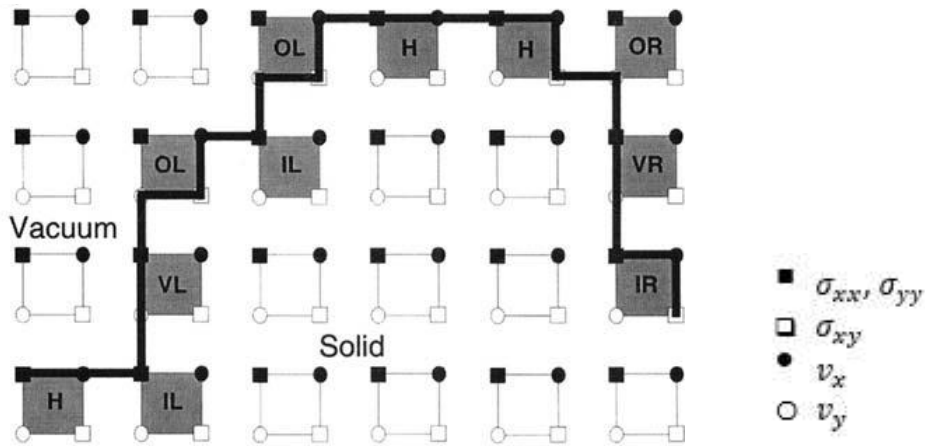


Figure 2.5: Staggered finite difference grid at the free surface of a anticline with the classification of grid points along the free surface described in Table 2.2 as depicted by Robertsson (1996)

Table 2.2: Classification of grid points along the free surface and the mirrored components according to the image method after Robertsson (1996).

Point Classification	H	VL	IL	OL	VR	IR	OR
boundary	Horizontal	Vertical, air to the left	Inner corner, air upper left	Outer corner, air left	Vertical, air to the right	Inner corner, air upper right	Outer corner, air right
Vertically imaged components	σ_{yy}	-	-	σ_{yy}, σ_{xy}	-	σ_{xy}	σ_{yy}
Horizontal imaged components	-	σ_{xx}	-	σ_{xx}, σ_{xy}	σ_{xx}	-	σ_{xx}, σ_{xy}
Components set to zero	-	-	$\sigma_{yy}, \sigma_{xx}, r_{xx}, r_{yy}$	σ_{xy}, r_{xy}	-	σ_{xx}, σ_{yy}	-

A different approach is to use an implicit definition of a free surface by embedding the boundary within the model grid. Here the parameters of the model grid are altered to create a layer on top of the model with the desired model properties (Köhn, 2011). This approach has the benefit of the relative ease of implementation since no special cases have to be considered and the surface is modelled in the same way as internal interfaces (Graves, 1996).

As for the definition of the parameters above the surface, the vacuum formulation can be used where $v_p, v_p, \rho \rightarrow 0$ above the free surface. This formulation however does not fulfil the traction free surface condition of equation (2.60) (Zahradník et al., 1993). The vertical stress component exactly on the surface may not be equal to zero since the surface is handled as any other discontinuity in the model, which leads to erroneous surface waves in the simulated wavefield (Zeng et al., 2012). The problem in using this formulation is that the system is only stable while using second-order spatial

difference operators and higher order operators lead to instabilities in regions, where $\rho \rightarrow 0$ (Graves, 1996).

To combat this problem and generate more accurate Rayleigh waves a parameter averaging scheme may be implemented. A distinct increase in stability is achieved using a harmonic averaging of the Lamè parameters (Moczo, 2002). To fulfil a part of the traction free surface condition the average shear modulus $\mu_{i,k}$ at the surface grid node is zero if any of the averaged node's value is equal to zero. This ensures that the shear stress σ_{xy} is always equal to zero at the free surface (Mittel, 2002). This parameter averaging scheme can be extended to the parameter averaging scheme for the reciprocal values of the densities $\frac{1}{\rho_x}$ and $\frac{1}{\rho_y}$ resulting in the averaging scheme (Zeng et al., 2012)

$$\frac{1}{\rho_{i+\frac{1}{2},k}} = \begin{cases} 0 & \text{if } \rho_{i,k} = \rho_{i+1,k} = 0 \\ \frac{2}{\rho_{i,k} + \rho_{i+1,k}} & \text{otherwise} \end{cases}, \quad (2.62)$$

$$\frac{1}{\rho_{i,k+\frac{1}{2}}} = \begin{cases} 0 & \text{if } \rho_{i,k} = \rho_{i,k+1} = 0 \\ \frac{2}{\rho_{i,k} + \rho_{i,k+1}} & \text{otherwise} \end{cases}, \quad (2.63)$$

$$\mu_{i+\frac{1}{2},k+\frac{1}{2}} = \begin{cases} \frac{4}{\frac{1}{\mu_{i,k}} + \frac{1}{\mu_{i+1,k}} + \frac{1}{\mu_{i,k+1}} + \frac{1}{\mu_{i+1,k+1}}} & \text{if } \mu_{i,k}, \mu_{i+1,k}, \mu_{i,k+1}, \mu_{i+1,k+1} \neq 0 \\ 0 & \text{otherwise} \end{cases}. \quad (2.64)$$

Using this averaging method greatly improves the stability of modeling a free surface with a vacuum formulation and fulfils the traction-free boundary condition. The parameter averaging introduces a fictitious layer with the thickness of half a grid spacing which shifts the free surface half a grid spacing above its actual location (Figure 2.6). This results in only the shear stress σ_{xy} being located directly on the free surface and the vertical stress component σ_{yy} being below the free surface and therefore does not have to be set to zero (Zeng et al., 2012).

This improved vacuum formulation can easily be extended without further conditions to an irregular free surface, since at any other point on the free surface the stress components will always have a value of zero due to the average rigidity $\mu_{i+\frac{1}{2},k+\frac{1}{2}}$ being zero (Zeng et al., 2012).

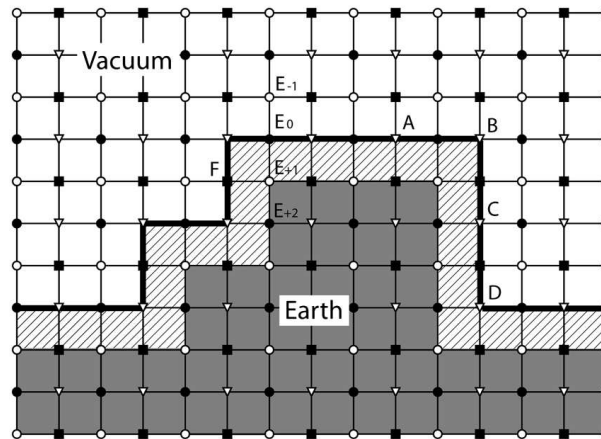


Figure 2.6: Grid for an irregular free-surface using the improved vacuum formulation as depicted by Zeng et al. (2012). The shadowed area represents the fictitious layer with a width of half a grid spacing, while the bold line depicts the location of the actual free-surface. For a description points annotated by Letters A through E refer to Zeng et al. (2012).

2.8. Source implementation

The conservation of momentum equation (2.11) is in fact also influenced by a seismic moment tensor M_{ij} which enables the rewriting of equation (2.11)

$$\rho \frac{\partial^2 u_i}{\partial t^2} = \sum_j \frac{\partial(\sigma_{ij} + M_{ij})}{\partial x_j} + f_i . \quad (2.65)$$

Modeling the wavefield requires an excitation of the numerical grid by a source term. This may either be done as a stress perturbation through the moment tensor $M_{ij}(x, t)$ or as an external body force $f_i(x, t)$ as described in equation (2.65). The scalar moment M_0 determines the energy radiated by the source

$$M_0 = \frac{1}{\sqrt{2}} \left(\sum_{ij} M_{ij}^2 \right)^{1/2} . \quad (2.66)$$

It is used to scale the components of the normalized moment tensor which determines the radiation pattern of waves. An explosive source has equal forcings along each axis and corresponds to the diagonal elements of M_{ij} (Igel, 2016):

$$M_{ij}^{expl} = \delta_{ij} M_0 , \quad (2.67)$$

where δ_{ij} is the Kronecker delta defined as $\delta_{ij} = \begin{cases} 1 & \text{if } i = j \\ 0 & \text{if } i \neq j \end{cases}$.

The wavefield may be initialized directly by incrementing the discrete source function as an input on the right-hand side of equation (2.11). This rather simple approach produces singularities which tend to produce numerical instabilities. To avoid this effect a number of injection techniques have been developed (Virieux et al., 2012).

Singularities may be avoided by defining a point source as a region around the source point in which the scattering field is computed. At the boundaries of this region the incident wavefield is estimated via an analytical solution for a homogeneous full space. This incident wavefield is added for propagations outside the region and subtracted for propagations inside the region (Alterman & Karal, 1968). This region may be defined as a box around the source point (Virieux et al., 2012).

Since the implementation by Alterman and Karal (1968) relies on first estimating the wavefield with an analytical solution, problems might arise, if a source is located in a heterogeneous region of the model, close to the free surface or is not located on a grid point. To more accurately model the point source as a spatial delta pulse function Hicks (2002) proposed using a spatial sinc function with a period of half the numerical grid spacing. In a one-dimensional medium this function is defined as:

$$\text{sinc}(x) = \frac{\sin(\pi x)}{\pi x} \quad (2.68)$$

The sinc function enables a source, which is located between two grid points, to be modelled as nodal body forces around the source point. If the source is located directly on a grid node, it is modelled as a delta pulse. If this is further windowed to limit the spatial extent of the defined source using a Kaiser windowing function the source is model more accurately (Hicks, 2002). The implementation for a point source in the middle of two grid nodes in a one-dimensional model is shown in Figure 2.7.

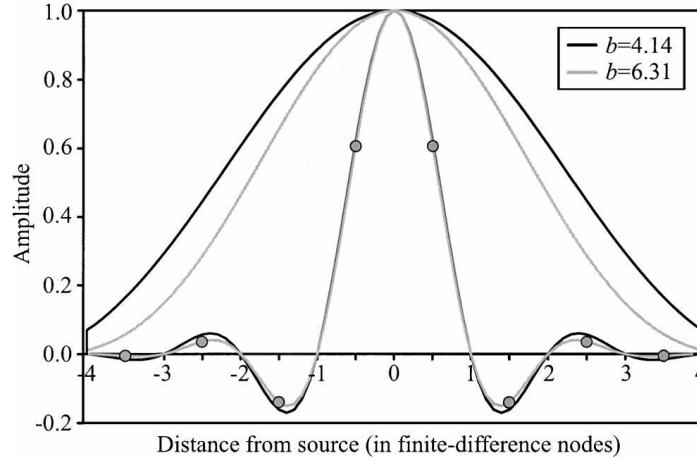


Figure 2.7: Kaiser windowing functions with different windowing parameters applied to the sinc functions for a source located in the middle of two grid points. The implementation of the source function is done at the grid nodes with the corresponding value at the circles after Hicks (2002).

Asymmetric sources such as explosive point sources may be modelled as body forces by simply using the spatial derivative of the sinc function:

$$\partial_x \text{sinc}(x) = \frac{\cos(\pi x) - \text{sinc}(x)}{x} \quad (2.69)$$

The asymmetry of this derivative is depicted in Figure 2.8, note that at the actual source point the function has a value of 0, resulting in the source function being injected around the source point. An explosive source injected into a 2D space can be injected through the body force vector $f_n(x, y)$ for the discrete point n on the FD grid (Hicks, 2002):

$$f_n(x, y) = \begin{pmatrix} f_n(x, y)_x \\ f_n(x, y)_y \end{pmatrix} = \begin{pmatrix} S \partial_x d_n(x) d_n(y) \\ S d_n(x) \partial_y d_n(y) \end{pmatrix} \quad (2.70)$$

where S is the source function and d_n the product of the windowing function and sinc function:

$$d_n(x) = W \text{sinc}(x) \quad (2.71)$$

The asymmetry of the spatial derivative $\partial_x d_n(x)$ causes particle motion and stresses to be positive on either side of the source point. This enables the implementation of monopole and dipole point source (Hicks, 2002).

If a free surface is present in the vicinity of the source point the part above the free surface may be mirrored below with an inverse sign according to the image method for a free surface boundary condition. This improves the accuracy of the modeling of sources close to the near surface if an explicit surface condition is applied (Hicks, 2002). The same approach may also be implemented to sample the wavefield at arbitrary positions (Virieux et al., 2012).

The implementation of a source might have numerical artefacts, such as for an explosive source where non-radial components might be introduced due to numerical artefacts (Igel, 2016).

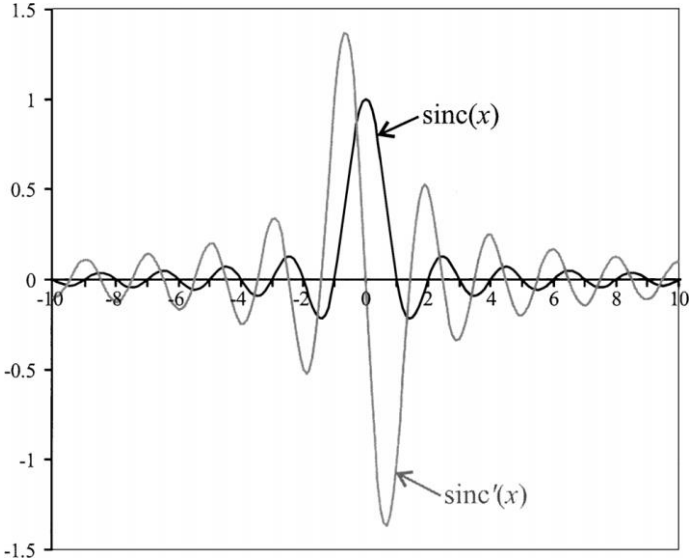


Figure 2.8: sinc function ($\text{sinc}(x)$) and spatial derivative of sinc function ($\text{sinc}'(x)$) after Hicks (2002)

3. Programs and implementations

To test both free surface boundary conditions, the image method and improved vacuum formulation, two 2D FD waveform modeling algorithms are employed, `ve2d_ref` and DENISE Black Edition. These numerically calculate the wavefield on a discrete spatial grid. Within the framework of numerical simulations, one question should always be asked: how accurate is the numerical result? This question is simple to answer if the true solution is known, one may just compute the difference of the numerical result to the true solution and give an estimate for the error. If the true solution is in fact unknown, this becomes rather complex to estimate.

One strategy is to compute a model with a very high resolution, so it has an assumed high accuracy and use this as a reference solution. This approach has the downside that simulating a model with very high resolution is computationally very expensive. A result of one numerical method can also be compared with the results of different algorithms or other numerical method to determine its accuracy (Igel, 2016).

Another approach is to evaluate the change that occurs with each stepwise increase in resolution. If no significant change occurs with further increases in resolution, the model has converged towards its presumably best estimate. This procedure is called a convergence test, which is commonly performed to evaluate the behaviour of numerical methods (Igel, 2016). The effectiveness of a convergence test is generally dependent on its convergence behaviour and the assumption that increases in resolution result in increases in accuracy. However, there is no guaranty that a model actually converges towards the true solution, and it might not do so, even if a convergence trend is observed.

In terms of waveform modeling, the analytical solution to the seismic wave equation are true solutions for simple models, which are useful for evaluating the accuracy numerical solutions. For simple models, such as elastic homogeneous full and half-spaces, analytical solutions exist, and the accuracy of numerical methods can be directly tested for. This approach however is impossible for models with an inhomogeneous model space or irregular topography and no direct comparison to a true solution is possible, since none exists.

The first step to determine the accuracy and required spatial discretisation is to compare the numerical solutions to analytical solutions. These free surface boundary conditions, implemented in different modeling algorithms, are compared to the analytical solutions of simple elastic homogeneous test models to determine their accuracy for different spatial discretisations. The setup of these homogeneous test models is outlined in section 3.3.2 for both modeling algorithms.

To determine the comparability of both modeling algorithms and the correct source implementation the first model used is an elastic homogeneous full space, discussed in chapter 5. Here the only influences present for the modeling are the source implementation, the absorbing boundary conditions, and the algorithm itself. This is useful to ensure a comparability between both modeling algorithms employed during the remaining investigation of free surface conditions. The second test model is an elastic homogeneous half-space with a free surface boundary aligned with the grid axis, which is described in chapter 6. Here, the accuracies of the free surface boundary conditions of the image method and improved vacuum formulation are evaluated by comparing it to the analytical solution.

The introduction of a free surface not aligned with the FD-grid introduces more numerical instabilities (Bohlen & Saenger, 2006) and ,therefore, has to be considered. No analytical solution exists for a non-planar free surface, but a homogeneous half-space may be rotated to allow testing the introduction of an unaligned free surface. In the FD grid space this corresponds to the introduction of a stepped

staircase function describing the free surface boundary. Here, a comparison to an analytical solution is still possible due to the coordinate transformation applied to analytical solution. This is performed for the last homogeneous test model, a tilted homogeneous half-space with a free surface boundary, outlined in chapter 7. The comparison to the analytical solution is a good measure for the accuracy of the numerical result and may validate the free surface boundary. To better evaluate the behaviour of a convergence test for a setting, where no true solution is known, the behaviour of convergence tests under known conditions is also evaluated.

Lastly, the convergence behaviour of both free surface boundary conditions is evaluated for an inhomogeneous model with a topographic free surface on the SAFOD model, which is described in chapter 8. Since no true solution is known for such a model, convergence tests have to be performed, where the difference between the subsequent spatial discretisations is evaluated. Here only a discretisation that exhibits a good combination of computational efficiency and convergence to a numerical result - which might not be a true solution - can be determined.

3.1. Analytical solution

For simple elastic and homogeneous models, an analytical solution exists and can be computed in a similar approach as described in Section 2.2. First the Green's function for a point in the model is calculated and then convolved with the source function yielding a function of displacement or particle velocity.

The program EX2DVAEL by Berg et al. (1994) is used to compute the analytical solution for an elastic homogeneous 2D half-space with a free surface boundary. This program calculates the horizontal and vertical displacement or particle velocity response from a compressional point source according to the Cagniard-De Hoop method (Berg et al., 1994). The analytical solution for this half-space is the true solution of the elastic wave equation in this simple model and is seen as the ground truth. Numerically computed seismograms can be compared to it, to determine their accuracy. No analytical solutions exist for models with an irregular surface.

3.2. Numerical waveform modeling programs

To test the accuracy effect of the free surface boundary conditions PSV waveform modeling has been performed using two modeling programs DENISE Black Edition and ve2d_ref. Both programs implement slightly different modeling algorithms and have different functionalities and implementations, which are described in the following.

3.2.1. DENISE Black Edition

DENISE Black Edition is a full wave inversion code by Köhn et al. (2012) with the forward modeling code based on the forward code SOFI2D by Bohlen and Milkereit (2001). The forward code incorporates the use of variable spatial FD operators of second to 16th order for elastic wave propagation or viscoelastic wave propagation after Robertsson et al. (1994) and Bohlen and Milkereit (2001).

The forward modeling algorithm uses Moczo's (2002) parameter averaging scheme, which increases the accuracy of the simulation. This is extended to incorporate the averaging scheme for the improved vacuum formulation after Zeng et al. (2012). An explicit free surface boundary condition may be implemented along the top boundary layer, where instead of an absorbing boundary, a planar free

surface with the image method after Levander (1988) can be used. For the absorbing boundary frame, convolutionally perfectly matched layer (C-PML) boundaries after Komatitsch and Martin (2007) are added along the model edges.

The source implementation was changed for the following investigations with an explosive point source. The source was changed not to be initialized with the first derivative of the defined source function. Instead, the source function is directly to initializing the wavefield. The derivative changes the frequency content of the used wavelet and alters the wavelet shape. This shape does not match up with any analytical solution for particle velocities.

Using the derivative as a source function acts in the frequency domain as a multiplication with the complex frequency, which changes both phase and the spectral amplitude of a signal. This change of waveform and frequency spectrum for a 4 Hz Ricker wavelet as the source function (as defined in Section 3.3.1) is shown in Figure 3.1. For the 4 Hz Ricker wavelet a frequency shift of the centre frequency from 4 to 4.5 Hz is observed while the maximum frequency stays the same but amplitude increases (Figure 3.1).

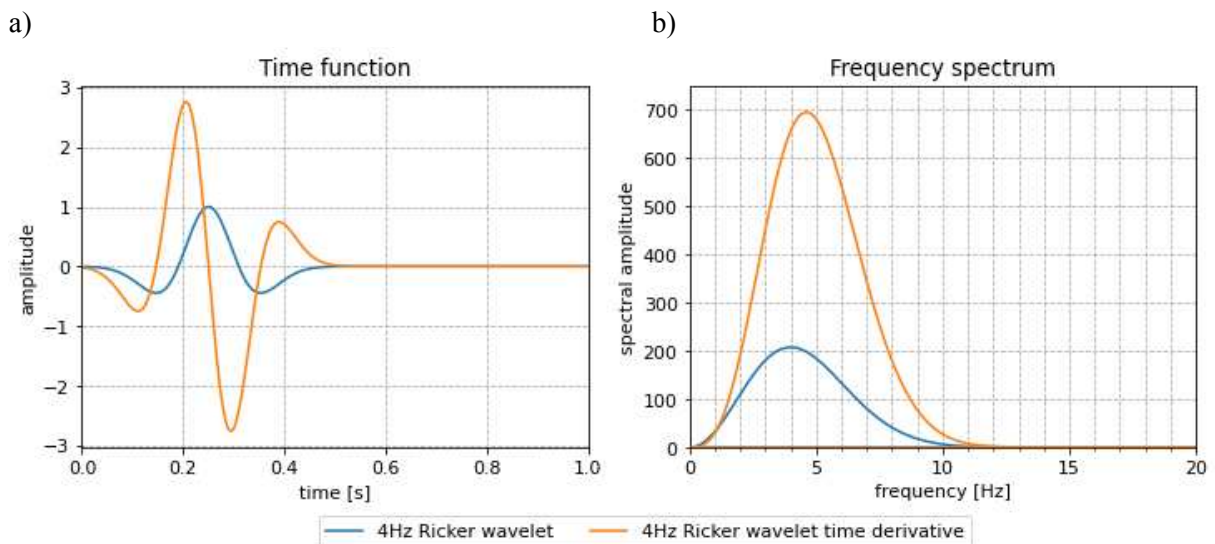


Figure 3.1: Time function (a) and frequency spectrum (b) of a Ricker wavelet with a centre frequency of 4 Hz and its time derivative.

3.2.2. Viscoelastic wavepropagation in 2 dimensions (ve2d_ref)

Viscoelastic wavepropagation in 2 dimensions (VE2D refined or ve2d_ref) is a viscoelastic waveform modeling code developed by Robertsson et al. (1994) which has been extended to incorporate a topographic free surface boundary and a grid refinement process (Robertsson, 1997). The main feature of this code is the definition of the free surface boundary condition according to the image method for an irregular surface after Robertsson (1996). This surface boundary condition is explained in detail in Section 2.7.

The grid is split into two horizontal layer regions with different grid spacings. The upper region incorporates the free surface and has a three times smaller grid sampling than the lower layer to resolve the free surface boundary better. This variable definition of the grid is useful in reducing computation times while still modeling surface waves accurately (Bohlen & Saenger, 2006). For the sake of comparison with other modeling programs, which do not include such a feature the grid of the

model space was defined with a homogeneous grid spacing but the lower absorbing boundary was still defined with a grid spacing three times higher.

The wavefield modeling is performed exclusively viscoelastically with a second order FD-scheme in time and space domain and damping is controlled by one relaxation $L = 1$ using three memory variables (r_{xx} , r_{yy} and r_{xy}) determined by a quality-factor model (Robertsson et al., 1994). For the absorbing boundary a sponge layer boundary is implemented using the viscoelastic damping to absorb the wavefield inside the boundary frame with a linear gradient function.

3.3. Model parametrisation

In the following the model parametrisation of both `ve2d_ref` and DENISE Black Edition is described, which is applied to all the homogeneous test models of elastic full and half-spaces. This requires the definition of a source function, which determines the propagated frequencies and wavelengths through the model, determining the spatial resolution and time steps required to avoid numerical artefacts.

3.3.1. Source function

Modeling the wavefield requires a source function as shown in equation (2.11). This source function is then implemented according to the source implementations discussed in section 2.8.

A ricker wavelet was chosen as a source function due to its numerical advantage. One reason for the advantage of the ricker wavelet is the gentle sloping at the beginning and end of the wavelet, which avoids a step. Another factor for its numerical properties is the strong roll-off in the frequency spectrum, which limits the propagated frequencies effectively. These features of the Ricker wavelet are visualised in Figure 3.2 for a time shifted wavelet. Therefore, for all following tests a time shifted Ricker wavelet with a centre frequency of 4 Hz has been selected. The Ricker wavelet source function can be defined as

$$f(t) = A (1 - 2 \tau(t)^2) e^{-\tau(t)^2} , \quad (3.1)$$

$$\tau(t) = \frac{\pi(t - \frac{1}{f_c})}{\frac{1}{f_c}} , \quad (3.2)$$

with A being the amplitude and f_c the centre frequency of the wavelet. Here the time shift has been integrated into the definition of the Ricker wavelet through the term $\frac{1}{f_c}$ in $\tau(t)$.

The time function and frequency spectrum for a Ricker wavelet with a centre frequency of 4 Hz are depicted in Figure 3.2. The amplitude spectrum in Figure 3.2b the maximum frequency with a notable amplitude contained in the source function is roughly 12 Hz here the amplitude has decreased by a magnitude of 10^3 compared to the maximum spectral amplitude of 210. Beyond this frequency the spectral amplitude is too small to have a significant impact on the waveform and is in the range of numerical uncertainties. This maximum frequency is later used to estimate the required grid spacing.

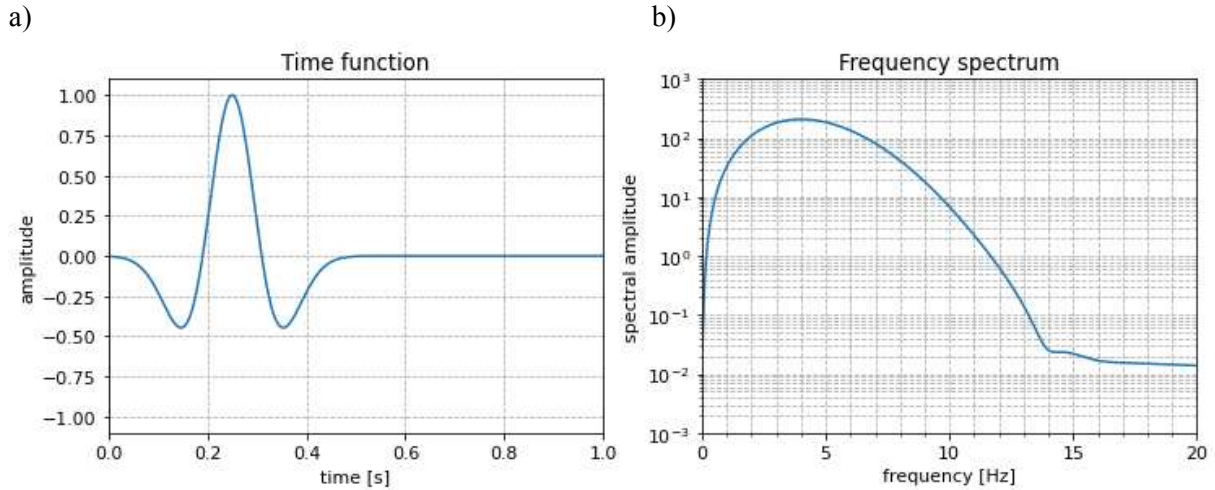


Figure 3.2: a) Time function of a Ricker wavelet with a centre frequency of 4 Hz. b) Amplitude spectrum of the wavelet.

3.3.2. Test model dimensions, boundaries, and modeling parameters

The test models were kept at a comparable scale to the SAFOD model with a horizontal and vertical extent of 25 km and 5.5 to 10 km respectively. The parameters of the test models were set to the rounded arithmetic average parameter of the SAFOD model, resulting in $v_p = 4300 \text{ m s}^{-1}$, $v_s = 2200 \text{ m s}^{-1}$, $\rho = 2500 \text{ kg m}^{-3}$. The modeling is done using an elastic PSV finite difference modeling on a 2D standard staggered grid. Only one of the used finite difference modellers DENISE Black Edition can model an elastic wavefield, while the ve2d_ref has only the capability to model a viscoelastic wavefield. Therefore, for ve2d_ref an elastic modeling is approximated by setting the quality factor to very high values inside of the model space. The quality factors for P- and S-wave $Q_P = Q_S = 10^{10}$ were chosen for waveform modeling with ve2d_ref.

Another difference between DENISE Black Edition and ve2d_ref is the type of absorbing boundary used. While DENISE Black Edition can use a C-PML boundary, ve2d_ref uses a sponge layer boundary. For ve2d_ref the sponge layer was chosen to have a width of 4000 m with a linear taper from the model Q_P and Q_S values to $Q_P = Q_S = 2$ with a taper width of half the boundary width. This splits the sponge layer in an inner boundary defined by the start of the taper, an intermediate boundary defined by the change between taper and sponge layer, and the outer boundary, which is the actual model boundary as seen in Figure 3.3a. This boundary is quite wide and increases the computational cost of the model significantly. To reduce the computational cost and since a grid refinement is implemented in ve2d_ref, the lower sponge layer of the model is defined in grid spacing three times that of the model space. This splits the sponge layers of ve2D_ref also split into coarse and fine sampling as shown in Figure 3.3a.

For DENISE Black Edition a C-PML boundary with a width of 40 grid points for every step length, with a damping velocity of 4300 m/s, with a frequency within the C-PML boundary layer of 4 Hz and with a quadratic damping function was selected. Here a similar differentiation can be used, where the outer boundary is the model boundary and the start of the C-PML is the inner boundary (Figure 3.3b).

Figure 3.3 depicts a general setup of models of both ve2D_ref and DENISE Black Edition. As is visible in Figure 3.3, the sponge layer must be defined extremely thick to dampen the incoming wavefield (Figure 3.3a), while the C-PML (Figure 3.3b) has a fraction (it varies with chosen spatial discretisation) of the width of the sponge layer. Even with the definition of the sponge layer with three

times the grid spacing of the model space, the C-PML is still far more computationally efficient, simply due to memory requirements of the large sponge layers.

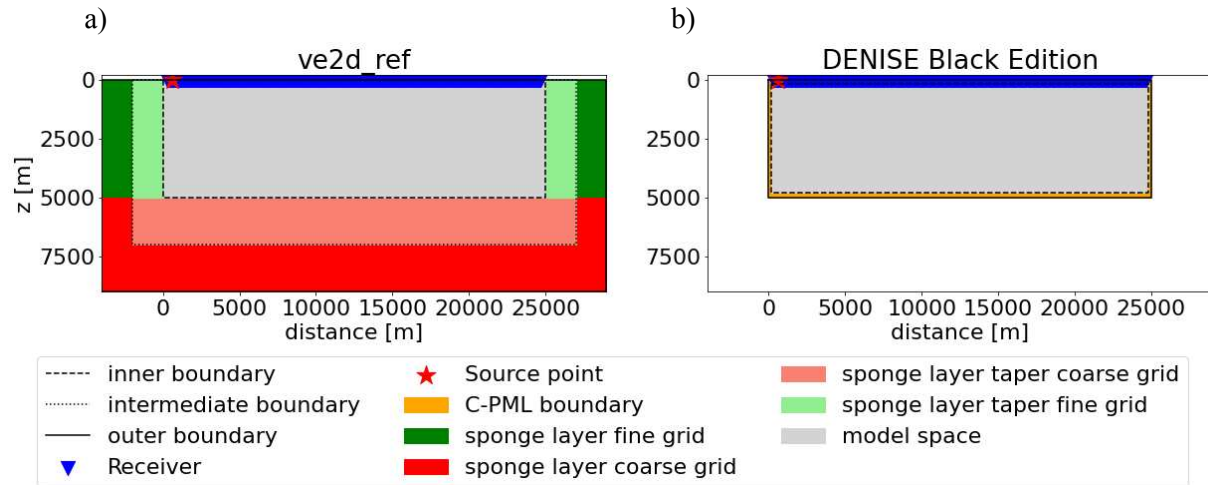


Figure 3.3: Schematic of a general model for *ve2d_ref* (a) and *DENISE Black Edition* (b) including its boundaries.

To discretize a model with these parameters an appropriate grid spacing must be found. This grid spacing should sample the minimum wavelength 15 to 30 times to achieve accurate results, and finer sampling is required if a free surface unaligned with the grid is introduced (Bohlen & Saenger, 2006). With the highest frequency of 12 Hz as given by the source function defined in section 3.3.1 and the slowest wave velocity $v_s = 2200 \text{ m s}^{-1}$ the shortest propagated wavelength amounts to 183.3 m. A spatial sampling rate of 30 samples per minimum wavelength as suggested by Bohlen and Saenger (2006) would result in 6.1 m grid spacing.

For the accuracy and convergence tests grid spacings above and below this value have been chosen, ranging from 20 m to 2.5 m. This range was selected to cover a wide range of grid spacings to observe a convergence behaviour in the modelled data. The spacings were selected to have an exponential increase of $\sqrt{2}$ from lowest to highest, resulting in seven models with the spacings of 2.5, 3.5355, 5, 7.071, 10, 14.142 and 20 m. This method of determining the grid spacing was selected so they would plot equidistant on a logarithmic scale. The ratio $\sqrt{2}$ was selected, causing real numbered grid spacing values, in order to produce more values in a limited interval, so a trend would be more clearly visible in a convergence test.

The minimal time step required for numerical stability was calculated using the Courant-Friedrichs-Lewy criterion as described in equation (2.51) assuming elastic wave propagation and using a second order FD stencil. To enable producing comparable seismograms a timestep below this threshold is selected, which is a factor of the seismogram sampling rate of 2 ms. A convenient way to reference the spatial resolution of a model discretisation is to determine its grid points per wavelength (ppw), typically referring to the minimum wavelength propagated within the model. Here, the test models are defined with a resolution ranging from 9 to 73 ppw regarding the minimum wavelength of the S-wave velocity of 183.3 m. A summary of the grid spacing, time steps and resolution for each model is given in Table 3.1.

For the test models 489 receivers are placed at horizontal distances from 300 to 24700 m with a lateral spacing of 50 m. Due to the irregularity of the grid spacing, some receivers are not located at the exact

locations for grid spacings of 20, 14.142, 7.071 and 3.5355 m, which might result in additional differences to exact analytical solutions.

Table 3.1: Grid spacing and time steps for the used test models.

Model parameter	Model 1	Model 2	Model 3	Model 4	Model 5	Model 6	Model 7
Grid spacing [m]	20	14.142	10	7.071	5	3.5355	2.5
Maximum time step for stability [s]	0.003289	0.002326	0.001644	0.001163	0.000822	0.000581	0.000411
Time step [s]	0.002	0.001	0.001	0.0005	0.0004	0.00025	0.0002
Samples per minimum wavelength [ppw]	9.16	12.96	18.33	25.92	36.66	51.84	73.32
Samples per minimum P-wavelength [ppw]	16.54	23.39	33.08	46.78	66.154	93.56	132.31

A sufficiently buried explosive point source was used to stimulate the wavefield with a Ricker-wavelet with a centre frequency of 4 Hz as a source function as discussed in section 3.3.1. Computation of the wavefield is carried out for all models over a time period of 10 s using a second order FD operator in both ve2d_ref and DENISE Black edition. I chose a second order FD operator due to the stability issues for free surface conditions according to the improved vacuum formulation after Zeng et al. (2012) were higher order operators may cause instability. The second order FD operator was chosen for modeling with both DENISE Black Edition and ve2d_ref to keep the error comparable, and not be influenced by the added accuracy of higher order FD-schemes.

For models including a free surface, the free surface condition of the improved vacuum formulation is used in DENISE Black Edition, while ve2d_ref uses the image method for an irregular free surface after Robertsson (1996). The for a flat free surface aligned with the grid axis the image method after Levander (1988) is additionally tested with DENISE Black Edition.

The improved vacuum formulation requires the parameters v_p , v_s , $\rho \rightarrow 0$ for grid points above the surface. The averaging scheme for reciprocal values of densities ρ_x and ρ_z as well as rigidity μ allows to set values for densities to zero without a loss of stability (Zeng et al., 2012). The velocities above the free surface are set to values close to zero to ensure stability. The values of $v_p = 0 \text{ m s}^{-1}$, $v_s = 0.000001 \text{ m s}^{-1}$, $\rho = 0 \text{ kg m}^{-3}$ are assigned to grid points above the free surface when using the improved vacuum formulation in DENISE Black Edition. Meanwhile no special attention needs to be directed towards grid points above the free surface when using the image method, these calculations are simply wasted.

A summary of parameters used for modeling in every test model is presented in Table 3.2 and a summary of parameters specific to modeling with DENISE Black Edition and ve2d_ref in.

Table 3.2: Overview of model parameters for test models

Model parameter	Value
V_p	4300 m/s
V_s	2200 m/s
Density	2500 kg/m ³
Source	Explosive point source
Source function	4 Hz Ricker wavelet
Number of receives	489
Horizontal receiver spacing	50 m
Receiver sampling time	2 ms
Recorded time	10 s

Table 3.3: Overview of algorithm specific parameters for modeling with ve2D_ref and DENISE Black Edition

Model parameter	DENISE Black Edition	Ve2D_ref
Modeling	Elastic FD modeling	Visco-elastic FD modeling
FD Order	2	2
Q_p and Q_s	-	10 ¹⁰
Boundary condition	C PML-boundary	Sponge layer
Boundary width	40 grid points	4000 m
Free surface condition (if applicable)	Improved vacuum formulation after Zeng et al. (2012) and image method after Levander (1988) for grid-aligned half-space	Image method after Robertsson (1996)

4. Processing of synthetic data

The numerically computed particle velocities of the receivers in the model and the computed wavefields are analysed throughout this thesis. Some processing of these is necessary to conduct accuracy and convergence tests and to analyse the numerically computed wavefields qualitatively. These processing steps and calculation of errors performed throughout this study are discussed below.

4.1. Synthetic amplitude normalisations

The amplitude of numerically computed seismograms depends on the spatial discretisation. The amplitudes of two simulations should not be compared directly with each other or to an analytical solution, rather the effect of the discretisation must first be removed. Furthermore, different simulation algorithms produce synthetic seismograms of different amplitudes depending on the specific modeling algorithms used in the program.

The modelled synthetic seismograms for an elastic full space (described in chapter 5) at 100 m offset are displayed in Figure 4.1 alongside the analytical solution for this model. Here the relationship between the discretisation of the grid and the amplitude is displayed clearly, with larger grid spacings having higher amplitudes than smaller ones. This holds true for both modeling programs `ve2d_ref` (Figure 4.1a) and DENISE Black Edition (Figure 4.1b). The computed seismograms of DENISE Black Edition have an amplitude smaller than the analytical solution by a factor of 10^6 .

To allow a comparison to the analytical solution, the amplitude of the synthetic seismograms should be normalized to the amplitude of the analytical solution. This can be done by finding a relation which equalizes all synthetic traces to the amplitude of an analytical solution. This amplitude relation is different for both modeling programs and has been determined empirically for each. This method of adjusting the amplitude by a constant factor preserves the amplitude information of the modelled seismograms and the relation of amplitude to offset.

The best fit of the amplitude altered synthetic seismograms $\tilde{a}(t)$ to the analytical solution for models computed with `ve2d_ref` was determined to be the division of the seismogram amplitude a by the grid spacing dh of the model:

$$\tilde{a}(t) = \frac{a(t)}{dh^2} \quad (4.1)$$

The resulting amplitude for a horizontal seismogram at 100 m offset in an elastic homogeneous full space is plotted in Figure 4.2a.

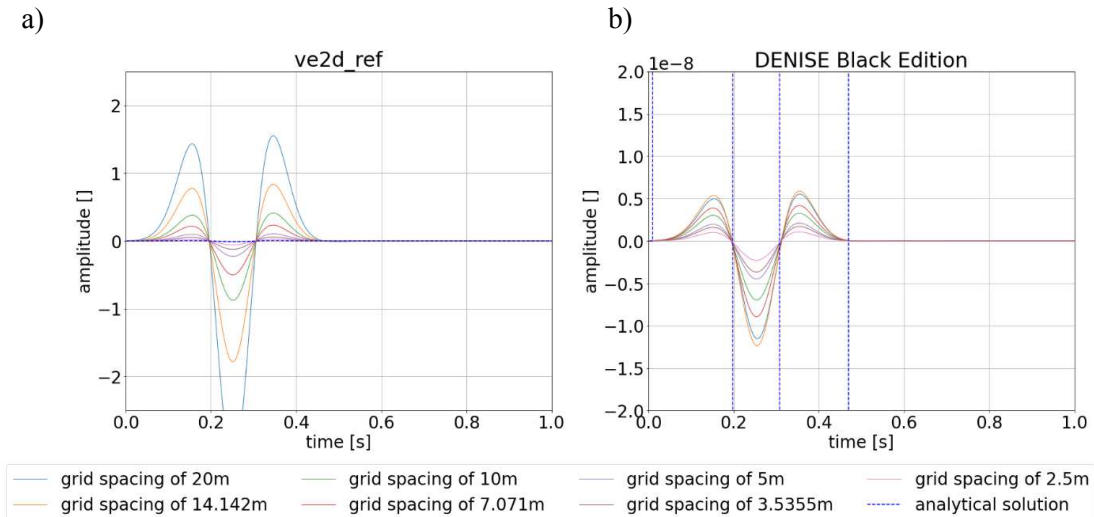


Figure 4.1: Synthetic seismograms of the horizontal component at an offset of 100 m from an explosive point source computed for all grid spacings in an elastic homogeneous full space for the modeling programs *ve2d_ref* (a) and *DENISE Black Edition* (b) compared to the analytical solution.

For *DENISE Black Edition* the transfer function, that best fitted the amplitude depended on the time step dt as well as the grid spacing dh and a constant factor $1.5 \cdot 10^9$, since the inverse of this factor is coded into the source implementation of *DENISE Black Edition*. This gives the relation for the transformed particle velocity amplitudes \tilde{a} at the time t :

$$\tilde{a}(t) = 1.5 \frac{a(t)}{dh^2} dt 10^9 \quad (4.2)$$

This results in the amplitude fit as displayed in Figure 4.2b for a horizontal receiver in an elastic homogeneous full space at 100 m offset for an explosive point source.

Both amplitude corrections shown in Figure 4.2 yield a good fit, but some signals for some grid spacings do not match the amplitude of the analytical solution very well. From here on, the amplitudes calculated in this way are referred to as true amplitudes.

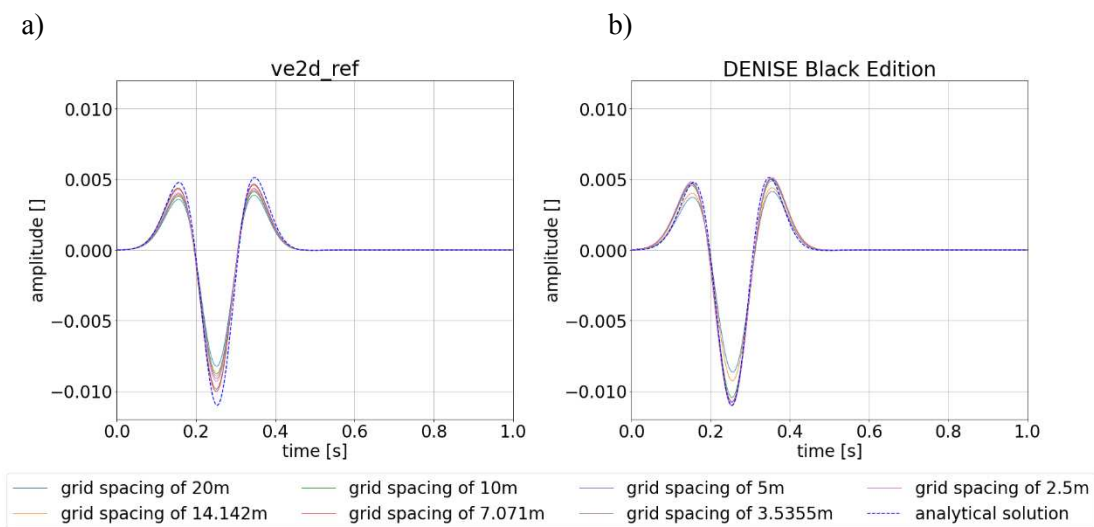


Figure 4.2: Synthetic seismograms amplitude corrected of the horizontal component at an offset of 100 m from an explosive point source computed for all grid spacings in an elastic homogeneous full space for the modeling programs *ve2d_ref* (a) and *DENISE Black Edition* (b) corrected with the respective transfer functions compared to the analytical solution. A second method of normalizing the

amplitude is the use trace normalisation. Trace normalized data is used in the error calculation for the process of full waveform inversion as a easy to implement solution to a variety of issues with the process of simulating wavefields (Bleibinhaus, 2016). The process of trace normalisation reduces effects of amplitude decay with offset due to attenuation and geometrical spreading (Thiel et al., 2018) as well as balancing the shot energy for multiple shots to the same level. Using a trace normalized L2-norm as the misfit function yields more robust results when applying FWI to field data, than an ordinary L2-norm (Przebindowska, 2013). However, trace normalization has no effect on time-varying relative amplitudes occurring within a trace, such as effects generated by the 2D-approximation, which account for 3D effects (Thiel et al., 2018).

The normalized amplitude \tilde{a}_n at the n -th point in the timeseries can be calculated as

$$\tilde{a}_n = \frac{a_n}{\sqrt{\frac{1}{N} \sum_{i=1}^N a_i^2}}, \quad (4.3)$$

where a_n is the original amplitude at the n -th point in the timeseries.

The resulting amplitudes for a horizontal seismogram at 100 m offset in an elastic homogeneous full space is displayed in Figure 4.3a for `ve2d_ref` and in Figure 4.3b DENISE Black Edition. Figure 4.3 clearly shows the very good amplitude match achieved by trace normalisation in both cases with only minimal mismatches.

Trace normalisation effectively removes the amplitude effects related to offset while retaining phase and relative amplitude information. Since all traces are normalized by their RMS value, balancing all amplitudes to the same level, the relative amplitude variation within each trace is preserved.

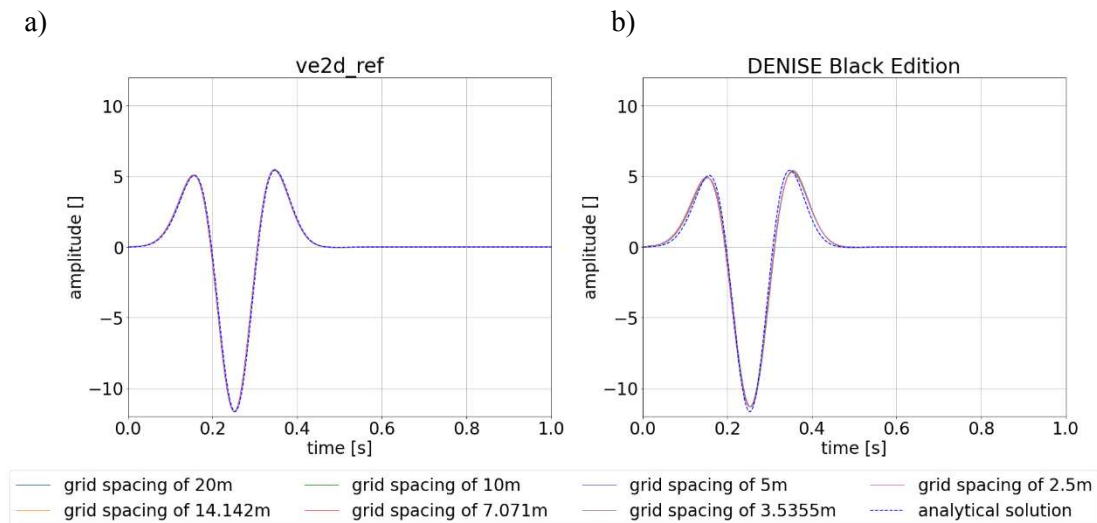


Figure 4.3: Trace normalized Synthetic seismograms of the horizontal component at an offset of 100 m from an explosive point source computed for all grid spacings in an elastic homogeneous full space for the modeling programs `ve2d_ref` (a) and DENISE Black Edition (b) compared to the trace normalized analytical solution.

4.2. Error calculation

Testing the accuracy of a modeling method requires a method to quantify the difference to an analytical solution or a different modeling in a simple manner. A common method to quantify an error is by calculating the L2-norm error, which is the L2-norm of the difference between synthetic

seismograms $f(t)$ and the seismogram of the analytical solution $q(t)$ normalized by the L2-norm of the analytical solution $q(t)$:

$$E = \frac{\sum_i^N (f(i dt) - q(i dt))^2}{\sum_i^N (q(i dt))^2} \quad (4.4)$$

This error calculation has a particular sensitivity to time shifts, which cause a high error even with an otherwise similar waveform. On the other hand amplitude differences are weighted less and an additional comparison of the waveform is necessary to determine accuracy (Bohlen & Saenger, 2006). The measure of this error is still very useful as this or similar error calculations are commonly used within full-waveform inversions. This method will be used in the following test models where analytical solutions exist to measure the error of a synthetic seismogram.

The relative error calculated with equation (4.4) can also be applied to measure the relative difference between two different synthetic seismograms. When this is done for multiple synthetic seismograms simulated with different grid spacings, a convergence test is performed. There the difference between the synthetic seismograms should consecutively decrease with smaller grid spacings, which is a useful measure when no analytical solution is available to gage the accuracy of a simulation.

Here the relative difference between two spatial discretisations is calculated by adapting equation (4.4), where the analytical solution q is replaced by the modelled traces of the higher grid spacing. This gives the relation for the relative difference

$$E = \frac{\sum_i^N (f_l(i dt) - f_h(i dt))^2}{\sum_i^N (f_h(i dt))^2}, \quad (4.5)$$

where f_l and f_h are the seismogram data of the smaller and higher simulated grid spacing.

To gage the error of simulations, it is useful to investigate the seismograms over the whole simulated time. Then the effects of unwanted reflections from the boundaries are also considered, which are to some extent impossible to completely remove. But to test the accuracy of the simulation itself, only time windows over an arrival can be analysed and the error estimated. This can be done for P-waves and surface waves, although there will always be an overlap at smaller offsets since the wave also have to properly separate. The error calculation is performed in these time windows for all models using the amplitude corrected or trace normalized synthetic seismograms.

4.3. Wavefield investigation

To better understand the phases found in simulated seismograms the wavefields are investigated throughout the tests performed during this study. Velocity or displacement fields are cumbersome to interpret since one phase maybe partially present in both horizontal and vertical components. Instead, the spatial divergence and curl of the displacement vector \vec{u} is used. This has the benefit, that the divergence ($\nabla \cdot \vec{u}$) is related to the total compressional energy (E_P) and the curl ($\nabla \times \vec{u}$) to the shear energy (E_S). These can be calculated as (Dougherty & Stephen, 1988)

$$\begin{aligned} E_P &= (\lambda + 2\mu)(\nabla \cdot \vec{u})^2, \\ E_S &= \mu(-\nabla \times \vec{u})^2, \end{aligned} \quad (4.6)$$

where λ and μ are the Lamé parameters.

The curl and divergence of the wavefields are computed for snapshots using the particle velocities saved for the entire model. The compressional and shear energies separate the P and S-waves

occurring in the simulated wavefields. Rayleigh waves contain both compressional and shear energies, and therefore are visible in both.

5. Elastic homogeneous full space

The simplest possible model for which an analytical solution exists is an elastic homogeneous full space. However, numerically the dimensions must be finite, and to avoid artefacts from the boundaries, appropriate conditions must be implemented. Therefore, the modeling uncertainty in a homogeneous full space should only be influenced by the FD scheme and the absorbing boundary condition implemented. Both the FD scheme and the boundary conditions can be implemented in various ways, and the goal of this section is to evaluate the differences of the two modeling algorithms (ve2d_ref and DENISE Black Edition).

The program EX2DVAEL by Berg et al. (1994) can only calculate the analytical solution for an elastic homogeneous half-space. To compute the analytical solution for an elastic homogeneous 2D full space, the source and receivers are embedded at a depth of 100 km, so the signal never reaches the surface within the simulated time of 10 s. The numerically modelled traces are compared to this analytical solution.

5.1. Model specifics

The model chosen to approximate an elastic homogeneous 2D full space has the spatial dimensions of 25000 m in horizontal and 6000 m in vertical direction. These dimensions mimic the refraction survey at the SAFOD site as described by J. A. Hole et al. (2006). Absorbing boundaries were added along the borders of the model space extending the total model. Modeling with ve2d_ref adds sponge layer boundaries at the bottom and left and right edges of the model, while the top boundary has to be accounted for explicitly extending the model. Sponge layers in ve2d_ref are split into a coarse and fine discretisation. The bottom sponge layer of the model is defined entirely in the coarse grid spacing, to save computational resources, while the side and upper sponge layers boundaries are defined in the fine discretisation as depicted in Figure 5.1a. For DENISE Black Edition a C-PML boundary with a width of 40 grid points is defined around the model space (Figure 5.1b).

An explosive point source and receiver array of 489 receivers were embedded in the vertical centre of the model space at the vertical coordinate $z = 0$ m. The model space extends vertically ± 3000 m from the receiver array and is surrounded by the absorbing boundary frame as depicted in Figure 5.1 for both modeling algorithms. The source point is placed at the same vertical coordinate ($z = 0$ m) as the receiver array, and laterally at 600 m. The general model parameters are given in Table 3.2, with seven models according to the spatial and temporal discretisations outlined in Table 3.1.

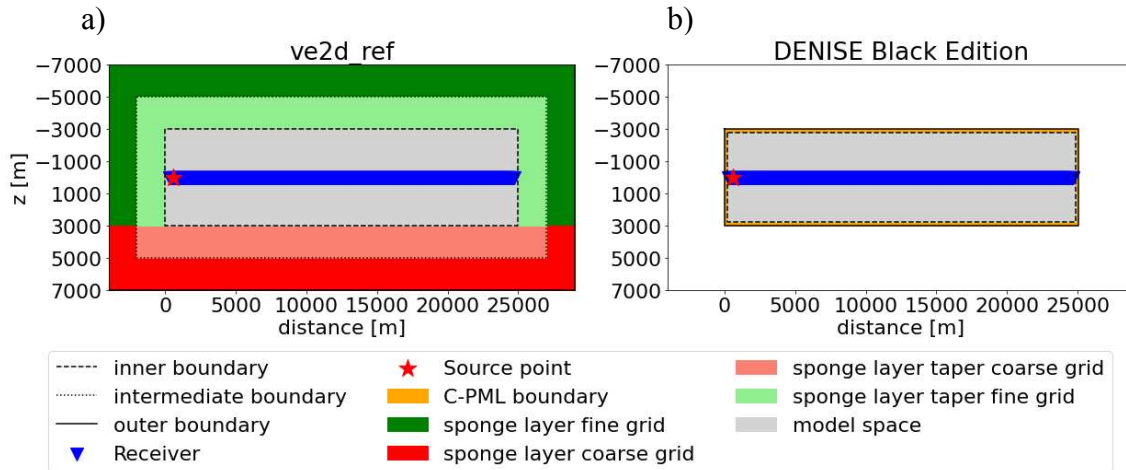


Figure 5.1: Schematic of a model of an elastic homogeneous full space for `ve2d_ref` (a) and `DENISE Black Edition` (b).

5.2. Modelled wavefields

In an infinite elastic homogeneous full space, the P-wave is the only wave phase present in the entire model when this space is excited by a compressional point source. In this case, the wavefield is expected to consist of a single circularly propagating P-wave wavefront.

5.2.1. Spatial divergence

The spatial divergence contains the compressional energy of the wavefield (as discussed in section 4.3) and should show the circular P-wave wavefront generated by the explosive point source. The spatial divergence of the simulated wavefield is plotted at 4 s in time for `ve2d_ref` in Figure 5.2a and `DENISE Black Edition` in Figure 5.2b. As is clearly visible in Figure 5.2 and the most prominent phase in the wavefield modelled with `DENISE Black Edition` and `ve2d_ref` is the P-wave, which is interfered with by artificial P-waves reflected at the upper and lower absorbing boundaries. These are located vertically at ± 3000 m in both variants of the model.

For `ve2d_ref` (Figure 5.2a) there are spurious reflected P-waves generated near the inner boundary. This is an effect of a positive velocity change happening at the beginning of the boundary taper. This would be expected to rather occur at the end of the taper directly at the sponge layer boundary. The P-wave traveling into the boundary taper exhibits a faster travel speed while decaying in amplitude. One reason for this is the definition of the taper in terms of the relaxation times, which introduces a steep impedance gradient creating the artificial reflected P-waves.

Spuriously reflected P-waves are also generated by the C-PML boundaries of `DENISE Black Edition` Figure 5.2b. Here the amplitude of the reflections varies with the incidence angle and the performance of the C-PML is worse at low incidence angles (section 2.6). These low incidence angles occur at long offsets, where the reflection amplitudes increase due to the near parallel incidence.

A difference in the absorbing boundary frames used in the respective modeling algorithms is visible. The artefacts of the C-PML boundaries of `DENISE Black Edition` generally produce lower amplitudes than the sponge layer artefacts of `ve2d_ref`.

The sponge layer of `ve2d_ref` is effective at eliminating the reflections from the edge of the model but introduces new artifacts near the inner boundary. The reflections from lower and upper inner boundary have the same characteristics and exhibit no notable difference. The change in FD grid spacing from

fine to coarse in `ve2d_ref` at the lower inner boundary ($z = 3000\text{ m}$) does not seem to create additional artefacts. This means that the sponge layer boundary may be defined in a coarser spatial discretisation than the model space to save computation time.

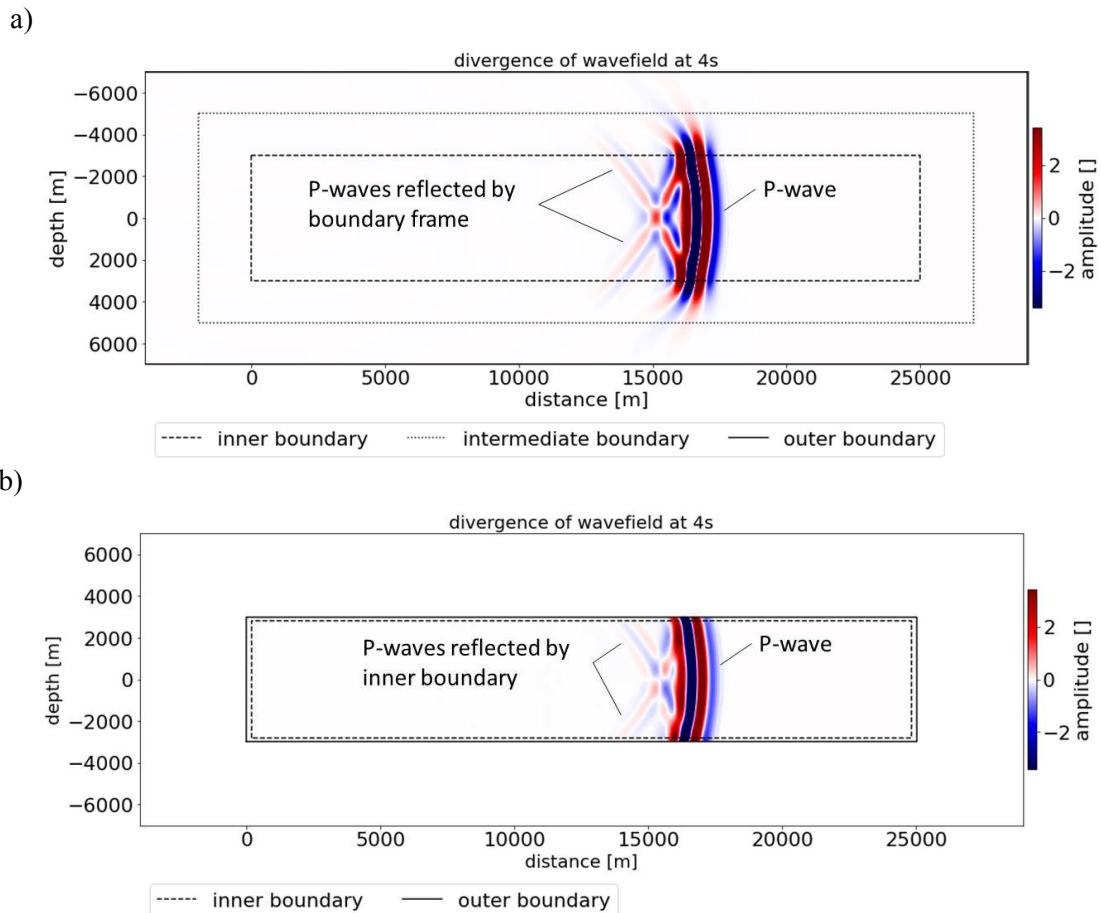


Figure 5.2: Spatial divergence of the wavefield modelled with `ve2d_ref` (a) and DENISE Black Edition (b) for a grid spacing of 5 m at 4 s in time.

5.2.2. Spatial curl

The spatial curl of the simulated wavefield is plotted at 4 s in time for `ve2d_ref` in Figure 5.3a and DENISE Black Edition in Figure 5.3b. At the inner boundary PS-conversions are occurring for both modeling algorithms, which are visible in the curl of the wavefields. It is important to note that the amplitude of these PS-conversions is small, and these are only prominent in the curl computed with `ve2d_ref` (Figure 5.2b), since no other wave phases are present. The inner boundary of the sponge layers again produces the PS-conversions in `ve2d_ref` visible in the curl (Figure 5.2b) and no conversions are visible at the actual boundary. This is caused by the definition of the taper in terms of the relaxation times introducing a change in P- and S-wave velocities. The upper and lower boundary exhibit no notable change except for a polarity change of the PS-conversions, which is to be expected due to the flipped direction of the incoming P-wave.

These PS-conversions also occur at the C-PML boundaries in DENISE Black Edition but are barely noticeable due to the amplitudes propagated through the C-PML.

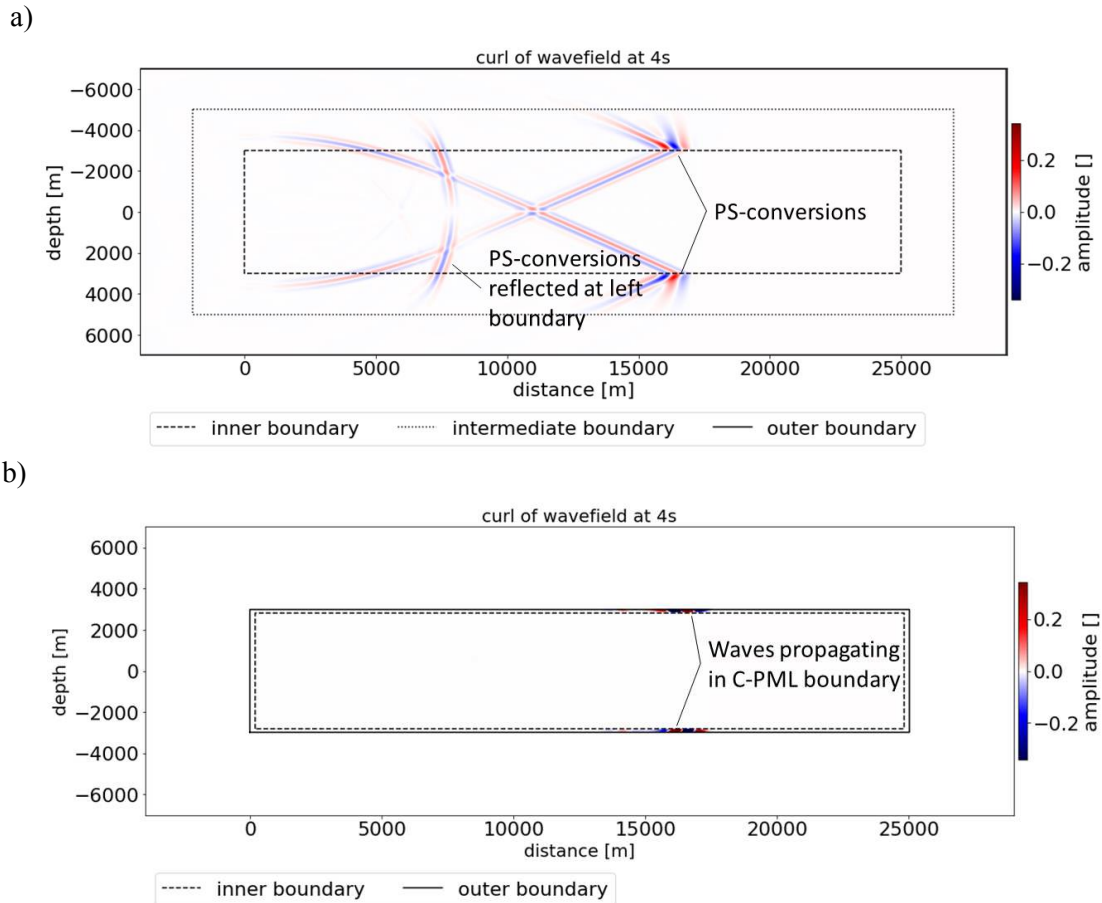


Figure 5.3: Spatial curl of the wavefield modelled with `ve2d_ref` (a) and `DENISE Black Edition` (b) for a grid spacing of 5 m at 4 s in time. The amplitude scale used here is scaled to 10% of the amplitude of maximum amplitude of the spatial divergence in Figure 5.2. The space outside the outer boundary in is not used in the model.

5.3. Receiver components

Two quantities are recorded at the receiver locations, the horizontal and vertical particle velocities, corresponding to quantities on the standard staggered grid. These are saved at receiver locations in the model, generating synthetic seismograms for both horizontal and vertical components. These seismograms should match the analytical solution as closely as possible, when conducting waveform modeling.

5.3.1. Horizontal particle velocity

An explosive source in a homogeneous full space will in an ideal space only generate a radial displacement or particle velocity signal, which is the horizontal component of the receivers in the model discussed here. As already seen for the wavefields above numerical simulations are not perfect and inaccuracies are introduced by various means. The trace normalized horizontal components for all grid spacings compared with the analytical solutions for receivers with a spacing of 2000 m are displayed in Figure 5.4 for data modelled with `ve2d_ref` and in Figure 5.5 for `DENISE Black Edition`. The modelled traces are compared with the analytical solution computed with the program `EX2DVAEL` (Berg, 1994).

The only wave propagated in the ideal full space model is the P-wave, which is clearly visible in the horizontal receiver components (Figure 5.4 and Figure 5.5). Additionally, a second wave-phase with a hyperbola shaped moveout is visible in horizontal receiver component for both modeling algorithms. These arrivals have a higher amplitude at long offsets in data modelled with `ve2d_ref` (Figure 5.4) than with DENISE Black Edition (Figure 5.5). These arrivals coincide with the reflected P-waves of the upper and lower boundary frames in both modeling algorithms visible in the divergence of both wavefields and can therefore be attributed to reflections of the absorbing boundary frame. Any other numerical inaccuracies such as the PS-conversions have to small amplitudes to be noticed in the horizontal receiver components. Comparing the modelled traces to the analytical solution these arrivals are the main source of inaccuracies on the horizontal component for this model.

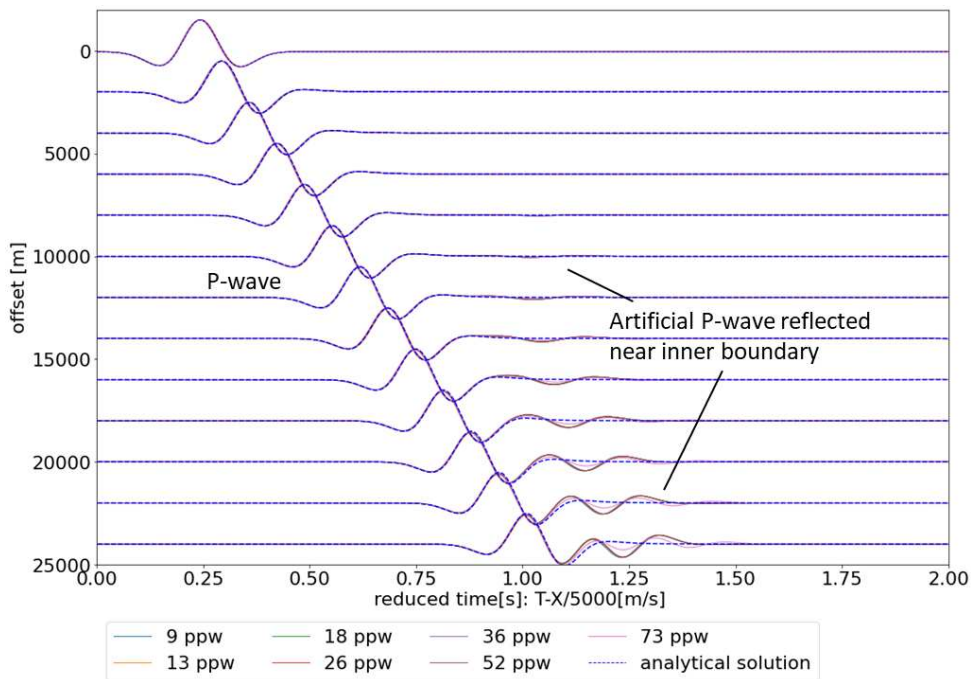


Figure 5.4: Trace normalized horizontal component for different offsets modelled with `ve2d_ref` in a pseudo elastic homogeneous full space with $Q=10^{10}$.

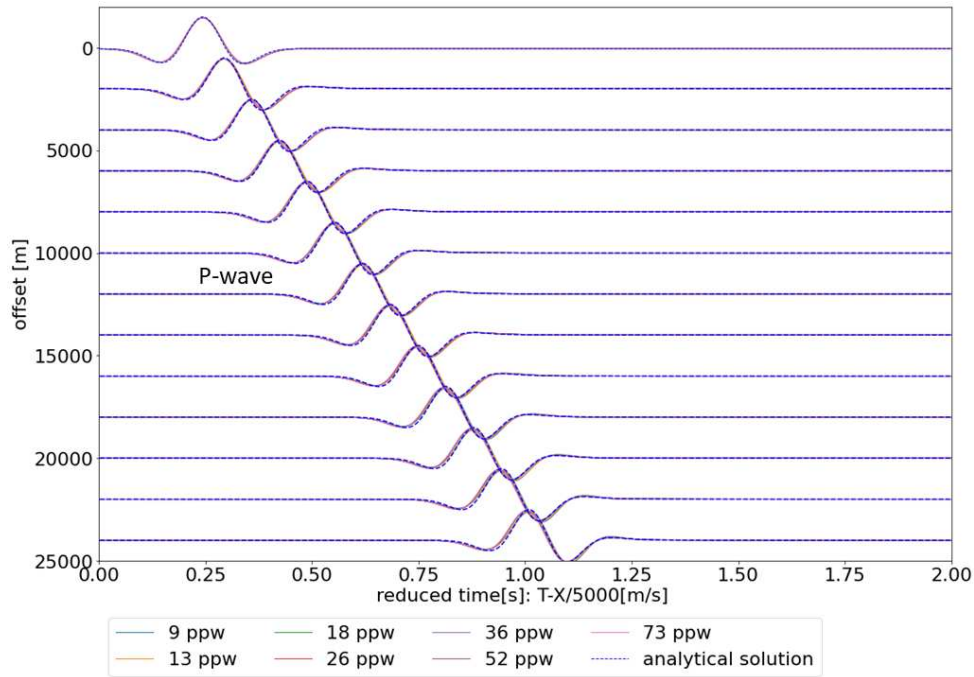


Figure 5.5: Trace normalized horizontal component in reduced time for different offsets modelled with DENISE Black Edition in an elastic homogeneous full space.

To gauge the accuracy of the waveform modeling, the relative difference between synthetic and analytical traces is calculated according to equation (4.4). This may be done for true amplitude and trace normalized data.

The relative errors over the offset are plotted in Figure 5.6 for `ve2d_ref` and in Figure 5.7 for DENISE Black Edition, each for true amplitude (a) and trace normalized data (b). The zigzagging of the relative error values in both modeling algorithms occurs due to the receiver points not being located in exactly the same position, as some grid spacings are not a common denominator of the receiver spacing.

The relative error for the true amplitude modeling with `ve2d_ref` (Figure 5.6 a) remains at a constant level of 2% for all spatial discretisations up to an offset of 12000 m, where it starts to rise until it reaches 25% at an offset of 25000 m, the maximum offset modelled. The trace-normalized data (Figure 5.6b) has a similar behaviour. For offsets below 12000 m the error is less than 1%. A common feature for both the true amplitude and trace normalized data, is the lower error for the smallest grid spacing (highest ppw), which has a maximum relative error of 8% and 7% respectively. This effect might be related to the fine discretisation model. The errors at long offsets are caused by the artificial P-waves reflected near the inner boundary which increase in amplitude over offset compared to the direct P-wave.

For data modelled with DENISE Black Edition (Figure 5.7) all grids above 18 ppw seem to have a similar error development over offset, while it is different for coarser grids (9 and 13 ppw). Errors for grid discretisations above 18 ppw increase from a relative error of 1% at offsets below 5000 m to 3% at higher offsets. Grids with a discretisation of 9 and 13ppw react differently in that the error at small offsets is higher (between 1 and 3%), while at offsets above 15000 m an increase in relative error is visible. The true amplitude (Figure 5.7a) and trace normalized data (Figure 5.7b) exhibit almost identical relative errors. Here the errors at offsets greater than 5000 m are also caused by the artificial P-wave reflected by the C-PML boundary.

The main source of errors in the horizontal component are numerical artefacts generated at the inner boundaries. These artefacts increase in significance over offset and have a higher impact on the

relative error when using sponge layers than with C-PML boundaries. Here it is important to note, that the efficiency of reducing artefacts of C-PML decreases in this application in narrow models with offset due to its problems with grazing incidences.

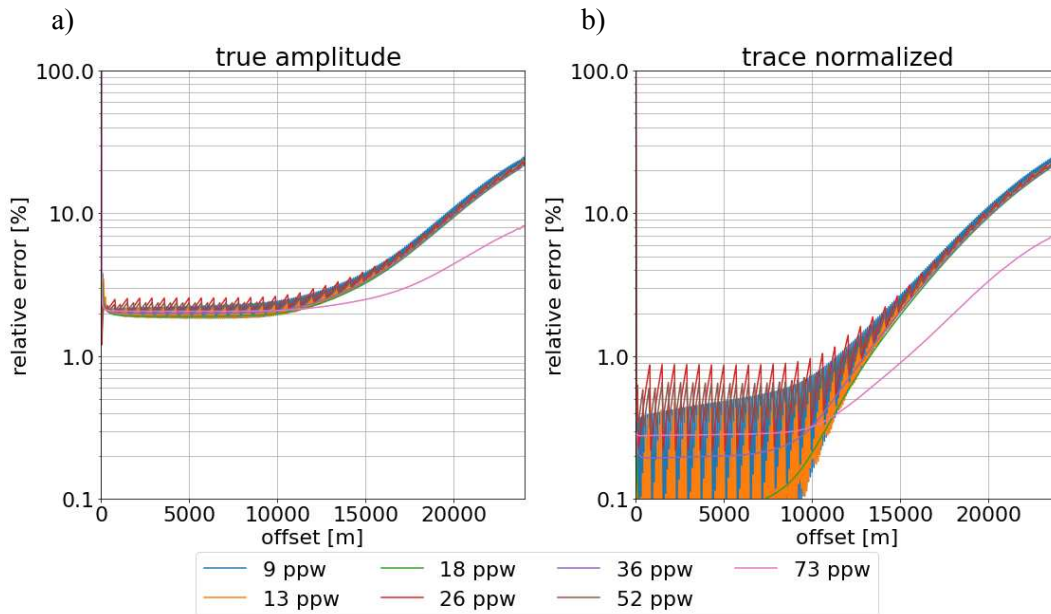


Figure 5.6: Relative error of the horizontal component with *ve2d_ref* as a function of offset for true amplitude (a) and trace normalized (b) data modelled in an elastic homogeneous full space.

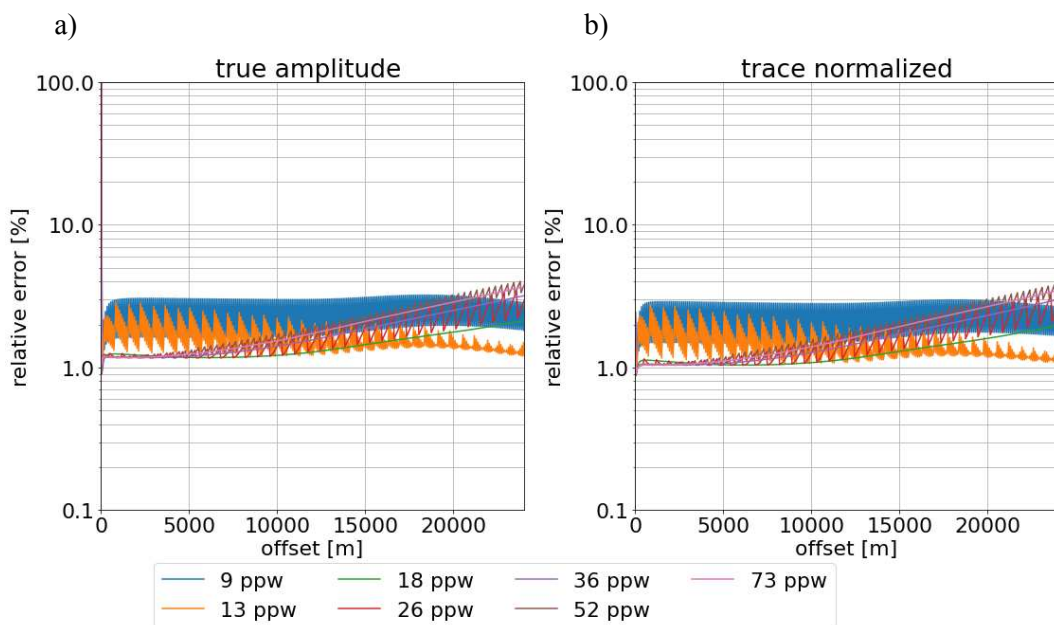


Figure 5.7: Relative error of the horizontal component with *DENISE Black Edition* as a function of offset for true amplitude (a) and trace normalized (b) data modelled in an elastic homogeneous full space.

5.3.2. Vertical particle velocity

Since the P-wave is a longitudinal wave, receivers should only have a signal on components oriented radial to the source. The component perpendicular to the wave path should have no signal, which is

the case for the vertical component for the source and receiver setup chosen in this model. However, a signal is present on the vertical component in both modeling programs.

The trace normalized vertical components for all grid spacings compared with the analytical solutions for receivers at 2000 m spacing are displayed in Figure 5.8 and Figure 5.9 for data modelled with `ve2d_ref` and DENISE Black Edition respectively. In both cases the amplitude of the vertical has a maximum amplitude in the near field of up to 10% of amplitude of the horizontal components. This ratio varies significantly with spatial discretisation, where coarser grids producing higher amplitudes on the vertical component. While the shape of the signal on the vertical component is comparable to that of the horizontal component, the amplitudes of the traces modelled with `ve2d_ref` (Figure 5.8) have an inverse amplitude compared to the amplitudes modelled with DENISE Black Edition (Figure 5.9) for the grid discretisations of 9, 13, 26 and 52 ppw.

There are three distinct artificial arrivals visible on the vertical components for both modeling programs (Figure 5.8 and Figure 5.9), rapidly decaying direct P- and S-waves and reflected P-waves that increase in amplitude with offset. The artificial direct S-wave is barely visible due to its small amplitude and is easily mistaken for numerical noise. In `ve2d_ref` (Figure 5.8) an additional late arrival is noticed which seems to be a multiple of the earlier artificial P-wave.

These arrivals on the vertical component are caused by three factors, the reflected P-waves at the absorbing boundary frame, the setup of the standard staggered grid and the source implementation of a compressional point source. The direct S-wave is the result of numerical artefacts from the initialisation of the wavefield., while the direct P-wave stems from the vertical offset by $dh/2$ of the vertical particle velocity defined in the standard staggered grid (section 2.3). The amplitude of the P-wave decreases so rapidly, because the curvature of the direct P-wave front decreases with offset. Artificial arrivals later than the direct waves are the result of the absorbing boundaries used. These numerical artefacts have small amplitudes compared to the signal on the horizontal component, rarely exhibiting amplitudes higher than 1% of the horizontal amplitude.

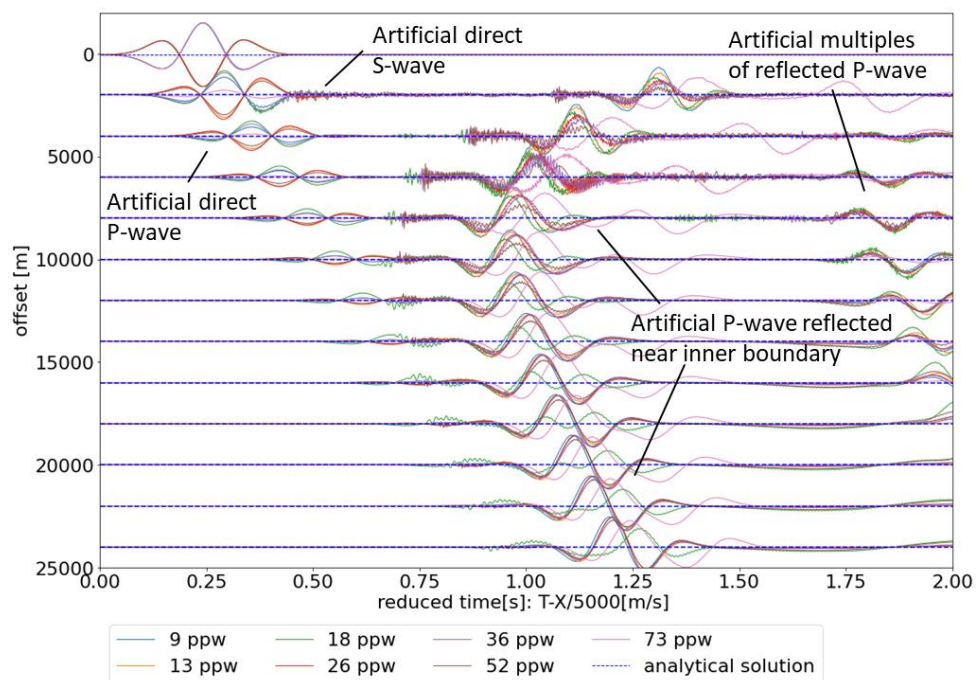


Figure 5.8: Trace normalized vertical component for different offsets modelled with `ve2d_ref` in a pseudo elastic homogeneous full space with $Q=10^{10}$.

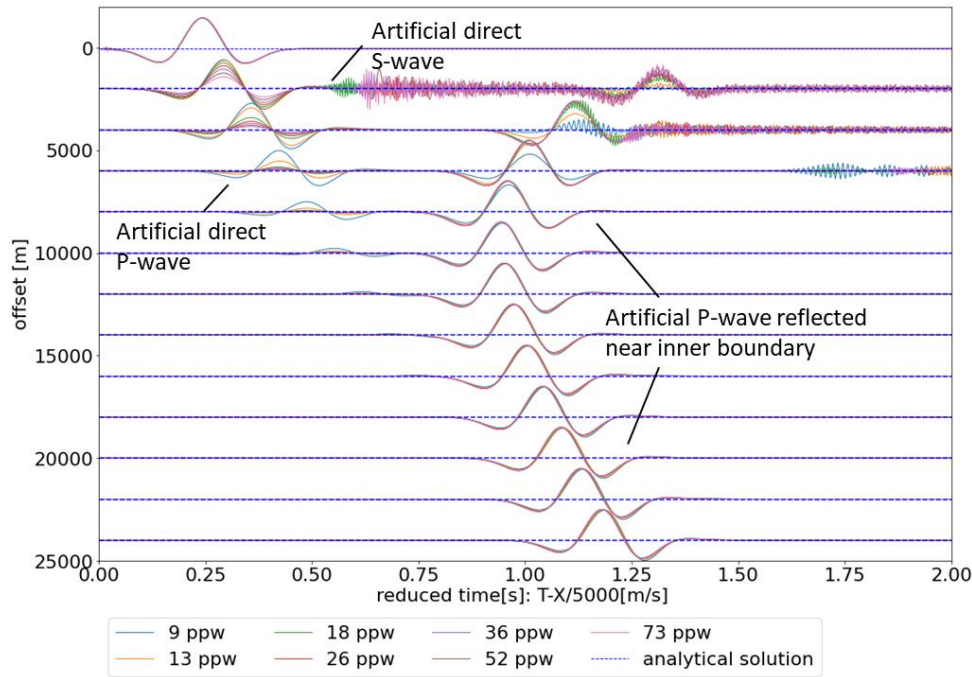


Figure 5.9: Trace normalized vertical component in reduced time for different offsets modelled with DENISE Black Edition in an elastic homogeneous full space.

For the vertical component, a direct comparison to the corresponding component of the analytical solution according to equation (4.4) cannot be done, because the analytical solution has a value of zero for all traces which would yield undefined values. Instead, the L2-norm of the vertical component of the synthetic traces is normalized by the L2-normalized vector component of the analytical solution, still adhering to the calculation in equation (4.4). Furthermore, such a comparison would be meaningless with trace normalized data as all amplitude data of the different components would be lost.

The results are depicted in Figure 5.10a for `ve2d_ref` and in Figure 5.10a for DENISE Black Edition. Both modeling algorithms start with a rapid decrease of the error with the increasing offset, starting from up to 10% to values below $10^{-2}\%$ with generally finer grid discretisations reaching subsequently smaller values down to $10^{-4}\%$.

The errors on the vertical component relative to the vector component for `ve2d_ref` (Figure 5.10a) reach a minimum around the offset between 2000 and 8000 m, followed by a slight increase. At offsets above 20000 m a plateau is reached, which is specific to each grid discretisation higher resolution grids producing lower errors. The exceptions are grids with 18 ppw (10 m grid spacing), which show a decrease in relative error at large offsets, and 73 ppw (2.5 m grid spacing), which reaches a minimum at 1000 m and then increases steadily to an error of 0.5%.

For DENISE Black Edition, the relative errors of the vertical component to the vector component (Figure 5.10b) reach a minimum at offsets of between 2000 and 7000 m, with the location and value of the minimum is depending on the grid spacing. This is followed by an increase in relative error up to 10% at maximum offsets.

The error on the vertical component for both modeling algorithms at small offsets is caused mostly by the standard staggered grid itself, rather than by reflections of an absorbing boundary. It persists even if the source point is moved to the centre of the model space (vertically and horizontally), where no interaction with a boundary is possible at small offsets below 3000 m. The error at large offsets on the other hand is caused by P-wave reflections of the upper and lower absorbing boundary frames. These

reflections interfere with the P-wave at offsets greater than 9000 m for `ve2d_ref` and above 7000 m for DENISE Black Edition.

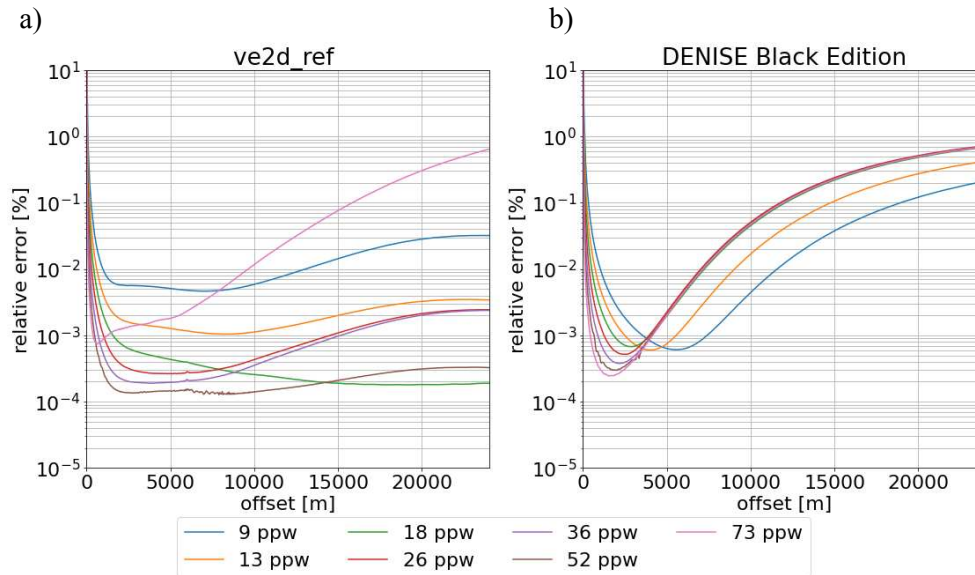


Figure 5.10: Comparison of difference between synthetic and analytical vertical component for an elastic homogeneous full space normalized to the analytical vector component for data modelled with `ve2d_ref` (a) and DENISE Black Edition (b).

5.3.3. Mean relative error

The error of a specific model can be summed up as the mean error of all simulated traces. The expectation from such a plot is, that the error will decrease with a finer discretisation (higher ppw). The mean relative error is calculated for both the horizontal and vertical component and the results for both `ve2d_ref` and DENISE Black Edition are shown in Figure 5.11.

The error of the horizontal component (Figure 5.11a) has an almost constant error for both modeling algorithms indicating that the modeling has already converged to the minimum. Here DENISE Black Edition shows a slight decrease at lower ppw, while `ve2d_ref` exhibits a decrease at the finest spatial discretisation.

The mean error of the vertical component relative to the vector component (Figure 5.11b) shows different trends for the two modeling algorithms. DENISE Black Edition exhibits an overall increase in error from 0.05% to 0.2% from 9 to 18 ppw, which plateaus at 0.2% for finer discretisations. The error for `ve2d_ref` decreases from 0.03 to 0.005% between 9 and 52 ppw and then peaks at the 73 ppw to 0.1%.

The majority of this error is caused by artefacts from absorbing boundaries. In general, the sponge layers of `ve2d_ref` produce higher errors on the horizontal component than the C-PML boundaries of DENISE Black Edition. The vertical component has an inverse behaviour, where sponge layers produce fewer artefacts than the C-PML boundaries. However, the amplitudes of the horizontal artefacts are much higher than the vertical artefacts and have a greater impact on the modeling accuracy.

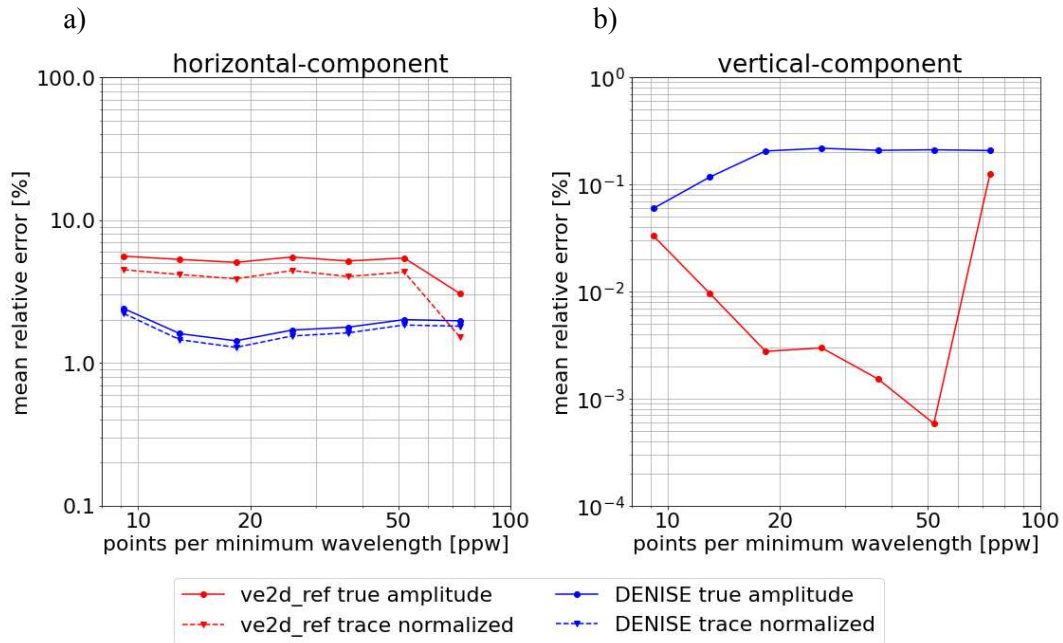


Figure 5.11: Mean relative error of horizontal component (a) and mean error of vertical component relative to vector component (b) for simulated spatial discretisations.

5.4. Summary of modeling errors

Overall, the error of the modelled data to the analytical solution is small for relative errors of the horizontal component of 1% and 2% for DENISE Black Edition and ve2d_ref respectively in the near offsets, where the wavefield is undisturbed in the P-wave window. The increase in error at longer offsets for ve2d_ref coincides with the arrivals from the artificial reflected wavefields of the absorbing boundaries. Here the sponge layers of ve2d_ref perform worse than the C-PML boundaries resulting in higher errors at longer offsets, all at a higher computational cost. Since it is not computationally viable to further increase the boundary size of the sponge layers in this model, the higher error at the long offsets must be accepted. However, the error may be reduced by increasing the size of the model space. For the remaining models the inner boundary was shifted further away from the receiver array to reduce these errors, which was not possible for this model due to memory constraints.

On the vertical component the error is greater for the C-PML boundaries, but these artefacts have smaller amplitudes. The error on the vertical component in the near field may be significant, but the error at large offsets can likely be ignored due to its rapid decrease.

6. Elastic homogeneous half-space with a horizontal free surface

To test the validity of the 2D FD simulation in case of an elastic homogeneous half-space with a free surface boundary, two boundary conditions – the image method and improved vacuum formulation – are considered. For this simple model an analytical solution exists and can be computed with EX2DVAEL (Berg et al., 1994). The analytical solution has been calculated with a source in a depth of 40 m beneath the free surface and receivers 5 m below the free surface at a regular horizontal spacing of 50 m.

6.1. Model specifics

For the model of a half-space with a horizontal free surface boundary aligned with the horizontal grid axis three variants of defining the free surface were tested. The size of the model space was chosen to be similar in dimension to the SAFOD model with a horizontal and vertical extent of 25000 m, and 5500 m, respectively. Each of the following models is initialized with these dimensions and for each, the spatial and temporal parametrisations described in Table 3.1 were applied. The simulations performed on these grids were carried out with the general parameters given in Table 3.2 for all three cases.

The first variant of an elastic homogeneous half-space model was tested with the program `ve2d_ref` which implements the image method of Robertsson (1996) discussed in section 2.7 as a free surface condition. The free surface is aligned horizontally with the grid and placed at the top boundary of the model and a schematic of this model is displayed in Figure 6.1a. This placement is possible because the grid is artificially extended above the surface by the grid points required for the imaging of stress components.

Secondly an elastic homogeneous half-space with a free surface condition of the image method after Levander (1988) was modelled with DENISE Black Edition. The horizontal free surface boundary is again placed at the top boundary of the model as shown in Figure 6.1a.

The last variant of an elastic homogeneous half-space was modelled using DENISE Black Edition. In this model variant, the surface condition of the improved vacuum formulation according to Zeng et al. (2012) is implemented. This variant includes a vacuum layer with a thickness of 200 m above the free surface of the elastic half-space to avoid any possible interaction with the upper model boundary. Since in the vacuum layer v_p is zero and the rigidity μ is set to zero by the parameter averaging scheme above the free surface, no seismic waves should propagate in this layer. This model setup with the 200 m wide vacuum layer is shown in Figure 6.1b for a grid spacing of 10 m.

The receivers for all three of these models are placed one grid point below the respective free surface with a horizontal receiver spacing of 50 m as shown in Figure 6.1 for a grid spacing of 10 m. The explosive point source is placed 40 m below the horizontal free surface to ensure a proper wavefield generation.

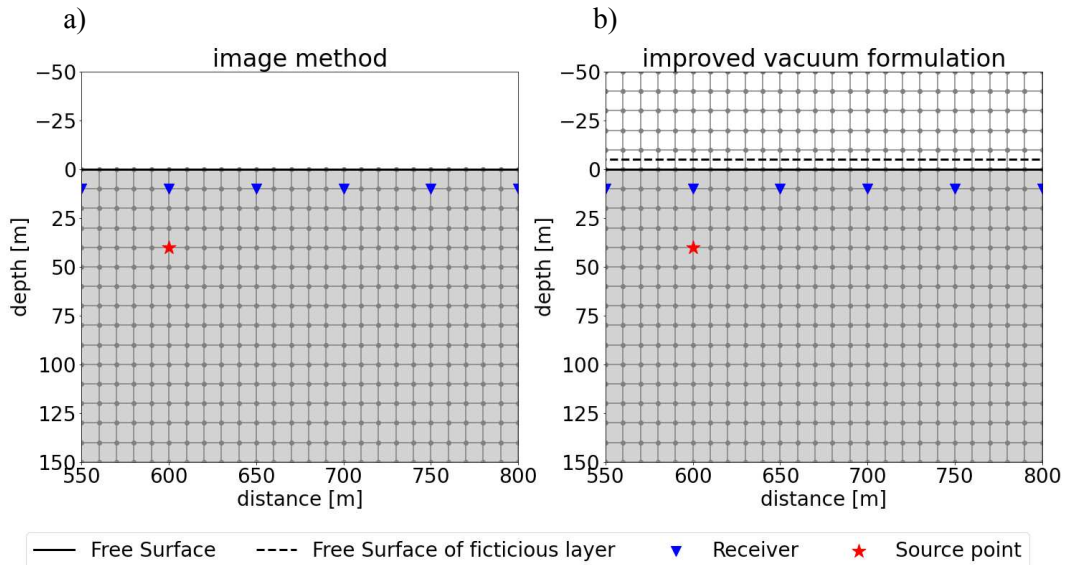


Figure 6.1: Schematic for a model of an elastic homogeneous half-space for an exemplary grid spacing of 10 m and two different surface conditions the image method (a) and improved vacuum formulation (b).

6.2. Modelled wavefields

In an infinite elastic homogeneous half-space with a free surface boundary excited by an explosive point source, four wave phases are generated, a P-wave produced by the explosive source, and an S-wave, a Rayleigh wave and a PS-wave produced by the interaction with the free surface. While P- and S-waves have a circular wavefront propagating through the medium, the Rayleigh wave propagates along the free surface. PS-waves are generated at the free surface by the P-wave and have a linear wavefront propagating into the medium. Out of all these phases the Rayleigh wave should have the largest amplitude.

In the following discussion I only show the spatial divergence and curl of the image method modelled with `ve2d_ref` and the improved vacuum formulation modelled with DENISE Black Edition, since the wavefield of the image method with DENISE Black Edition is qualitatively almost identical to the wavefield of the improved vacuum formulation for this model.

6.2.1. Spatial divergence

The spatial divergence of wavefields modelled with a grid spacing of 5 m (36 ppw) at a time of 4 s for the image method modelled with `ve2d_ref` and the improved vacuum formulation with DENISE Black Edition are depicted in Figure 6.2. As with the homogeneous full space, the spatial divergence shows the P-wave, and additionally the Rayleigh-wave traveling along the free surface with approximately the same amplitude for both the image method of `ve2d_ref` (Figure 6.2a) and the improved vacuum formulation of DENISE Black Edition (Figure 6.2b). Both numerically modelled wavefields show artefacts related to the absorbing boundaries. A common artefact is the artificial P-wave reflected near the inner boundary which has a higher amplitude in `ve2d_ref` when using sponge layers than with C-PML boundaries. The sponge layers also produce SP-conversions visible in the divergence (Figure 6.2a), which are generated by the interaction with the sponge layer taper near the inner boundary.

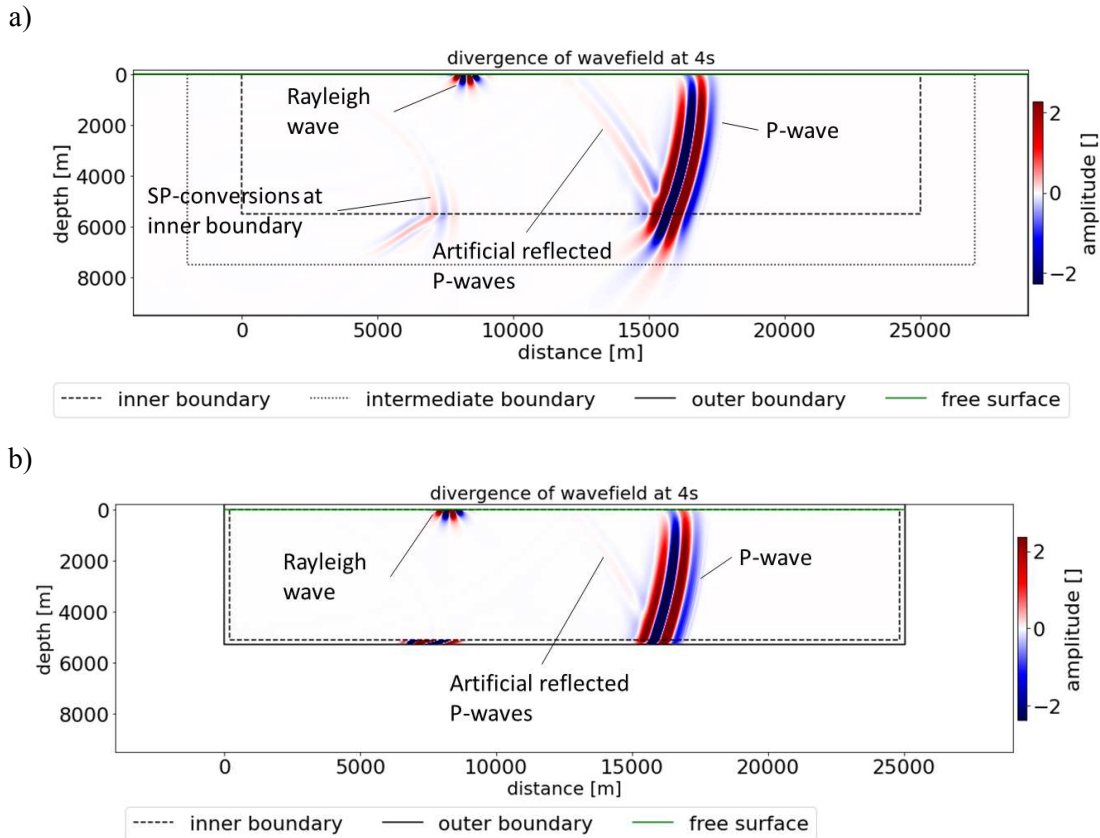


Figure 6.2: Spatial divergence at 4 s in time of the wavefields modelled with the image method in `ve2d_ref` (a) and the improved vacuum formulation in `DENISE Black Edition` (b) with a grid spacing of 5 m. The different phases are labelled in the panels.

6.2.2. Spatial curl

The curl of the wavefields at 4s in time modelled with a grid spacing of 5 m (36 ppw) for both the image method of `ve2d_ref` and the improved vacuum formulation of `DENISE Black Edition` are depicted in Figure 6.3a and Figure 6.3b, respectively. The curl shows the wavefronts of the Rayleigh, S- and PS-waves as the main features. The S-wave travels at a similar speed to the Rayleigh wave and interferes with it for most of the simulation, only separating properly at large offsets. The PS-wave has the same arrival time as the P-wave and cannot be separated from it near the free surface, where the receivers are located.

Noticeable artefacts are only visible in the curl of the wavefields computed with `ve2d_ref` (Figure 6.3a), where the sponge layers cause reflections of the S-wave near the inner boundary. Here, PS-conversions also occur, which have only small amplitudes and are barely visible in the computed wavefield. The C-PML boundaries of `DENISE Black Edition` (Figure 6.3b) cause only barely noticeable artefacts in the curl.

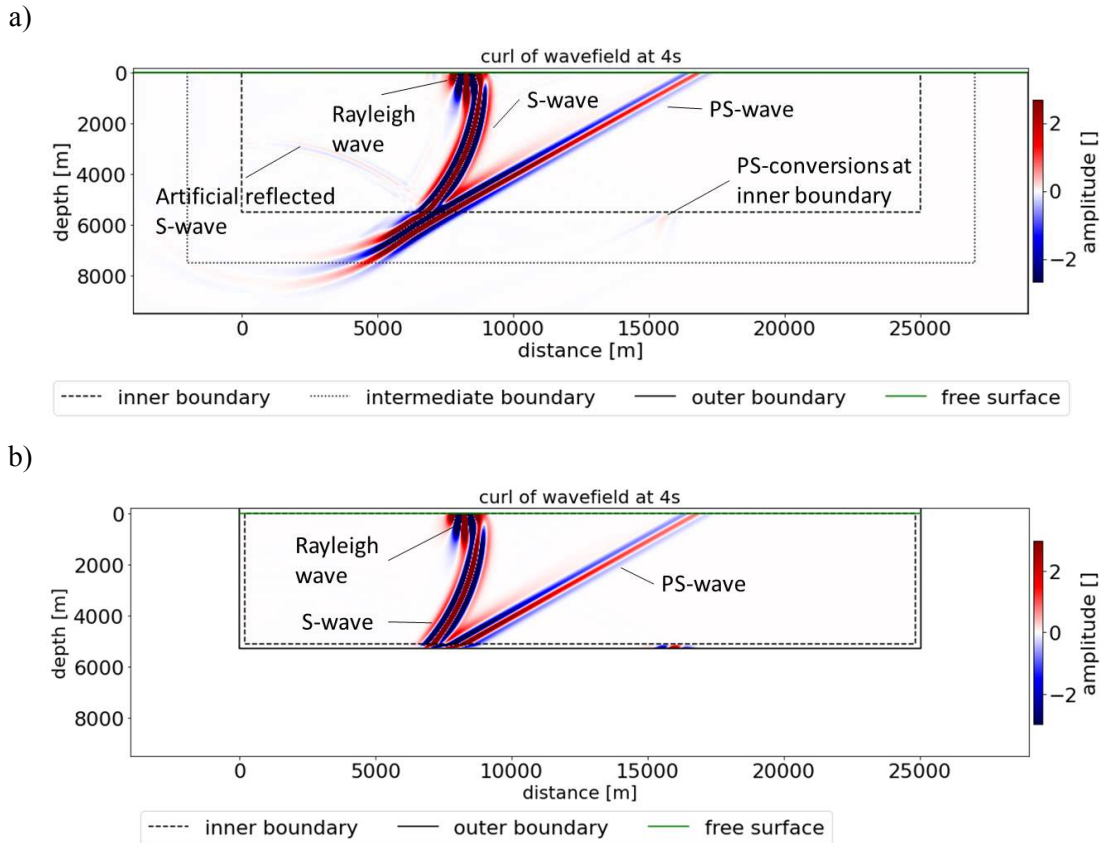


Figure 6.3: Spatial curl at 4 s in time of the wavefields modelled with the image method in *ve2d_ref* (a) and the improved vacuum formulation in *DENISE Black Edition* (b) with a grid spacing of 5 m. The different phases are labelled in the panels.

6.3. Receiver components

The focus of this section lies on the horizontal receiver component. The vertical component exhibits a similar behaviour as the horizontal component and is therefore not discussed in detail here, but is shown in Appendix A.

6.3.1. Horizontal component

The trace normalized horizontal component traces with a 2000 m offset spacing for all computed spatial discretisations are displayed for the image modelled with *ve2d_ref* in Figure 6.4 and the image method and improved vacuum formulation modelled with *DENISE Black Edition* in Figure 6.5 and Figure 6.6, respectively. Traces of each modeling are compared with the analytical solution for an elastic homogeneous half-space. The most prominent wave phase for receivers at the free surface in the homogeneous half-space is the Rayleigh wave. This results in other phases having a smaller relative amplitude compared to the surface wave.

In Figure 6.4, Figure 6.5 and Figure 6.6 lower amplitude phases are more visible at longer offsets (above 20000 m) since the Rayleigh wave does not propagate further than to 20000 m offset in the simulated timeframe. At these longer offsets, the P-wave first arrivals become the highest amplitude phase, and the artificial reflections become visible as three distinct phases in seismograms computed with *ve2d_ref* (Figure 6.4). These artefacts are the P-waves and PS-waves reflected at the inner boundary, and the first of these artefacts is the P-wave reflected at the lower inner boundary.

For long offset traces modelled in DENISE Black Edition (Figure 6.5 and Figure 6.6), only one artifact phase is visible, which is the artificial P-wave reflected at the lower C-PML boundary. These artefacts do not interfere with the P-wave for any of the modelled grids.

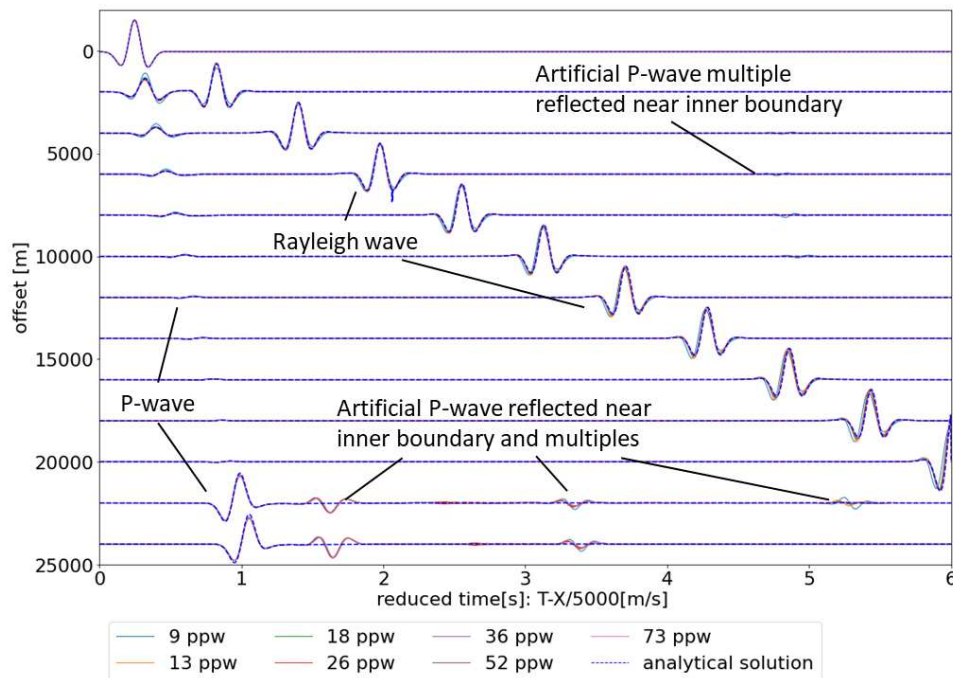


Figure 6.4 Trace normalized horizontal component in reduced time for different offsets modelled with *ve2d_ref* in an elastic homogeneous half-space and a free surface boundary defined with the image method.

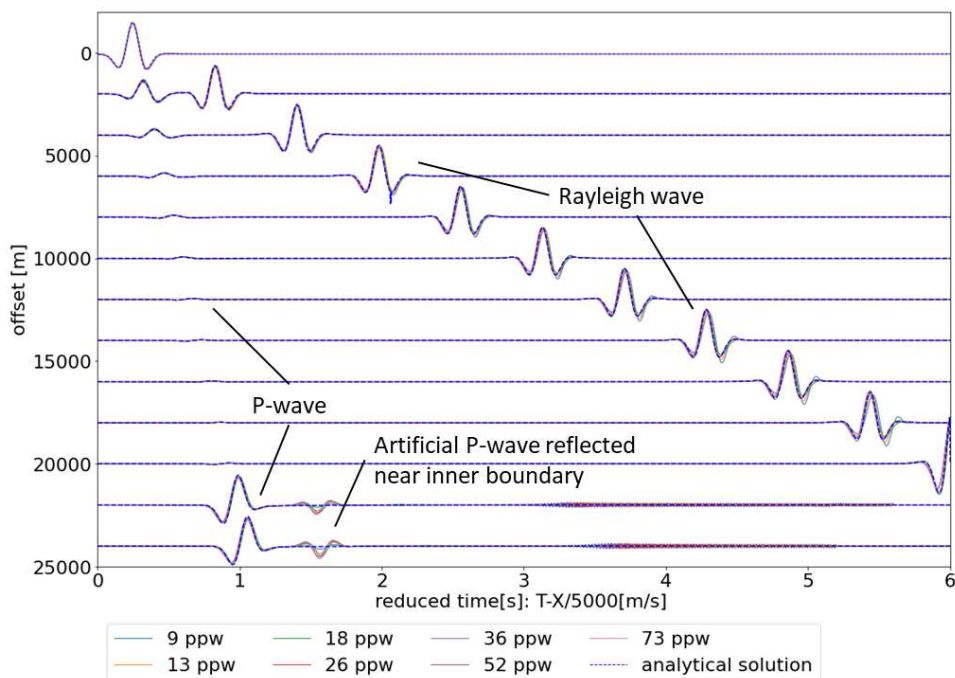


Figure 6.5: Trace normalized horizontal component in reduced time for different offsets modelled with DENISE Black Edition in an elastic homogeneous half-space using the image method to define the free surface boundary.

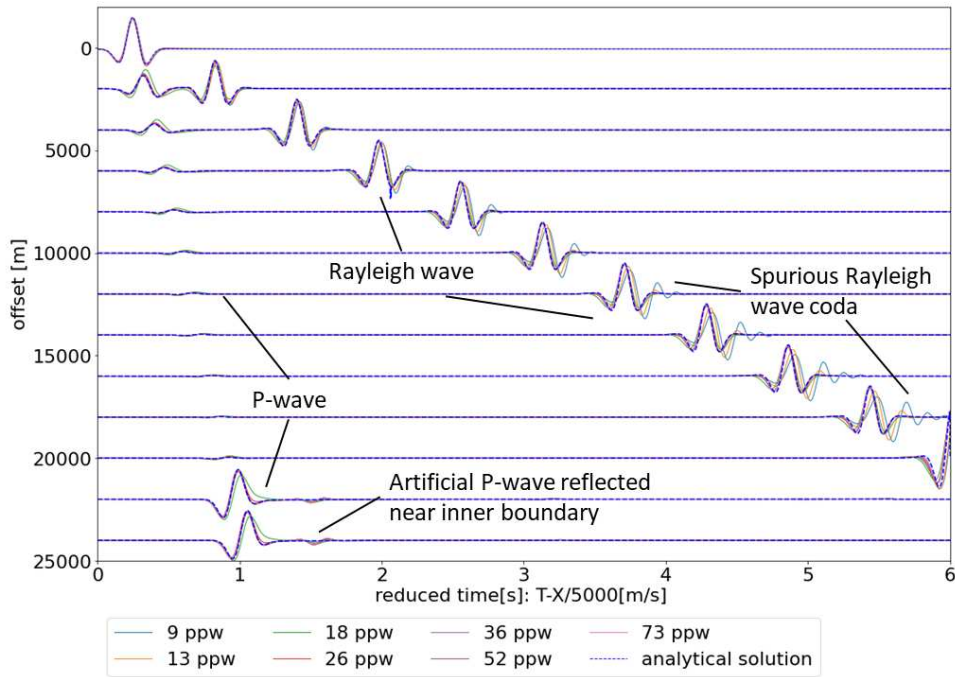


Figure 6.6: Trace normalized horizontal component in reduced time for different offsets modelled with DENISE Black Edition in an elastic homogeneous half-space with an improved vacuum formulation free surface boundary.

A comparison of the waveforms modelled with the image method (Figure 6.4 and Figure 6.5) and the improved vacuum formulation (Figure 6.6) shows a significant difference. While the image method manages to simulate the Rayleigh wave and the P-wave reasonably accurately for all discretisations, the improved vacuum formulation in DENISE Black Edition introduces numerical inaccuracies in the form of spurious Rayleigh wave coda. These have a significant amplitude for coarse spatial discretisations (9, 13 and 18 ppw). These inaccuracies grow with offset, increasingly shifting the phase of the wavelet and misaligning the peaks and troughs with the analytical solution. This effect is reduced with higher spatial resolution and is mostly present for the surface waves, less so in the first arrivals.

The inaccuracy of the simulated data is estimated by calculating the relative error to the analytical solution according to equation (4.4) for both true amplitude and trace normalized data. Since the P-wave has a considerably smaller amplitude than the surface waves, the error of each arrival is considered separately, otherwise errors of surface waves would outweigh the P-wave errors due to the higher amplitude. Separate time windows for the P-wave and Rayleigh wave have been chosen, which are plotted in Figure 6.7 over the shot gather of the analytical solution. The windows for the P-wave and Rayleigh wave have a length of 0.6 and 0.8 s, respectively, and are chosen long enough to capture the numerical inaccuracies as seen in Figure 6.6 for the Rayleigh waves modelled using the improved vacuum formulation.

These P-wave and Rayleigh wave time windows have an overlap at small offsets (Figure 6.7), where the P-wave and Rayleigh wave have not yet separated. In these offset regions, the errors in each time window are influenced by the other phase, which is expected to be more significant for the P-wave due to the higher amplitudes of the Rayleigh wave.

The S-wave is also present in the data, but only separates from the Rayleigh wave at offsets greater than approximately 12000 m and becomes a noticeable wave phase in the modelled data. Therefore, a separate window for the S-wave is not considered.

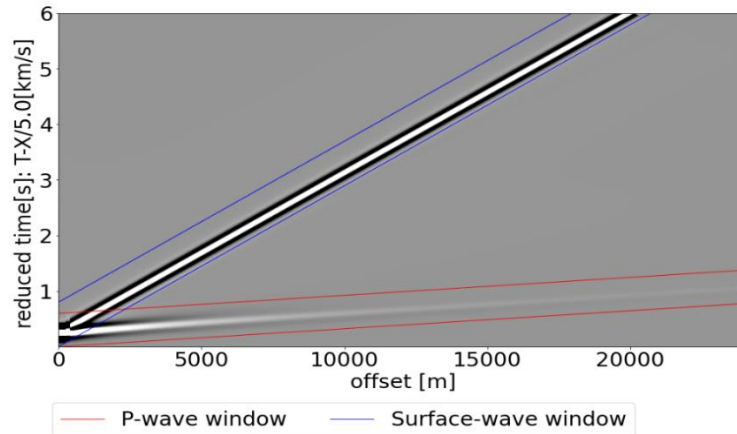


Figure 6.7: Shot gather of the horizontal component of the analytical solution for a homogeneous full space with the time window over the P-wave and surface wave in reduced time.

The relative error for the P-wave time window for a homogeneous half-space with a free surface boundary implemented according to the image method modelled in `ve2d_ref` and DENISE Black Edition is shown in Figure 6.9a,b and Figure 6.9c,d, respectively. The zigzagging for grid discretisations of 9, 13, 26 and 52 ppw (grid spacings of 3.5355, 7.071, 14.142 and 20 m) is created due to the misalignment of grid points to the receiver points.

Both modeling algorithms produce a similar general relative error level of 2% for true amplitudes (Figure 6.9a, Figure 6.9c and Figure 6.9e). Errors at offsets smaller than 2000 m exhibit an interference from Rayleigh waves, since these only fully separate from the P-wave at this point. At these low offsets the relative errors are generally reducing with a decrease in grid spacing, mimicking the errors of the surface wave discussed later. Otherwise, the error is constant over the entire offset for all grids modelled in `ve2d_ref` with the image method. Modeling with `ve2d_ref` produces P-waves with a constant relative error between 2 and 3%. The relative error of trace normalized data (Figure 6.9b) exhibits the same trend with values below 1%. This reduction in error by the trace normalisation is an effect of equalizing the amplitudes so that only differences in relative amplitude are recognised as such errors. The constant low relative error for all modelled spatial discretisations indicates that the numerically modelled P-wave has already converged to its minimal error.

The image method, as implemented in DENISE Black Edition also produces relative errors at a level of 2% with true amplitude data (Figure 6.9c). While coarse discretisations of 13 ppw and below have constant relative errors over offset, the denser spatial discretisations exhibit an increase with offset. This increase is also present in trace normalized data (Figure 6.9d), although here the overall relative error is reduced.

The implementation of the improved vacuum formulation as a free surface condition in DENISE Black Edition generates traces with relative errors for true amplitude data (Figure 6.9e) with a constant error level after the separation of P- and surface waves. The relative error at small offsets, where the P-wave and Rayleigh wave separate, is dependent on the spatial discretisation. Here, the fine discretisations have low errors of 2%. Fine grid discretisations of 36 ppw and above exhibit an increase in relative error with offset. The behaviour of the relative error is similar for trace normalized data (Figure 6.9f), although at lower overall errors of less than 3%. Discretisations of 18 and 26 ppw exhibit anomalously high errors between 10 and 11% for true amplitude data and at lower errors for trace normalized data. Here, the P-wave is distorted while Rayleigh waves remain largely unaffected. The reason for this effect is unclear, but it remains consistent throughout many simulations and redefinitions of the model.

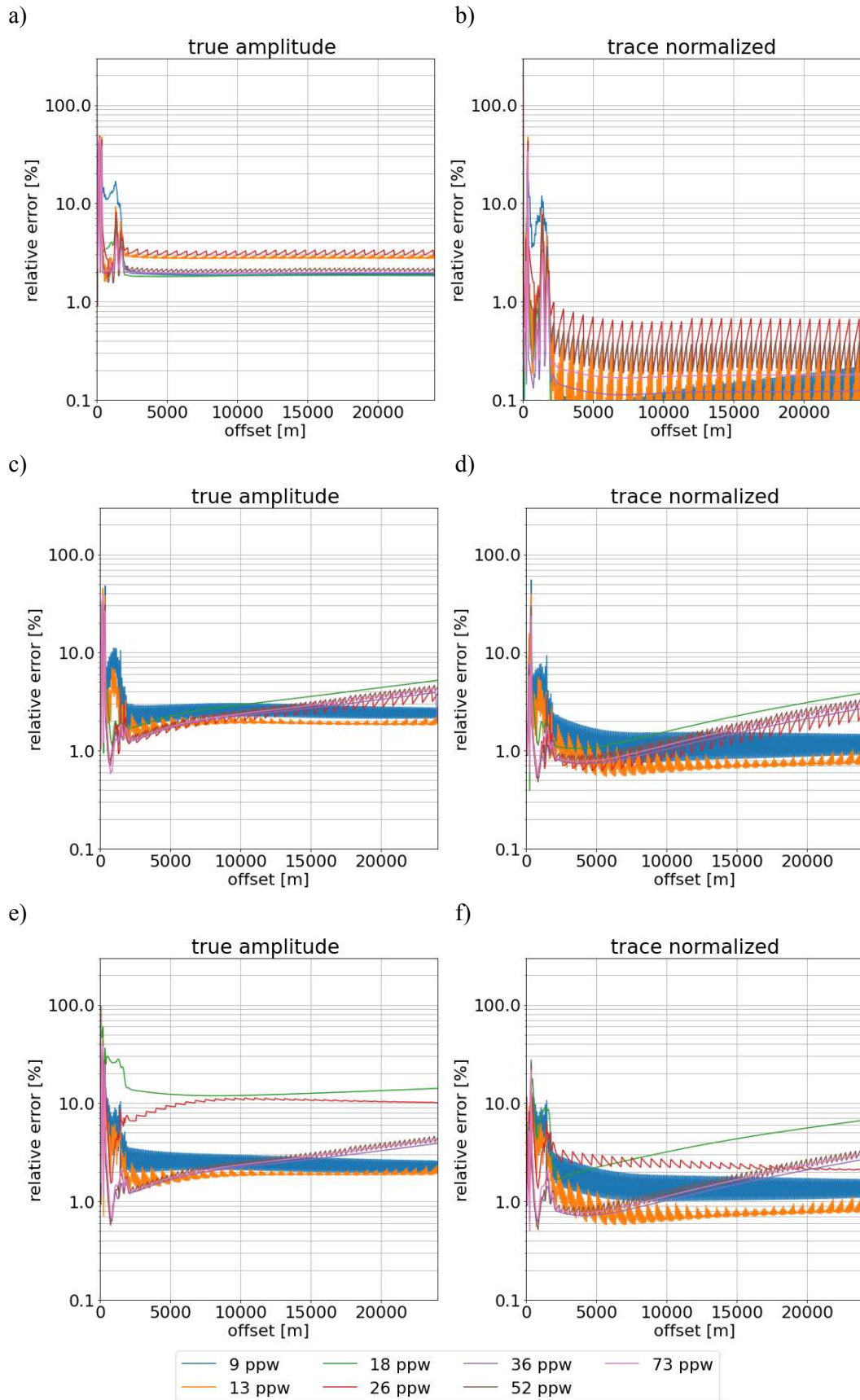


Figure 6.8: Relative error to the analytical solution of the horizontal component for true amplitude (left column) and trace normalized data (right column) in the P-wave time window computed with the image method in *ve2d_ref* (a and b) and in DENISE Black Edition (c and d) and with the improved vacuum formulation in DENISE Black Edition (e and f)

The relative error calculated for the Rayleigh wave time window for offsets up to 20000 m, since this is the maximum distance the surface wave travels within the simulated timeframe. The resulting offset plots are shown in Figure 6.9 for the free surface according to the image method with `ve2d_ref` (Figure 6.9a and b) and DENISE Black Edition (Figure 6.9c and d) and improved vacuum formulation modelled with DENISE Black Edition (Figure 6.9e and f).

The image method of `ve2d_ref` produces a Rayleigh wave with relative error that increases with offset for both modeling algorithms and spatial resolution (Figure 6.9a, b, c, and d). The increase over offset is caused by a mix of numerical artefacts and general cumulative inaccuracies caused by the number of FD operations, which increases at larger offsets. This increase is greater for implementations with DENISE Black Edition (Figure 6.9c and Figure 6.9e) than for `ve2d_ref` (Figure 6.9a). The decrease in error with increasing grid resolution is an effect dispersion related to the free surface boundary condition.

The implementation in `ve2d_ref` has a relative error for true amplitude data (Figure 6.9a), which decreases with increasing spatial resolution from 30% to 1-2% for offsets between 2000 and 5000 m. The exception is the irregular grid spacing 14.142 m (26 ppw), which has a lower error of 1% for small offsets that increases to 20 and 10% over the entire offset range. The image method in DENISE Black Edition (Figure 6.9c) also exhibits a decrease in relative error with the increasing spatial resolution and an increase in error for all discretisations with offset. Finer grid discretisations above 26 ppw experience a higher increase with offset than higher coarser grids (18 ppw and below).

Trace normalisation generally results in an overall reduction in relative error for both modeling programs (`ve2d_ref` Figure 6.9b and DENISE Black Edition Figure 6.9d). For trace normalized data of the image method of `ve2d_ref`, the relative error (Figure 6.9b) reaches a minimum at an offset of 2000 m, where the P- and Rayleigh waves separate. The error increases more rapidly with offset for the trace normalized data (Figure 6.9b), but reaches lower values than the true amplitude data (Figure 6.9a). This is caused by the process of trace normalisation, since the main source of error at these offsets are small differences in amplitudes, as the wavelet becomes more distorted with more computation steps.

The improved vacuum formulation also exhibits a decrease in relative error for true amplitude (Figure 6.9e) as well as trace normalized data (Figure 6.9f) with finer spatial sampling, and a rapid decrease occurs between a grids with 18 and 26 ppw. For higher resolutions above 26 ppw, the decrease in error occurs less rapidly. Furthermore, the relative error shows an increase with offset for smaller grid spacings similar to the one observed in the P-wave time window (Figure 6.8) and an overall increase with offset. In contrast to Rayleigh waves in models using the image method, trace normalisation does not lower the relative error significantly when using the improved vacuum formulation.

In the near field, for offsets below 400 m, the relative errors spike to values above 40% for all discretisations and modeling algorithms. These errors decrease rapidly and these effects have disappeared for offsets above 1000 m. Here, the near field of the source is generating problems, which might be caused by inherent flaws of a regular Cartesian grid on which a high curvature wavefront is computed.

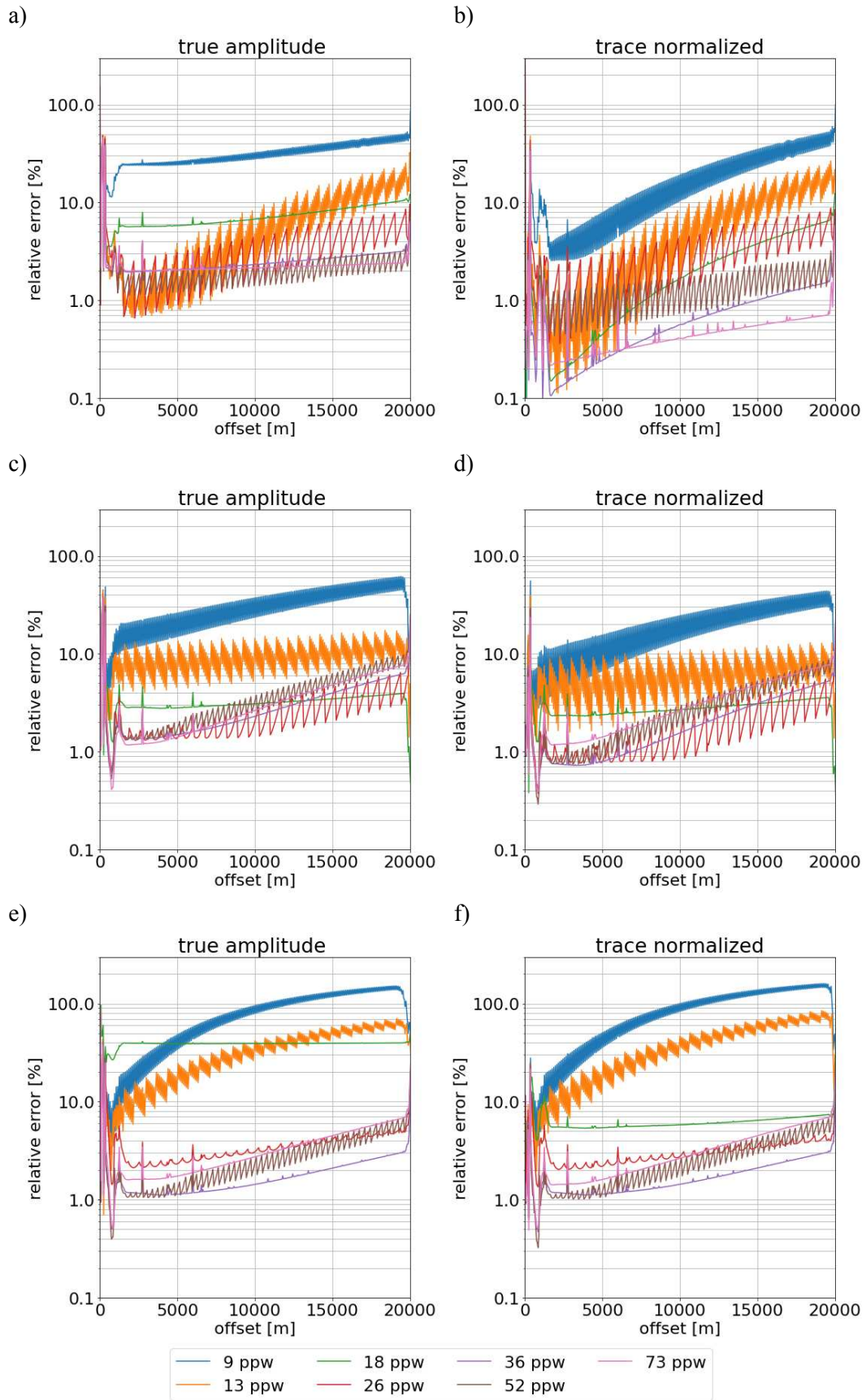


Figure 6.9: Relative error to the analytical solution of the horizontal component for true amplitude (left column) and trace normalized data (right column) in the surface wave time window computed with the image method in *ve2d_ref* (a and b) and in *DENISE Black Edition* (c and d) and with the improved vacuum formulation in *DENISE Black Edition* (e and f)

6.3.2. Mean relative error

To quantify the accuracy of synthetic data the mean relative error of all receivers is a good measure of the overall accuracy of a simulation. The mean error is calculated as the arithmetic mean of the relative error of all receiver stations of a spatial discretisation according to equation (4.4). The evaluation of these errors for all grid discretisations shows the convergence behaviour of a numerical method to the true solution. Generally, the error is expected to reduce with increasing spatial resolution, avoiding numerical artefacts related to grid dispersion, which may also be caused by a discrete boundary such as a free surface.

Average relative errors of the P-wave of all receivers at offsets from 500 to 24100 m plotted for the image method implemented with `ve2d_ref` and DENISE Black Edition, as well as for the improved vacuum formulation with DENISE Black Edition, for the horizontal component in Figure 6.10a and for the vertical component in Figure 6.10b, for both trace normalized and true amplitude data. The error behaviour with no near field (offsets <500 m) is almost identical for both the horizontal (Figure 6.10a) and vertical component (Figure 6.10b).

The image method in both `ve2d_ref` and DENISE Black Edition exhibits a stable error over for all simulated grids, where errors show values between 1 and 3% for true amplitude data. These values are equivalent for the horizontal (Figure 6.10a) and vertical components (Figure 6.10b). Trace normalisation reduces the errors below 1% for the image method with `ve2d_ref`, while trace normalisation causes less of a reduction in DENISE Black Edition.

The improved vacuum formulation spikes in error at a grids of 13 and 18 ppw for both true amplitude and trace normalized data, but has for all other discretisations almost identical relative errors to the image method simulated with DENISE Black Edition.

These almost stable low errors for the image method indicate that the numerically computed P-wave has already reached its minimal error. The accuracy test of the improved vacuum formulation on the other hand, shows that discretisations of 36 ppw are needed in order not to introduce high errors.

If the near field below 500 m offset is included in the evaluation of the mean error, the errors drastically change for the vertical component (Figure 6.10d). Here, the error increases to values above 10% for true amplitude data and to 2 to 6% for trace normalized data. The trace normalized is less affected by the inclusion of the near field, since the normalisation of amplitudes reduces the high error in the near field. Meanwhile, the error in the horizontal component (Figure 6.10c) is less affected by the introduction of the near field. This difference may be an effect of the high curvature of the wavefront at small offset, which affects the horizontal component less than the vertical component.

The mean relative error of the Rayleigh wave of all receivers at offsets from 500 to 24100 m plotted for the image method implemented with `ve2d_ref` and DENISE Black Edition, as well as for the improved vacuum formulation with DENISE Black Edition, for the horizontal component in Figure 6.11a and for the vertical component in Figure 6.11b.

For the Rayleigh wave, a reduction in average error with increasing spatial resolution is observed in both the horizontal (Figure 6.11a) and vertical components (Figure 6.11b). Here the trace normalized data exhibits slightly lower errors than the true amplitude data, which is more pronounced in the horizontal component (Figure 6.11a). The convergence behaviour is the same for both true amplitude and trace normalized data with the trace normalized data.

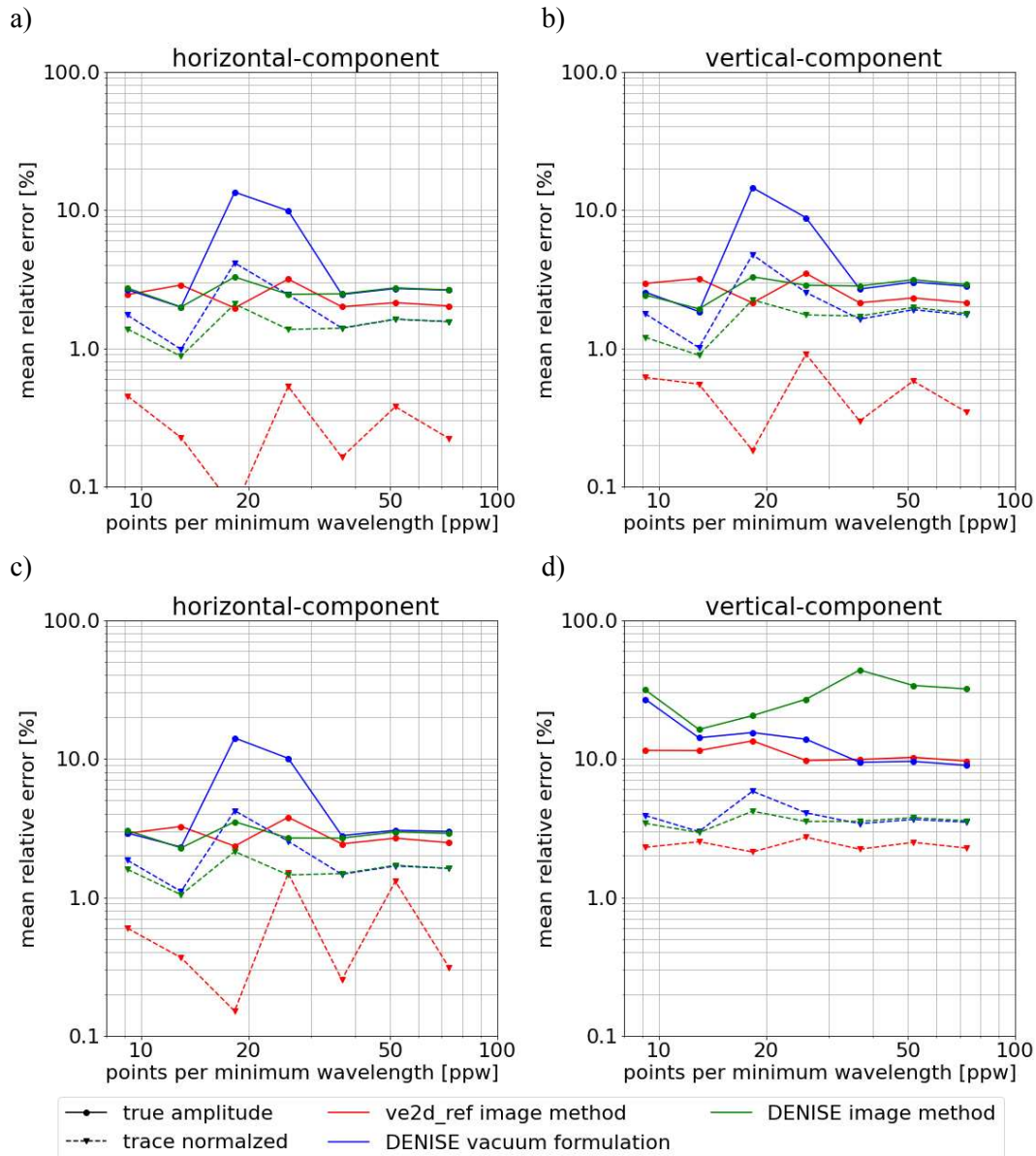


Figure 6.10: Mean relative error of the P-wave for true amplitude and trace normalized for the horizontal (left column) and vertical component (right column). a) and b) exclude the near field offsets <math>< 500\text{ m}</math> (500 m to 24100 m) while c) and d) consider all offsets (0 m to 24100 m).

The image method converges steadily to lower errors with each increase in spatial resolution. This is true for wavefields modelled with DENISE Black Edition and ve2d_ref. The image method modelled with DENISE Black Edition reaches a minimum mean error at a discretisation of 26 ppw in the horizontal component and at 18 ppw in the vertical component and increases only with higher resolution due to the accumulation of numerical inaccuracies with a high number of calculations. The image method simulated with ve2d_ref on the other hand continuously reduces the mean error with increasing resolution. This difference between the modeling programs might be caused by the specific algorithms applied within them.

The improved vacuum formulation modelled with DENISE Black Edition exhibits a different convergence behaviour. Here the mean errors show a steeper reduction, which flattens out abruptly at discretisations above 26 ppw. The reduction is especially abrupt for true amplitude data, where there is a drop from 40 to 4% between 18 and 26 ppw. This very abrupt convergence is caused by the reduction of the distortion of the Rayleigh wavefront that occurs between 18 and 26 ppw.

If the near field is included in the calculation of the mean relative errors for the Rayleigh wave (Figure 6.11c and d), a gap appears between true amplitude and trace normalized data. Inclusion of the near field dramatically increases the error for the vertical component (Figure 6.11d), where errors increase by up to a factor of 10. As with the P-wave, the mean error of the horizontal component of the Rayleigh wave (Figure 6.11c) shows less of an effect by the near field, where the error increases only by 1 or 2%, which is still significant.

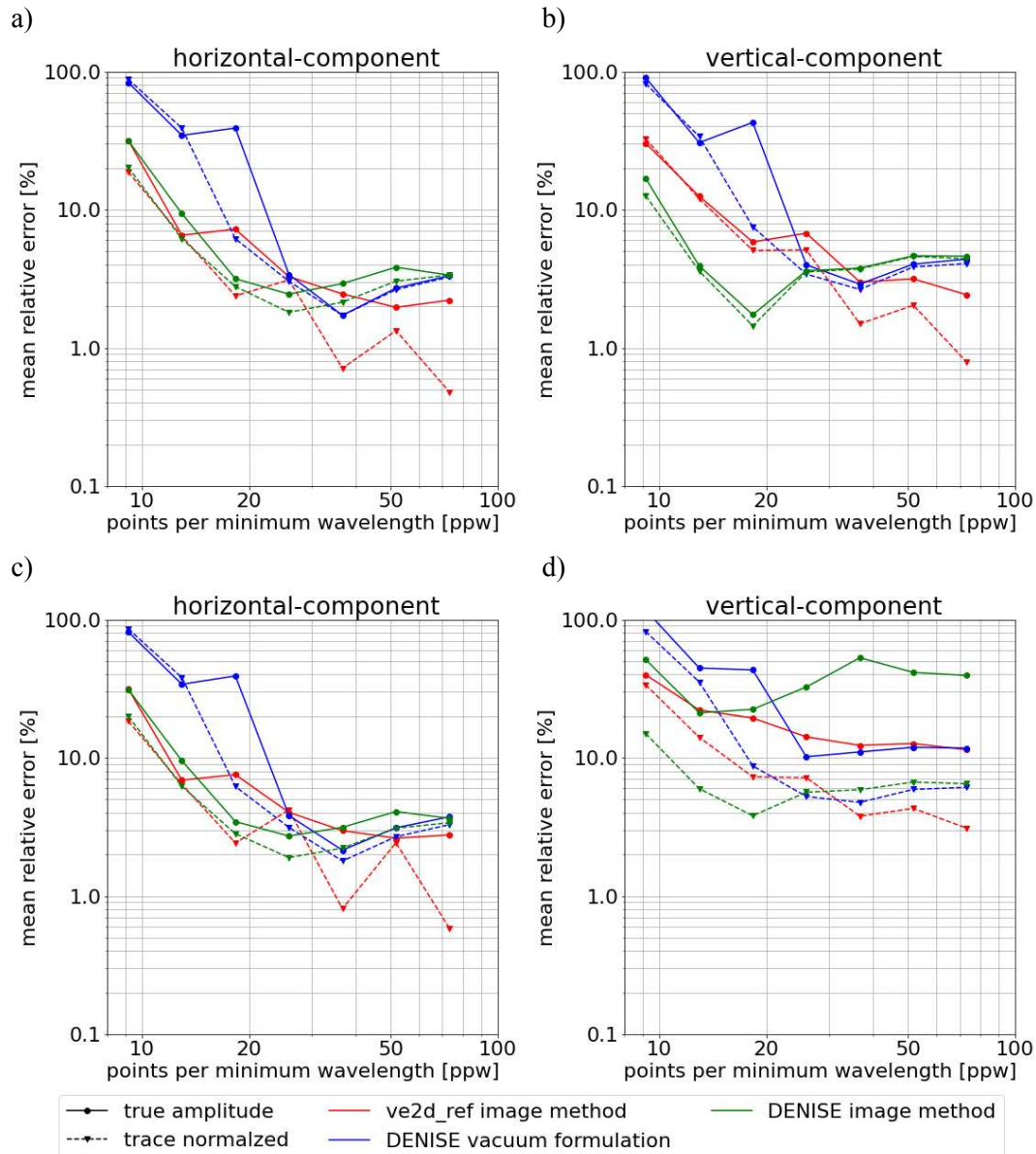


Figure 6.11: Mean relative error of the Rayleigh wave for true amplitude and trace normalized for the horizontal (left column) and vertical component (right column). a) and b) exclude the near field offsets <500 m (500 to 24100 m) while c) and d) consider all offsets (0 to 20000 m).

The average error may also be estimated for the whole traces which gives a good estimate for the accuracy of the entire model, including all numerical artefacts produced during the modeling. The resulting relative error for the entire modelled traces is plotted for horizontal and vertical receiver components ignoring the near field in Figure 6.12a and Figure 6.12b, respectively. The error calculated for the whole trace is almost identical to the error of surface wave window (Figure 6.11) for true amplitude data on both components (if the near field is ignored) and for trace normalized data.

This similarity of whole trace and Rayleigh wave error occurs due to the surface wave being the dominant phase of the recorded seismic signals with higher amplitudes, and therefore higher errors, than other phases.

A slight increase in error of the whole trace compared to the Rayleigh wave time window is noticed for trace normalized data. This occurs due to the relativisation of amplitudes when trace normalisation is applied.

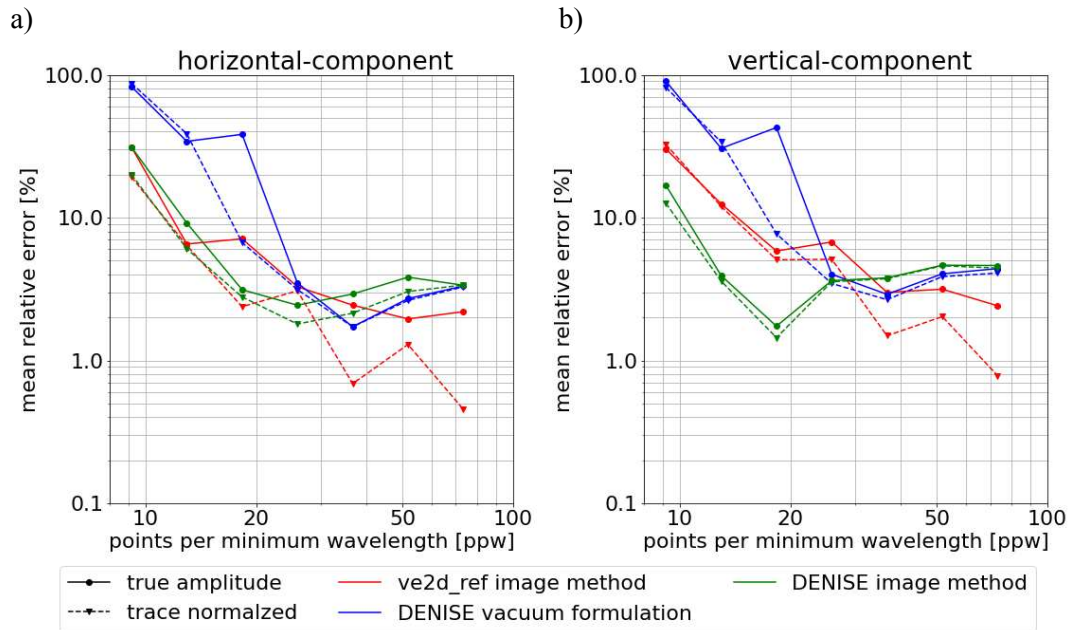


Figure 6.12: Mean relative error for the entire trace of true amplitude and trace normalized data excluding the near field (500 to 20000 m) for the horizontal (a) and vertical component (b) plotted for the different free surface boundary condition implementations.

6.4. Convergence tests

More complex models do not have an analytical solution, making it impossible to determine the error to an exact solution. In this case, to find the best spatial discretisation a convergence test is conducted, where the change between each of the simulations is considered. As the simulated data approaches the best solution, the change to the previous simulated discretisation should grow smaller. At the point, where the differences no longer change significantly, the best model discretisation combining accuracy and computational affordability is found.

The relative differences between two grid discretisations are calculated according to equation (4.5) and to evaluate the entire simulation the average is used to observe the change of the modelled receiver components. For these tests the nearfield (offsets < 500 m) was not considered in the calculation of the convergence tests.

The relative differences of the P-wave are displayed for the implementation of the image method in ve2d_ref and DENISE Black Edition, as well as for the improved vacuum formulation in DENISE Black Edition for the horizontal component in Figure 6.13a and the vertical component in Figure 6.13b. Both components exhibit an almost identical behaviour in the convergence test for the respective modeling algorithms. The general trend of the convergence test is a reduction of relative differences with finer grid discretisations, which varies between the implementations. For the P-wave there is a general increase in relative difference occurring between 18 and 26 ppw, which is less

pronounced in `ve2d_ref` than in DENISE Black Edition. Between these two grids, the relative error is also experiencing the largest decrease for all modeling algorithms, which is the cause of this spike in relative difference.

The image method with `ve2d_ref` has the smallest increase between 18 and 26 ppw and an otherwise smooth decrease to lower differences with finer discretisations from 1 to 0.1%. The image method modelled with DENISE Black Edition exhibits an increase in difference until 26 ppw and then drops to low differences indicating only small changes in the modelled wavefield.

The improved vacuum formulation exhibits the highest increase in relative difference with true amplitude values as high a 90%, which indicates a sudden change of the wavefield which then only changes very little changes between fine grids of 36 ppw and higher.

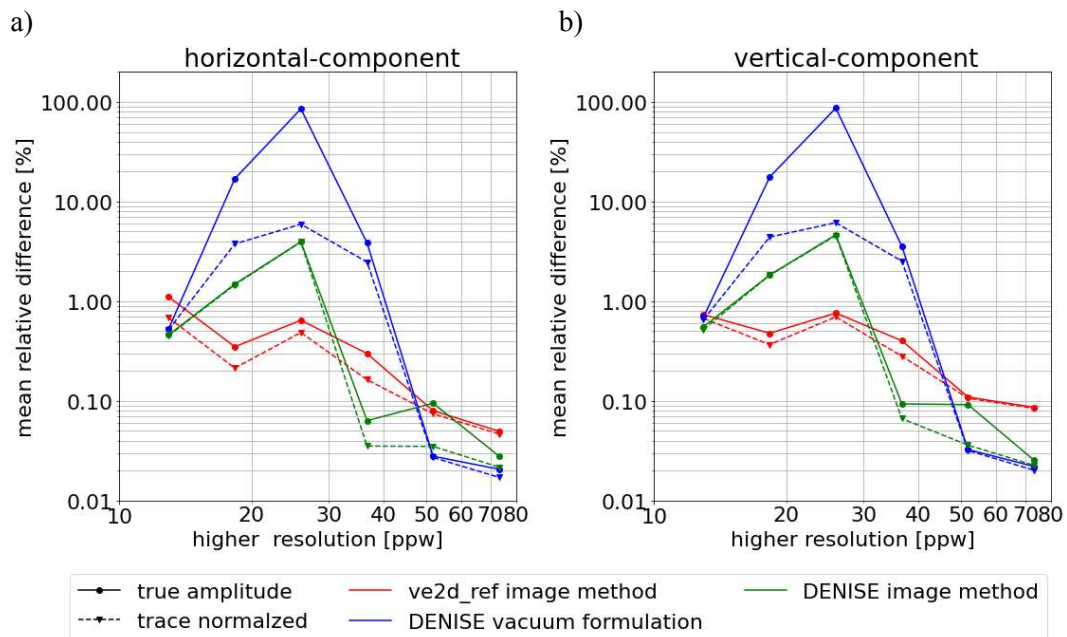


Figure 6.13: Convergence test for an elastic homogeneous half-space for the P-wave for the horizontal (a) and vertical component (b). Relative difference is calculated according to equation (4.5) and only higher resolution grid is denoted on the x-axis.

The relative differences of the Rayleigh wave are also calculated for all modeling algorithms in Figure 6.14a for the horizontal component and in Figure 6.14b for the vertical component. There is a general decreasing trend, which differs slightly for both components, with vertical components (Figure 6.14b) exhibit slightly less differences between fine grids than horizontal components (Figure 6.14a).

The relative difference of the image method simulated with `ve2d_ref` again decreases continuously with smaller discretisations until almost no change in the wavefield is observed. The image method computed with DENISE Black Edition follows a similar trend but has a small step, where the difference suddenly decreases to values below 1%, again indicating reaching the most efficient solution.

The improved vacuum formulation of DENISE Black Edition exhibits an increase in relative difference followed by a sudden drop between 13 and 18 ppw for trace normalized data and 18 and 26 ppw for true amplitude data. This behaviour closely resembles the behaviour of the relative error, which is causing the behaviour in the convergence test.

The convergence of both the P-wave and Rayleigh wave is well represented in the conducted convergence tests. These closely reflect the behaviour of the error for both components of the Rayleigh wave, but increase features of the error in the P-wave.

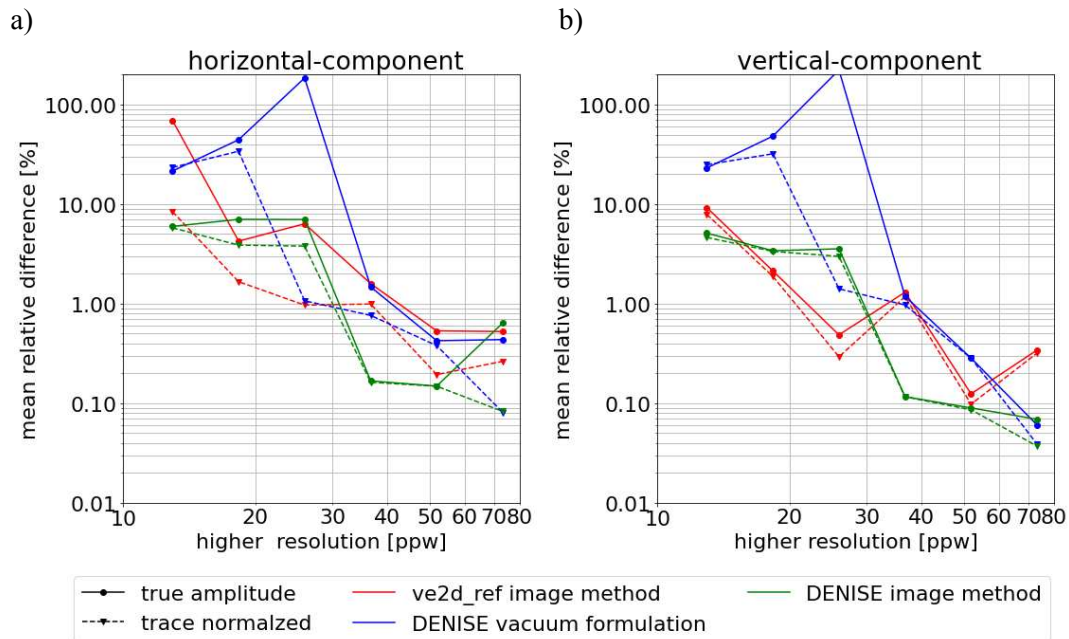


Figure 6.14: Convergence test for an elastic homogeneous half-space for the Rayleigh wave for the horizontal (a) and vertical component (b). Relative difference is calculated according to equation (4.5) and only higher resolution grid is denoted on the x-axis.

6.5. Summary of modeling errors

The spatial sampling rates for the P-wave show some significant differences, but the relative error is quite small and the main convergence has most likely already happened at lower grid discretisations. The Rayleigh waves on the other hand, are converging and reach minima between 36 ppw for the improved vacuum formulation and 26 ppw for the image method. While the image method converges smoother towards a minimum, the vacuum formulation has a rapid convergence at a critical point, which is noticeable in both the offset behaviour and the mean error. Furthermore, the vacuum formulation experiences an error spike in the P-wave at resolutions between 18 and 26 ppw for unclear reasons. However, the P-wave is distorted in this simulation, while Rayleigh waves remain unaffected. The reason for this effect at 18 ppw (10 m grid spacing) remains unclear, but it remains consistent throughout many simulations and redefinitions of the model. A similar but less significant increase is highlighted by the convergence test for the image method as well, which is not noticed in the relative error.

The nearfield (offsets < 500 m) exhibits high errors for both free surface conditions, which are unavoidable and must be removed for any evaluation of the entire modeling accuracy. Since no such errors are observed for a homogeneous full space (also excited with an explosive point source), the source implementation is not the cause of this error. Rather, it is the interaction of the source close to the free surface with the free surface itself and the subsequent generation of S- and Rayleigh waves. These inaccuracies dissipate quickly and are only relevant in the very near field, but have a large impact on the error of simulated data. The trace normalized data is significantly less affected by the near field inaccuracies, due to the removal of amplitude data and only relative amplitude are

considered, while preserving the overall convergence trend. Therefore, the main factor of contributing to the relative error is the amplitude in the near field.

The relative error for the entire timeseries of recorded receiver stations is furthermore dominated by the error of the strongest phase present and may be used to assess the error and convergence behaviour of the most dominant wave phase. However, this is only valid when considering sections containing the dominant wave phase in the recorded traces.

7. Elastic homogeneous half-space with a tilted free surface

The goal of this test is to evaluate the accuracy of the modeling in the presence of a tilted surface. This can be evaluated in an elastic homogeneous half-space, for which an analytical solution exists. A tilted half-space only differs in the rotation of the reference frame to a certain tilt angle, but in the Cartesian indexed model, this results in a stepped staircase function for the free surface.

An angle limited test was performed up to a tilt angle of 20° , since this is a commonly encountered range of dipping angles in land seismic surveys. These models do not cover the whole range of possible tilt angles but tests have shown that the behaviour of the error of wavefield simulations is symmetrical around an angle of 45° and for the standard staggered grid increases with increasing angle up to 45° (Bohlen & Saenger, 2006).

The analytical solution for the tilted half-spaces are computed with program EX2DVAEL by Berg et al. (1994). The source and receiver coordinates were adjusted for each computed tilt angle with a coordinate transformation.

7.1. Model specific parameters

In this investigation tests were performed at discrete tilt angles of 1° , 5° , 10° and 20° for the free surface boundary conditions, the image method with `ve2d_ref` and improved vacuum formulation implemented in DENISE Black Edition. The tilted free surface is realised through a stepped staircase function, where a common approach is to assign grid points less than half a vertical step length away from the actual location of the free surface are assigned to the free surface boundary. A schematic of a model with a free surface assigned with this scheme for a step length of 10 m and a 10° tilted free surface is shown for the image method in Figure 7.1a and improved vacuum formulation in Figure 7.1b.

There are different methods for generating the stepped staircase function, but since all assignments create a surface with the same length of a stair step, the method should not have a significant impact on the simulation stability other than creating diffractions at different positions in the model. The free surface was chosen to start on the left side at a depth of 40 m in the model space, dipping downwards. At the left and right edge of the model the free surface was continued horizontally in the boundary sponge layers used in `ve2d_ref`. This was done to limit the vertical extent required for the model with high tilt angles, since continuing a 20° dipping free surface into a 4000 m thick sponge layer would require an additional 2630 m of vertical extent, which exceeded the memory restrictions. The tilted free surface was continued into the boundary for the slimer C-PML- boundaries used in DENISE Black Edition.

The model space was defined to have the dimensions of 25000 m horizontally and 10000 m vertically without the boundary layers. Each of the tested tilted models was initialized with the spatial and temporal grid settings described in Table 3.1 and the general modeling parameters described in Table 3.2 for both free surface boundary conditions in the respective modeling programs.

The receivers for the tilted homogeneous half-space models were placed one grid point below the free surface with a horizontal receiver spacing of 50 m. The source point was placed 40 m below the free surface at a horizontal coordinate of 600 m in the model space.

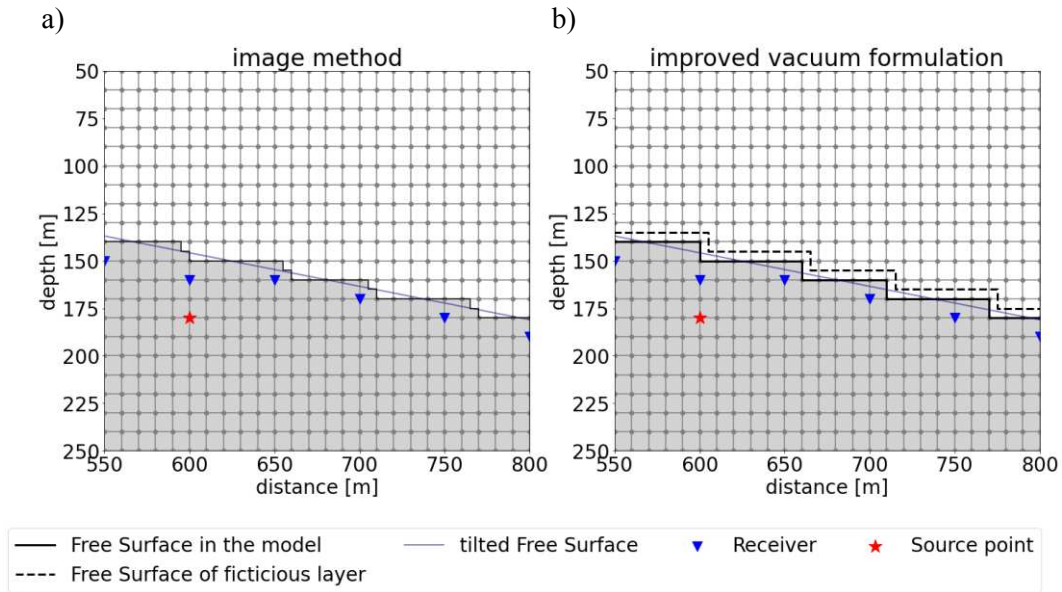


Figure 7.1: Schematic of models for two free surface boundary conditions, left image method and right improved vacuum formulation in a tilted homogeneous half-space with a dipping angle of 10° and an exemplary grid spacing of 10 m.

7.2. Numerically modelled wavefields

The tilted elastic homogeneous half-space is analytically an identical model to the half-space aligned with the grid axis with the only difference being a coordinate transform. This means that also the wavefields should have the exact same phases and wave propagation. The explosive point source produces a P-wave and its interaction with the free surface causes a S-wave, Rayleigh wave and PS-wave to occur.

In this section the numerically modelled wavefields are discussed for a tilted free surface. Due to length constraints this is done on the example of a free surface with a tilt angle of 10° .

7.2.1. Spatial divergence

The divergence of the simulated wavefield for a model with 5 m grid spacing and 10° dipping free surface are displayed at 3 and 6.5 s in time for a free surface boundary defined with the image method in `ve2d_ref` in Figure 7.2(a and c) and with the improved vacuum formulation in DENISE Black Edition in Figure 7.2(b and d). The tilted free surface has different effects on the spatial divergence for both free surface boundary conditions.

The image method in `ve2d_ref` develops artefacts in the form of spurious coda waves for the P-wave as well as the Rayleigh wave (Figure 7.2a). These spurious codas are visible over the entire wavefront for the P-wave and still exist if the source is moved away from the absorbing boundary frame. The amplitude of these decreases with increased spatial resolution of the FD-grid and at the highest resolution of 73 ppw the spurious P-wave coda no longer have significant amplitudes. These spurious coda waves are caused by the stepped staircase function of the free surface near the source point.

The improved vacuum formulation does not develop spurious coda artefacts for the P-wave and rather creates a distorted and phase shifted P-wave wavefront traveling through the medium (Figure 7.2b). Directly at the free surface boundary the P-wavefront is smeared out at the end of the arrival elongating the wavelet (Figure 7.2b). The Rayleigh wave develops artificial coda while propagating along the surface, which increase in amplitude with increasing offset.

At later times further numerical artefacts caused by both the absorbing boundaries and stepped staircase function of the free surface become visible in the spatial divergence for both free surface conditions. Artificially reflected P-waves and SP-conversions are generated near the inner boundary for the sponge layers of `ve2d_ref` (Figure 7.2c) and C-PML boundaries of DENISE Black Edition (Figure 7.2d). These artificial P-waves are in both cases also reflected by the free surface.

Both image method of `ve2d_ref` (Figure 7.2c) and improved vacuum formulation of DENISE Black Edition (Figure 7.2d) further cause P-waves to be created by the Rayleigh waves at the free surface in regular intervals. These are caused by the steps of the free surface boundary.

7.2.2. Spatial curl

The distinct effects the stepped staircase function has on the wavefields for both free surface conditions are also visible in the curl, which is displayed at 3 and 6.5 s in time for a model with 5 m grid spacing and 10° tilted free surface defined with the image method of `ve2d_ref` in Figure 7.3(a and c) and with the improved vacuum formulation of DENISE Black Edition in Figure 7.3(b and d).

The image method of `ve2d_ref` also generates spurious coda artefacts for the S-wave and Rayleigh wave in the curl (Figure 7.3a). Here, the S-wave exhibits spurious coda across the entire wavefront. For the Rayleigh wave the spurious coda waves are also observed and travel along the free surface defined with the image method. As with the P-wave in the spatial divergence, the amplitude of these spurious coda waves decreases with increasing spatial resolution.

Spurious coda waves are also observed with Rayleigh waves in the curl along the free surface defined with the improved vacuum formulation (Figure 7.3b). In the curl (Figure 7.3b) a distortion of the S-wave and PS-wave is also noticed, which is a result of the distortion and phase shift observed in the P-wave. This degeneration of the waveform of S-wave and PS-wave is also dependent on the spatial resolution of the grid and disappears with increasing spatial resolution.

As the wavefield progresses in time, numerical artefacts also become more pronounced. The Rayleigh waves also cause diffracted S-waves in the curl, that are generated by the stepped staircase function of the free surface. These S-wave artefacts generally have lower amplitudes for the improved vacuum formulation of DENISE Black Edition (Figure 7.3d) than for the image method of `ve2d_ref` (Figure 7.3c). The absorbing boundaries cause little artefacts in the curl and the only artefact visible are PS-conversions occurring near the inner boundary for sponge layers of `ve2d_ref` (Figure 7.3c). C-PML boundaries of DENISE Black Edition do not seem to directly cause any noticeable artefacts in the curl (Figure 7.3d).

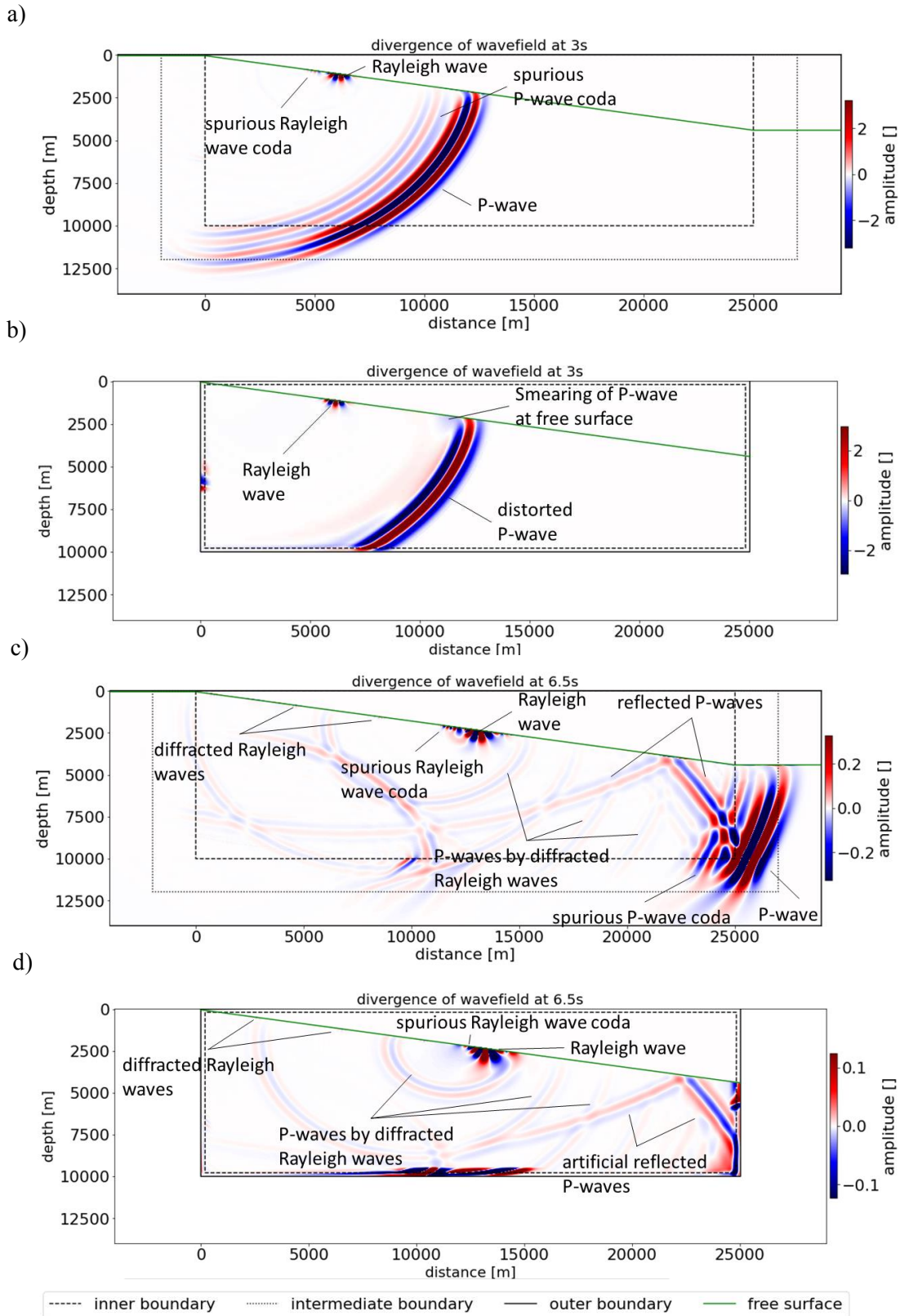


Figure 7.2: Spatial divergence of the wavefield at 3 (a and b) and 6.5 s in time (c and d) for a homogeneous half-space with a resolution of 36 ppw and free surface boundary with a tilt of 10° according to the image method with `ve2d_ref` (a and c) and improved vacuum formulation of DENISE Black Edition (b and d). The different wave phases are labelled accordingly.

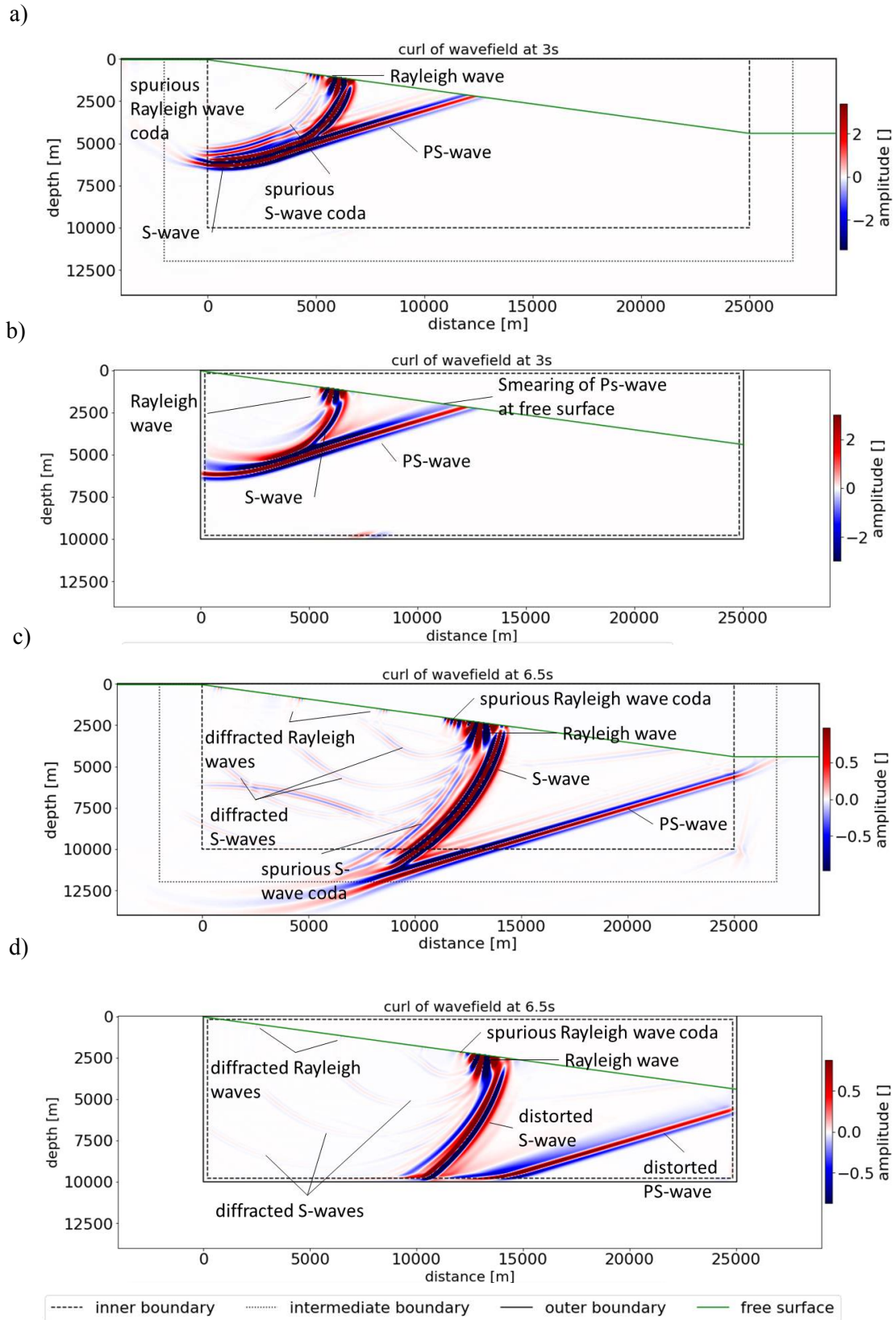


Figure 7.3: Spatial curl of the wavefield at 3 (a and b) and 6.5 s in time (c and d) for a homogeneous half-space with a resolution of 36 ppw and free surface boundary with a tilt of 10° according to the image method with `ve2d_ref` (a and c) and DENISE Black Edition (b and d). The different wave phases are labelled accordingly.

7.3. Receiver components

As with the numerically calculated wavefields, discussing all horizontal and vertical components for all tilted free surface models would go beyond the extend of this work. Rather the general numerical inaccuracies of the simulated seismograms are discussed using the example of a 10° tilted free surface. Most of the variants of a tilted half-space exhibit the same trends with differing errors. Furthermore, the errors on both components exhibits a very similar behaviour and the general trends may be shown with only one component for brevity. To maintain consistency throughout this work, the focus again lies on the horizontal component since both P-wave and surface wave information is contained there. The relative errors over offset for the horizontal component simulated for models with a tilted free surface of 1 , 5 and 20° are displayed in Appendix B.

7.3.1. Horizontal component

The introduction of a stepped staircase function as the free surface is generating significantly more numerical inaccuracies. This is visualized for the image method of `ve2d_ref` in Figure 7.4 and for the improved vacuum formulation of DENISE Black Edition in Figure 7.5 for a tilted free surface with an angle of 10° . Both free surface conditions experience large numerical inaccuracies for the Rayleigh waves, which are delayed and distorted significantly. Coarser spatial discretisations exhibit spurious Rayleigh wave coda long past the ending of the surface waves of the analytical solution. The observed spurious coda take longer to dissipate using the image method of `ve2d_ref` (Figure 7.4) than the improved vacuum formulation of DENISE Black Edition (Figure 7.5).

The P-wave also does not remain unaffected, and distortions and delays are noticed as well. Here the vacuum formulation (Figure 7.5) has visible higher distortions at long offsets than the image method. The free surface according to the image method of `ve2d_ref` (Figure 7.4) generates spurious coda for the P-wave while causing little change of the waveform. The amplitude of the spurious coda caused by the image method of `ve2d_ref` decreases with increasing resolution for both P-waves and Rayleigh waves.

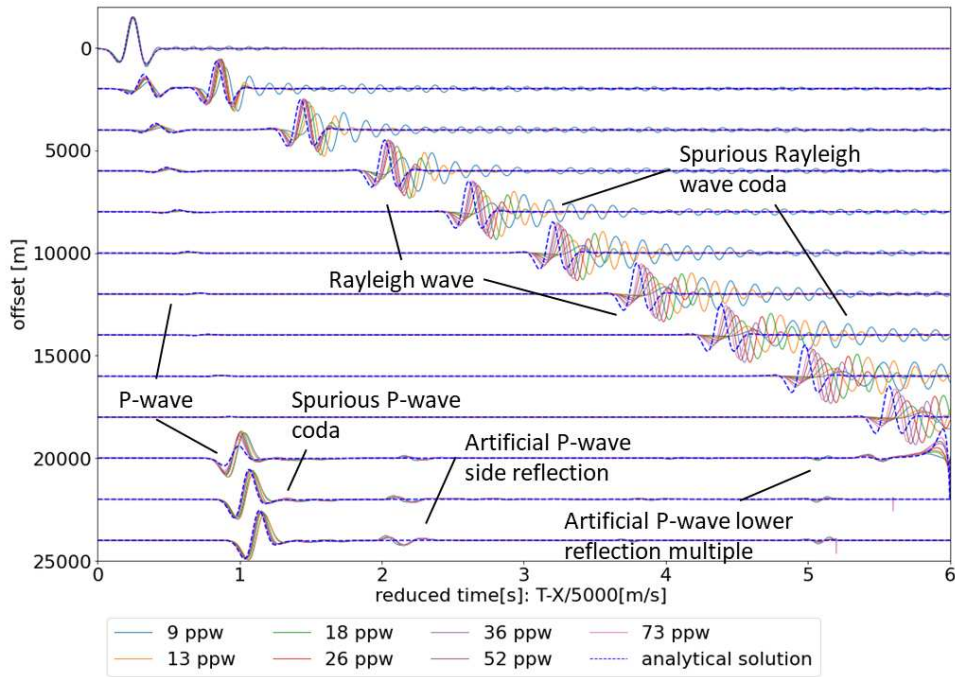


Figure 7.4: Trace normalized horizontal component in reduced time for different offsets modelled in a 10° tilted elastic homogeneous half-space with a free surface boundary according to the image method of `ve2d_ref`.

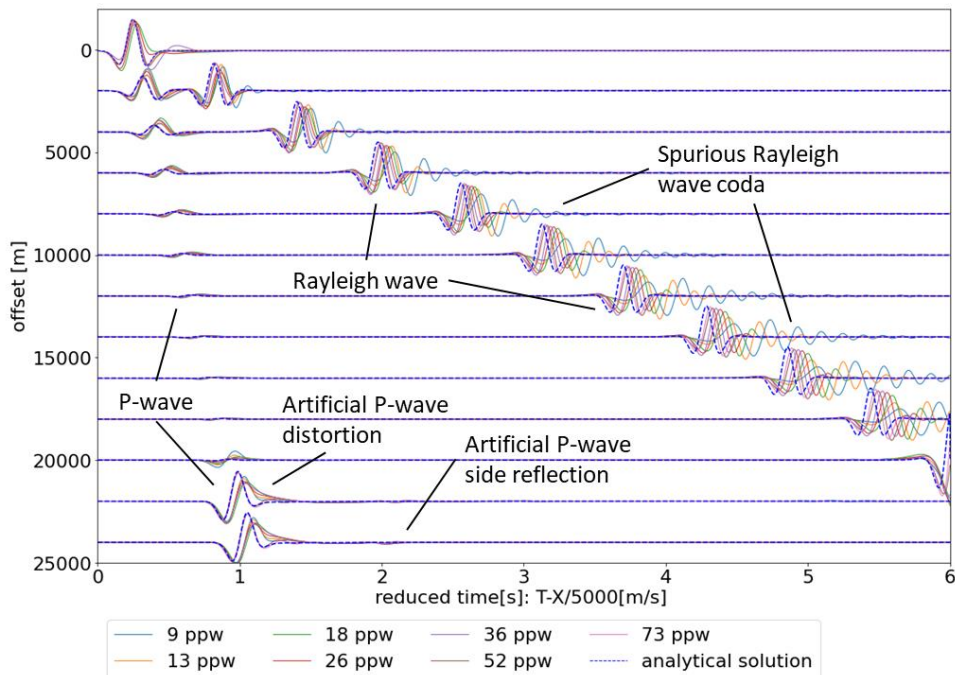


Figure 7.5: Trace normalized horizontal component in reduced time for different offsets modelled in a 10° tilted elastic homogeneous half-space with a free surface boundary according to the improved vacuum formulation of `DENISE Black Edition`.

The error of the simulated receivers can again be evaluated via comparison with the analytical solution through the relative error as calculated in equation (4.4). The behaviour of the error is investigated along changing offset to assess the numerical accuracy of the simulated wavefield.

Due to the large and long spurious Rayleigh wave coda, a narrow time window over the Rayleigh wavefront may not be a good estimate of accuracy of simulated receiver stations. Since the error of the

whole trace is dominated by the error of the surface wave, the relative error for the surface wave is estimated through the error of the entire simulated trace. This is, furthermore, a good estimate of the accuracy of the whole simulation and how the diffractions caused by the free surface step function (as seen in the wavefields Figure 7.2 and Figure 7.3), are affecting the accuracy. The P-wave is less affected by its spurious coda and distortions, and can still be effectively analysed in a narrow time window with a length of 0.6 s.

The relative error of each trace for the P-wave time window is plotted in Figure 7.6(a and b) for a free surface according to the image method of `ve2d_ref` and in Figure 7.6(c and d) for the improved vacuum formulation of DENISE Black Edition for true amplitude and trace normalized data. Here, the first 2000 m offsets are dominated by the error of the high amplitude Rayleigh wave, since below this offset the P-wave and Rayleigh wave have not separated properly. These offsets should be ignored for an evaluation of the P-wave accuracy and its error behaviour over offset. Both free surface conditions exhibit a similar behaviour over offset for the P-wave, where at long offsets errors reach an almost constant value.

For the image method of `ve2d_ref` (Figure 7.6a and b) the error reaches a plateau at offsets above 10000 m. This plateau value decreases with increasing spatial resolution for both true amplitude (Figure 7.6a) and trace normalized data (Figure 7.6b). The behaviour between 2000 and 10000 m offset varies with the spatial discretisation. Fine discretisations of 26 ppw and below continuously increase in error up to 10000 m offset. The error of coarse discretisations first increases steeply and reaches a maximum error between 3000 and 5000 m. After reaching the maximum the error of coarse grids decreases and reaches a constant level above 10000 m. This behaviour of coarse grids is more pronounced in the true amplitude (Figure 7.6a) data than in the trace normalized data (Figure 7.6b).

Defining the free surface using the improved vacuum formulation of DENISE Black Edition results in a different error behaviour for the P-wave (Figure 7.6c and d). The general level of the error is drastically decreased for fine spatial discretisations compared to coarse discretisations. This drop in error is present in both true amplitude and trace normalized data and decreases the error by approximately a factor of 20. This rapid drop in error is caused by the sudden reduction of the distortion of the P-wavefront at finer spatial discretisations.

However, the behaviour of the error of both coarse and fine grids is quite similar. The relative error increases with offset between 2000 and 5000 m for fine grid discretisations. The error increases up to offsets of 7000 m for coarse discretisations. For offsets above 5000 m for fine grids or 7000 m for coarse grids the error decreases slightly with increasing offset for true amplitude data (Figure 7.6c), while it remains constant for trace normalized data (Figure 7.6d).

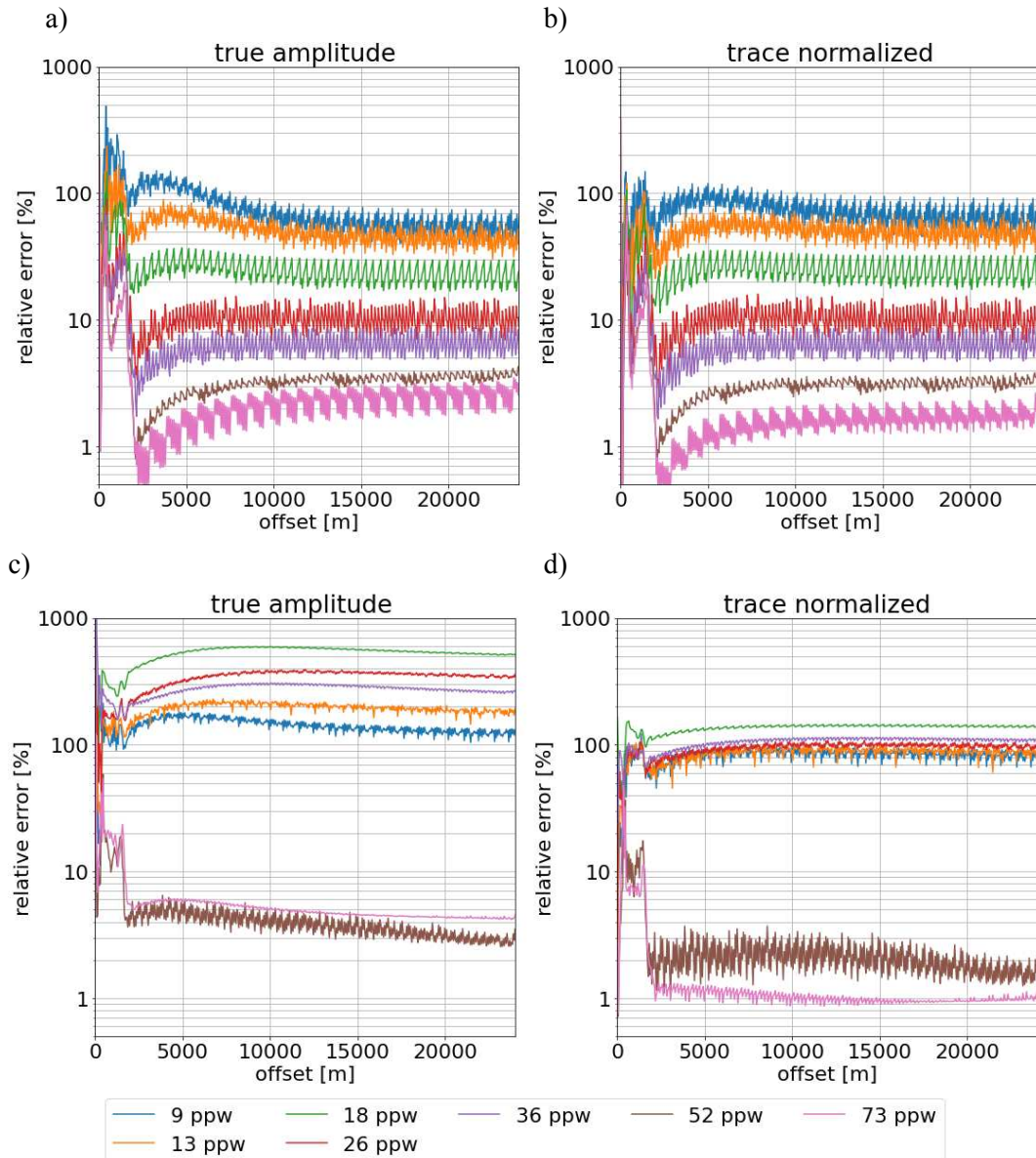


Figure 7.6: Relative error of the horizontal receiver component to the analytical solution in the P-wave window for an elastic homogeneous half-space with a 10° tilted free surface according to the image method of `ve2d_ref` (a and b) and the improved vacuum formulation of DENISE Black Edition (c and d) for true amplitude (left column) and trace normalized data (right column).

The relative error over the offset for true amplitude and trace normalized data for the whole trace is plotted in Figure 7.7(a and b) for the image method and in Figure 7.7(c and d) for the improved vacuum formulation. These errors are dominated by the Rayleigh wave up to an offset of 20000 m, due to its high amplitude. Above 20000 m offset the error closely follows the error of the P-wave discussed previously.

Both implemented free surface conditions generate Rayleigh waves that exhibit a dramatic increase in relative error with offset and high overall errors. Both the image method of `ve2d_ref` (Figure 7.7a and b) and the improved vacuum formulation of DENISE Black Edition (Figure 7.7c and d) show high errors of 100% at offsets of 15000 m even for the finest discretisation of 73 ppw. The increase of error over offset is a result of the increasing spurious Rayleigh wave coda with offset, which are a consequence of the stepped staircase function of the free surface and the unavoidable diffraction points it creates.

The image method of `ve2d_ref` exhibits a continuously decreasing error for the Rayleigh wave as well. The relative error for the image method (Figure 7.7a and b) again show differing behaviours of fine and coarse spatial discretisations. Fine discretisations show a continuous increase in relative error with increasing offset. This increase is varied with the spatial discretisation, where finer grids exhibit less steep increases but increase to the same plateau value. The rate of increase also stays constant for both true amplitude (Figure 7.7a) and trace normalized data (Figure 7.7b). For the coarse discretisations the error behaves similarly as for the P-wave creating a maximum between 2000 and 5000 m offset with a higher initial increase.

The relative errors of the improved vacuum formulation in DENISE Black Edition (Figure 7.7c and d) exhibit a similar significant decrease in error at grid resolution of 52 ppw. This drop is however less pronounced. The rapid decreases are a consequence of a reduced distortion of the wavelet, resulting in significantly lower errors. The behaviour over offset differs here for coarse and fine grid spacings too. Fine grids have an increasing error with increasing offset for the entire observed Rayleigh wave. This behaviour is changed by trace normalisation (Figure 7.7d) to lower values compared to true amplitude data (Figure 7.7c). Coarse grids have a constant high error and only show a short but steep increase at low offsets.

For the near field (<500 m offset) a very high error is observed with both modeling algorithms, which is decreased when trace normalisation is applied.

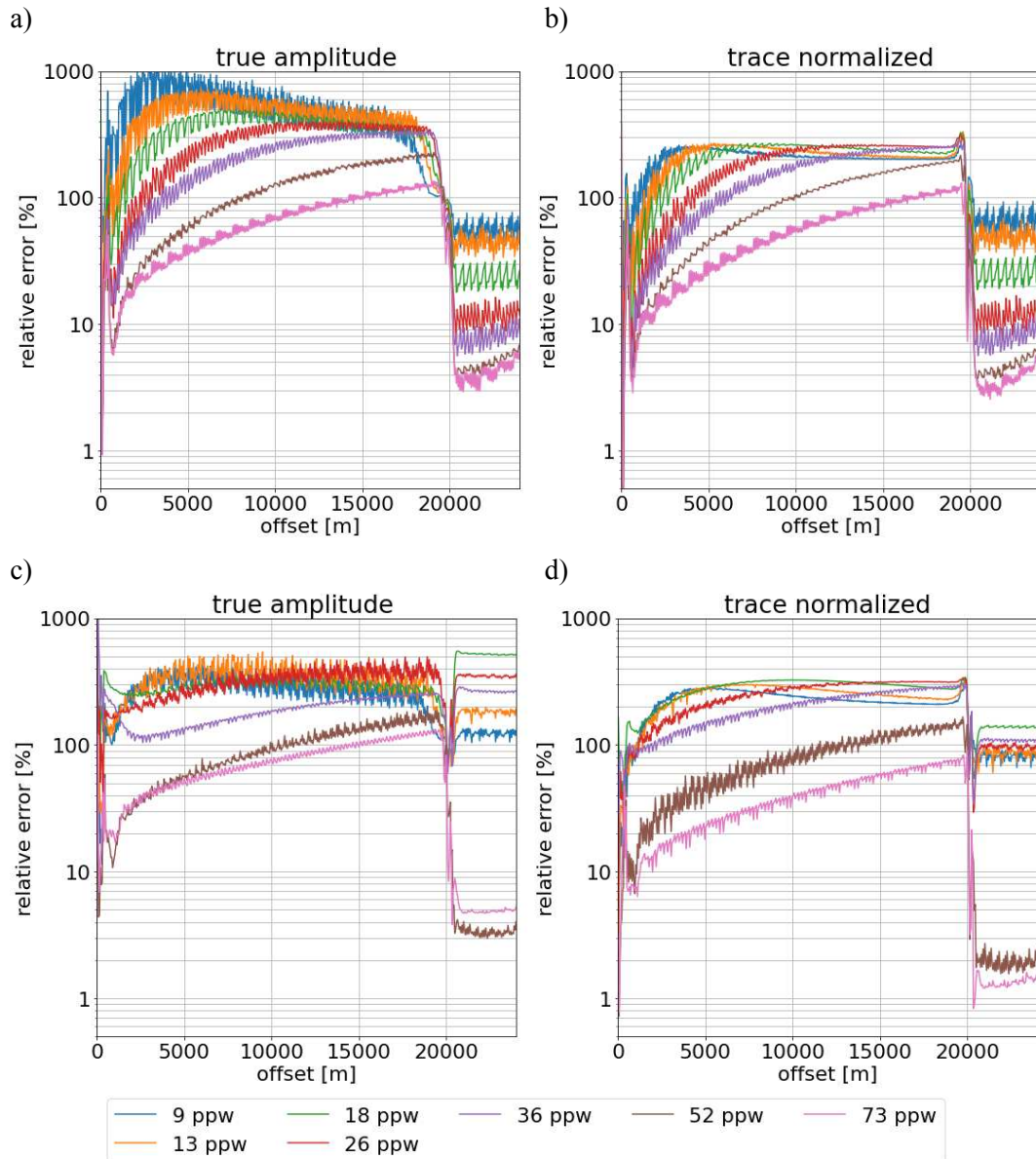


Figure 7.7: Relative error of the horizontal receiver component to the analytical solution in the whole simulated traces for an elastic homogeneous half-space with a 10° tilted free surface according to the image method of `ve2d_ref` (a and b) and the improved vacuum formulation of DENISE Black Edition (c and d) for true amplitude (left column) and trace normalized data (right column).

The arithmetic mean of the error may also be calculated across all traces creating a measure of accuracy for an entire simulation. This error is plotted for all grid spacings, true amplitude and trace normalized data for all calculated tilted surfaces in Figure 7.8a for the image method of `ve2d_ref` and in Figure 7.8b for the improved vacuum formulation of DENISE Black Edition in the P-wave window. The image method has a smooth convergence trend towards lower errors for trace normalized data (Figure 7.8a dotted lines). Here the error of trace normalized data converges to a mean relative error of 3% and below, at the finest simulated spatial discretisation of 73 ppw. The true amplitude data (Figure 7.8a) generally exhibits higher relative errors and a less smooth convergence where the overall reduction trend is still present.

A tilted free surface according to the improved vacuum formulation of DENISE Black Edition creates a different convergence behaviour displayed in Figure 7.8b. Here, for dipping angles above 1° a sudden drop in error occurs between grid discretisations of 36 and 52 ppw for dips of 10° and 20° , or

between 52 and 73 ppw for 5° . For a tilt angle of 1° a small reduction is noticed between 52 and 73 ppw. Both true amplitude and trace normalized data, exhibit the same rapid convergence at the specified grid resolutions. After this rapid decrease in error little to no change is noticed in the relative error with decreasing grid spacing.

Trace normalized average errors (Figure 7.8b dotted lines) again exhibit lower values than the true amplitude errors (Figure 7.8b solid lines) and the difference between the errors is more severe at low tilt angles 1 and 5° , where average true amplitude errors may have values ten times higher than trace normalized errors.

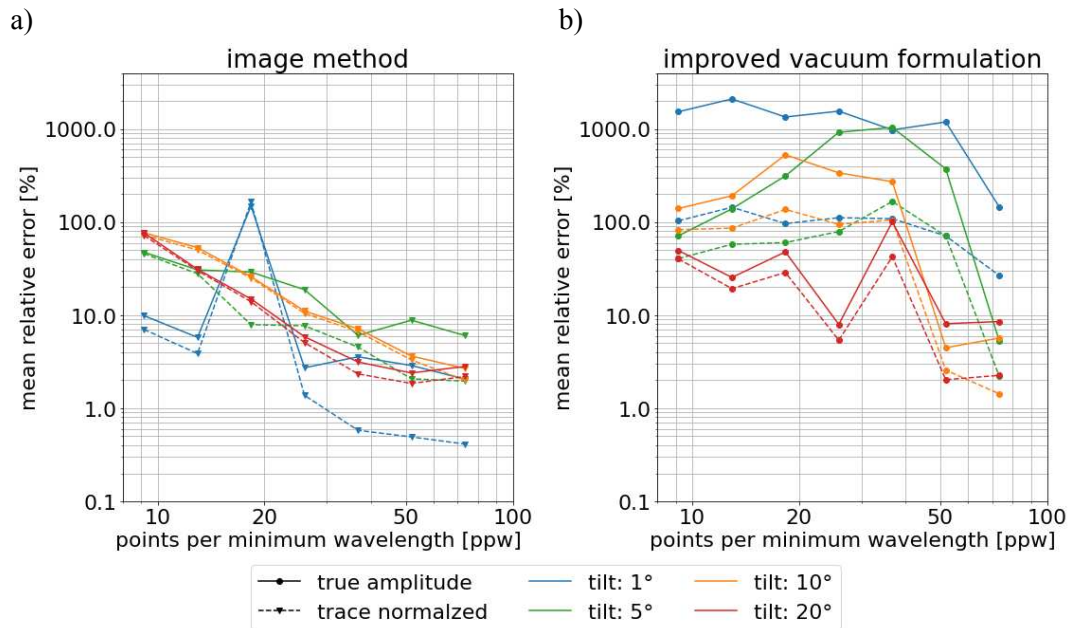


Figure 7.8: Mean relative error for the P-wave of the horizontal receiver components for free surfaces according to the image method of `ve2d_ref` (a) and improved vacuum formulation of DENISE Black Edition (b) with different tilts. The errors are calculated for 500 to 24100 m offset.

The same relative error is calculated for the whole trace to analyse the inaccuracies of the entire simulated wave field which is dominated by the surface waves. The resulting error for true amplitude and trace normalized horizontal receiver component data across all offsets for the whole trace is depicted in Figure 7.9a for the image method of `ve2d_ref` and in Figure 7.9b for the improved vacuum formulation of DENISE Black Edition.

Over the whole trace the relative errors of the improved vacuum formulation of DENISE Black Edition and the image method of `ve2d_ref` differ for the trace normalized errors. Here the improved vacuum formulation generates lower errors than the image method at the smallest discretisation of 72 ppw except for 1° tilt where the image method produces better results. True amplitude data, however, exhibits roughly the same errors for the image method and improved vacuum formulation. Both free surface conditions have a similar convergence to low errors as seen in the P-wave window. Trace normalized data generally yields lower errors than true amplitude data while exhibiting the same convergence trend.

The error of the image method (Figure 7.9a) has a smooth trend towards lower errors with finer spatial discretisation. The decrease in relative error follows a similar trend for all tilts and dips 5° , 10° and 20° show a parallel behaviour. The decrease results in errors for the smallest grid spacing of 25 to 50% for

these tilts, while the 1° tilt has a lower error of 3% for trace normalized data. Here smaller dips generate also smaller errors for both true amplitude and trace normalized data.

The convergence behaviour of the whole trace for the improved vacuum formulation (Figure 7.9b) is different than in the P-wave window. While the whole trace still exhibits a constant error level for low points per minimum wavelength which ends with a sudden decrease. This decrease is less severe than observed in the P-wave window. The decrease is less significant for the whole trace due to the Rayleigh wave still being time shifted at far offsets even at the finest grid discretisation of 73 ppw.

A significant decrease in error is still observed for 5 and 10° between grids of 52 and 73 ppw, but not for a 20° tilt. Furthermore, the rapid decrease in error is way more noticeable in the true amplitude data than in trace normalized data as seen in tilts 1° , 5° and 10° (Figure 7.9b). The error behaviour also shows an additional smooth decrease in error for all tilts to a certain extent.

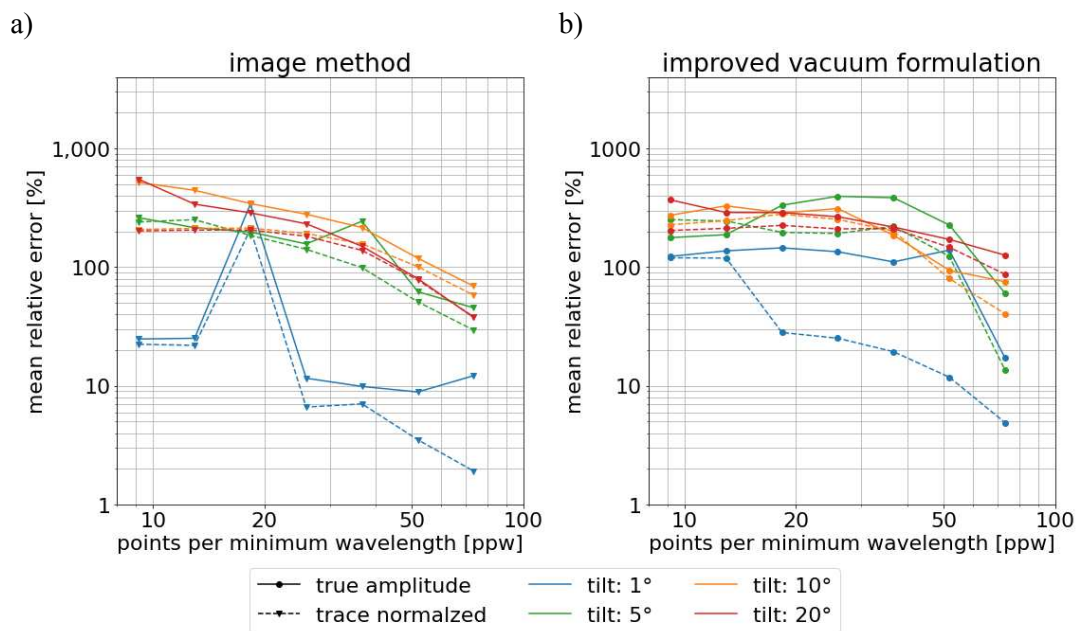


Figure 7.9: Mean relative error over the whole trace of the horizontal receiver components for free surfaces according to the image method of *ve2d_ref* (a) and improved vacuum formulation of *DENISE Black Edition* (b) for different tilts. The errors are calculated for 500 to 20000 m offset.

A major factor affecting the accuracy of the simulated data is the tilt of the free surface which results in a stepped staircase function for the surface. The general assumption is that the relative error increases with increasing tilt angle within the simulated 20° , due to the introduction of more sources of numerical inaccuracy caused by the stepped staircase of the free surface. However, this is not the case for all simulated methods.

The change of the mean relative error over the tilt angle of the free surface is plotted for the image method in Figure 7.10a and for the improved vacuum formulation in Figure 7.10b. The behaviour of the mean relative error over the tilt angle is completely different between the two formulations. The image method produces low errors for small tilt angles that increase with tilt angle, while the improved vacuum formulation exhibits high errors at very low tilt angles of 1° which decrease as the tilt angle is increased.

The relative errors of the P-wave computed with the image method (Figure 7.10a) exhibit a rapid change between 1° and 5° and remain constant or decrease slightly for tilt angles up to 20° .

For the improved vacuum formulation, the relative error of the P-wave (Figure 7.10b) behaves differently with dipping angle and is also depended on the sampling of the spatial discretisation. Small dip angles produce a very high error which never drops below 30%, even at the lowest grid spacing. This error decreases with an increasing dip angle and at tilts between 5 and 20° the improved vacuum formulation yields similar mean errors of trace normalized data as the image method for the highest resolution of 73 ppw. However, the true amplitude error still has higher errors for the vacuum formulation.

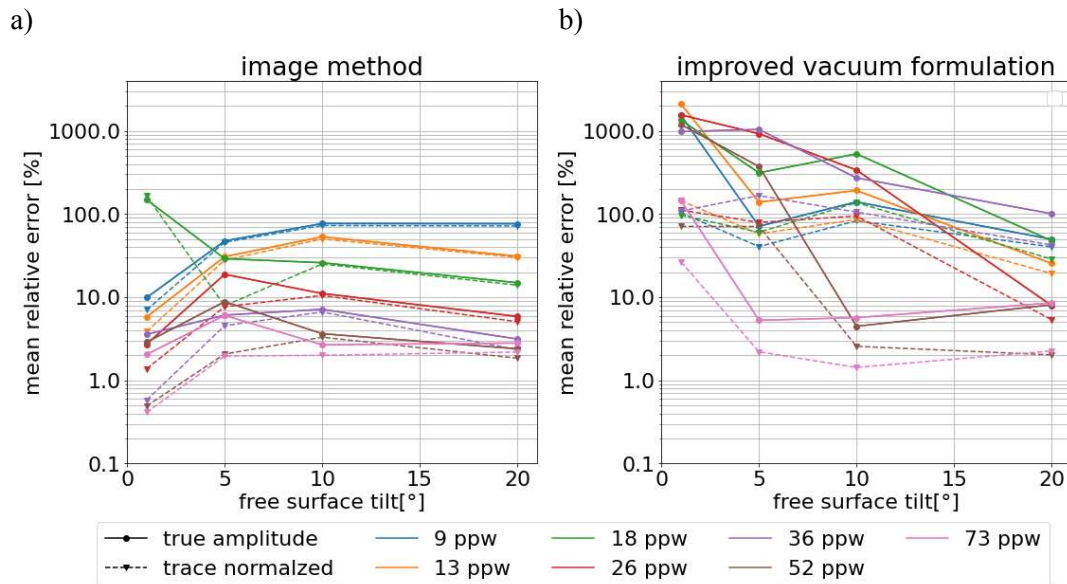


Figure 7.10: Mean relative error of the P-wave of the horizontal receiver components for the image method of *ve2d_ref* (a) and improved vacuum formulation of *DENISE Black Edition* (b) plotted against the dip angle of the free surface. The errors are calculated for 500 to 24100 m offset.

For Rayleigh waves simulated on a standard staggered grid the error of the simulated data increases with the tilt up to 45° and decreases afterwards (Bohlen & Saenger, 2006). This behaviour is also observed here, but the behaviour across the dipping angles is different for both implementations of the free surface boundary condition. The change of the mean relative error over the tilt is plotted for all calculated grid discretisations in true amplitude and trace normalized data depicted in Figure 7.11a for the image method and Figure 7.11b for the improved vacuum formulation.

Both formulations show an increase in error with tilt angle. The image method (Figure 7.11a) has a steeper increase of relative error for both trace normalized and true amplitude data between the tilts of 1 and 5°. This rapid increase occurs due to the increase of tailing higher amplitudes with the introduction of more step functions in the free surface. Meanwhile, the improved vacuum formulation (Figure 7.11b) exhibits a more gradual increase in error at low tilt angles for the Rayleigh wave.

The improved vacuum formulation is more affected by the introduction of a step function since the relative error (Figure 7.11b) has a higher initial error at 1° tilt which increases less for smaller grid spacings than for coarse discretisations. Here the errors at fine grid discretisations are considerably lower for tilts between 5 and 10° but higher for 20° than observed in the image method.

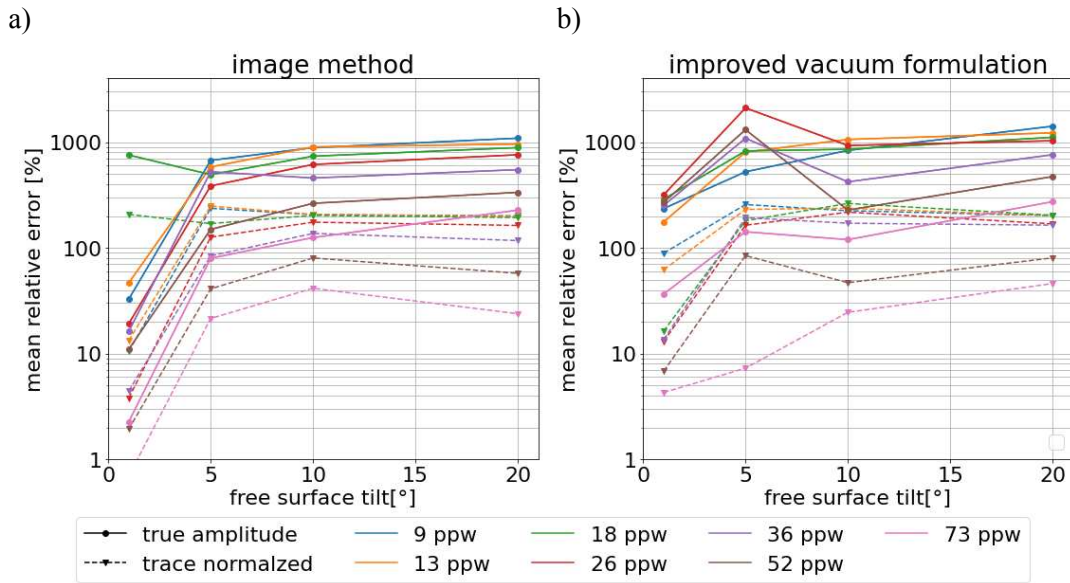


Figure 7.11: Mean relative error of the whole traces of the horizontal receiver components for the image method of *ve2d_ref* (a) and improved vacuum formulation of *DENISE Black Edition* (b) plotted against the dip angle of the free surface. The errors are calculated for 500 to 20000 m offset.

7.4. Convergence tests

Since the free surface of inhomogeneous models also includes topography the effects of a tilted free surface in the convergence test should be evaluated. The relative difference between two grid discretisations is calculated according to equation (4.5) and the arithmetic mean of all traces is used to quantify the relative difference across the whole simulation.

This relative difference for the P-wave in the horizontal component is plotted for the image method in Figure 7.12a and the improved vacuum formulation Figure 7.12b. The convergence test for the image method (Figure 7.12a) has a similar behaviour for the trace normalized data as the error to the analytical solution, where the difference between two grid discretisations decreases with finer grids. This trend is present for all tilts except for a tilt of 1° where an increase is caused by a spike in relative error of one spatial discretisation. Here a decrease from a difference of 10% at coarse grids to a difference below 1% over the course of all computed spatial discretisations is observed.

The P-wave does not have clear convergence behaviour for the improved vacuum formulation (Figure 7.12b). Here, the difference between grid discretisations behaves erratic and is plagued by recurring spikes in relative difference. However, an overall reduction in relative difference is not observed. Between the spatial discretisations, where a drop in error is observed in the accuracy test (section 6.3.2), the relative difference tends to also produce a spiking high value. One such spike is observed for a tilted free surface of 10 and 20° between 36 and 52 ppw and for 5° between 52 and 72 ppw (Figure 7.12b). These distinct spikes in relative difference are without prior knowledge hard to distinguish from other difference spikes observed in the data. These spikes are caused due to a sudden change of the timeseries, when the relative error suddenly decreases and rapidly converges towards the true solution. A more noticeable feature is the sudden drop in difference after the error is already at low values. This is visible for tilts of 10 and 20° but for 5 and 1° no such drop in the convergence test is visible since no finer discretisations have been simulated (Figure 7.12b).

The same relative difference between spatial discretisations is calculated for true amplitude and trace normalized data for a free surface with the image method in Figure 7.13a and for the improved vacuum formulation in Figure 7.13b for the whole traces.

The relative difference in the convergence test for the image method (Figure 7.13a) follows the trend in the relative error closely decreasing with each grid pair further, creating a smooth convergence trend. This trend is interrupted for a tilt of 1° by a spike in differences caused by a simulation with a high error at 18 ppw. The true amplitude data yields higher differences than the trace normalized error for some instances, but generally they exhibit similar values.

The relative difference for the whole traces in the convergence test for the improved vacuum formulation (Figure 7.13b) trends generally slowly to lower differences with finer grid discretisation. However as with the P-wave the relative differences tend to behave erratically and are plagued by spikes across, which are less severe than in the P-wave but still considerate. This erratic behaviour reduces at higher tilt angle (10 and 20°), where the difference trend is almost smooth towards lower differences.

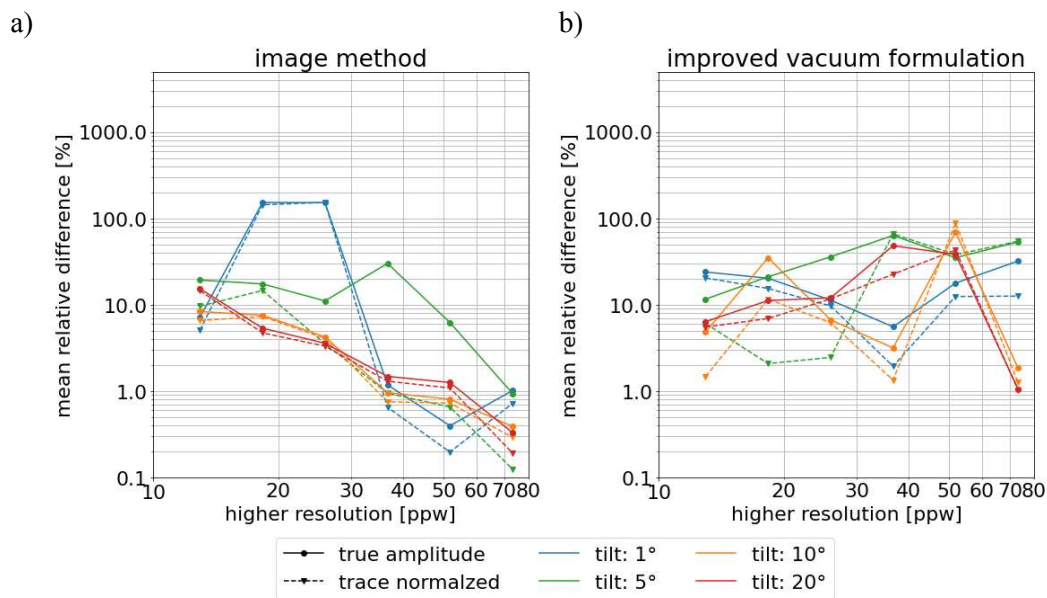


Figure 7.12: Convergence test for tilted elastic homogeneous half-spaces with different tilts for the P-wave for the image method of *ve2d_ref* (a) and improved vacuum formulation of *DENISE Black Edition* (b). The relative difference is computed according to equation (4.5) and only the higher resolution grid is noted on the x axis.

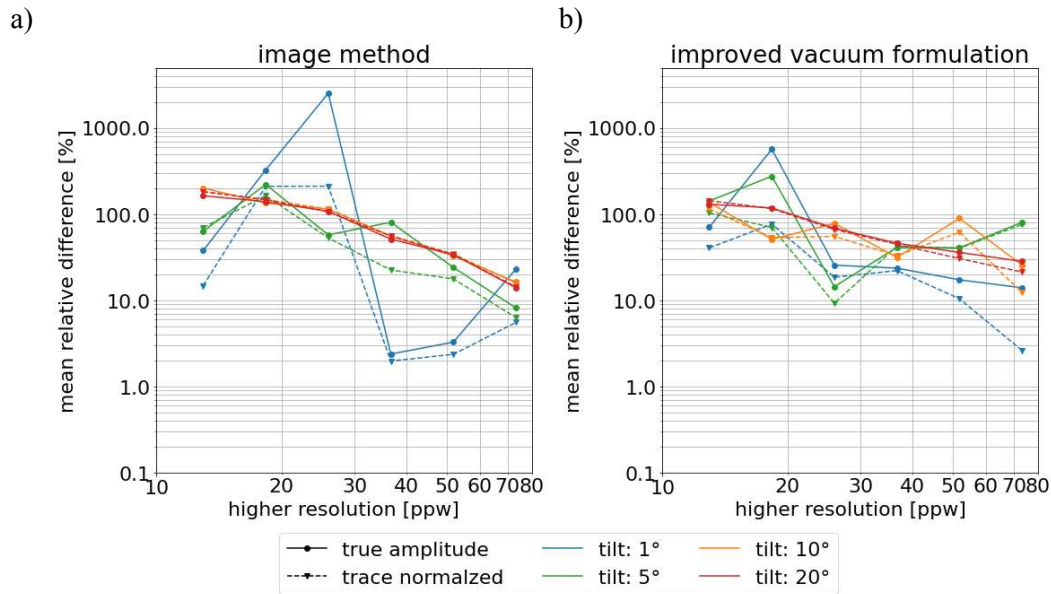


Figure 7.13: Convergence test for tilted elastic homogeneous half-spaces with different tilts for the whole trace for the image method of *ve2d_ref* (a) and improved vacuum formulation of *DENISE Black Edition* (b). The relative difference is computed according to equation (4.5) and only the higher resolution grid is noted on the x axis.

7.5. Summary of modeling errors

The introduction of a stepped staircase function to the surface has severe effects on the accuracy of the FD modeling. The image method and improved vacuum formulation have different effects on the modelled wavefronts. While the image method develops tailings following the wavefronts through the whole model space the improved vacuum formulation creates a smearing at the free surface for all wave phases. These effects reduce with an increase in spatial resolution and depend on the tilt angle. Since the effects occur regardless of the placement of the source these features of the wavefields are attributed to the interaction with a step in the staircase function of the free surface. These artefacts of the free surface boundary condition are the main contributors to the error of the simulated wavefields and should be reduced by increasing the spatial resolution to achieve accurate results.

In contrast to a grid-aligned free surface the P-wave is also affected severely by the interaction with free surface. While for both free surface conditions the P-wave is little affected by the offset, their behaviour with grid discretisation and tilt are very different. The tilt of the free surface for the image method in the range from 1 to 20° exhibits an increasing error with increasing tilt angle, while the improved vacuum formulation has the opposite trend. There the error decreases with increasing tilt.

The convergence behaviour with spatial grid discretisation for the image method has an expected smoothly decreasing trend while the improved vacuum formulation has to reach a critical point in the resolution, where the error decreases rapidly. This point is variable with the tilt angle and lower tilts need a finer grid sampling to reach it. For this critical point to be reached a maximum of 132 grid points per minimal P-wave wavelength (at 73 ppw) is needed to model the P-wave with adequate accuracy if a tilted free surface is present. This large and sudden decrease is also detectable in convergence tests as a spike in the difference between the modelled data for two spatial discretisations, which might be useful for more complex models.

The surface wave on the other hand exhibits an increase in error with offset and with tilt angle for both free surface conditions. Here the trend of the image method is steeper at lower angles than for the

improved vacuum formulation. The sudden and steep decrease in error of the improved vacuum formulation is still present, when considering the Rayleigh waves. The relative errors of the improved vacuum formulation after reaching the critical point are even lower than for the image method. However, the image method is less affected by very low tilt angles and the error for 1° is still lower than the improved vacuum formulation.

This leads to the conclusion that the image method might need longer to converge to errors equivalent to the improved vacuum formulation after reaching its critical point. But to test this even finer discretisations are necessary. The critical point in grid discretisation is also visible in the convergence tests but is difficult to identify and in more complex models might be easily misinterpreted. The image method on the other hand exhibits a smoothly decreasing trend for the most part.

8. Inhomogeneous model with a topographic free surface

Full waveform modeling is used to simulate the wave field of complex inhomogeneous models, which do not have an analytical solution the modeling may be compared to. This makes estimating the accuracy of simulation immensely more complicated. Both free surface boundary conditions approach the true analytical solution in homogeneous half-spaces with finer grid discretisations, so the assumption can be made, that the modeling will also approach the unknown true solution in inhomogeneous models. Hence a convergence tests are used to estimate a good spatial resolution of the grid.

The convergence behaviour of the surface conditions in `ve2d_ref` and DENISE Black Edition should be tested in a complex model with a complex topography. For these tests I use the models of a refraction survey near Parkfield California at the SAFOD drill site conducted in 2003 across the San Andreas Fault (J. A. Hole et al., 2006). For the purpose of these convergence tests four shots in different parts of the model have been selected to test the convergence behaviour of the free surface conditions implemented in the viscoelastic FD modeling `ve2d_ref` and DENISE Black Edition.

8.1. SAFOD Seismic refraction survey

The seismic refraction survey across the San Andreas Fault was conducted in 2003 near Parkfield, California. It was designed to cut the San Andreas Fault perpendicular at the location of the SAFOD with a total length of 46 km and its centre located at the SAFOD drill site (J. A. Hole et al., 2006). The model is of particular interest due repeating earthquakes of magnitude 2 near the town of Parkfield, CA in a section of the San Andreas fault, that is characterized by a permanent aseismic creep and micro earthquakes (Hickman et al., 2004). The SAFOD drill site is located in the transitions zone between the permanent creep zone to the north and the seismic Parkfield segment to the south of the site (Gratier et al., 2014).

The survey profile runs perpendicular to the San Andreas fault in this area from the Salinian terrane in the SW crossing the Buzzard Canyon Fault (BCF), San Andreas Fault (SAF), Gold Hill Fault (GHF) and Southwest Fracture Zone (SWFZ) across the Franciscan terrane, which is separated by the Waltham Canyon Fault to the Great Valley Sequence to NE (Figure 8.1) (Bleibinhaus et al., 2007; J. A. Hole et al., 2006). The Salinian terrane to the SW is characterized by high P-wave velocities (above 4.5 km/s) and is overlain by Cenozoic sediments with dipping contact to the SW. In the NE the low velocity Franciscan terrane and Great Valley Sequence are separated by the steep dipping Waltham Canyon Fault. The NE Great Valley Sequence and Franciscan terrane are separated to the SW Salinian terrane by the San Andreas Fault and associated Faults (J. A. Hole et al., 2006).

The conducted seismic survey used a fixed receiver array consisted of 912 three-component digital accelerometers placed with a spacing of 50 m which is decreased to a spacing of 25 m in the area 2.5 km around the San Andreas Fault. Shot spacing was chosen to decrease with proximity to the San Andreas Fault from a 1 km spacing along the line to 0.5 km. 63 explosive sources in shallow boreholes were fired with varying dimensions from 25 kg in the shorter spaced section to 100 kg and 200 kg explosions at the far ends of the line (J. A. Hole et al., 2006).

An overview of the survey area is provided in Figure 8.1 where two gaps in the receiver array are present due to lack of landowner permission (J. A. Hole et al., 2006). The survey has a significant

topographic profile with a variation of approximately 800 m and ranging from 300 to 1100 m above sea level.

This survey has been the subject of many investigations to further characterize area around the SAFOD drill site. Investigations of the P-wave velocity structure for this specific survey have been performed via travel time tomography by J. A. Hole et al. (2006) and by waveform tomography by Bleibinhaus et al. (2007). The investigation of the subsurface structure was extended to P- and S-waves through travel time tomography by T. Ryberg et al. (2012). These models further refined the upper crustal structure of the central California Coast Ridge in the vicinity of the SAFOD site (T. Ryberg et al., 2012).

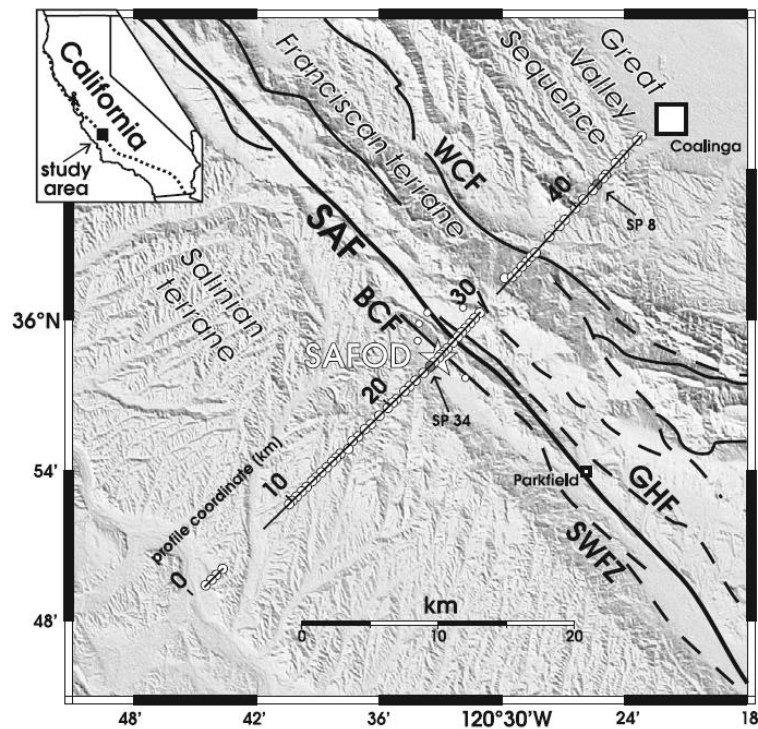


Figure 8.1: Map of the SAFOD site and the seismic survey conducted in 2003 near Parkfield, CA. circles denote shots and the black line from SW to NE denotes the receiver line with the model coordinates (distance along the profile in kilometres) after J. A. Hole et al. (2006)

8.2. Model parametrisation

For the waveform modeling a model space reaching from 6.5 km along the survey profile to 47 km distance along the profile with a vertical extent of 1.2 km above sea level to a depth of 5.9 km below sea level was chosen. This reduction of the model size is performed due to the gaps in survey profile at the beginning in the SW as seen in Figure 8.1. In this section the model is poorly constrained, and the structures of interest are in the NW section of the profile.

Viscoelastic waveform modeling requires the input of 5 input parameters: velocity of P-wave (V_p) and S-wave (V_s), density (ρ), and quality factors for P- and S-waves (Q_p and Q_s). Modeling with both waveform modeling algorithms uses the same initial models in the model space to which the boundary layers are added onto. For V_p and V_s the models by T. Ryberg et al. (2012) inverted through travel time tomography were used. These were provided with a regular horizontal and vertical spacing of 36.15 m. Since the model was prepared to perform a FWI both velocity models have been smoothed with a

circular moving average filter with a radius of 1 km in order to decrease the likelihood of an inversion getting stuck in a local minimum. The density model was derived from the smoothed V_p model using the Gardner's equation which is defined as

$$\rho = \alpha V_p^\beta, \quad (8.1)$$

where $\alpha = 310$ and $\beta = 0.25$ (G. H. F. Gardner et al., 1974).

Viscoelastic waveform modeling requires a quality factor model. The quality factor models used here were produced by Bennington et al. (2008) in their study of seismic attenuation in the area. The models have been extended to the required size and a low Q area has been added and smoothed with a moving average filter with a radius of 1.5 km by Zeiß (2021, pers. com., 24 June) for both Q_p and Q_s -models. The attenuation using the quality factor with one relaxation mechanism is defined by the relaxation frequencies and one value τ , which must be inverted for (Bohlen & Milkereit, 2001). This is not needed while modeling with `ve2d_ref` but is necessary for modeling with DENISE Black Edition. For this, τ has been inverted for using the Levenberg-Marquart method for the phase velocity and frequency of the used source wavelet (Bohlen & Milkereit, 2001), resulting in $\tau = 0.012$ and relaxation frequency $f_l = 3.16$ Hz.

These models have been discretised for a number of grid spacings, which have been chosen identical to the grid spacings used for the homogeneous test models: 20, 14.142, 10, 7.071, 5, 3.5355 and 2.5 m. All the spatial discretisations were interpolated using the Kriging interpolation. The resulting models for V_p , V_s and the density are displayed in Figure 8.2a, b and c respectively for a grid spacing of 5 m with the values above the free surface removed. The models for Q_p and Q_s are shown in Figure 8.3 also for a grid spacing of 5 m.

The free surface of the 2D model was approximated by linear interpolation between the elevations of the receiver stations of the recorded data and set to one grid point above the receiver positions. To apply this topography to the model a stepped staircase function is generated, and all synclines or anticlines have a width at the top layer of three grid points or more.

The wavefield was simulated for a total of four shots all located in different areas of the model to test the robustness of the modeling under different conditions. The shot positions in the model are potted in Figure 8.2 and Figure 8.3 with the names denoted as SP08, SP17, SP34 and SP56. All source positions were buried 40 m below the free surface to ensure a proper initialisation of the wavefield with the source function of a Ricker-wavelet with a centre frequency of 4 Hz as discussed in Chapter 3.3.1. This wavelet is obviously not representative of the recorded signal but was chosen for its numerical stability. All shots were simulated on each grid discretisation with the time step outlined in Table 3.1. The synthetic receiver stations are located at the receiver locations of the real survey and have a sampling rate of 2 ms.

All relevant modeling parameters for both DENISE Black Edition with the improved vacuum formulation implemented and `ve2d_ref` with the image method are summarized in Table 8.1 and the parameters specific to the modeling programs is summarized in Table 3.3.

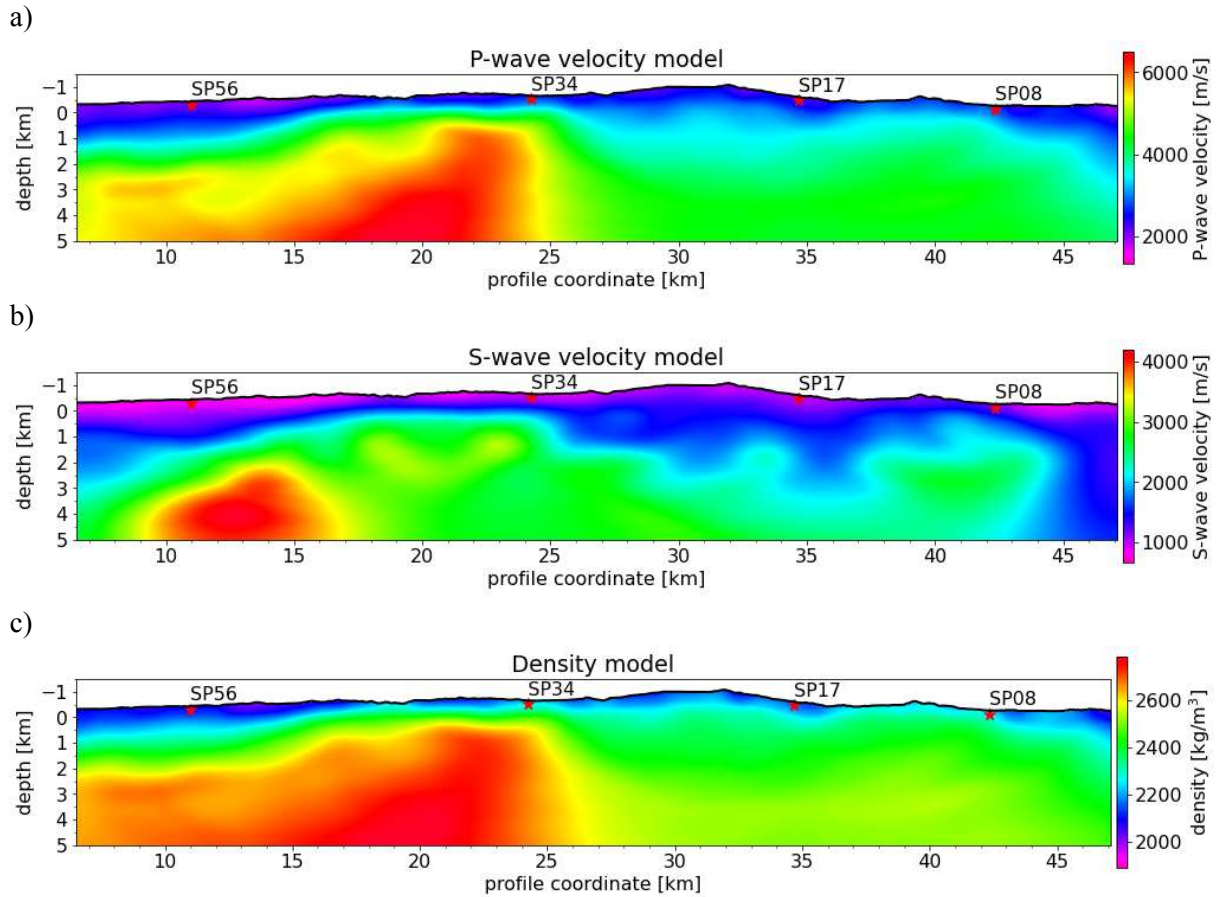


Figure 8.2: Smoothed SAFOD models of a) P-wave velocity b) S-wave velocity and c) density model for a grid spacing of 5 m with the simulated shot locations (red stars). Only the model space is shown.

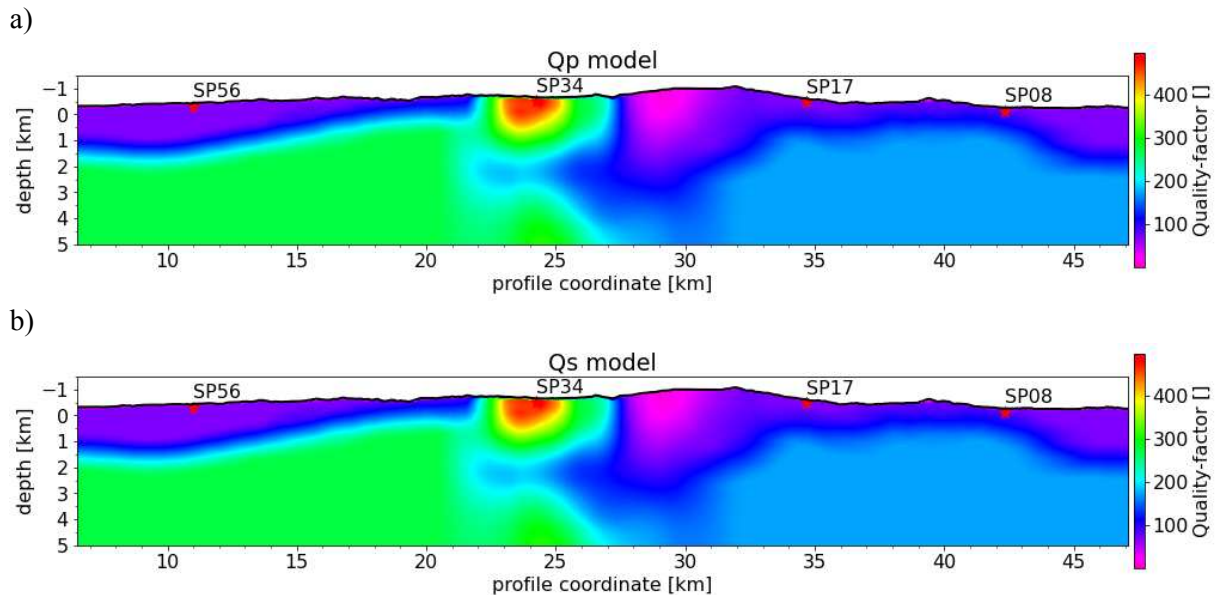


Figure 8.3: Damping quality factor SAFOD models of a) P-wave quality factor b) S-wave quality factor for a grid spacing of 5 m with the simulated shot locations (red stars). Only the model space is shown.

Table 8.1: Overview of modeling parameters for the SAFOD model

Model parameter	Value
Modeling	Visco-elastic FD PSV modeling
Spatial FD Order	2
Density	2500 kg/m ³
Source type	Explosive point source
Source function	4 Hz Ricker wavelet
Receiver sampling time	2 ms
Recorded time	10 s

8.3. Numerically modelled wavefields

For an inhomogeneous model such as the SAFOD model the exact shape of the wavefield in the subsurface is unknown. Generally speaking, due to the inhomogeneity of the model body waves no longer travel in circular wavefront but are distorted due to the variation in seismic velocity. The surface waves generated within the model become dispersive also due to the variation in seismic velocity. Furthermore, peaks and troughs might act as strong diffraction points for all wave phases. To have a closer look at the wave phases propagating throughout the model, the spatial divergence and curl are computed for the numerically computed wavefields at discrete times. In the following the spatial divergence and curl of the wavefields computed for of SP34 are discussed.

8.3.1. Spatial divergence

The spatial divergence of the wavefield at 2.50 s in time is depicted for the image method in Figure 8.4a and the improved vacuum formulation in Figure 8.4b for a model with a grid spacing of 5 m. The general shape of the divergence for both free surface conditions is similar, but the image method (Figure 8.4a) produces more pronounced coda waves than the improved vacuum formulation. These artefacts are well visualized at the first P-wave phase (phase 1 in Figure 8.4a and b).

Within the divergence several wave phases are observed. There are two separate P-wave arrivals visible with a primary (phase 1 in Figure 8.4) and secondary P-wave (phase 5 in Figure 8.4). These P-waves are reflected at the free surface, but the reflections are mostly interfered with closely following phases. A special channelled direct P-wave phase (phase 6 in Figure 8.4) is propagating in the shallow regions of the model, which is also observed in real data recordings. This direct P-wave which is channelled in the sedimentary layer over the bedrock of the Salinian terrane (Bleibinhaus et al., 2007). The Rayleigh waves (phase 3 in Figure 8.4) are also present in the divergence traveling along the free surface. These are diffracted at syn- and anticlines and generate P-waves in the divergence further complicating the wavefield. Due to the inhomogeneity of the model, the S-waves also generate SP-conversions as they travel through the model (phase 10 in Figure 8.4).

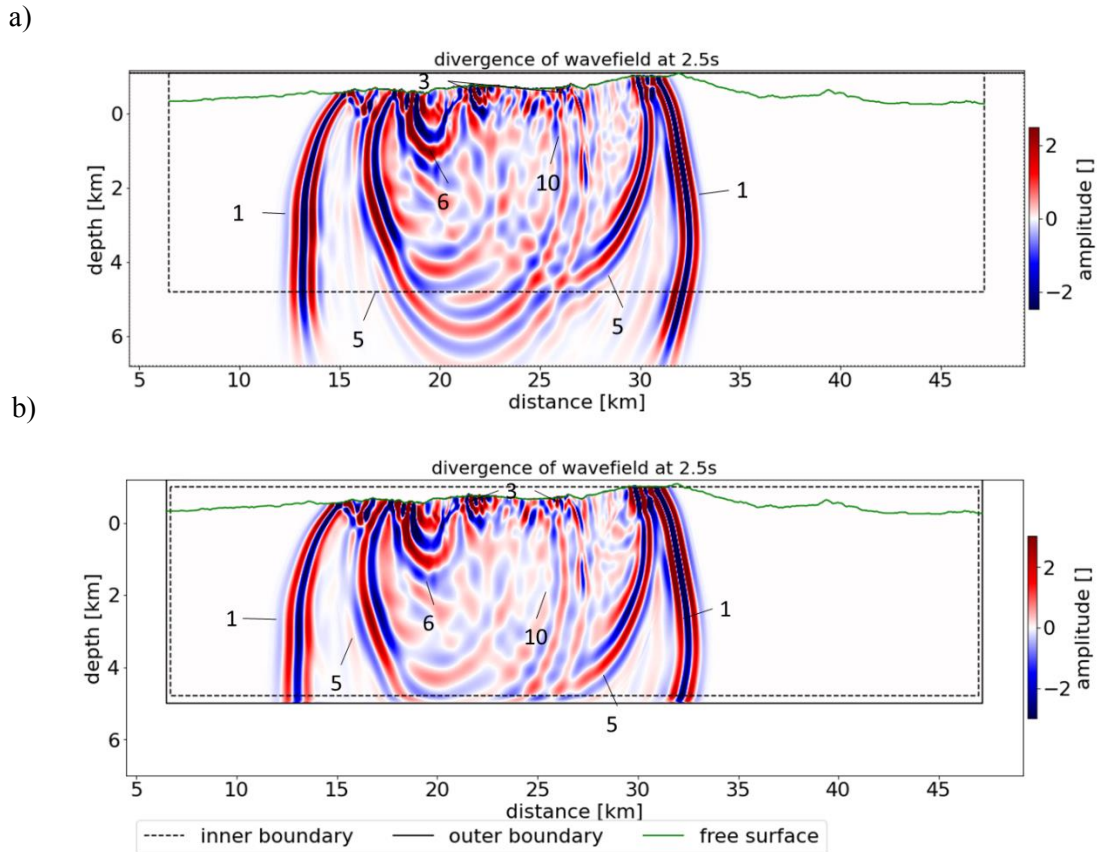


Figure 8.4: Spatial divergence of the wavefield at 2.5s in time computed with a free surface according to the image method of `ve2d_ref` (a) and improved vacuum formulation of DENISE Black Edition (b) for a model with $dh = 5m$. The vertical axis is exaggerated by a factor of 2 to make phases distinguishable. Annotated wave phases: 1: primary P-wave, 3: Rayleigh wave, 5: secondary P-wave, 6: channelled direct P-waves, 10 SP-conversions.

8.3.2. Spatial curl

The spatial curl of the wavefields at 2.50 s in time are depicted for the image method of `ve2d_ref` in Figure 8.5a and the improved vacuum formulation of DENISE Black Edition in Figure 8.5b for a model with a grid spacing of 5 m. The general shape of the curl is again similar with both modeling algorithms. One noticeable feature is the image method of `ve2d_ref` seems to produce higher amplitude coda behind the S-wave (phase 2 in Figure 8.5). These S-waves are also diffracted at the free surface.

The curl also shows several PS-waves (phase 4 in Figure 8.5) generated at the free surface by primary and secondary P-wave phases and the channelled direct P-wave. P-waves produce PS-conversions at depths in the model space. These are generated due to the inhomogeneity of the model at significant impedance changes. The Rayleigh waves (phase 3 in Figure 8.5) are imaged in the curl as well and are backscattered at the free surface and especially at syn- and anticlines.

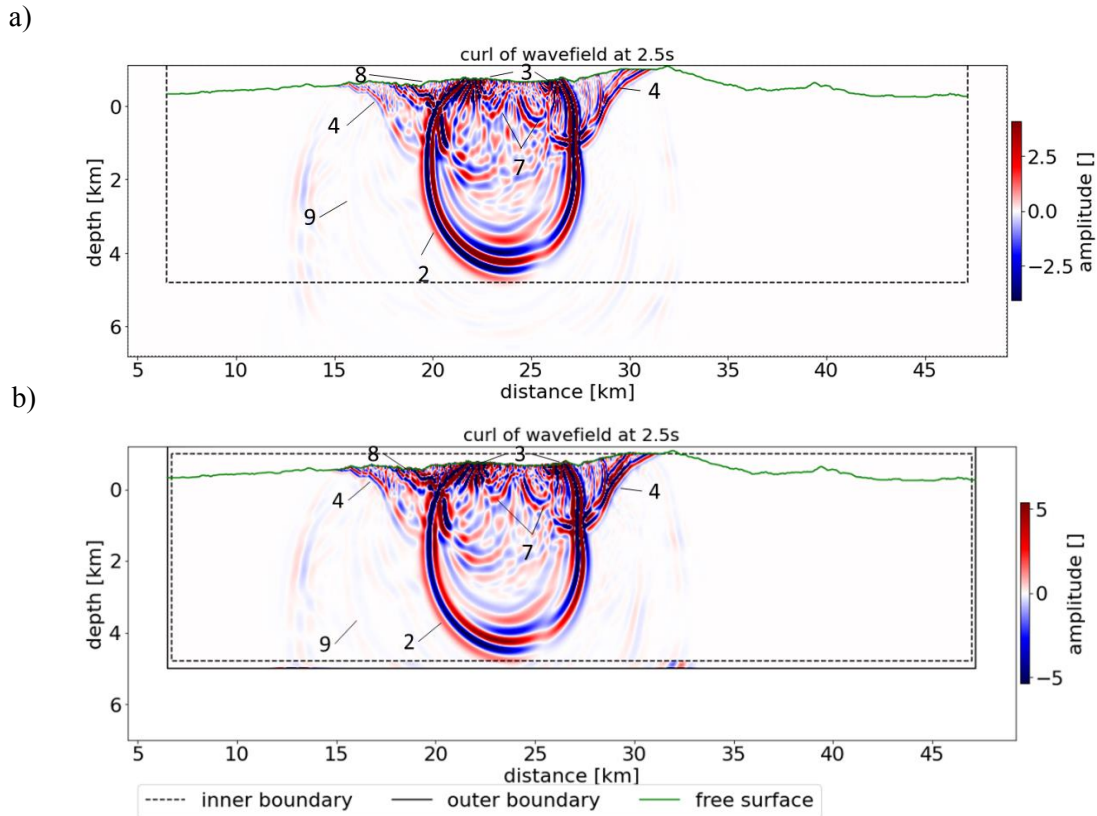


Figure 8.5: Spatial curl of the wavefield at 2.5s in time computed with a free surface according to the image method of `ve2d_ref` (a) and improved vacuum formulation of DENISE Black Edition (b) for a model with $dh = 5m$. The vertical axis is exaggerated by a factor of 2 to make phases distinguishable. Annotated wave phases: 2: S-wave, 3: Rayleigh wave, 4: PS-waves, 7: diffracted S-waves, 8: PS-waves of direct channelled P-wave, 9: PS-conversions.

8.4. Receiver components

The phases observed in the spatial divergence and curl are also present in the numerically computed receiver components. The introduction of an inhomogeneous model has some effects on the information contained in the components. A large part of the P-wave energy is contained in the vertical component due to the incidence angle of the seismic wavefront. Furthermore, the Rayleigh wave becomes dispersive due to the inhomogeneity on the seismic velocity model and the S-wave separates from it and is easily detectable as a separate wave phase in the seismograms.

To keep consistency throughout this investigation, the focus is put on the horizontal particle velocity. The vertical particle velocity shows similar results as the horizontal particle velocity.

8.4.1. Horizontal particle velocity

The horizontal particle velocity is depicted modelled for shot SP34 with a grid spacing of 5 m with the image method of `ve2d_ref` in Figure 8.6a and with the improved vacuum formulation of DENISE Black Edition in Figure 8.6b. All wave phases have significant diffractions and backscattering noticeable in the shot gathers for both free surface conditions. These are present at regular intervals for the surface waves as backscattered Rayleigh waves. For the S- and P-wave phases diffractions occur at the free surface.

Diffracted waves are noticeable throughout the entire shot gather but the strongest diffractions occur at anticlines or synclines of the free surface. For shot SP34 the strongest diffraction of the first arrival is located at 40 km along the profile (Figure 8.6a and b) and coincides with an anticline in the free surface. All observed diffractions in the shot gathers have a seemingly constant moveout across the entire simulated time for both image method and improved vacuum formulation.

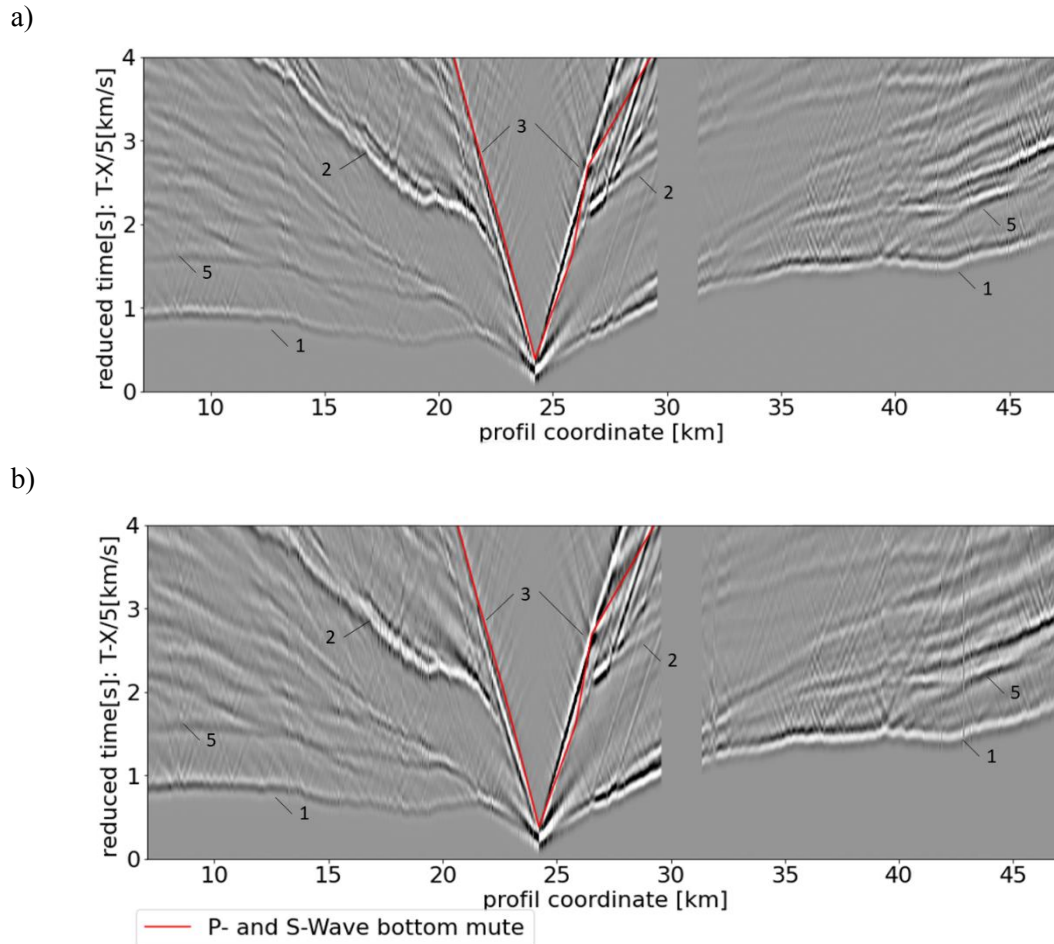


Figure 8.6: Shot gather of the trace normalized horizontal component of SP34 in reduced time modelled with a free surface boundary according to a) the image method with `ve2d_ref` and b) the improved vacuum formulation with `DENISE Black Edition`. Annotated wave phases: 1: refracted P-wave, 2: S-wave, 3: Rayleigh wave, 5: secondary P-wave.

8.5. Convergence tests

As already mentioned since no analytical solution exists a convergence test has to be performed. The relative difference between the spatial discretisations is calculated according to equation (4.5). To estimate the convergence of separate phases the relative difference is calculated for the whole trace and for the P-waves and S-waves, with the Rayleigh waves removed using a bottom mute as shown in Figure 8.6. The whole trace is representative of the error of the Rayleigh waves, since these have the highest amplitudes of all phases.

The relative differences between modelled grid discretisations over offset are displayed for the whole trace of SP34 for true amplitude and trace normalized data for the image method of `ve2d_ref` in Figure 8.7 (a and b) and for the improved vacuum formulation of `DENISE Black Edition` in Figure 8.7 (c and

d). Here the straight section of differences at 30 km along the profile is caused by a lack of receivers. The relative differences over offset of the other simulated shots exhibit a similar behaviour and are added in Appendix C.

The general behaviour of the relative differences with spatial resolution for each surface condition is similar to that observed for a tilted homogeneous half-space. The image method of `ve2d_ref` exhibits a continuous reduction of relative differences in both true amplitude (Figure 8.7a) and trace normalized data (Figure 8.7b). The improved vacuum formulation of DENISE Black Edition generally behaves more erratically and exhibits spikes and drops in differences across all spatial discretisations.

The behaviour of relative differences over the offset of the image method of `ve2d_ref` seem to keep at a level for trace normalized data (Figure 8.7b) or decrease slightly with offset for true amplitude data (Figure 8.7a). Near the shot point within 10 km offset the error increases for most simulated shots as for SP34 (Figure 8.7a and b), which is followed by a decrease in error over offset. These increases are a result of the Rayleigh waves increasing inaccuracies with offset.

The relative differences of the improved vacuum formulation of DENISE Black Edition (Figure 8.7c and d) have a highly variable behaviour. Within the simulated grid discretisations the behaviour varies and steep increases, constant differences and decreases over offsets are observed for amplitude data (Figure 8.7c). This highly variable behaviour of the differences is mostly removed with the application of trace normalisation (Figure 8.7d) and a more or less constant difference is observed for coarse grids. A decrease of differences over offset is observed for fine spatial discretisations. Additionally, an increase over offset happens as long as Rayleigh waves are observed in the trace.

Specific reasons for the high variability of the behaviour of relative differences with offset for the improved vacuum formulation of DENISE Black Edition are difficult to pinpoint. One reason for then change of the behaviour is the variation of incline and dip angles of the topographic free surface. These varying angles might locally affect the wavefield near the receivers causing the change in differences. This might not be happening for the image method since the improved vacuum formulation of DENISE Black Edition is sensitive to low free surface tilt angles.

The near field region for both free surface conditions is characterized by lower differences that steeply increase with offset. This behaviour is consistent throughout all simulated shots computed using the image method.

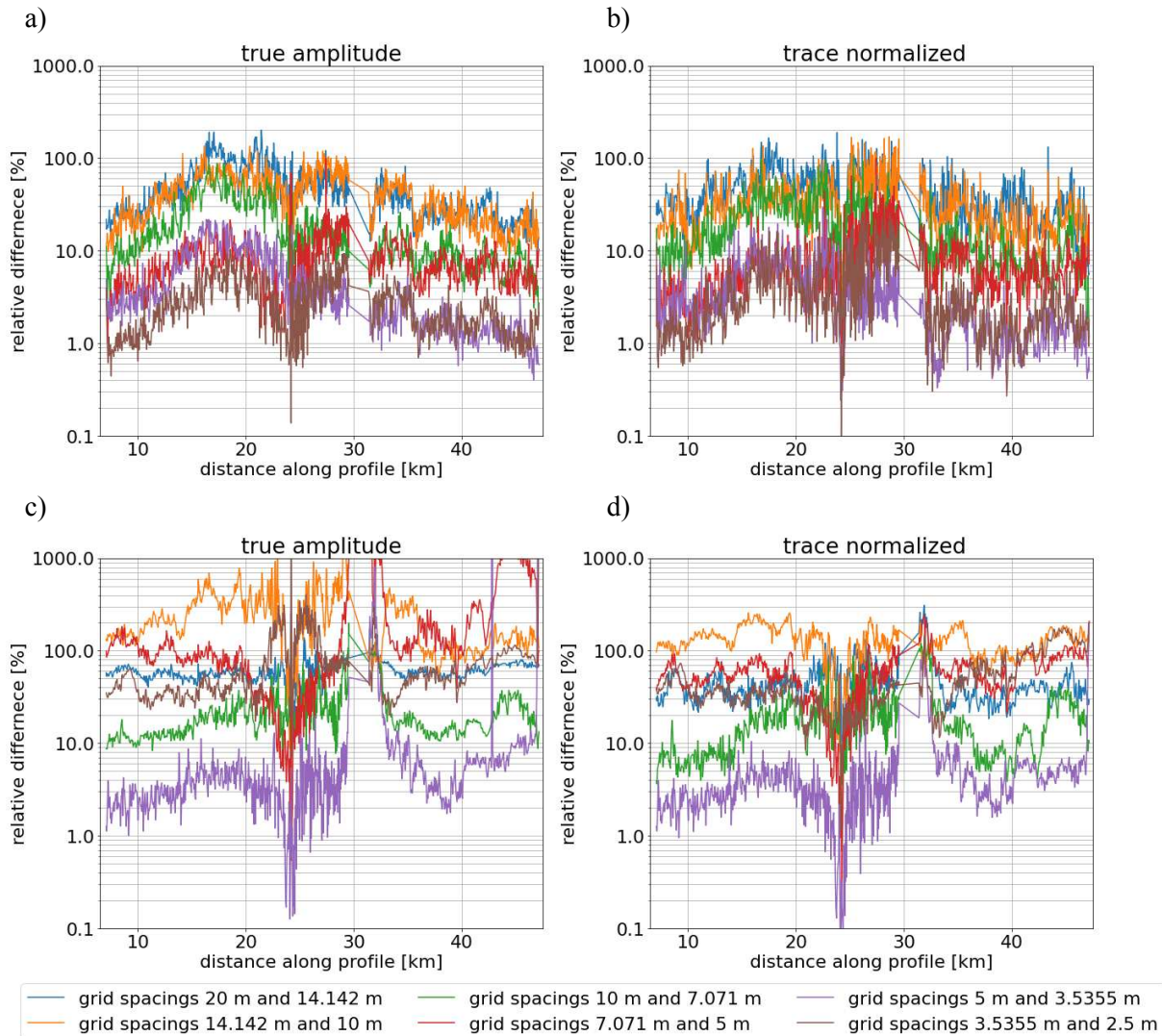


Figure 8.7: Relative difference of the horizontal components whole traces of SP34 between spatial discretisations over offset for the image method of `ve2d_ref` (a and b) and improved vacuum formulation of DENISE Black Edition (c and d) for true amplitude (left column) and trace normalized data (right column).

The relative differences over offset are plotted for the separated P-wave and S-wave arrivals of SP34 for true amplitude and trace normalized data for the image method of `ve2d_ref` in Figure 8.7(a and b) and for the improved vacuum formulation of DENISE Black Edition in Figure 8.7(c and d). The trends observed for the whole traces are mostly observed again for the P-wave and S-wave, especially at long offsets, where the two data sets are virtually identical.

Differences are observed near the shot point, where Rayleigh waves were removed. Here, the image method of `ve2d_ref` no longer shows a pronounced maximum of relative differences with offset at roughly 20 km along the profile. Instead, the differences stay constant with slight decreases at very high offsets at the ends of the model for both true amplitude (Figure 8.7a) and trace normalized data (Figure 8.7b).

A similar behaviour is observed for the improved vacuum formulation of DENISE Black Edition (Figure 8.7c and d), where the maxima of fine grids are removed too. But the general behaviour varies still and is either increasing with offset or staying at a constant level. Additionally large spikes in differences are observed for true amplitude data (Figure 8.7c). Trace normalisation again decreases the growth of differences over offset (Figure 8.7d).

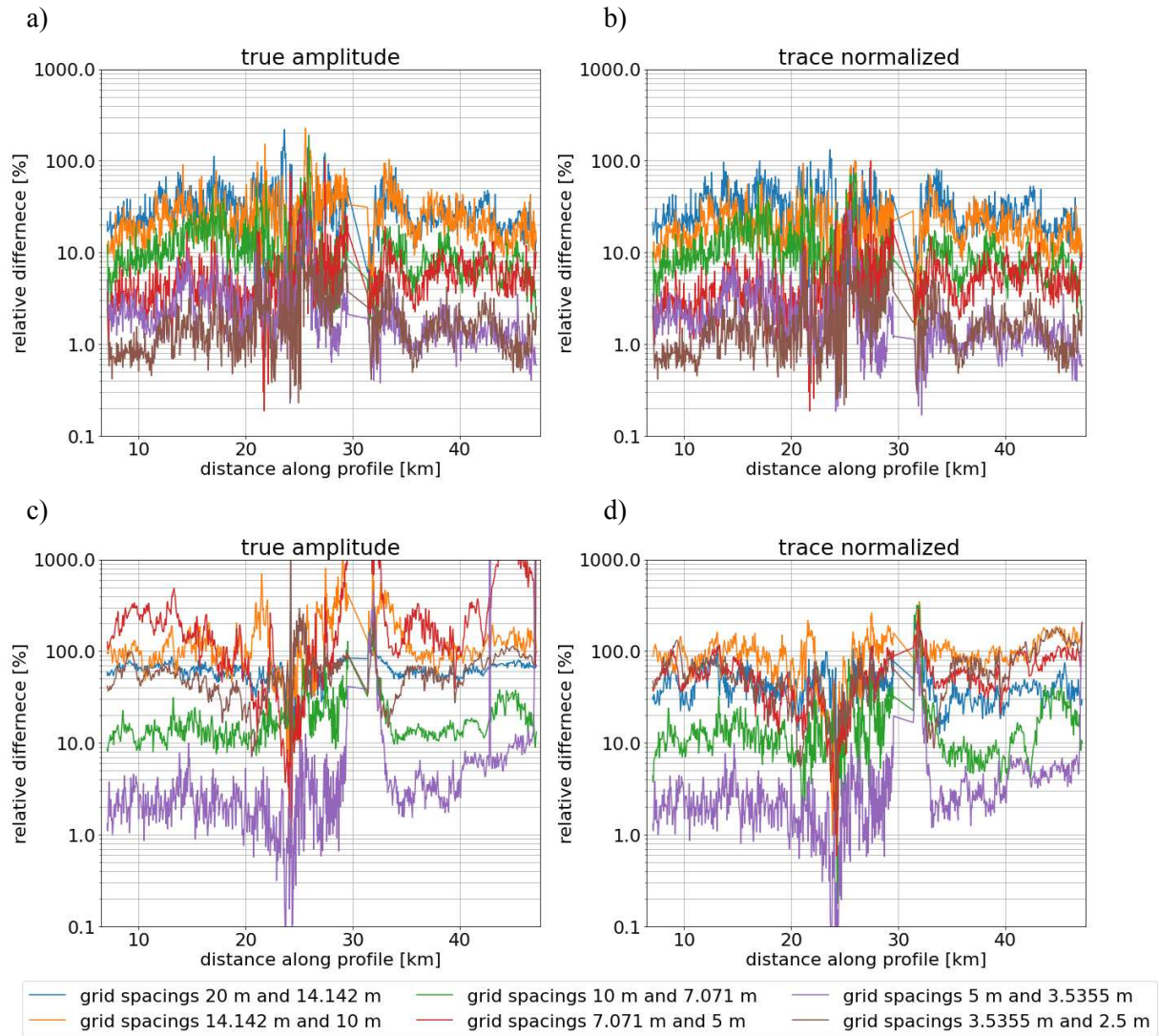


Figure 8.8: Relative difference of the horizontal components of the P -wave and S -wave of SP34 between spatial discretisations over offset for the image method of `ve2d_ref` (a and b) and improved vacuum formulation of DENISE Black Edition (c and d) for true amplitude (left column) and trace normalized data (right column).

For calculating the difference for the entire data every second receiver station within the dense receiver spacing in the middle of the model around the SAFOD drill site has been removed in order to not overvalue a certain range of offsets in each shot.

The resulting convergence tests for the whole receiver traces for true amplitude and trace normalized data is plotted in Figure 8.9a for the image method of `ve2d_ref` and in Figure 8.9b for the improved vacuum formulation of DENISE Black Edition. In order to examine the behaviour in the presence of the Rayleigh wave, the relative difference has been calculated only for traces where it is observed with in the simulated time frame. The behaviour of these two free surface conditions is very different from each other.

The relative difference of the image method of `ve2d_ref` (Figure 8.9a) develops a continuous decrease in relative differences with finer grids for all shots for trace normalized data. This changes from 50% relative difference at the coarsest grids to 2-3% at the finest two grid spacings. The behaviour between true amplitude and trace normalized data is not significantly different and the true amplitude data only occasionally produces higher differences.

For the improved vacuum formulation, the relative difference (Figure 8.9b) is highly variable for both true amplitude and trace normalized data. The trace normalized data fluctuates around a general decreasing trend with spatial resolution. These fluctuations are increasing relative differences by up to a factor of 100. The behaviour is even more erratic for true amplitude data, where relative differences have values similar to the trace normalized data for coarse discretisations, and rise to values over 100000% for fine spatial discretisations. This drastic increase in mean relative differences might be caused by a decrease in the distortion of the wavelet, as observed for the tilted homogeneous half-space.

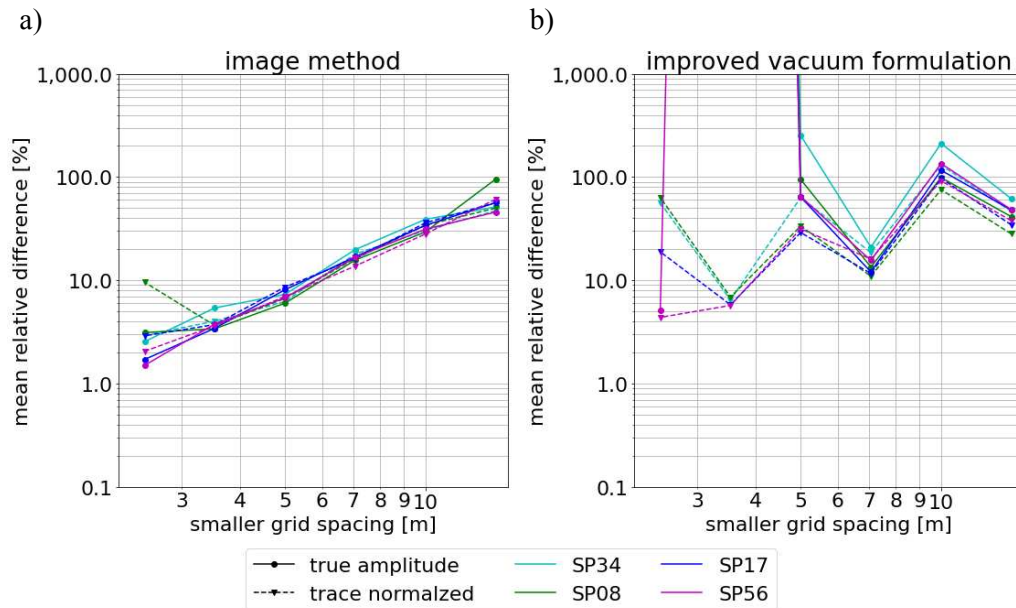


Figure 8.9: Convergence test for four different shots of the SAFOD model with a free surface according to the image method (a) and improved vacuum formulation (b) for the whole trace. The relative difference is computed according to equation (4.5) and only the higher resolution grid is noted on the x axis.

The relative difference in the P- and S-wave window is plotted in Figure 8.10a for the image method of ve2d_ref and in Figure 8.10b for the improved vacuum formulation of DENISE Black Edition for trace normalized and true amplitude data.

The convergence for the trace normalized data also has a smoothly decreasing trend for the image method for P- and S-wave arrivals (Figure 8.10a). Here the relative difference has similar values for all simulated shots decreasing to values between 1 and 2%.

As for the whole trace, the P- and S-waves modelled with the improved vacuum formulation (Figure 8.10b) have strongly fluctuating relative differences for both true amplitude and trace normalized data. These fluctuations are less severe than for the whole trace and a smaller, generally decreasing trend is noticeable. This trend is not as steep as observed in the whole trace and the fluctuations are the most prominent feature in the convergence tests. Relative differences generally decrease by a factor of 10 through the entire simulated grid spacings. Here the trace normalized data again exhibits smaller differences than the true amplitude data while following the same behaviour in the convergence test.

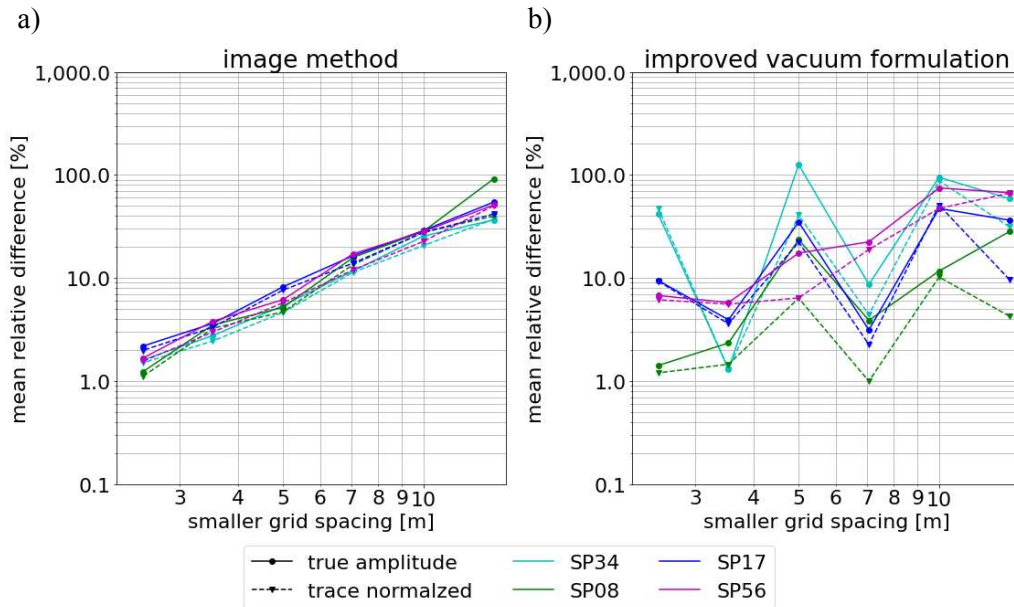


Figure 8.10: Convergence test for four different shots of the SAFOD model with a free surface according to the image method (a) and improved vacuum formulation (b) for the P- and S-wave. The relative difference is computed according to equation (4.5) and only the higher resolution grid is noted on the x axis.

8.6. Summary of the modeling

Modeling of an inhomogeneous model with a topographic free surface generates more complicated wavefields where the similar effects are observed as for a tilted free surface in a homogeneous model. The convergence tests performed to evaluate the required spatial discretisations to accurately model the full wavefield for the SAFOD model have varying results. The convergence of relative differences of the image method of `ve2d_ref` trends smoothly towards low values for both true amplitude and trace normalized data.

The differences between grid discretisations for P- and S-waves are comparable to values (below 3%) observed in the convergence tests for a tilted homogeneous half-space (chapter 7), where small errors below 10% occur. This might be an indication that the spatial resolution is sufficient to model P- and S-waves with the image method of `ve2d_ref`. However, to ensure this finer discretisations would be required to fully observe the convergence behaviour, which was not possible due to memory restrictions.

The convergence test for the improved vacuum formulation is difficult to interpret due to the erratic variation in relative difference. The P- and S-wave difference exhibit a general decrease which is overshadowed by large variations of the relative difference. Any spike in relative difference indicating a sudden increase in accuracy, as observed for a tilted homogeneous half-space (chapter 7) for the P- and S-waves is impossible to identify. If the surface waves are included in the evaluation of relative differences almost all simulated shots have extremely high differences for fine discretisations for true amplitude data. This might be an indication of a sudden increase in accuracy as seen for the tilted half-space. This however is not adequate to assume a sufficient accuracy and further finer discretisations would be needed to verify this.

9. Discussion

The accuracy of synthetic seismograms computed with FD modeling for free surfaces according to the image method and the improved vacuum formulation was investigated for a planar free surface aligned with the grid axis in an elastic homogeneous half-space. Since two different modeling programs were used during this work (ve2d_ref and DENSIE Black Edition), the comparability of these modeling algorithms was ensured by testing the accuracy in an elastic homogeneous full space and by using the image method for an elastic homogeneous half-space with a free surface aligned with the grid axis in both ve2d_ref and DENSIE Black Edition.

The image method of ve2d_ref and of DENSIE Black Edition have comparable results and the major differences in errors are caused by the implementation of different absorbing boundary conditions (sponge layers and C-PML respectively). The errors these two boundary conditions generate weak reflections of P-waves and S-waves near the inner boundary of the model. These cause significant errors at long offsets and interfere with the recorded arrivals reducing their accuracy. C-PML boundaries generate lower errors than sponge layers, while having a fraction of the computational costs. To further decrease the errors at long offsets the boundaries have to be placed further from the receiver array, which might not be computationally viable.

These tests lead to the conclusion that the findings are not specific to the modeling algorithms and results of more complicated models, as the tilted homogeneous half-space with a free surface and the inhomogeneous model with a topographic free surface, can be attributed to the free surface conditions. It is important to note though that a direct comparison of the free surface conditions of the image method and the improved vacuum formulation in the same modeling algorithm would be beneficial.

The image method and improved vacuum formulation have a different convergence trend to low errors. These behaviours are observed for a planar free surface aligned with the grid and tilted free surfaces, where they are more pronounced. The image method steadily converges to low errors with increasing grid discretisation for both P-waves and Rayleigh waves. The improved vacuum formulation has rather stable high errors and, as a critical point in the grid resolution is reached, experiences a rapid decrease in error. The drop in error is more significant for P-waves than for Rayleigh waves, but this critical point might not have been reached for Rayleigh waves traveling along a tilted free surface.

These behaviours of the error are also visible in the convergence tests conducted. The relative differences between the seismograms of two spatial discretisations gives a measure of the change of the wave field with each step in spatial resolution. The results for the image method have a similar behaviour as for the errors, where the relative differences continuously decrease with increasing resolution. The improved vacuum formulation behaves more erratically and spikes in differences occur, when the critical point in spatial resolution is reached. Additionally general high fluctuations are observed if the free surface is not aligned with the grid axis.

Generally, the two different free surface conditions cause two types of inaccuracies at coarse spatial discretisations. These reduce with an increasing spatial resolution and are clearly observed with a free surface not aligned with the grid axis. The image method produces coda waves for all generated wave fronts, which propagate through the entire model space. The improved vacuum formulation on the other hand introduces distortion, stretching and time shift to the wavelets making up the entire wavefront for P-waves and S-waves. Additionally, a smearing of wavefronts is noticeable in the

divergence of wavefields directly at the free surface. Rayleigh waves also exhibit coda additionally to the distortion of the wavelet.

The errors of the Rayleigh wave of an elastic homogeneous half-space with a free surface aligned with the grid axis confirm the findings of Bohlen and Saenger (2006) that 15 to 30 ppw are a sufficient resolution. However, the lower end of this range is only valid for a free surface according to the image method, while the improved vacuum formulation required higher sampling rates of 25 to 30 ppw on a standard staggered grid.

The accuracy of the P-wave of both free surface conditions is affected differently by the tilt angle of the free surface. The image method shows an increase in relative error with increasing tilt angle for tilt angles below 20° , which steeply increases for low tilt angles ($<5^\circ$) and flattens out for higher angles. The improved vacuum formulation spikes in error at low tilt angles ($<5^\circ$) and decreases in error with increasing tilt angle. At 20° tilt angle the improved vacuum formulation exhibits similar errors for the finest discretisation as the image method. This leads to the conclusion, that the P-wave in the vacuum formulation is extremely sensitive to the introduction of steps in the free surface. The incidence angles of the P-wave to the free surface in these models are low, due to the homogeneity of the model and it is questionable, if this is also true for higher incidence angles commonly encountered inhomogeneous models. Depending on the tilt angle the relative errors for the P-wave for both free surface conditions are at comparable values of 3% for the trace normalized data at the finest discretisation of 132 grid points per minimum P-wave wavelength (finest discretisation of 72 ppw).

The error of the Rayleigh wave is also dependent on the tilt angle of the free surface. The behaviour for both free surface conditions is similar, and errors increase with increasing tilt angle. The improved vacuum formulation also exhibits a higher error at very low angles than the image method, which underlines the observation that the improved vacuum formulation is very sensitive towards steps in the free surface. Here further testing would be needed to determine the convergence behaviour since errors do not reach low error, hence a spatial discretisation of more than 72 points per minimum wavelength is required to accurately model Rayleigh waves.

If the free surface conditions are applied to an inhomogeneous model with a topographic surface, convergence tests using the relative differences between the simulated grid discretisations have to be performed to evaluate the convergence behaviour. Here the image method also exhibits a continuous decreasing trend of relative differences between grid discretisations. The improved vacuum formulation on the other hand has an erratic behaviour. Here a generally decreasing trend is observed, which is plagued by fluctuations making an interpretation difficult. There are extremely high spikes in differences observed in true amplitude data at higher resolution, which might be caused by rapid convergence as observed for a homogeneous model, but to determine a further decrease in grid spacing would be necessary.

10. Conclusion

This work investigates the accuracy of 2D FD waveform modeling for near surface sources in the presence of a free surface boundary defined by the image method and improved vacuum formulation. The full-waveform modeling was performed using two modeling algorithms, `ve2d_ref` implementing the image method and DENISE Black Edition implementing the improved vacuum formulation. The accuracy of the numerically modelled seismograms was determined by a comparison to an analytical solution for simple elastic homogeneous full and half-spaces. These accuracy tests were compared with convergence tests, evaluating the change between subsequent steps in spatial resolutions of the model grid, to determine their potential behaviour for inhomogeneous models. Accuracy tests, comparing both modeling algorithms in an elastic homogeneous full space, indicate a comparable error caused by the absorbing boundary conditions of DENISE Black Edition and `ve2d_ref`. Further comparisons of the image method for an elastic homogeneous half-space with a free surface aligned with the horizontal grid axis for both `ve2d_ref` and DENISE Black Edition suggest that effects observed for other more complex models can be generalized to the free surface conditions. The image method exhibits a steady reduction in error with an increase in spatial resolution for both P-waves and Rayleigh waves. This is true for horizontal and most tilted free surfaces in elastic homogeneous half-spaces. Its relative error increases for all phases with the tilt angle up to 20° . This steady convergence is also observed in the convergence tests, where relative differences decrease steadily with increasing spatial resolution. The improved vacuum formulation has a critical point of spatial resolution, where a rapid convergence to lower errors is observed. This behaviour is present for free surfaces aligned with the model grid and tilted free surfaces. The effect is more pronounced for tilted free surfaces and the spatial discretisation of this critical point varies with tilt angle. The tilt angle has a different behaviour for wave phases. The error increases with tilt angle for Rayleigh waves. For P-waves the error is high at low angles and decreases with tilt angle to values comparable with the image method. The behaviour of the improved vacuum formulation in convergence test is erratic and the rapid reduction in error, observed in the accuracy tests, has the effect of a spike in relative differences. This spike, indicating a reduction in error, is difficult to correctly identify without prior knowledge in homogeneous test models. The errors observed in the improved vacuum formulation are mainly the effect of distortions of the waveform. In the image method the inaccuracies are caused by spurious coda of all wave phases. These effects reduce with increasing spatial resolution. In inhomogeneous models the improved vacuum formulation has a difficult to interpret behaviour in convergence tests due to high fluctuations in relative differences. This makes the improved vacuum formulation cumbersome to handle for inhomogeneous models, although it achieves similar or even lower errors than the image method in numerical tests. The image method on the other hand is converging smoothly even in an inhomogeneous model with a topographic free surface and an interpretation of the convergence test is straight forward with smaller differences indicating a better numerical solution.

11. References

- Aki, K., & Richards, P. G. (2002). *Quantitative Seismology* (2nd ed.). Sausalito, Calif: University Science Books.
- Alterman, Z., & Karal, F. C. (1968). Propagation of elastic waves in layered media by finite difference methods. *Bulletin of the Seismological Society of America*, 58, 367–398.
- Bennington, N., Thurber, C., & Roecker, S. (2008). Three-Dimensional Seismic Attenuation Structure around the SAFOD Site, Parkfield, California. *Bulletin of the Seismological Society of America*, 98(6), 2934–2947. <https://doi.org/10.1785/0120080175>
- Berenger, J.-P. (1994). A perfectly matched layer for the absorption of electromagnetic waves. *Journal of Computational Physics*, 114(2), 185–200. <https://doi.org/10.1006/JCPH.1994.1159>
- Berg, P., If, F., Nielsen, P., & Skovgaard, O. (1994). Analytical reference solutions. *Modeling the Earth for Oil Exploration*, 421–427.
- Bleibinhaus, F. (2016). Full-Waveform Inversion of Controlled-Source Seismic Data. In M. Beer, I. A. Kougioumtzoglou, E. Patelli, & I. S.-K. Au (Eds.), *Encyclopedia of Earthquake Engineering* (pp. 1–13). Berlin, Heidelberg: Springer Berlin Heidelberg. https://doi.org/10.1007/978-3-642-36197-5_376-1
- Bleibinhaus, F., Hole, J. A., Ryberg, T., & Fuis, G. S. (2007). Structure of the California Coast Ranges and San Andreas Fault at SAFOD from seismic waveform inversion and reflection imaging. *Journal of Geophysical Research*, 112(B6). <https://doi.org/10.1029/2006JB004611>
- Bohlen, T., & Milkereit, B. (2001). Parallel 3D Viscoelastic Finite Difference Seismic Modeling. In *63rd EAGE Conference & Exhibition*. European Association of Geoscientists & Engineers. <https://doi.org/10.3997/2214-4609-PDB.15.P006>
- Bohlen, T., & Saenger, E. H. (2006). Accuracy of heterogeneous staggered-grid finite-difference modeling of Rayleigh waves. *GEOPHYSICS*, 71(4), T109-T115. <https://doi.org/10.1190/1.2213051>
- Cerjan, C., Kosloff, D., Kosloff, R., & Reshef, M. (1985). A nonreflecting boundary condition for discrete acoustic and elastic wave equations. *GEOPHYSICS*, 50(4), 705–708. <https://doi.org/10.1190/1.1441945>
- Collino, F., & Tsogka, C. (2001). Application of the perfectly matched absorbing layer model to the linear elastodynamic problem in anisotropic heterogeneous media. *GEOPHYSICS*, 66(1), 294–307. <https://doi.org/10.1190/1.1444908>
- Courant, R., Friedrichs, K., & Lewy, H. (1928). Über die partiellen Differenzgleichungen der mathematischen Physik. *Mathematische Annalen*, 100(1), 32–74. <https://doi.org/10.1007/BF01448839>
- Dougherty, M. E., & Stephen, R. A. (1988). Seismic energy partitioning and scattering in laterally heterogeneous ocean crust. *Pure and Applied Geophysics PAGEOPH*, 128(1-2), 195–229. <https://doi.org/10.1007/BF01772597>
- Fichtner, A. (2011). *Full Seismic Waveform Modeling and Inversion*. Berlin, Heidelberg: Springer Berlin Heidelberg.

- Gao, Y., Song, H., Zhang, J., & Yao, Z. (2017). Comparison of artificial absorbing boundaries for acoustic wave equation modeling. *Exploration Geophysics*, 48(1), 76–93. <https://doi.org/10.1071/EG15068>
- Gardner, G. H. F., Gardner, L. W., & Gregory, A. R. (1974). Formation velocity and density —The diagnostic basics for stratigraphic traps. *GEOPHYSICS*, 39(6), 770–780. <https://doi.org/10.1190/1.1440465>
- Gottschämmer, E., & Olsen, K. (2001). Accuracy of the Explicit Planar Free-Surface Boundary Condition Implemented in a Fourth-Order Staggered-Grid Velocity-Stress Finite-Difference Scheme. *Bulletin of the Seismological Society of America*, 91(3), 617–623. <https://doi.org/10.1785/0120000244>
- Gratier, J. P., Renard, F., & Vial, B. (2014). Postseismic pressure solution creep: Evidence and time-dependent change from dynamic indenting experiments. *Journal of Geophysical Research: Solid Earth*, 119(4), 2764–2779. <https://doi.org/10.1002/2013JB010768>
- Graves, R. W. (1996). Simulating seismic wave propagation in 3D elastic media using staggered-grid finite differences. *Bulletin of the Seismological Society of America*, 86(4), 1091–1106. <https://doi.org/10.1785/BSSA0860041091>
- Hickman, S., Zoback, M., & Ellsworth, W. (2004). Introduction to special section: Preparing for the San Andreas Fault Observatory at Depth. *Geophysical Research Letters*, 31(12), n/a-n/a. <https://doi.org/10.1029/2004GL020688>
- Hicks, G. J. (2002). Arbitrary source and receiver positioning in finite-difference schemes using Kaiser windowed sinc functions. *GEOPHYSICS*, 67(1), 156–165. <https://doi.org/10.1190/1.1451454>
- Hole, J. A., Ryberg, T., Fuis, G. S., Bleibinhaus, F., & Sharma, A. K. (2006). Structure of the San Andreas fault zone at SAFOD from a seismic refraction survey. *Geophysical Research Letters*, 33(7). <https://doi.org/10.1029/2005GL025194>
- Holeberg, O. (1987). Computational aspects of the choice of operator and sampling interval for numerical differentiation in large-scale simulation of wave phenomena *Geophysical Prospecting*, 35(6), 629–655. <https://doi.org/10.1111/J.1365-2478.1987.TB00841.X>
- Hoop, A. T. de. (1960). A modification of cagniard's method for solving seismic pulse problems. *Applied Scientific Research, Section B*, 8(1), 349–356. <https://doi.org/10.1007/BF02920068>
- Igel, H. (2016). *Computational Seismology*: Oxford University Press.
- Köhn, D. (2011). Time Domain 2D Elastic Full Waveform Tomography (PhD thesis). Christian-Albrechts-Universität, Kiel.
- Köhn, D., Nil, D. de, Kurzmann, A., Przebindowska, A., & Bohlen, T. (2012). On the influence of model parametrization in elastic full waveform tomography. *Geophysical Journal International*, 191(1), 325–345. <https://doi.org/10.1111/J.1365-246X.2012.05633.X>
- Komatitsch, D., & Martin, R. (2007). An unsplit convolutional perfectly matched layer improved at grazing incidence for the seismic wave equation. *GEOPHYSICS*, 72(5), SM155-SM167. <https://doi.org/10.1190/1.2757586>
- Komatitsch, D., & Tromp, J. (1999). Introduction to the spectral element method for three-dimensional seismic wave propagation. *Geophysical Journal International*, 139(3), 806–822. <https://doi.org/10.1046/J.1365-246X.1999.00967.X>

- Lele, S. K. (1992). Compact finite difference schemes with spectral-like resolution. *Journal of Computational Physics*, 103(1), 16–42. [https://doi.org/10.1016/0021-9991\(92\)90324-R](https://doi.org/10.1016/0021-9991(92)90324-R)
- Levander, A. R. (1988). Fourth-order finite-difference P-SV seismograms. *GEOPHYSICS*, 53(11), 1425–1436. <https://doi.org/10.1190/1.1442422>
- Mittet, R. (2002). Free-surface boundary conditions for elastic staggered-grid modeling schemes. *GEOPHYSICS*, 67(5), 1616–1623. <https://doi.org/10.1190/1.1512752>
- Moczo, P. (2002). 3D Heterogeneous Staggered-Grid Finite-Difference Modeling of Seismic Motion with Volume Harmonic and Arithmetic Averaging of Elastic Moduli and Densities. *Bulletin of the Seismological Society of America*, 92(8), 3042–3066. <https://doi.org/10.1785/0120010167>
- Przebindowska, A. (2013). *Acoustic Full Waveform Inversion of Marine Reflection Seismic Data*.
- Rienstra, S. W., & Hirschberg, A. (2004). An introduction to acoustics. *Eindhoven University of Technology*, 18, 19.
- Robertsson, J. O. A. (1996). A numerical free-surface condition for elastic/viscoelastic finite-difference modeling in the presence of topography. *GEOPHYSICS*, 61(6), 1921–1934. <https://doi.org/10.1190/1.1444107>
- Robertsson, J. O. A., Blanch, J. O., & Symes, W. W. (1994). Viscoelastic finite-difference modeling. *GEOPHYSICS*, 59(9), 1444–1456. <https://doi.org/10.1190/1.1443701>
- Ryberg, T., Hole, J. A., Fuis, G. S., Rymer, M. J., Bleibinhaus, F., Stromeyer, D., & Bauer, K. (2012). Tomographic Vp and Vs structure of the California Central Coast Ranges, in the vicinity of SAFOD, from controlled-source seismic data. *Geophysical Journal International*, 190(3), 1341–1360. <https://doi.org/10.1111/J.1365-246X.2012.05585.X>
- Sánchez-Sesma, F. J., Iturrarán-Viveros, U., & Kausel, E. (2013). Garvin’s generalized problem revisited. *Soil Dynamics and Earthquake Engineering*, 47, 4–15. <https://doi.org/10.1016/j.soildyn.2012.11.006>
- Sochacki, J., Kubichek, R., George, J., Fletcher, W. R., & Smithson, S. (1987). Absorbing boundary conditions and surface waves. *GEOPHYSICS*, 52(1), 60–71. <https://doi.org/10.1190/1.1442241>
- Tarantola, A. (1984). Inversion of seismic reflection data in the acoustic approximation. *GEOPHYSICS*, 49(8), 1259–1266. <https://doi.org/10.1190/1.1441754>
- Thiel, N., Hertweck, T., & Bohlen, T. (2018). Comparison of acoustic and elastic full-waveform inversion of 2D towed-streamer data in the presence of salt. *Geophysical Prospecting*. Advance online publication. <https://doi.org/10.1111/1365-2478.12728>
- Virieux, J. (1986). P-SV wave propagation in heterogeneous media: Velocity-stress finite-difference method. *GEOPHYSICS*, 51(4), 889–901. <https://doi.org/10.1190/1.1442147>
- Virieux, J., Etienne, V., Cruz-Atienza, V., Brossier, R., Chaljub, E., & Coutant, O., et al. (2012). Modeling Seismic Wave Propagation for Geophysical Imaging. In M. Kanao (Ed.), *Seismic Waves - Research and Analysis*. InTech. <https://doi.org/10.5772/30219>
- Zahradník, J., Moczo, P., & Hron, F. (1993). Testing four elastic finite-difference schemes for behavior at discontinuities. *Bulletin of the Seismological Society of America*, 83(1), 107–129. <https://doi.org/10.1785/BSSA0830010107>
- Zeng, C., Xia, J., Miller, R. D., & Tsoflias, G. P. (2012). An improved vacuum formulation for 2D finite-difference modeling of Rayleigh waves including surface topography and internal discontinuities. *GEOPHYSICS*, 77(1), T1-T9. <https://doi.org/10.1190/GEO2011-0067.1>

Used Software

- Berg, P. (1994). *EX2DVAEL*. Retrieved from <http://www.quest-itn.org/library/software/ex2ddir-ex2delel-ex2dvael.html>
- Köhn, D. (2020). *DENISE-Black-Edition v1.4*. Retrieved from <https://github.com/daniel-koehn/DENISE-Black-Edition>
- Robertsson, J. (1997). *ve2d_ref*. Edited by Bleibinhaus, F. (2009), Received from Bleibinhaus, F. in 2022.

List of figures

Figure 2.1: Greens function for a 2D acoustic homogeneous medium for a receiver at 500 m offset from the source.	8
Figure 2.2: Comparison of source function (4 Hz Ricker-wavelet) and the acoustic analytical solution at 0 m offset in time- (a) and frequency domain (b)	8
Figure 2.3: Horizontal response function in normalized time and amplitude for a source at $h = 1$ and a receiver at $x = z = 1$ for a Poisson's ratio of $\nu = 0.25$ as shown by Sánchez-Sesma et al. (2013)10	10
Figure 2.4: Standard staggered grid geometry in a discrete spatial 2D Cartesian coordinate system as described by Virieux (1986) and Levander (1988).	12
Figure 2.5: Staggered finite difference grid at the free surface of a anticline with the classification of grid points along the free surface described in Table 2.2 as depicted by Robertsson (1996)	20
Figure 2.6: Grid for an irregular free-surface using the improved vacuum formulation as depicted by Zeng et al. (2012). The shadowed area represents the fictitious layer with a width of half a grid spacing, while the bold line depicts the location of the actual free-surface. For a description points annotated by Letters A through E refer to Zeng et al. (2012).	21
Figure 2.7: Kaiser windowing functions with different windowing parameters applied to the sinc functions for a source located in the middle of two grid points. The implementation of the source function is done at the grid nodes with the corresponding value at the circles after Hicks (2002)..	23
Figure 2.8: sinc function ($\text{sinc}(x)$) and spatial derivative of sinc function ($\text{sinc}'(x)$) after Hicks (2002)	24
Figure 3.1: Time function (a) and frequency spectrum (b) of a Ricker wavelet with a centre frequency of 4 Hz and its time derivative.	27
Figure 3.2: a) Time function of a Ricker wavelet with a centre frequency of 4 Hz. b) Amplitude spectrum of the wavelet.....	29
Figure 3.3: Schematic of a general model for ve2d_ref (a) and DENISE Black Edition (b) including its boundaries.	30
Figure 4.1: Synthetic seismograms of the horizontal component at an offset of 100 m from an explosive point source computed for all grid spacings in an elastic homogeneous full space for the modeling programs ve2d_ref (a) and DENISE Black Edition (b) compared to the analytical solution.....	34
Figure 4.2: Synthetic seismograms amplitude corrected of the horizontal component at an offset of 100 m from an explosive point source computed for all grid spacings in an elastic homogeneous full space for the modeling programs ve2d_ref (a) and DENISE Black Edition (b) corrected with the respective transfer functions compared to the analytical solution.....	34
Figure 4.3: Trace normalized Synthetic seismograms of the horizontal component at an offset of 100 m from an explosive point source computed for all grid spacings in an elastic homogeneous full space for the modeling programs ve2d_ref (a) and DENISE Black Edition (b) compared to the trace normalized analytical solution.	35
Figure 5.1: Schematic of a model of an elastic homogeneous full space for ve2d_ref (a) and DENISE Black Edition (b).	39
Figure 5.2: Spatial divergence of the wavefield modelled with ve2d_ref (a) and DENISE Black Edition (b) for a grid spacing of 5 m at 4 s in time.	40

Figure 5.3: Spatial curl of the wavefield modelled with ve2d_ref (a) and DENISE Black Edition (b) for a grid spacing of 5 m at 4 s in time. The amplitude scale used here is scaled to 10% of the amplitude of maximum amplitude of the spatial divergence in Figure 5.2. The space outside the outer boundary in is not used in the model.	41
Figure 5.4: Trace normalized horizontal component for different offsets modelled with ve2d_ref in a pseudo elastic homogeneous full space with $Q=10^{10}$	42
Figure 5.5: Trace normalized horizontal component in reduced time for different offsets modelled with DENISE Black Edition in an elastic homogeneous full space.	43
Figure 5.6: Relative error of the horizontal component with ve2d_ref as a function of offset for true amplitude (a) and trace normalized (b) data modelled in an elastic homogeneous full space.	44
Figure 5.7: Relative error of the horizontal component with DENISE Black Edition as a function of offset for true amplitude (a) and trace normalized (b) data modelled in an elastic homogeneous full space.	44
Figure 5.8: Trace normalized vertical component for different offsets modelled with ve2d_ref in a pseudo elastic homogeneous full space with $Q=10^{10}$	45
Figure 5.9: Trace normalized vertical component in reduced time for different offsets modelled with DENISE Black Edition in an elastic homogeneous full space.	46
Figure 5.10: Comparison of difference between synthetic and analytical vertical component for an elastic homogeneous full space.	47
Figure 5.11: Mean relative error of horizontal component (a) and mean error of vertical component relative to vector component (b) for simulated spatial discretisations.	48
Figure 6.1: Schematic for a model of an elastic homogeneous half-space for an exemplary grid spacing of 10 m.	50
Figure 6.2: Spatial divergence at 4 s in time of the wavefields modelled with the image method in ve2d_ref (a) and the improved vacuum formulation in DENISE Black Edition (b) with a grid spacing of 5 m. The different phases are labelled in the panels.	51
Figure 6.3: Spatial curl at 4 s in time of the wavefields modelled with the image method in ve2d_ref (a) and the improved vacuum formulation in DENISE Black Edition (b) with a grid spacing of 5 m. The different phases are labelled in the panels.	52
Figure 6.4 Trace normalized horizontal component in reduced time for different offsets modelled with ve2d_ref in an elastic homogeneous half-space and a free surface boundary defined with the image method.	53
Figure 6.5: Trace normalized horizontal component in reduced time for different offsets modelled with DENISE Black Edition in an elastic homogeneous half-space using the image method to define the free surface boundary.	53
Figure 6.6: Trace normalized horizontal component in reduced time for different offsets modelled with DENISE Black Edition in an elastic homogeneous half-space with an improved vacuum formulation free surface boundary.	54
Figure 6.7: Shot gather of the horizontal component of the analytical solution for a homogeneous full space with the time window over the P-wave and surface wave in reduced time.	55
Figure 6.8: Relative error to the analytical solution of the horizontal component for true amplitude (left column) and trace normalized data (right column) in the P-wave time window computed with the image method in ve2d_ref (a and b) and in DENISE Black Edition (c and d) and with the improved vacuum formulation in DENISE Black Edition (e and f).	56

Figure 6.9: Relative error to the analytical solution of the horizontal component for true amplitude (left column) and trace normalized data (right column) in the surface wave time window computed with the image method in <code>ve2d_ref</code> (a and b) and in DENISE Black Edition (c and d) and with the improved vacuum formulation in DENISE Black Edition (e and f)	58
Figure 6.10: Mean relative error of the P-wave for true amplitude and trace normalized for the horizontal (left column) and vertical component (right column). a) and b) exclude the near field offsets <500 m (500 to 24100 m) while c) and d) consider all offsets (0 to 24100 m).	60
Figure 6.11: Mean relative error of the Rayleigh wave for true amplitude and trace normalized for the horizontal (left column) and vertical component (right column). a) and b) exclude the near field offsets <500 m (500 to 24100 m) while c) and d) consider all offsets (0 to 20000 m).	61
Figure 6.12: Mean relative error for the entire trace of true amplitude and trace normalized data excluding the near field (500 to 20000 m) for the horizontal (a) and vertical component (b) plotted for the different free surface boundary condition implementations.	62
Figure 6.13: Convergence test for an elastic homogeneous half-space for the P-wave for the horizontal (a) and vertical component (b). Relative difference is calculated according to equation (4.5) and only higher resolution grid is denoted on the x-axis.	63
Figure 6.14: Convergence test for an elastic homogeneous half-space for the Rayleigh wave for the horizontal (a) and vertical component (b). Relative difference is calculated according to equation (4.5) and only higher resolution grid is denoted on the x-axis.	64
Figure 7.1: Schematic of models for two free surface boundary conditions, left image method and right improved vacuum formulation in a tilted homogeneous half-space with a dipping angle of 10° and an exemplary grid spacing of 10 m.	67
Figure 7.2: Spatial divergence of the wavefield at 3 (a and b) and 6.5 s in time (c and d) for a homogeneous half-space with a resolution of 36 ppw and free surface boundary with a tilt of 10° according to the image method with <code>ve2d_ref</code> (a and c) and improved vacuum formulation of DENISE Black Edition (b and d). The different wave phases are labelled accordingly.	69
Figure 7.3: Spatial curl of the wavefield at 3 (a and b) and 6.5 s in time (c and d) for a homogeneous half-space with a resolution of 36 ppw and free surface boundary with a tilt of 10° according to the image method with <code>ve2d_ref</code> (a and c) and DENISE Black Edition (b and d). The different wave phases are labelled accordingly.	70
Figure 7.4: Trace normalized horizontal component in reduced time for different offsets modelled in a 10° tilted elastic homogeneous half-space with a free surface boundary according to the image method of <code>ve2d_ref</code>	72
Figure 7.5: Trace normalized horizontal component in reduced time for different offsets modelled in a 10° tilted elastic homogeneous half-space with a free surface boundary according to the improved vacuum formulation of DENISE Black Edition.	72
Figure 7.6: Relative error of the horizontal receiver component to the analytical solution in the P-wave window for an elastic homogeneous half-space with a 10° tilted free surface according to the image method of <code>ve2d_ref</code> (a and b) and the improved vacuum formulation of DENISE Black Edition (c and d) for true amplitude (left column) and trace normalized data (right column).	74
Figure 7.7: Relative error of the horizontal receiver component to the analytical solution in the whole simulated traces for an elastic homogeneous half-space with a 10° tilted free surface according to the image method of <code>ve2d_ref</code> (a and b) and the improved vacuum formulation of DENISE Black Edition (c and d) for true amplitude (left column) and trace normalized data (right column).	76

- Figure 7.8: Mean relative error for the P-wave of the horizontal receiver components for free surfaces according to the image method of `ve2d_ref` (a) and improved vacuum formulation of DENISE Black Edition (b) with different tilts. The errors are calculated for 500 to 24100 m offset. 77
- Figure 7.9: Mean relative error over the whole trace of the horizontal receiver components for free surfaces according to the image method of `ve2d_ref` (a) and improved vacuum formulation of DENISE Black Edition (b) for different tilts. The errors are calculated for 500 to 20000 m offset. 78
- Figure 7.10: Mean relative error of the P-wave of the horizontal receiver components for the image method of `ve2d_ref` (a) and improved vacuum formulation of DENISE Black Edition (b) plotted against the dip angle of the free surface. The errors are calculated for 500 to 24100 m offset. 79
- Figure 7.11: Mean relative error of the whole traces of the horizontal receiver components for the image method of `ve2d_ref` (a) and improved vacuum formulation of DENISE Black Edition (b) plotted against the dip angle of the free surface. The errors are calculated for 500 to 20000 m offset. 80
- Figure 7.12: Convergence test for tilted elastic homogeneous half-spaces with different tilts for the P-wave for the image method of `ve2d_ref` (a) and improved vacuum formulation of DENISE Black Edition (b). The relative difference is computed according to equation (4.5) and only the higher resolution grid is noted on the x axis. 81
- Figure 7.13: Convergence test for tilted elastic homogeneous half-spaces with different tilts for the whole trace for the image method of `ve2d_ref` (a) and improved vacuum formulation of DENISE Black Edition (b). The relative difference is computed according to equation (4.5) and only the higher resolution grid is noted on the x axis. 82
- Figure 8.1: Map of the SAFOD site and the seismic survey conducted in 2003 near Parkfield, CA. circles denote shots and the black line from SW to NE denotes the receiver line with the model coordinates (distance along the profile in kilometres) after J. A. Hole et al. (2006). 85
- Figure 8.2: Smoothed SAFOD models of a) P-wave velocity b) S-wave velocity and c) density model for a grid spacing of 5 m with the simulated shot locations (red stars). Only the model space is shown. 87
- Figure 8.3: Damping quality factor SAFOD models of a) P-wave quality factor b) S-wave quality factor for a grid spacing of 5 m with the simulated shot locations (red stars). Only the model space is shown. 87
- Figure 8.4: Spatial divergence of the wavefield at 2.5s in time computed with a free surface according to the image method of `ve2d_ref` (a) and improved vacuum formulation of DENISE Black Edition (b) for a model with $dh = 5m$. The vertical axis is exaggerated by a factor of 2 to make phases distinguishable. Annotated wave phases: 1: primary P-wave, 3: Rayleigh wave, 5: secondary P-wave, 6: channelled direct P-waves, 10 SP-conversions. 89
- Figure 8.5: Spatial curl of the wavefield at 2.5s in time computed with a free surface according to the image method of `ve2d_ref` (a) and improved vacuum formulation of DENISE Black Edition (b) for a model with $dh = 5m$. The vertical axis is exaggerated by a factor of 2 to make phases distinguishable. Annotated wave phases: 2: S-wave, 3: Rayleigh wave, 4: PS-waves, 7: diffracted S-waves, 8: PS-waves of direct channelled P-wave, 9: PS-conversions. 90
- Figure 8.6: Shot gather of the trace normalized horizontal component of SP34 in reduced time modelled with a free surface boundary according to a) the image method with `ve2d_ref` and b) the improved vacuum formulation with DENISE Black Edition. Annotated wave phases: 1: refracted P-wave, 2: S-wave, 3: Rayleigh wave, 5: secondary P-wave. 91

Figure 8.7: Relative difference of the horizontal components whole traces of SP34 between spatial discretisations over offset for the image method of ve2d_ref (a and b) and improved vacuum formulation of DENISE Black Edition (c and d) for true amplitude (left column) and trace normalized data (right column). 93

Figure 8.8: Relative difference of the horizontal components of the P-wave and S-wave of SP34 between spatial discretisations over offset for the image method of ve2d_ref (a and b) and improved vacuum formulation of DENISE Black Edition (c and d) for true amplitude (left column) and trace normalized data (right column)..... 94

Figure 8.9: Convergence test for four different shots of the SAFOD model with a free surface according to the image method (a) and improved vacuum formulation (b) for the whole trace. The relative difference is computed according to equation (4.5) and only the higher resolution grid is noted on the x axis..... 95

Figure 8.10: Convergence test for four different shots of the SAFOD model with a free surface according to the image method (a) and improved vacuum formulation (b) for the P- and S-wave. The relative difference is computed according to equation (4.5) and only the higher resolution grid is noted on the x axis. 96

List of tables

Table 2.1: Results for the factor h for FD orders of 2 nd to 12 th order for Taylor and Holberg FD operators calculated according to equation (2.52) after Köhn (2011).....	17
Table 2.2: Classification of grid points along the free surface and the mirrored components according to the image method after Robertsson (1996).	20
Table 3.1: Grid spacing and time steps for the used test models.....	31
Table 3.2: Overview of model parameters for test models.....	32
Table 3.3: Overview of algorithm specific parameters for modeling with ve2D_ref and DENISE Black Edition.....	32
Table 8.1: Overview of modeling parameters for the SAFOD model.....	88

Appendix A

Relative errors of the vertical component for a flat free surface

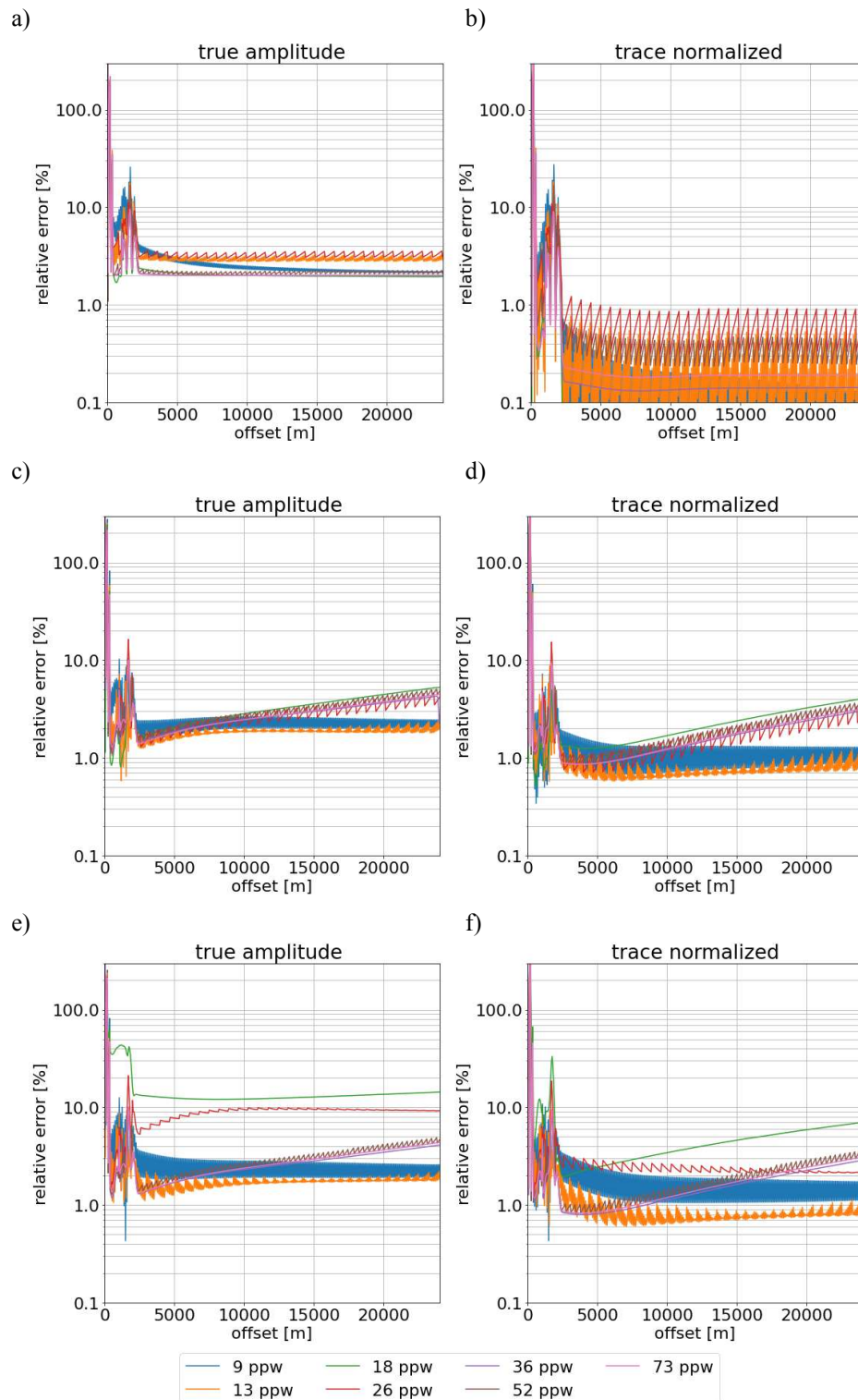


Figure A-1: Relative error of the vertical component for true amplitude (left column) and trace normalized data (right column) in the P-wave time window computed with the image method in *ve2d_ref* (a and b) and in DENISE Black Edition (c and d) and with the improved vacuum formulation in DENISE Black Edition (e and f)

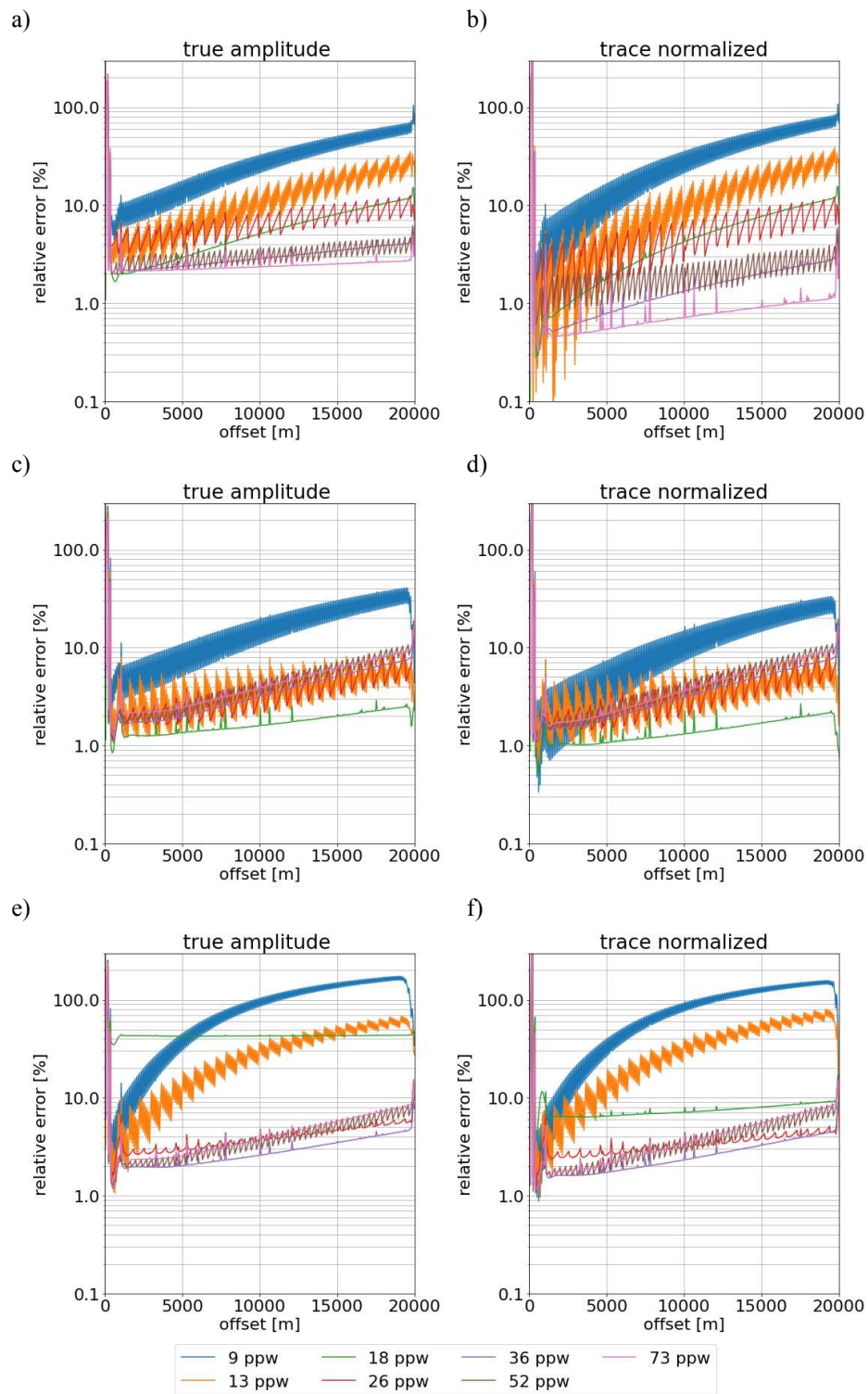


Figure A-2: Relative error of the vertical component for true amplitude (left column) and trace normalized data (right column) in the Rayleigh wave time window computed with the image method in *ve2d_ref* (a and b) and in DENISE Black Edition (c and d) and with the improved vacuum formulation in DENISE Black Edition (e and f).

Appendix B

Relative errors over offset for tilted free surfaces with 1, 5 and 20°

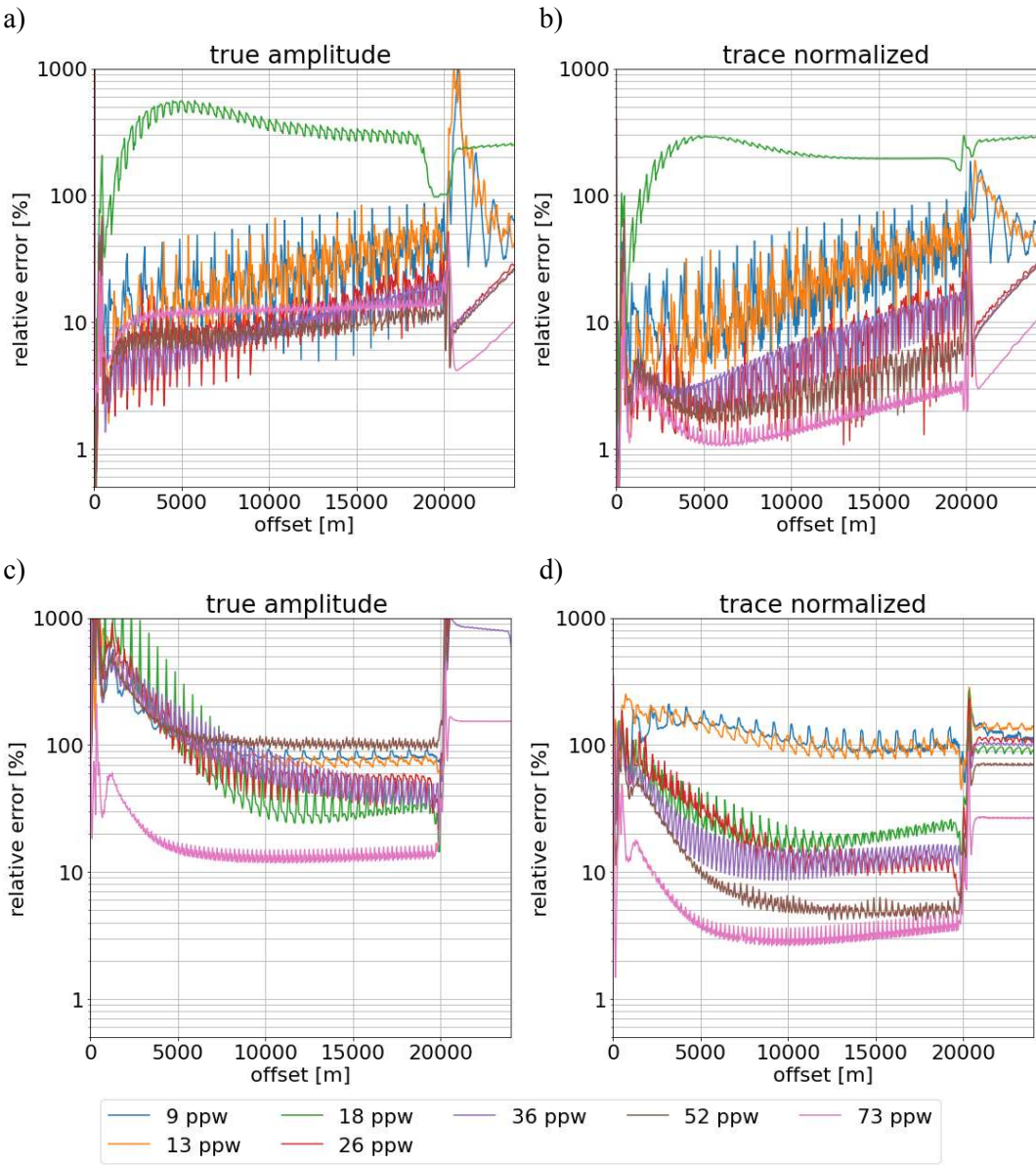


Figure B-1: Relative error of the horizontal receiver component to the analytical solution in the whole simulated traces for an elastic homogeneous half-space with a 1° tilted free surface according to the image method of *ve2d_ref* (a and b) and the improved vacuum formulation of *DENISE Black Edition* (c and d) for true amplitude (left column) and trace normalized data (right column).

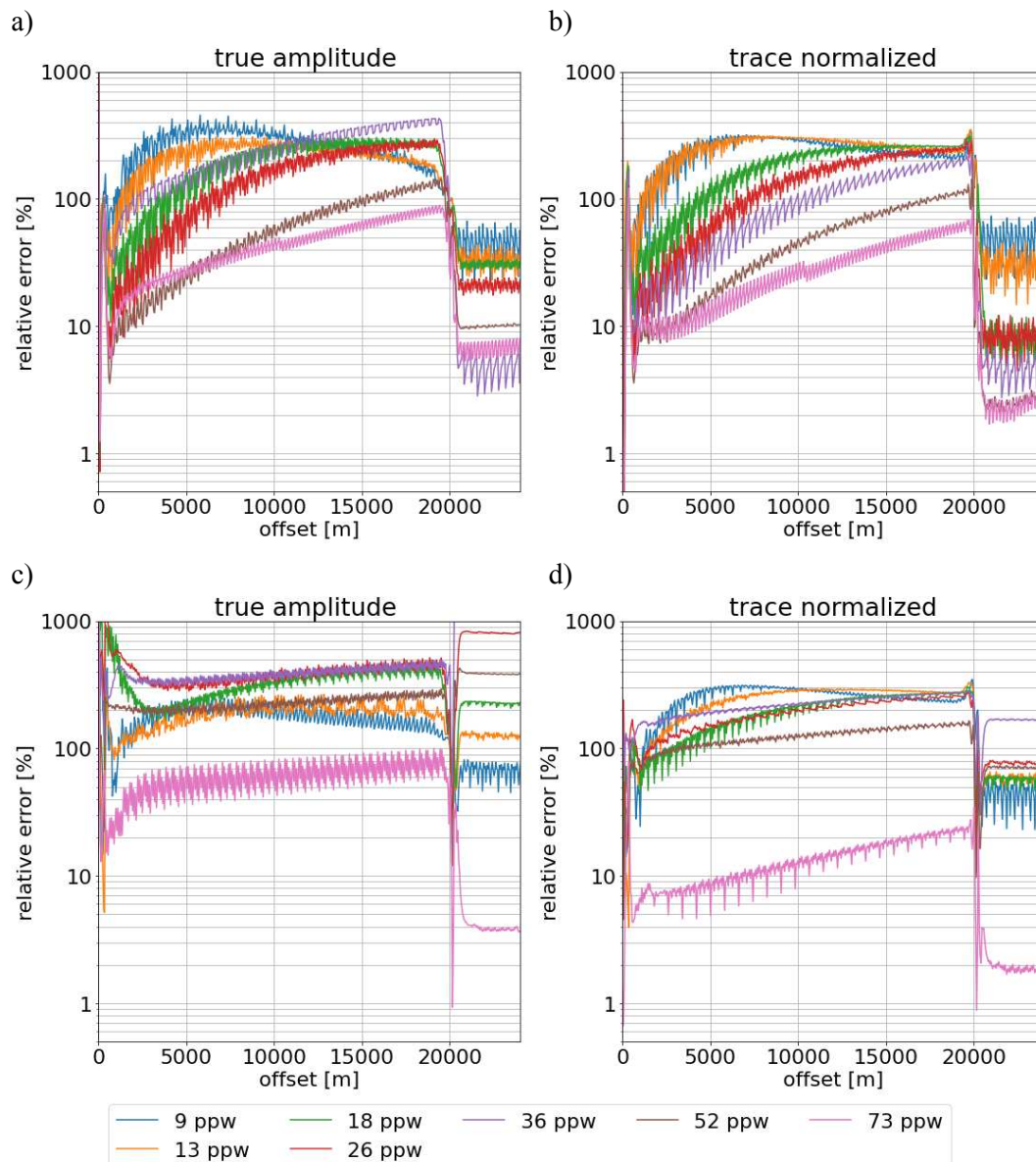


Figure B-2: Relative error of the horizontal receiver component to the analytical solution in the whole simulated traces for an elastic homogeneous half-space with a 5° tilted free surface according to the image method of *ve2d_ref* (a and b) and the improved vacuum formulation of *DENISE Black Edition* (c and d) for true amplitude (left column) and trace normalized data (right column).

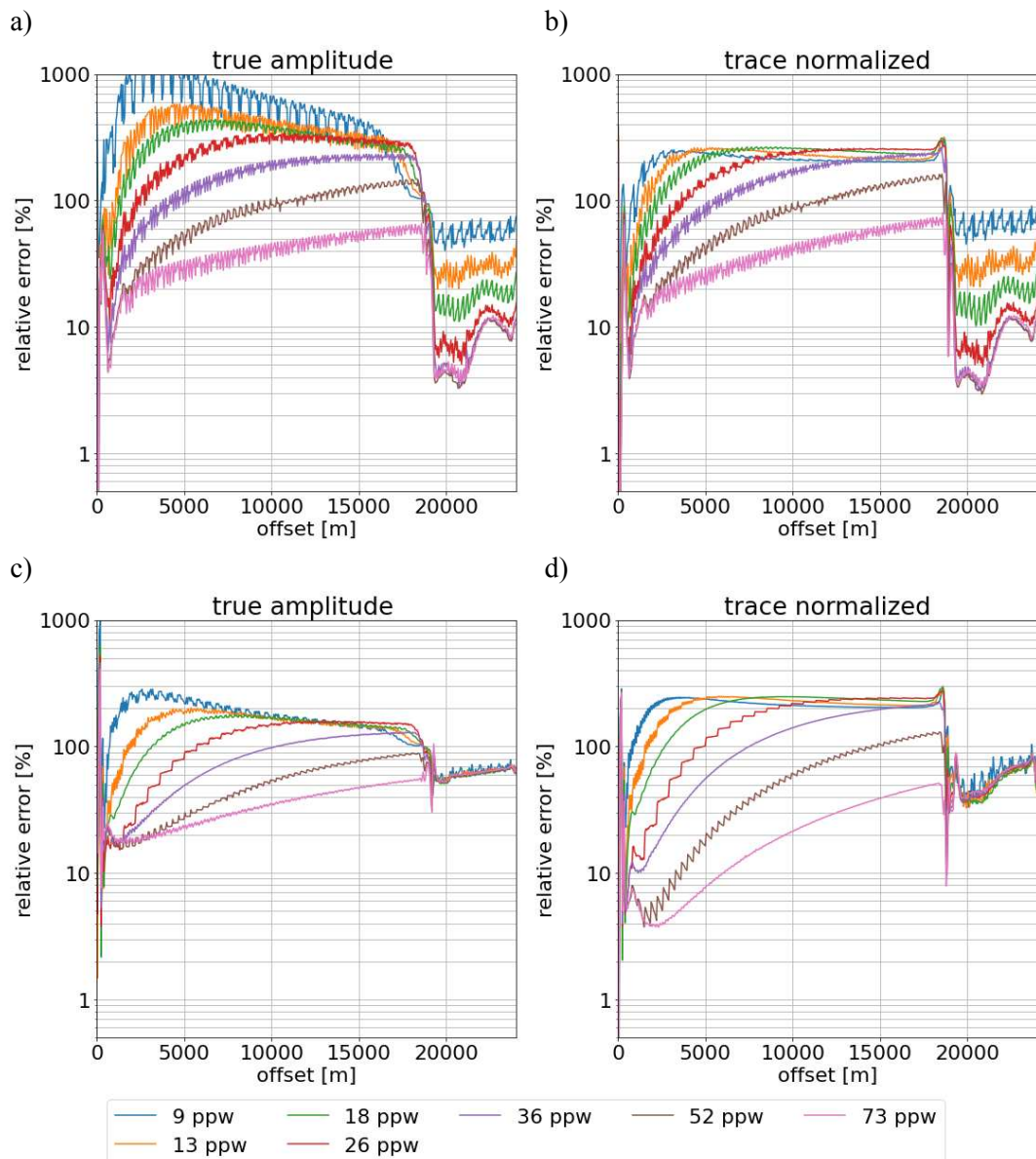


Figure B-3: Relative error of the horizontal receiver component to the analytical solution in the whole simulated traces for an elastic homogeneous half-space with a 20° tilted free surface according to the image method of `ve2d_ref` (a and b) and the improved vacuum formulation of `DENISE Black Edition` (c and d) for true amplitude (left column) and trace normalized data (right column).

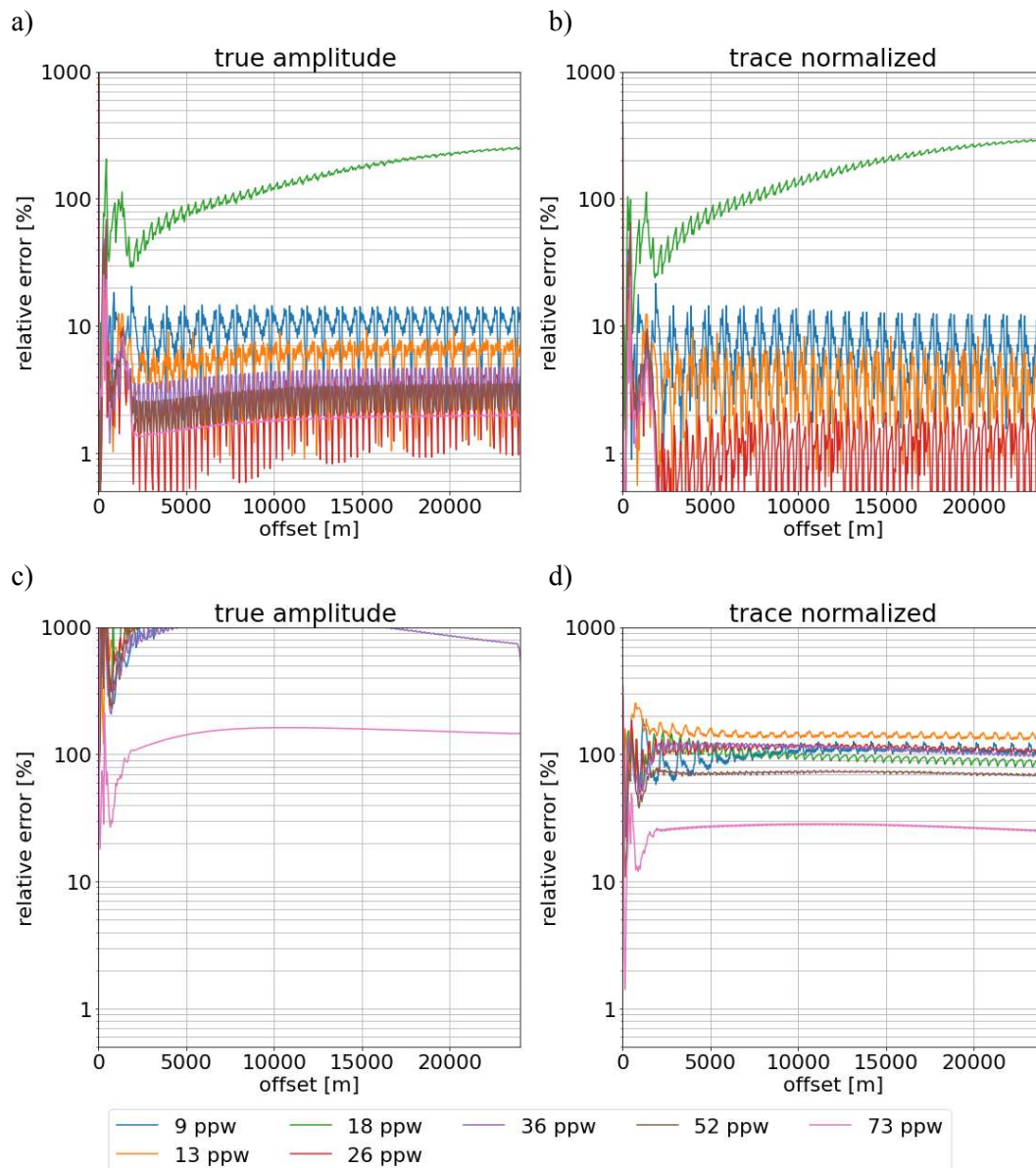


Figure B-4: Relative error of the horizontal receiver component to the analytical solution in the P-wave window for an elastic homogeneous half-space with a 1° tilted free surface according to the image method of `ve2d_ref` (a and b) and the improved vacuum formulation of `DENISE Black Edition` (c and d) for true amplitude (left column) and trace normalized data (right column).

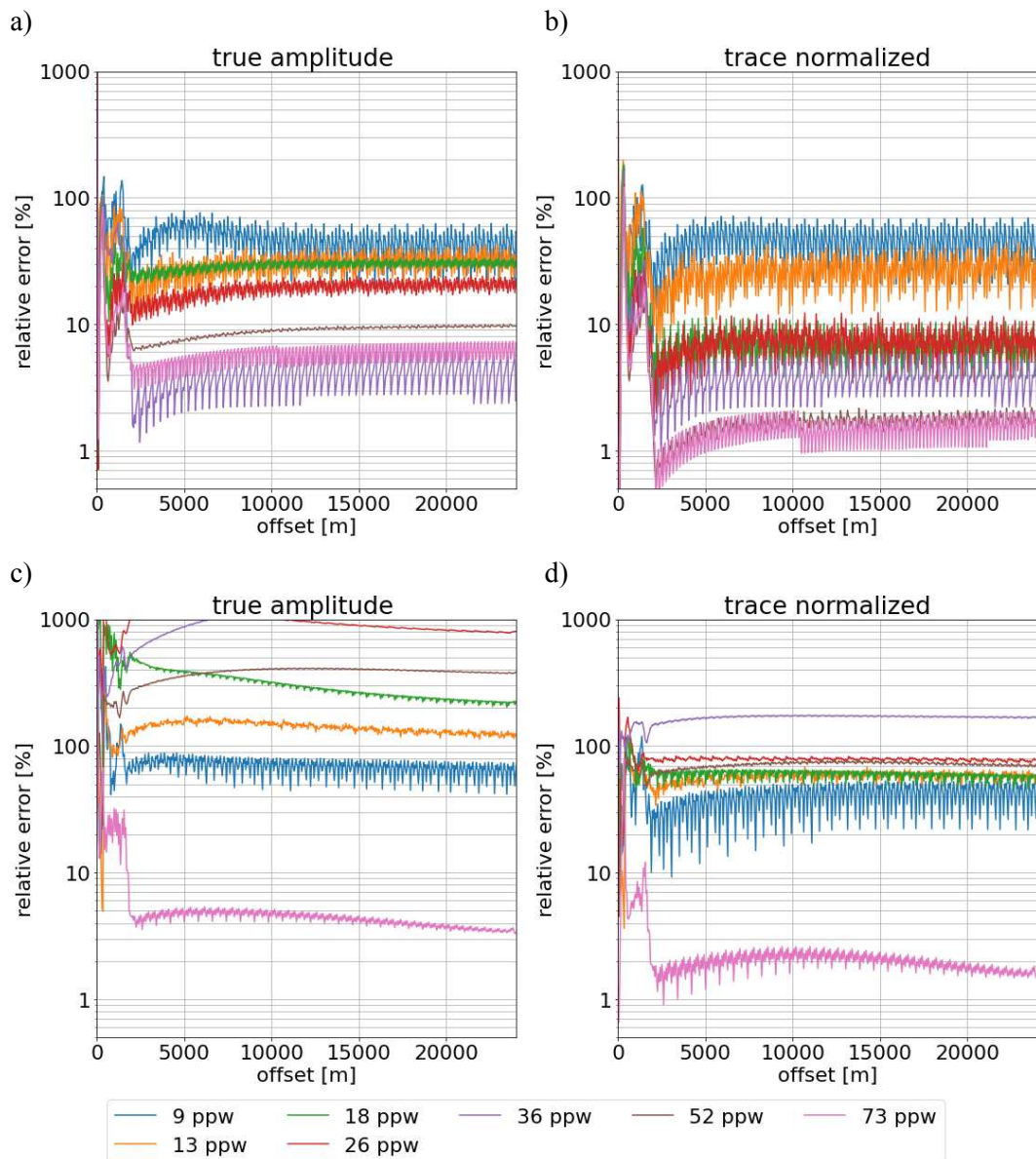


Figure B-5: Relative error of the horizontal receiver component to the analytical solution in the P-wave window for an elastic homogeneous half-space with a 5° tilted free surface according to the image method of `ve2d_ref` (a and b) and the improved vacuum formulation of DENISE Black Edition (c and d) for true amplitude (left column) and trace normalized data (right column).

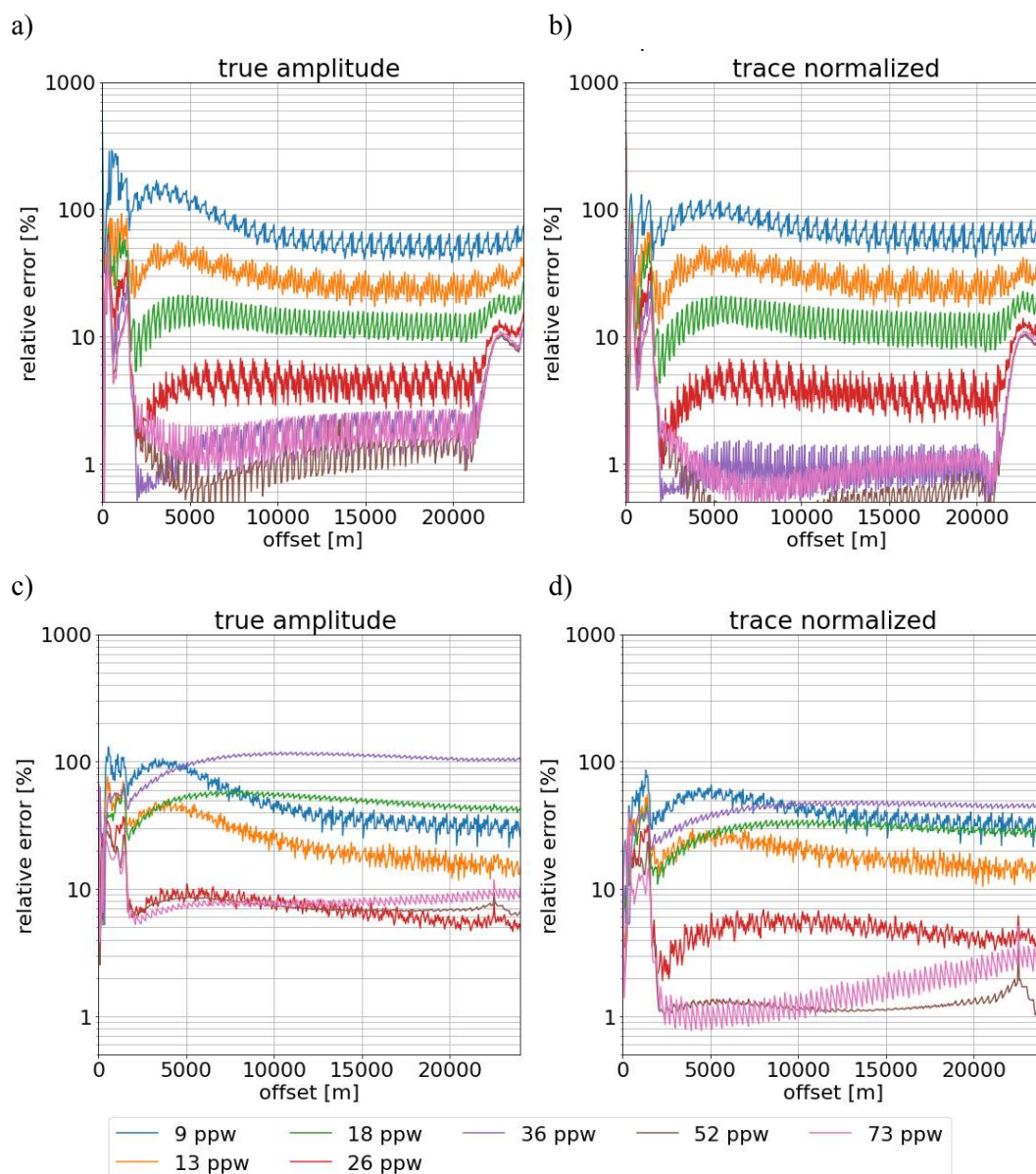


Figure B-6: Relative error of the horizontal receiver component to the analytical solution in the P-wave window for an elastic homogeneous half-space with a 20° tilted free surface according to the image method of *ve2d_ref* (a and b) and the improved vacuum formulation of *DENISE Black Edition* (c and d) for true amplitude (left column) and trace normalized data (right column).

Appendix C

SAFOD model convergence over offsets horizontal component

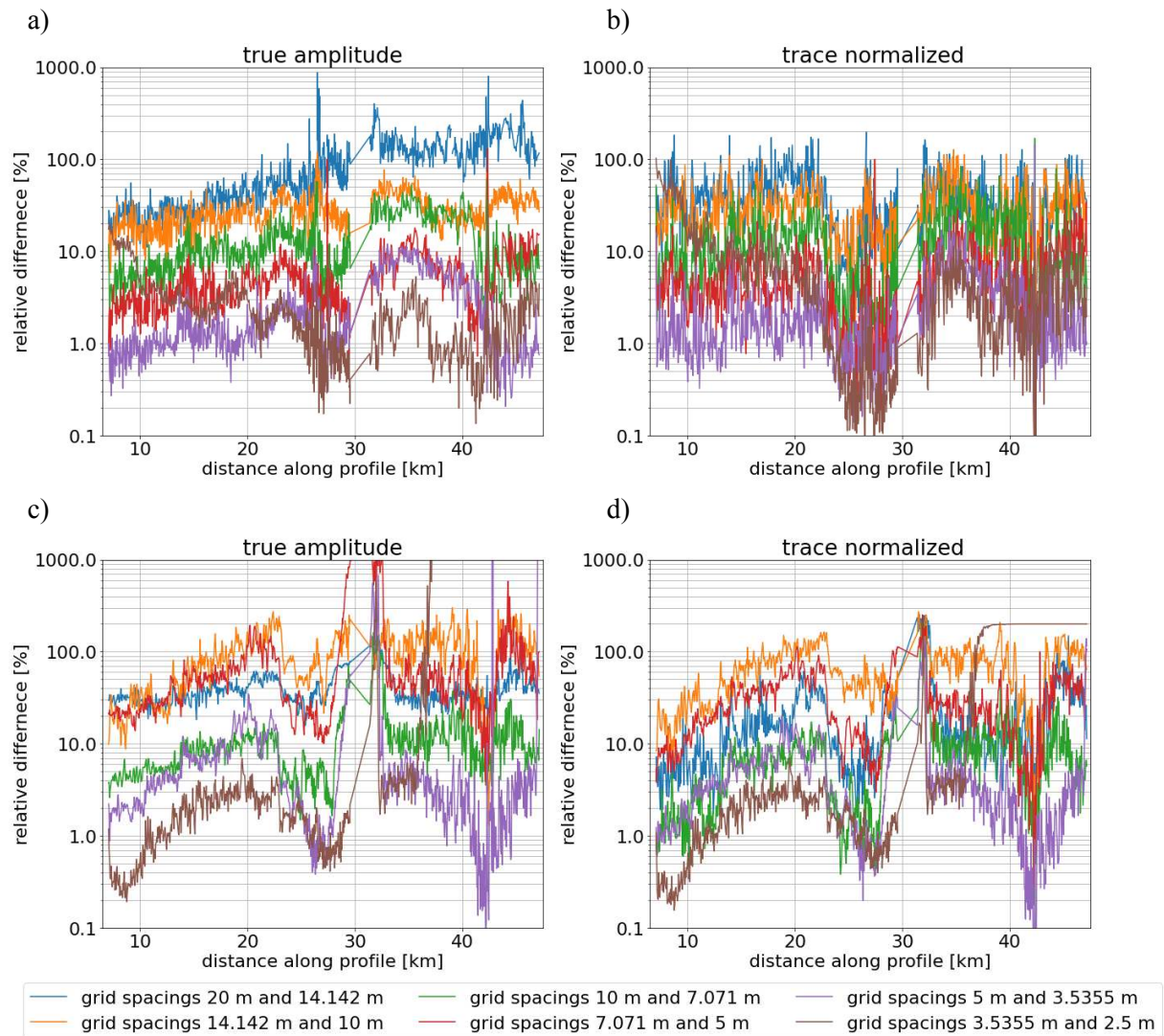


Figure C-1: Relative difference of the horizontal components whole traces of SP08 between spatial discretisations over offset for the image method of *ve2d_ref* (a and b) and improved vacuum formulation of DENISE Black Edition (c and d) for true amplitude (left column) and trace normalized data (right column).

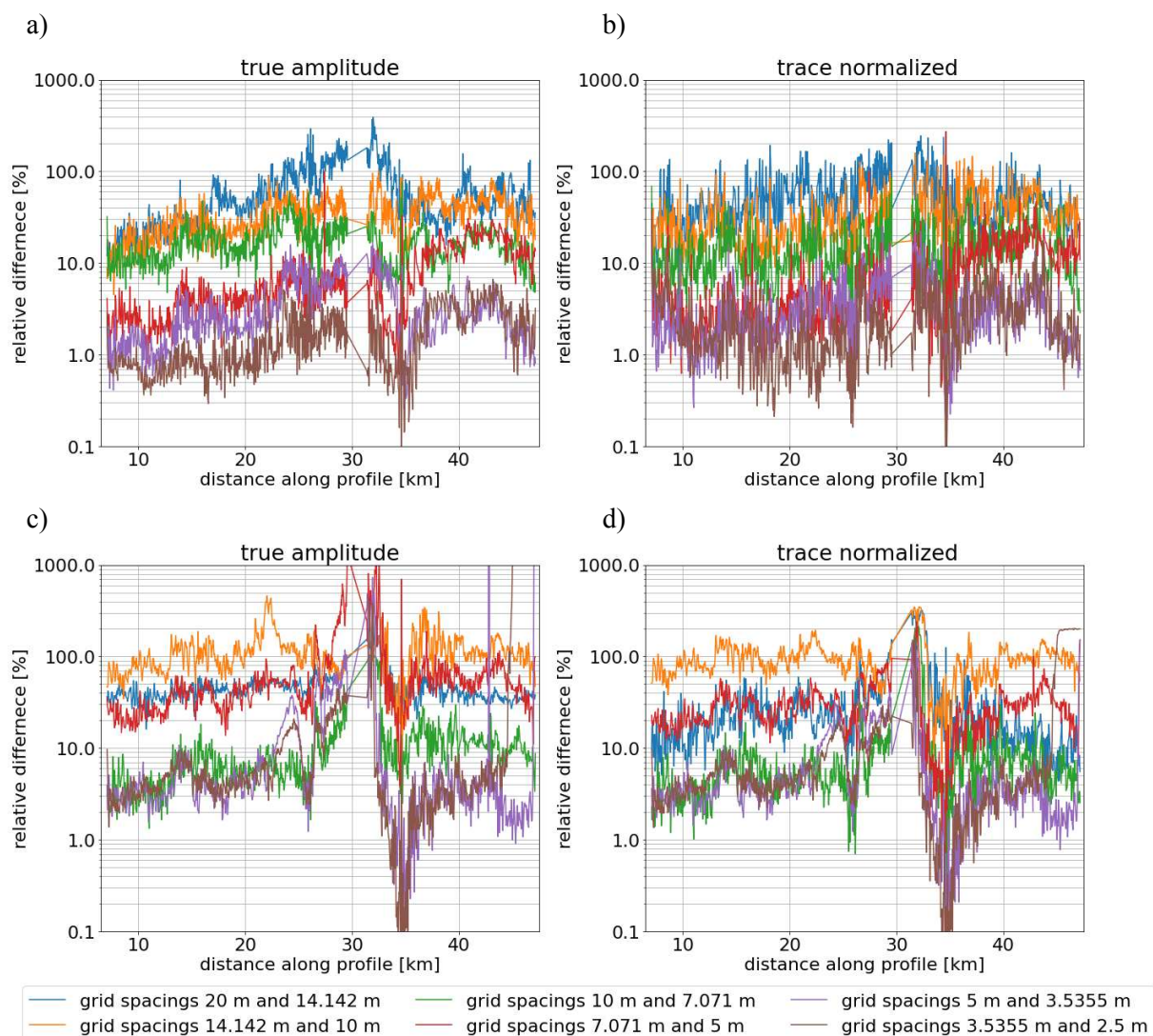


Figure C-2: Relative difference of the horizontal components whole traces of SP17 between spatial discretisations over offset for the image method of `ve2d_ref` (a and b) and improved vacuum formulation of DENISE Black Edition (c and d) for true amplitude (left column) and trace normalized data (right column) of the for the.

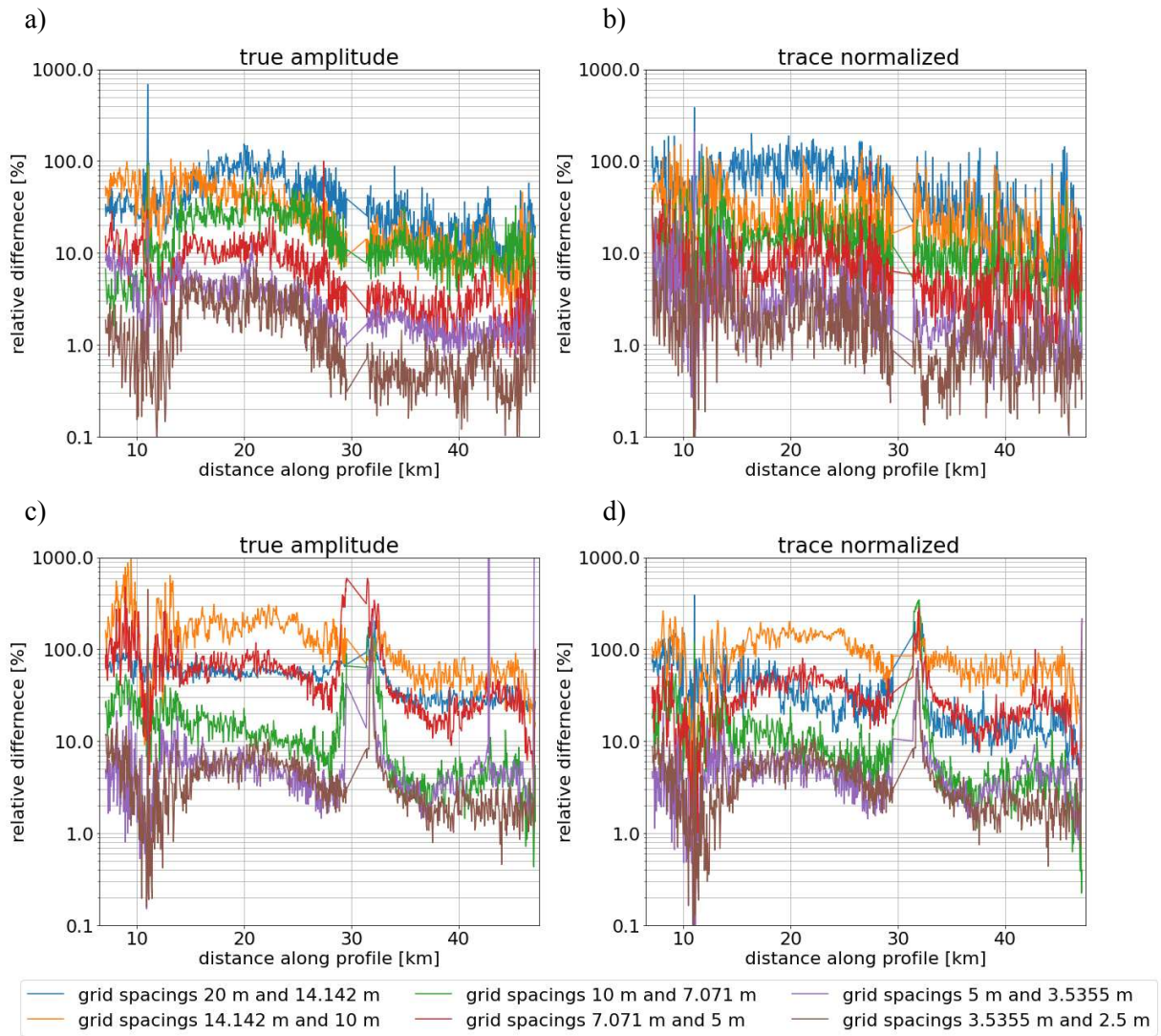


Figure C-3: Relative difference of the horizontal components whole traces of SP56 between spatial discretisations over offset for the image method of *ve2d_ref* (a and b) and improved vacuum formulation of DENISE Black Edition (c and d) for true amplitude (left column) and trace normalized data (right column).

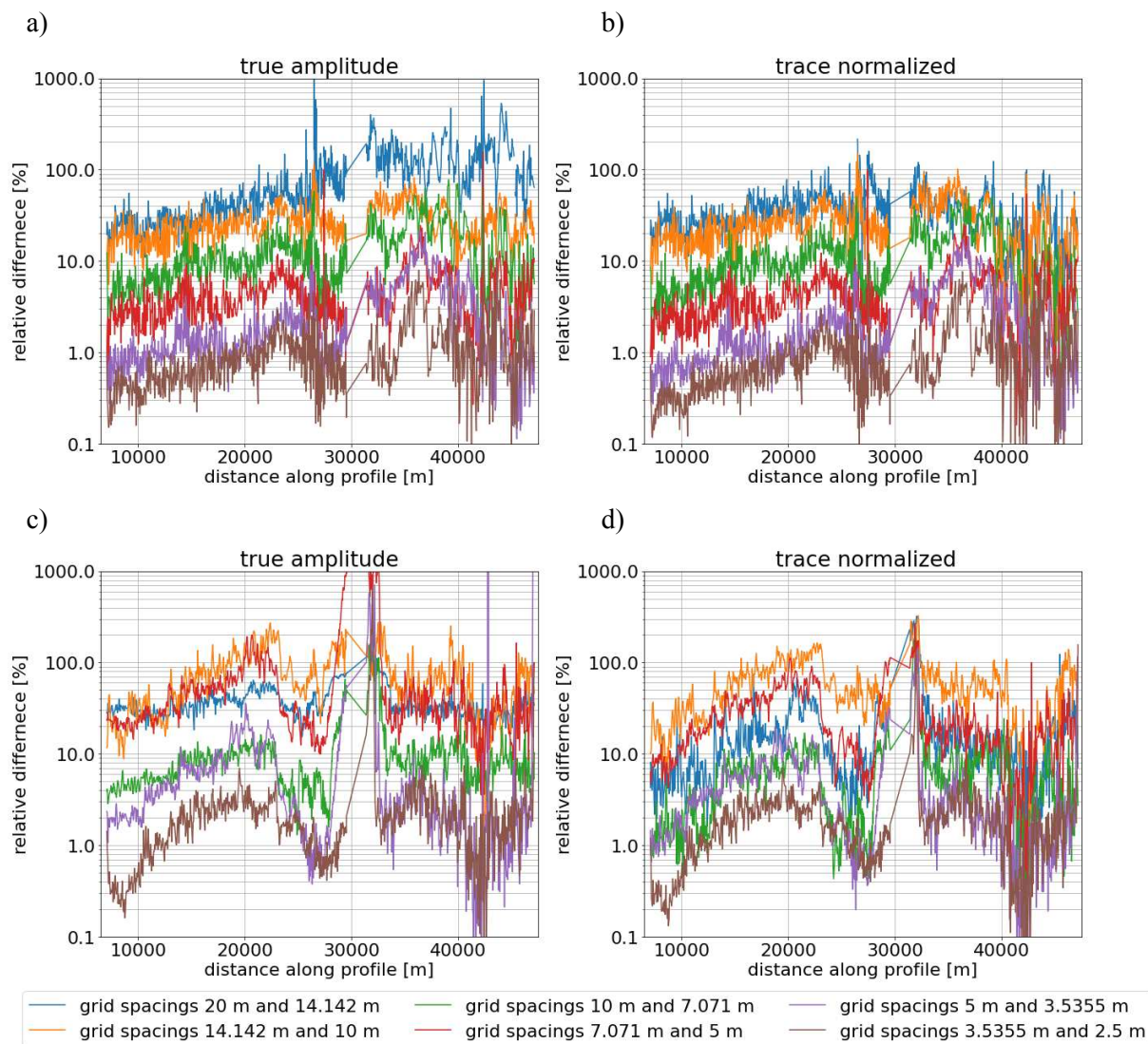


Figure C-4: Relative difference of P- and S-waves of the horizontal components of SP08 between spatial discretisations over offset for the image method of `ve2d_ref` (a and b) and improved vacuum formulation of DENISE Black Edition (c and d) for true amplitude (left column) and trace normalized data (right column).

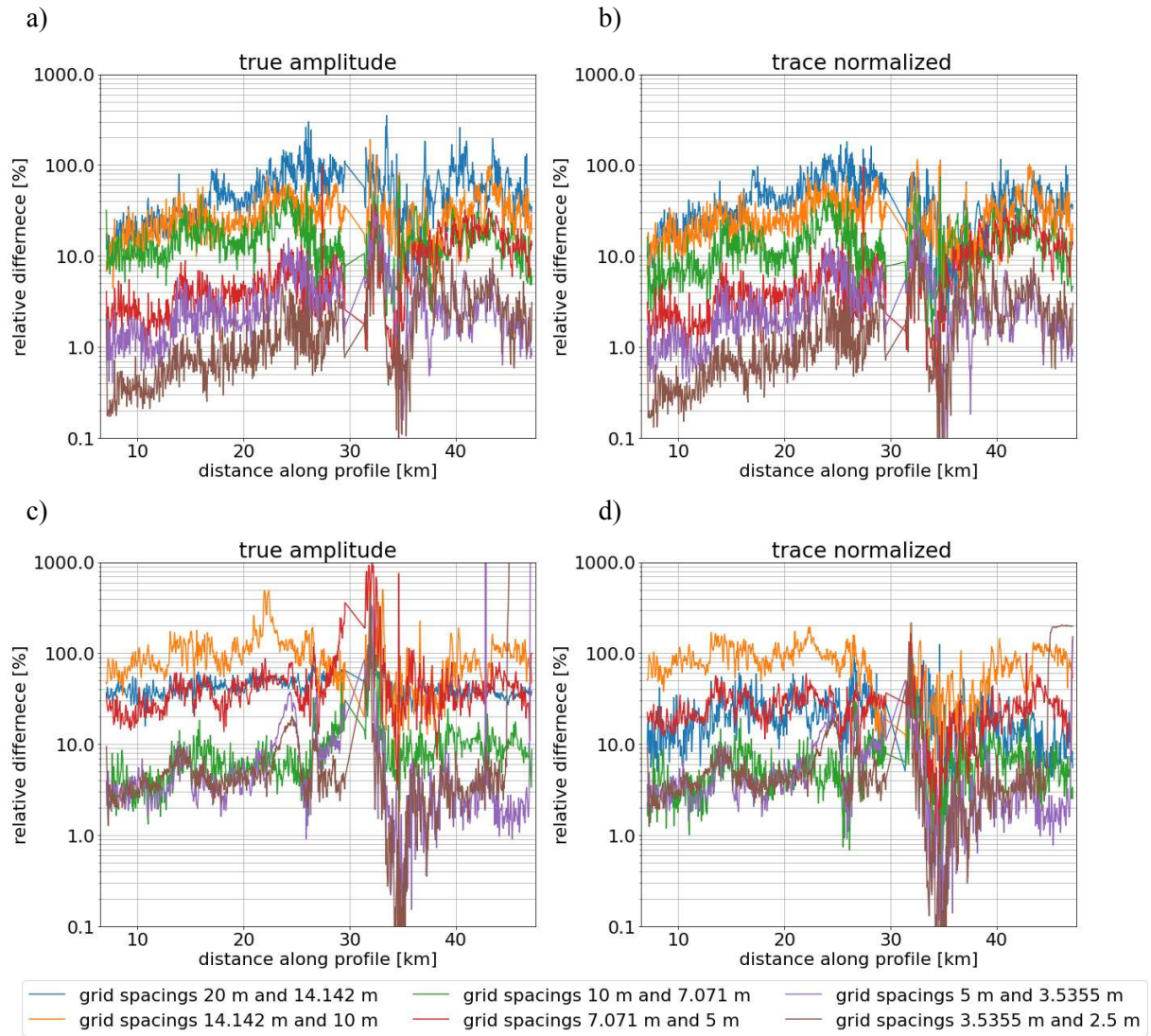


Figure C-5: Relative difference of P- and S-waves of the horizontal components of SP17 between spatial discretisations over offset for the image method of *ve2d_ref* (a and b) and improved vacuum formulation of DENISE Black Edition (c and d) for true amplitude (left column) and trace normalized data (right column).

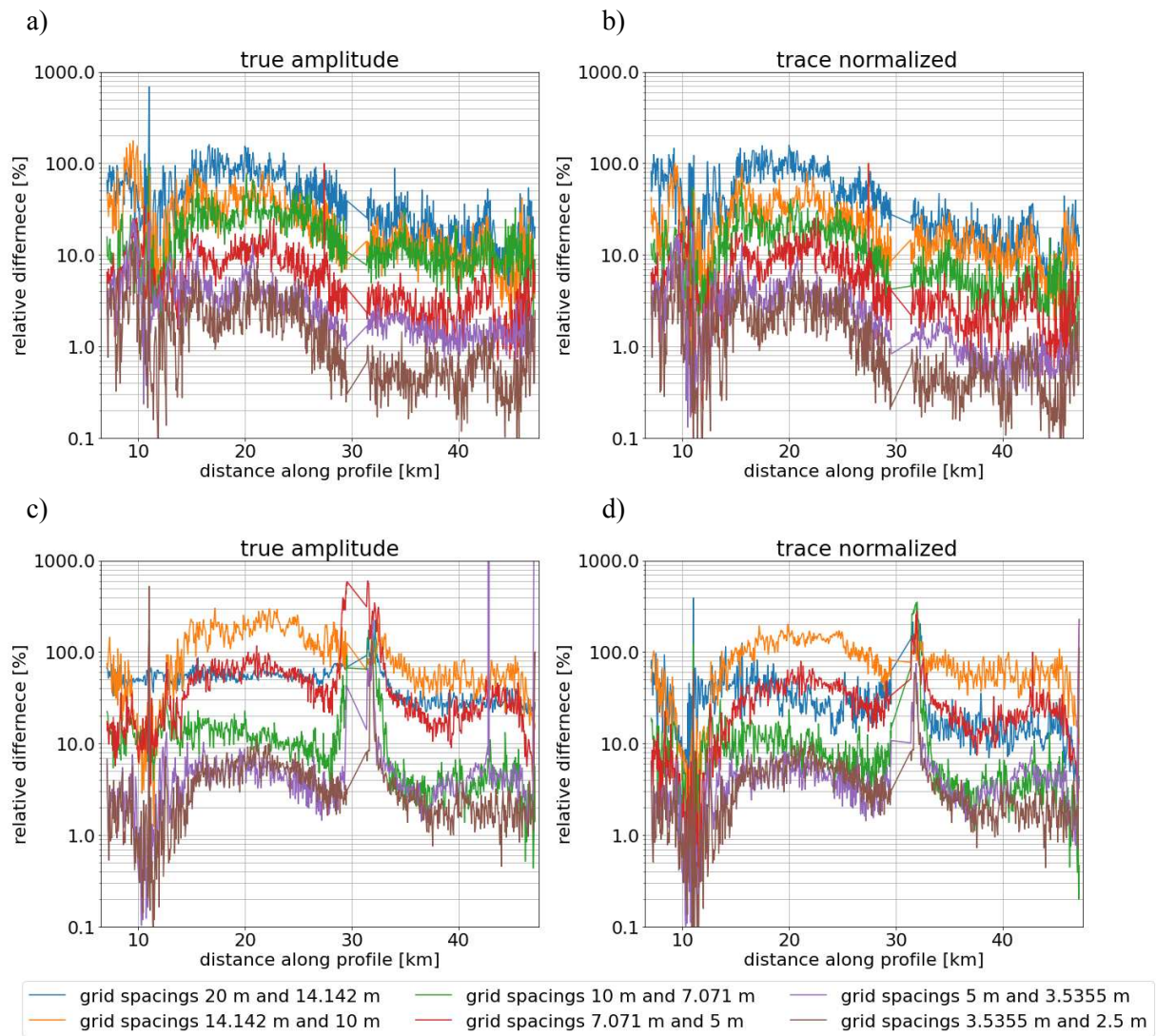


Figure C-6: Relative difference of P- and S-waves of the horizontal components of SP56 between spatial discretisations over offset for the image method of *ve2d_ref* (a and b) and improved vacuum formulation of *DENISE Black Edition* (c and d) for true amplitude (left column) and trace normalized data (right column) of the for the.